Dissertation
submitted to the
Combined Faculty of
Natural Sciences and Mathematics
of the
Ruperto-Carola-University of Heidelberg,
Germany
for the degree of
Doctor of Natural Sciences

Put forward by

Dipl. Phys. Jennifer Schober
Born in: Miltenberg, Germany

Oral examination: 15 October 2014

On the Role of the Turbulent Dynamo in the Evolution of Cosmic Magnetic Fields

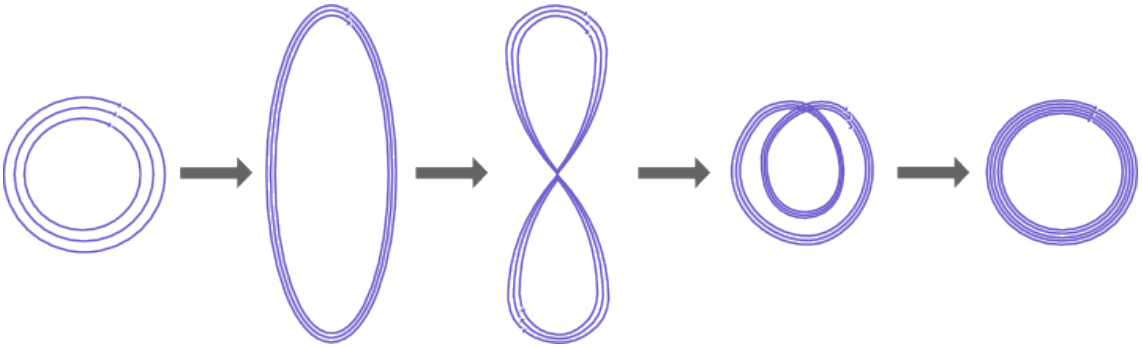

Referees:

Prof. Dr. Ralf S. Klessen

Prof. Dr. Matthias Bartelmann

To my parents.

Zusammenfassung

Ziel dieser Arbeit ist es den Ursprung von Magnetfeldern im Universum zu erforschen. Wir schlagen vor, dass der turbulente oder auch kleinskalige Dynamo, der in Gegenwart von Turbulenz Saatfelder auf kurzen Zeitskalen verstärkt, eine wichtige Rolle in der Entwicklung kosmischer Magnetfelder spielt. Das theoretische Modell des turbulenten Dynamos wird auf verschiedene astrophysikalische Umgebungen verallgemeinert, wobei der Schwerpunkt auf der Beschreibung unterschiedlicher Turbulenzspektren liegt. Wir leiten analytische Lösungen für die Wachstumsrate des Dynamos in der kinematischen Phase her und diskutieren die darauf folgende nicht-lineare Phase sowie die Saturierung. Nach heutigem Erkenntnisstand findet ein effizientes Treiben von Turbulenz in der Entwicklung des Universums späestens während der Entstehung der ersten Sterne und Galaxien statt. Hier wird gravitative Energie durch Akktretion von umliegendem Gas in die Dunkle Materie Halos in chaotische Bewegungen umgewandelt. Wir modellieren diese Prozesse semianalytisch und implementieren Magnetfeld-Verstärkung durch einen turbulenten Dynamo. Unsere Ergebnisse zeigen, dass ungeordnete Magnetfelder mit Stärken, die vergleichbar mit jenen in heutigen Galaxien sind, schon im primordialen Universum gegenwärtig gewesen sein können. Abschließend stellen wir eine potentielle Beobachtungsmethode für Magnetfelder in jungen Galaxien vor, mit der das von uns beschriebene Szenario für die Entwicklung kosmischer Magnetfelder untersucht werden könnte.

Abstract

The aim of this work is to explore the origin of magnetic fields in the Universe. We claim that the turbulent or small-scale dynamo, which amplifies weak seed fields on short timescales in the presence of turbulence, plays an important role in the evolution of cosmic magnetic fields. The theoretical model for the turbulent dynamo is generalized for various astrophysical environments, with a focus on different turbulence spectra. We derive analytical solutions for the dynamo growth rate in the kinematic phase and discuss the subsequent non-linear evolution as well as saturation. In the history of the Universe turbulence is expected to be driven efficiently at the latest during the formation of the first stars and galaxies, where gravitational energy is converted into chaotic motions as the dark matter halos accrete gas from the environment. We model these processes semi-analytically and implement magnetic field amplification by a turbulent dynamo. Our results show that unordered magnetic fields, with strengths comparable to the ones in local galaxies, were already present in the primordial Universe. A potential observational test for magnetic fields in young galaxies is suggested to probe our proposed scenario for the evolution of cosmic magnetic fields.

List of publications

The following publications are partially presented in this thesis.

1. **Schober J.**, Schleicher D. R. G. and Klessen R. S. (2014):
   X-Ray Emission from Starforming Galaxies - Signatures of Cosmic Rays and Magnetic Fields
   (submitted to Mon. Not. R. Astron. Soc.)

2. **Schober J.**, Schleicher D. R. G. and Klessen R. S. (2013):
   Magnetic Field Amplification in Young Galaxies
   (published in Astron. & Astrophys., 560:87)

3. Schleicher D. R. G., **Schober J.**, Federrath C.,Bovino S. and Schmidt W. (2013):
   The Small-Scale Dynamo: Breaking Universality at High Mach Numbers
   (published in New J. of Phys., 15:2)

4. Bovino S., Schleicher D. R. G. and **Schober J.** (2013):
   Turbulent Magnetic Field Amplification from the Smallest to the Largest Magnetic Prandtl Numbers: Implications of the Turbulent Spectra
   (published in New J. of Phys., 15:1)

5. **Schober J.**, Schleicher D. R. G., Bovino S. and Klessen R. S. (2012):
   The Small-Scale Dynamo at Low Magnetic Prandtl Numbers
   (published in Phys. Rev. E, 86:6)

6. **Schober J.**, Schleicher D. R. G., Federrath C., Glover S., Klessen R. S. and Banerjee R. (2012):
   The Small-Scale Dynamo and Non-Ideal Magnetohydrodynamics in Primordial Star Formation
   (published in Astrophys. J., 754:2)

7. **Schober J.**, Schleicher D. R. G., Federrath C., Klessen R. S. and Banerjee R. (2012):
   Magnetic Field Amplification by Small-Scale Dynamo Action: Dependence on Turbulence Models and Reynolds and Prandtl Numbers
   (published in Phys. Rev. E, 85:2)

8. Federrath C., Chabrier G., **Schober J.**, Banerjee R., Klessen R. S. and Schleicher D. R. G. (2011):
   Mach Number Dependence of Turbulent Magnetic Field Amplification: Solenoidal versus Compressive Flows
   (published in Phys. Rev. Let., 107:11)

Contents

CHAPTER 1

Introduction

1.1 The Mysterious Nature of Cosmic Magnetic Fields

In order to understand the formation, the evolution and the current properties of astrophysical objects, one needs to estimate the main forces acting on matter. With its infinitely extending range, gravity is the main candidate for shaping the large-scale structure of the Universe. However, with an estimated fraction of more than 99 %, baryonic matter is predominately in a plasma state, i.e. it includes electrically charged particles (see, e.g. Gurnett & Bhattacharjee, 2005). The dynamics of these are influenced by the second long-range fundamental force, the electromagnetic force. Indeed, observations show that the Universe is highly magnetized. Magnetic fields are observed on all scales, from planets (e.g. Stevenson, 2003) and stars (e.g. Donati & Landstreet, 2009) via galaxies (e.g. Beck & Wielebinski, 2013) up to the intergalactic medium, where fields might be correlated on Mpc-scales (e.g. Neronov & Vovk, 2010). In many cases, for instance in the interstellar medium, the magnetic energy density is comparable to the thermal energy density and the one of turbulence and cosmic rays (Draine, 2011). This phenomenon is known as energy equipartition and indicates a strong coupling between the individual energy components.
With these observational facts many urgent questions turn up, which can be categorized into two main complexes:

- How are magnetic fields generated and how do they evolve in time?
- How do magnetic fields influence astrophysical processes?

Even though we will discuss certain aspects of the second question, in this work we concentrate on the first, very general, question of their origin and evolution. This is a very active area of research (see, e.g. Kulsrud & Zweibel, 2008), which still yields many uncertainties and unknowns. Strongly debated questions are for example:

- Under which conditions can magnetic fields be generated?
- How strong are the first magnetic fields?
- How are they amplified in astrophysical motions?
- Which fraction of the magnetic energy is dissipated again?
- When and in which environments do magnetic fields reach dynamically important strengths?
- How is the magnetic energy distributed over spacial scales?
- How changes magnetic topology during the amplification and dissipation processes?

In this thesis we address most of the upper questions, while we concentrate on the question of how week magnetic seed fields are amplified to dynamically important magnitudes. For this purpose we use a semi-analytical approach, which allows us to follow the evolution of cosmic magnetic fields.

1.2 Magnetic Fields in the Universe

1.2.1 Origin and Evolution of Cosmic Magnetic Fields

Our suggestion for the origin of cosmic magnetic fields is illustrated in figure 1.1. In this section we discuss the basics of the evolution of magnetic fields in the Universe from the first weak seed fields to strong large-scale fields.

Magnetic Seed Fields

Presumably the first magnetic seed fields have already been generated in the very early Universe, i.e. during inflation (Turner & Widrow, 1988) and in the early cosmological phase transitions (see, e.g. Cheng & Olinto, 1994; Baym et al., 1996; Sigl et al., 1997). It is important to note that the coherence length of these fields is always limited by the Hubble length at the time of generation and that the magnetic fields are subsequently diluted by cosmic expansion.
Other generation mechanisms are possible in plasma physical processes, where the different dynamical behavior of electrons and ions is taken into account. The well-established Bierman battery (Biermann, 1950) is a consequence of two-fluid magnetohydrodynamics and operates when there are non-parallel gradients in density and temperature leading to charge separation and the generation of a magnetic field.
A common property of magnetic seed fields is, however, their extremely low field strength. Typical field strengths produced by a Biermann battery are of the order of 10^{-19} G (e.g. Gnedin et al., 2000; Xu et al., 2008), while generation mechanisms in the very early Universe typically predict a field strength many orders of magnitude

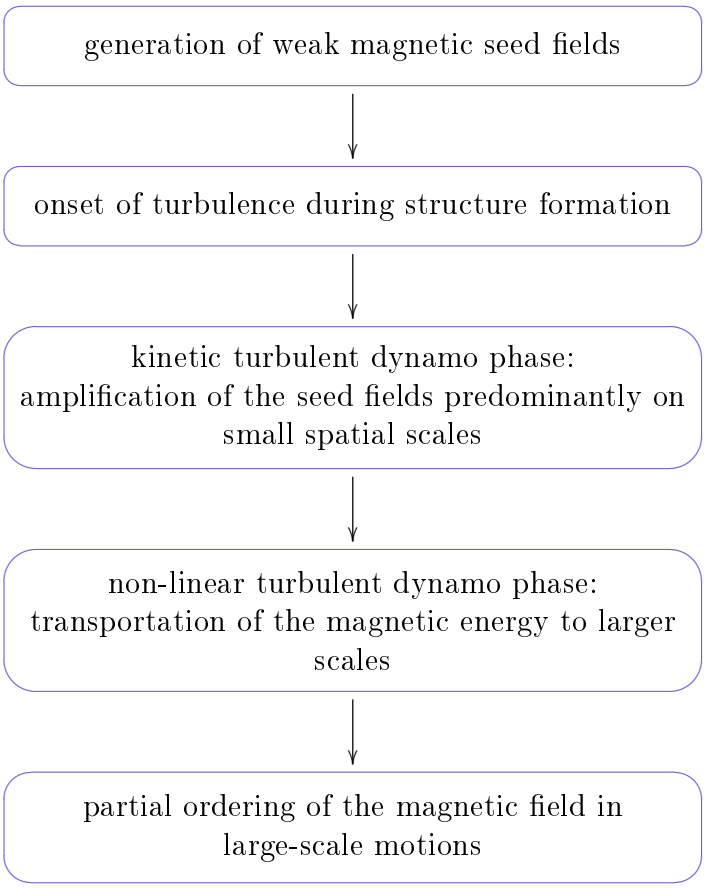

Figure 1.1:
Our suggestion for the origin of cosmic magnetic fields: From weak magnetic seed fields to dynamically important fields correlated on large scales via magnetohydrodynamical dynamos.

below that. Thus, in order to explain the nature of magnetic fields at present day, which reach values of 10^{-5} G in ordinary galaxies, phases of efficient field amplification are unavoidable.

Amplification by a Turbulent Dynamo

The magnetic field strength can be increased in gas motions, when the field lines are frozen into the fluid. Amplification takes place in gravitational compression that goes along with the formation of structure. The absolute factor by which the field strength increases solely in gas compression is, however, not sufficient to explain the magnetic fields in present-day astrophysical objects.
Very popular and more efficient mechanisms for field amplification are so-called *magnetohydrodynamical dynamos*, i.e. mechanisms that convert kinetic energy into

magnetic energy (see Brandenburg & Subramanian, 2005, for a detailed review). Especially the *small-scale* or *turbulent dynamo* seems to play an outstanding role in the history of cosmic magnetic fields, as it amplifies fields exponentially in time with very large growth rates on small scales. In presence of turbulence, the turbulent dynamo amplifies weak seed fields by randomly stretching, twisting and folding the field lines. As pointed out before, the amplification proceeds predominantly on tiny scales, however, the magnetic energy is transported also to larger scales in an inverse cascade during the non-linear dynamo phase (e.g. Schekochihin et al., 2002). The result is a strong unordered magnetic field that is present on all spatial scales between the viscous and the forcing scale of turbulence.
The requirement for small-scale dynamo action is certainly a sufficient amount of turbulence in an ionized medium. In the local Universe turbulence is omnipresent (see e.g. Elmegreen & Scalo, 2004, for a review on interstellar turbulence). We assume that this is also true for the primordial Universe, were turbulence is driven at the latest during the accretion of gas in structure formation (Greif et al., 2008). In combination with the presence of weak magnetic seed fields the turbulent dynamo is initiated. Thus, the formation of the first stars and galaxies marks not only an important transition from the dark to the bright Universe, but is also a crucial phase in the evolution of cosmic magnetic fields.
The existence of turbulent magnetic field amplification during structure formation has been observed in first high-resolution numerical simulations. For example, Sur et al. (2010) report the exponential growth of the magnetic energy in the collapse of a primordial minihalo leading to the presence of strong magnetic fields already during the formation of the first stars in the Universe. A turbulent dynamo also operates in the simulations of more massive halos (Latif et al., 2012), in which the first galaxies are expected to form. This conclusion is confirmed by Pakmor et al. (2014) in full cosmological simulations of Milky Way-like disk galaxies, in which tiny seed fields are amplified up to a significant fraction of the kinetic energy on short timescales.

Ordering of the Random Magnetic Fields

While the field amplification by the turbulent dynamo proceeds very fast during structure formation, it can only explain the build up of unordered magnetic fields. However, observations show that the field structure in local galaxies includes a large-scale ordered component (see e.g. Beck & Wielebinski, 2013). The ordering of the magnetic field presumably takes place in large-scale rotational motions, which are described by a *large-scale galactic dynamo*. The typical timescales of this large-scale dynamo should be comparable to the duration of galactic rotation and are thus usually very long.

1.2.2 Effects of Magnetic Fields on Astrophysical Processes

It is important to realize that cosmic magnetic fields and other astrophysical processes, like the formation of structure in the Universe, evolve in a dynamical interplay. The amplification and dissipation of magnetic energy is determined by the dynamics of astrophysical objects and the other way around.
In galaxies the magnetic energy density reaches values that are comparable to the thermal one, the turbulent kinetic one and the one of cosmic rays (Beck, 2007; Draine, 2011). This energy equipartition indicates a strong coupling between the individual energy components. We know from simulations and observations that the process of star formation is crucially influenced by the galactic magnetic fields. For instance the formation of molecular clouds, the birth places of stars, can be explained by instabilities in galaxies that result from magnetic fields. To the star formation process itself magnetic fields add on the one hand an additional pressure and on the other hand provide efficient additional ways to transport angular momentum via magnetic braking, the magneto-rotational instability and the formation of jets and outflows. These processes influence the properties of the generated stars strongly in terms of their multiplicity and mass distribution. Thus, in order to understand the evolution of galaxies and the stars within them the knowledge of the evolution of magnetic fields is crucial.

1.2.3 Prospects of Future Magnetic Field Observations

With future instruments we will be able to observe magnetic fields at higher redshifts and by this gain direct insights into their evolution in time. A very important role will play a new generation of giant radio telescopes, especially the *Square Kilometer Array* (SKA) and its pathfinders like the *Low Frequency Array* (LOFAR). Their sensibility is expected to be high enough in order to detect synchrotron radiation, a signature of cosmic rays spiraling around magnetic field lines and thus a measure for the field strength, up to redshifts of 3 for starburst galaxies (Murphy, 2009). A huge impact will probably also come from submillimeter observations of the *Atacama Large Millimeter/Submillimeter Array* (ALMA), which is expected to provide detailed observations of polarized light (Pérez-Sánchez & Vlemmings, 2013). The fraction of polarization includes information about the large-scale structure of magnetic fields. These and other new telescopes will provide unique observations, which can be used to test our suggested model for the evolution of cosmic magnetic fields.

1.3 Outline of this Thesis

The goal of this work is to better understand the evolution of the turbulent magnetic field during structure formation. To motivate our efforts of modeling amplification via a turbulent dynamo, we start with a description of magnetic fields in the local Universe in chapter 2. We summarize observational results ranging from small-scale objects like planets and stars, via the interstellar medium and galaxies up to intergalactic scales. The impact of magnetic fields on these astronomical objects is discussed.
In chapter 3 the theoretical principles of magnetic field amplification are summarized. Starting from the theory of hydrodynamics, the equations are extended such that the effects of ionized fluid particles and external magnetic fields are included, which is known as magnetohydrodynamics (see section 3.1). Secondly, we review some mechanisms of magnetic seed field generation from literature, taking into account origin from cosmology and plasma physics. These fields can be amplified in the motions of gas under the condition of flux freezing. Simple amplification concepts are discussed in section 3.3, while we give a phenomenological description of the magnetohydrodynamical dynamos in section 3.4.
The mathematical description of the turbulent dynamo is the topic of chapter 4. As it is the basis of any small-scale dynamo theory, the first section of this chapter is dedicated to review theoretical models of turbulence. We continue with a summary of the Kazantsev theory, which can be derived from the induction equation and describes the evolution of the turbulent magnetic field. In sections 4.2.4 and 4.2.5 we present our analytical results for the growth rate of the dynamo in different physical environments. The analytical calculations are extracted from Schober et al. (2012c) and Schober et al. (2012a) and are compared to numerical results from Bovino et al. (2013). A model for the subsequent non-linear evolution of the dynamo, in which back-reactions of the magnetic field on the dynamics of the fluid are taken into account, is given in section 4.3, where we closely follow Schleicher et al. (2013). Furthermore, we present a phenomenological model for the dynamo saturation in 4.4. The main findings from numerical simulations from Federrath et al. (2011) of magnetic fields in a turbulent box are discussed in section 4.5.
Our aim is to apply these theoretical results of the turbulent dynamo to the formation of the first stars and galaxies. Therefore, we review the current state of research of this era of the Universe in chapter 5. A well known result from simulations is that turbulence in structure formation is driven by accretion and also by supernova explosions, which initiates the small-scale dynamo. The timescales of the turbulent magnetic field amplification are roughly estimated for these astrophysical environments.
Chapter 6 summarizes our findings published in Schober et al. (2012b) for the magnetic field amplification in primordial star formation. With an one-zone model for the collapse of a primordial gas cloud, we follow the chemical and thermal evolution of the gas, which strongly influences the turbulent motions. On the basis of our

theoretical results for the dynamo growth rates, we can calculate the strength of the turbulent magnetic field as a function of particle density. With a simple model of the non-linear dynamo phase we follow the transport of magnetic energy to larger scales.
The discussion continues with a model of young galaxies in chapter 7, which is based on Schober et al. (2013). We model the physical processes in the primordial interstellar medium, including a detailed description of the plasma and the driving of turbulence. The magnetic field evolution is calculated for different types of galaxies and different types of turbulence. We compare the dynamo results with the field strengths one would expect from the distribution of stellar magnetic fields in supernova explosions.
In order to test the history of cosmic magnetic fields, observations are necessary. A common method to measure the field strength in local astronomical objects is the observation of synchrotron emission from cosmic rays. However, synchrotron emission is not the main cooling channel of cosmic rays at higher redshifts or in galaxies with extreme star formation, where instead inverse Compton scattering becomes important. We suggest an observational method fos tracing cosmic rays and magnetic fields via X-ray emission from inverse Compton scattering in chapter 8, which potentially could improve our knowledge on the evolution of magnetic fields in galaxies. This chapter follows closely Schober et al. (2014).
A broad discussion of the main results together with a compilation of open questions closes the thesis in chapter 9. Here we also provide an outlook to interesting projects that could lead to a deeper understanding of the evolution of cosmic magnetic fields.

CHAPTER 2

The Magnetized Universe

In this section we review the current state of research on magnetic fields on various astrophysical scales. Due to the complexity of this topic this review chapter cannot be complete and only covers selected points. Starting from magnetic fields of planets and stars, we move to larger scales up to galaxies, which have typical sizes of a few kpc, and to intergalactic fields with coherence length scales that might reach several Mpc. We summarize the observed structures and strengths of the fields and discuss selected effects they have on these objects. A compilation of the typical magnetic field strengths in different astronomical (and for comparison non-astronomical) objects can be found in table 2.1. It demonstrates the large variety of strengths and length scales of magnetic fields in the Universe.
There are several techniques for observing of magnetic fields. One of the most important technique is the observation of Zeeman splitting in spectral lines. In the Zeeman effect spectral lines split up into multiple lines in the presence of an external magnetic field. The energy difference between these closely spaced lines is directly proportional to the field strength. Another important observational method is radio synchrotron emission of cosmic rays gyrating around magnetic field lines. For determination of the field strength from the diffuse synchrotron emission, one, however, needs to make assumptions about the cosmic ray properties. A usual approach is assuming energy equipartition between the total magnetic and the cosmic ray energy density (Beck & Krause, 2005). While the last two techniques are used to determine the strength of the magnetic field, observation of polarized light yields also information about the field direction. Light from a background source gets linearly polarized when traveling through the dusty interstellar medium, in which magnetic fields align the elongated dust particles (Hoang & Lazarian, 2008). The dust then basically acts like a grid. Another very important tool to observe magnetic fields is an effect known as Faraday rotation, which also is based on linearly polarized light. When traveling through a magnetized medium, the polarization angle of a linearly polarized electromagnetic wave rotates. The change of the rotation angle depends on the line of sight magnetic field strength and the electron density.

object	field strength [G]	length scale [cm]
intergalactic medium	$\approx 10^{-16} - 10^{-6}$ (Neronov & Vovk, 2010)	$\approx 10^{13} - 10^{28}$
Milky Way	$\approx 10^{-5}$ (Beck & Wielebinski, 2013)	$\approx 10^{21}$
Earth (surface)	≈ 0.5 (Roberts & King, 2013)	$\approx 10^{8}$
refrigerator magnet	≈ 50	≈ 10
Sun (surface)	≈ 10 (Reiners, 2012)	$\approx 10^{11}$
Sun (sunspot)	$\approx 10^{3}$ (Solanki, 2003)	$\approx 10^{9}$
(medical) MRI magnet	$\approx 10^{4}$ (Wood et al., 2011)	≈ 100
pulsar	$\approx 10^{12}$ (Lorimer, 2008)	$\approx 10^{6}$
magnetar	$\approx 10^{15}$ (Ferrario & Wickramasinghe, 2007)	$\approx 10^{6}$

Table 2.1:
The magnetic field strengths and coherence length scales of selected astrophysical objects. For comparison we also list also typical numbers for magnets used by humans.

Apart from the observational signature of magnetic fields, we discuss in this chapter also their direct consequences on the respective astronomical object. Magnetic fields in stars lead to complicated physical processes especially on their surface. To the interstellar medium they add an additional pressure and by this influence the star formation process. Also important in that context is their ability to transport angular momentum. On galactic scales magnetic fields influence the dynamics of the interstellar medium and confine cosmic rays. The existence and possible consequences of intergalactic magnetic fields is a highly debated topic in current research.

2.1 Magnetic Fields in Planets and Stars

2.1.1 Magnetic Field of the Earth and Other Planets

The first astrophysical magnetic field discovered was the one of the Earth. Early theoretical explanations of a ferromagnetic origin failed as the temperature in the interior of the Earth is above the Curie temperature making ferromagnetism impossible. Observations reveal a dipole-like structure of the geological field, which fits well in the current picture in which the magnetic field is generated by a large-scale dynamo in the core of the Earth. The dynamo converts the kinetic energy from the highly conductive fluid inner core into magnetic energy (see section 3.4.1 for more details on large-scale dynamos). The result is a field, which has a dipole-like structure on and above the Earth surface. The typical field strength on the surface is of the order of 0.5 G (Roberts & King, 2013).
The magnetic field is extremely important for life on Earth, as it protects the surface from highly energetic particles coming mainly from the solar wind. The geological magnetic field, which reaches out far into space, traps charged particles and by this builds up the magnetosphere. The solar wind impinges from the magnetosphere and a bow shock develops. With the solar wind coming only from one direction, the magnetosphere becomes very asymmetric and builds up a tails pointing away from the Sun.
The magnetic field of the Earth is not unique. In fact, magnetic fields have been observed in all other planets of the solar system (Russell, 1991; Stevenson, 2003). Their origin lies probably also in planetary dynamos, which are either still active or already inactive. In the latter case, the magnetic field dissipates and becomes weaker in time. Currently, new observational techniques are developed that could allow detection of magnetism on planets around other stars then the Sun (Llama et al., 2013). A detection of this kind could help to decide whether an exoplanet is habitable or not.

2.1.2 Stellar Magnetic Fields

The era of observing extraterrestrial magnetic fields began in the early 20th century, when Hale (1908) detected Zeemann splitting of atomic absorption lines in sunspots. Today we know that the magnetic field of the Sun has a very complicated structure, which is illustrated in the snapshot in figure 2.1, and needs to be included in models to explain various stellar phenomena.
The appearance of sunspots, regions of lower temperature that rotate differentially with the stellar surface, is closely coupled to the magnetic field. Statistical observations of sunspots agree well with the predictions of theoretical α-Ω dynamo models (see also section 3.4.1 and Charbonneau (2010) for a detailed review article). The field is very strong in sunspots and reaches a typical strength of 3000 G, while the field strength on other sites of the stellar surface is only roughly 1-10 G. The concentration of magnetic energy in these regions can be explained in the model of

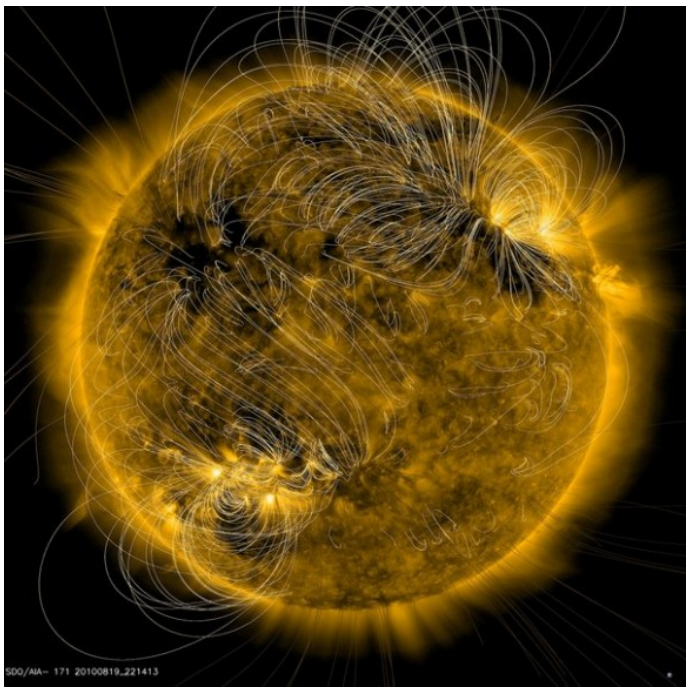

Figure 2.1:
Observations of magnetic field lines on the Sun on August 20, 2010. The white lines show closed field lines, which do not release solar wind, while the golden lines show open fields. This image was observed by the *Helioseismic and Magnetic Imager instrument* (HMI) at the *Solar Dynamics Observatory.*
image credit: NASA SDO / Lockheed Martin Space Systems Compan

magneto-convection, which says that the field is generated in the interior of the Sun and experiences subsequent magnetic buoyancy to the surface (see for example the review by Fan, 2009).
The magnetic field of the Sun plays also a major role in the corona. Here fast reconnection, i.e. conversion of magnetic energy into other energy forms like particle acceleration, generates solar flares with energies of up to 10^{32} erg on timescales of an hour (Shibata & Magara, 2011). Magnetic fields may also provide an explanation for the high temperatures of 10^6 K in the solar corona, which exceeds the surface temperature of only roughly 6000 K by orders of magnitude. These high temperatures in turn give rise to the solar wind.
Magnetic fields are commonly observed in other stars, from very low-mass M-dwarfs to super-massive O-stars (Donati & Landstreet, 2009). Especially observations of cool stars, i.e. stars with an outer convection layer similar to the Sun, are important to understand and test the α-Ω dynamo (Reiners, 2012). While magnetic fields are frequently observed in low-mass stars, only a few percent of the intermediate and high-mass stars have detectable magnetic fields (Landstreet, 1992).
Sights of extreme magnetic fields are stars at late evolutionary stages, i.e. white dwarfs and neutral stars (Ferrario & Wickramasinghe, 2007). In fact, the strongest known fields in the Universe have been observed in so-called magnetars with a strength of the order of 10^{15} G. We note that their magnetic fluxes are comparable to the ones of magnetic hot main sequence stars, which suggests that at least a large fraction of magnetic flux is conserved in stellar evolution.

2.2 Magnetic Fields in Molecular Clouds and their Impact on Star Formation

The *interstellar medium* (ISM) is the inhomogeneously distributed matter in galaxies in the space between stars (see Ferrière (2001) for a review). It is composed of ordinary matter, cosmic rays, i.e. highly energetic charged particles, and magnetic fields. The ordinary matter consists of neutral and ionized atoms, molecules and dust and ranges from densities of $n < 0.01$ cm^{-3} and temperatures of $T \approx 10^6$ K to $n > 100$ cm^{-3} and $T \approx 10 - 20$ K. The energy densities of the main components of the ISM, turbulence, cosmic rays and magnetic fields, are of the same order of magnitude, which indicates a strong coupling between them.
The ISM is of particular interest as it is the birthplace of stars, which form within its coldest and densest parts, so-called *molecular clouds* (McKee & Ostriker, 2007; Mac Low & Klessen, 2004). These objects come in different classes ranging from giant molecular clouds with a length scale of a few tens of a parsec, masses of 10^6 M$_\odot$ and hydrogen densities of roughly $100 - 1000$ cm^{-3}, down to very dense and cold cores of a size of a few tenth of a parsec, masses of $0.3 - 10^3$ M$_\odot$ and a density of $10^4 - 10^6$ cm^{-3} (see, e.g. Larson, 1981).
Observations of Zeemann splitting and polarization indicate that molecular clouds are highly magnetized (see, e.g. Crutcher, 1999; Bourke et al., 2001; Heiles & Crutcher, 2005; Crutcher, 2012). Detailed observations are available for example for the starless core L 183 (Crutcher et al., 2004). Dust polarization measurements indicate that its magnetic field is fairly regular. However, the slight dispersion in position angles is a sign of an additional turbulent component. The field strength detected in L 183 is roughly 80 μG in the dense core and less then 16 μG in the envelope. Another object, the magnetic field of which has been studied in detail, is NGC 1333 IRAS 4A. The field strength in the plane of the sky in this actively star forming region is roughly 5 mG (Girart et al., 2006). We show the morphology of the magnetic field in NGC 1333 IRAS 4A in figure 2.2. The magnetic field lines follow the theoretically predicted hourglass shape in an spherical collapse remarkably well (see also section 3.3.2).
In the following sections we diskuss the classical picture of star formation in these dense molecular clouds. We show how the presence of a magnetic field changes this very simplified picture and summarize the most important consequences, like the transport of angular momentum and disk instabilities.

2.2.1 The Jeans Criterion with Additional Magnetic Pressure

A star forms due to gravitational collapse of the gas, which sets in when the gravitational energy exceeds the internal pressure. In the classical star formation theory the internal pressure is identified with the thermal pressure. The collapse criterion

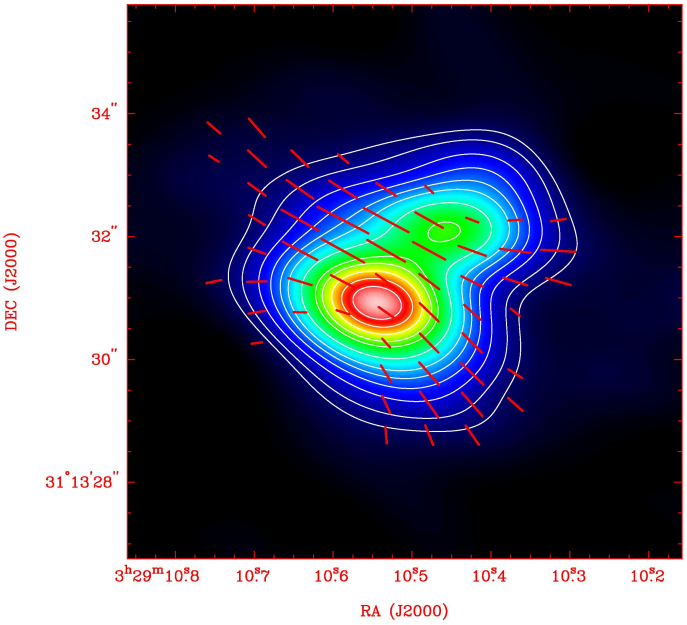

Figure 2.2:
High-angular-resolution observations of polarized dust emission in the low-mass protostellar system NGC 1333 IRAS 4A. The morphology of the magnetic field traces the theoretically expected hourglass shape.
image credit: Girart et al. (2006)

can then be estimated from comparison of the gravitational energy density

$$\frac{E_{\rm grav}}{V} = -\frac{3}{5}\frac{GM^2}{RV} = -\frac{3}{5}\frac{GM}{R}\rho \tag{2.1}$$

with the thermal energy density

$$\frac{E_{\rm th}}{V} = \frac{\rho}{m}kT. \tag{2.2}$$

Here $E_{\rm grav}$ and $E_{\rm th}$ are the total gravitational and thermal energies, respectively, G the gravitational constant, R, M, V are radius, mass and volume of the system with mass density $\rho = M/V$ and temperature T. The mass of a single particle is m. The system is gravitationally bound if

$$\frac{E_{\rm grav}}{V} + \frac{E_{\rm th}}{V} \leq 0, \tag{2.3}$$

which leads to the condition

$$c_{\rm s}^2 \leq \frac{3}{5}\left(\frac{4\pi}{3}\right)^{1/3} GM^{2/3}\rho^{1/3} \approx GM^{2/3}\rho^{1/3}, \tag{2.4}$$

where we introduce the isothermal sound speed $c_{\rm s} = (kT/m)^{1/2}$ and express the radius R by $(3M/(4\pi\rho))^{1/3}$. Hence we can define a critical mass for collapse

$$M_{\rm J} \equiv \frac{c_{\rm s}^3}{G^{3/2}\rho^{1/2}}, \tag{2.5}$$

the so-called *Jeans mass*. The scaling of $M_{\rm J}$ with $T^{3/2}$ and $\rho^{-1/2}$ indicates that stars from only in very cold and dense regions.

Magnetic fields, which are commonly observed in molecular clouds (see for example figure 2.2), add an additional pressure to the problem. Observations show that the magnetic pressure typically even exceeds the thermal pressure in the ISM (see e.g. Beck, 2007). We find the magnetic Jeans mass in the same way as the classical one by replacing the thermal energy density by the magnetic one, $B^2/(8\pi)$. This yields the stability criterion

$$\frac{B^2}{8\pi} - \frac{3}{5}\frac{GM^2}{RV} \leq 0. \tag{2.6}$$

The system is thus gravitationally bound if

$$M^2 \geq \left(\frac{5}{18G}\right)^{1/2} BR^2. \tag{2.7}$$

Note, that the last factor BR^2 can be identified as the magnetic flux $\Phi = B\pi R^2$. The corresponding *magnetic Jeans mass* is then defined as

$$M_{\mathrm{J,mag}} \equiv \left(\frac{5}{18\pi^2 G}\right)^{1/2} \Phi. \tag{2.8}$$

Clouds with a mass $M > M_{\mathrm{J,mag}}$ are gravitational unstable and called *supercritical*, where as *subcritical* clouds with $M < M_{\mathrm{J,mag}}$ are stabilized against collapse by the magnetic pressure.
An important quantity in magnetized star formation is the *critical mass-to-flux ratio*, which is given as

$$\left(\frac{M}{\Phi}\right)_{\mathrm{crit}} \equiv \left(\frac{M_{\mathrm{J,mag}}}{\Phi}\right)_{\mathrm{crit}} = \left(\frac{5}{18\pi^2 G}\right)^{1/2} \approx 0.17\ G^{-1/2}. \tag{2.9}$$

Our derivation of the critical mass-to-flux ratio assumes a spherical collapse. If the magnetic field has, however, some orientation, this assumption is not very good. A numerical calculation following the runaway collapse phase until the accretion phase (Tomisaka, 1998) yields for the mass-to-flux ratio

$$\left(\frac{M}{\Phi}\right)_{\mathrm{crit}} \approx 0.12\ G^{-1/2}, \tag{2.10}$$

which is indeed comparable to our analytical result above.
Molecular clouds can only collapse, when they are magnetically supercritical. Observations actually prefer the supercritical state of molecular clouds (Troland & Crutcher, 2008), which leads to the question, why the magnetic field in collapsing clouds is much weaker than expected from simple flux freezing. The most common explanation for this so-called magnetic flux problem in star formation is *ambipolar diffusion*, i.e. a decoupling of neutrals and ions.

2.2.2 Transport of Angular Momentum Through Magnetic Fields

Angular momentum in a rotating astronomical object with magnetic fields reaching into the ambient medium can be transported efficiently by magnetic stress. Here *Ferraro's law of isorotation* (Ferraro, 1937) plays an important role, which claims that a steady state can only be established, when the angular velocity is constant along the field lines. Assume an object holds a poloidal magnetic field and rotates differentially. Then due to the change of angular velocity as a function of radius a torodial field builds up. In this rearrangement of magnetic structure, magnetic stresses set in and work needs to be done. This leads to a beak reaction of the field, which tries to impose a rigid rotation on the object.

Magnetic Braking

The situation of magnetic stress forces in rotating objects described above is given in magnetized star formation. Here an angular velocity Ω of a collapsing cloud increases under the assumption of conserved angular momentum, $\Omega r^2 = const.$ If the central cloud is connected with the environmental ISM a magnetic stress sets in, which slows down the rotation of the cloud. This process is known as *magnetic braking*.
Magnetic braking has a great influence on the formation and fragmentation of protostellar disks. In fact, in simulations of magnetized star formation with fields strengths comparable to the observed ones no rotationally disks were found (e.g. Banerjee & Pudritz, 2007; Peters et al., 2011; Seifried et al., 2011). However, as we know from observations that disks are present in the earliest stages of protostellar evolution (Williams & Cieza, 2011), the conclusion from numerical simulations is obviously not correct. This problem is known as the *magnetic braking catastrophe*. Various solutions are suggested in literature, like the possible misalignment of magnetic field lines (Hennebelle & Ciardi, 2009), inclusion of turbulence in the simulation (Seifried et al., 2012) or turbulent reconnection (Santos-Lima et al., 2012). Which one of these solution really solves the magnetic braking catastrophe is, however, still under debate.

Jets and Outflows

Closely related to the appearance of disks are *stellar jets*, which receive their power from the release of gravitational energy during accretion. These high-velocity matter outflows have been observed frequently in low-mass star formation (e.g. Swift & Welch, 2008; Dunham et al., 2014). Recent observations have also detected jets in young high-mass stars (Arce, 2005) and even in brown dwarfs (Bourke et al., 2005). The correlation between the momentum transport rate of the CO molecular outflow with the one from the bolometric luminosity, which has been observed to follow a power law over six orders of magnitude in luminosity (Cabrit & Bertout,

1992), suggests that the generation mechanism of jets is similar for stars in all mass ranges.
Theory predicts stellar jets to arise from magnetized disks, assuming that the magnetic field is frozen in the gas and thus co-rotating (see for example the review by Pudritz et al., 2012). The magnetic field in the disk around the protostar is draged inwards in the accretion process. Simultaneously, the field gets winded up by the rotation of the disk, which leads to a transport of gas and angular momentum out of the disk. These so-called disk wind models for (stellar) jets were developed by Blandford & Payne (1982) and Pudritz & Norman (1983), who show that material gets ejected from the disk if the inclination angle between the magnetic field and the rotation axes is larger than roughly 30°. Collimation of the jets follows naturally from magnetic tension of the current carrying jet. We note, that also other jet models where suggested, for example the X-wind model (Shu et al., 1994, 2000), that show certain differences in the connection between the star, the disk and the magnetic field.
The presence of a jet has important consequences on a star and its disk (see for example the recent review by Frank et al., 2014). An important result is the mass loss of the stellar system through the outflow. Observations of young stellar objects suggest that the ratio of the jet mass flux over the accretion rate on the star is roughly 10 % (Cabrit, 2007; Agra-Amboage et al., 2009; Ellerbroek et al., 2013). These rates are, however, not constant in time, but change episodically. Furthermore, the flow of gas in a jet leads to a transport of angular momentum from the accretion disk (Blandford & Payne, 1982; Pudritz & Norman, 1983). The detailes of angular momentum transport depend crucially on the launching model of the jet and there are probably various mechanisms working simultaneously (Frank et al., 2014). Banerjee & Pudritz (2006) show in simulations of collapsing magnetized cloud cores that torsional Alfvèn waves transport the angular momentum very efficiently leading to a slow down of the rotation of the prestellar cores.
Also the implications of stellar jets on the environmental ISM can be very severe (Frank et al., 2014). Stellar jets penetrate very far into the clouds where they can drive turbulence and by this act as a self-regulating process in star formation. The results of how efficient this driving is are different in different numerical simulations. For example Mac Low (2000) finds that turbulence generated by randomly distributed jets decays again on a short time scale, while Li & Nakamura (2006) find that turbulence in the molecular cloud is maintained. With numerical simulations Banerjee et al. (2007) investigate in detail the way energy and momentum from jets is deposited into the environmental clouds. They conclude that collimated supersonic jets are not able to drive supersonic turbulence in a large volume, but only locally, while subsonic, rotational modes spread further. Important consequences of stellar jets on the parent cloud are moreover heating via shocks and a change of the chemical composition. All these effects can influence the subsequent star formation crucially.

Magneto-rotational Instability in Disks

Accretion disks play an important role in star formation. However, a long standing problem in astronomy were the high observed accretion rates, which cannot be explained by molecular viscosity, convection or tidal mixing. There needs to be an additional loss on angular momentum in accretion disks. A possible solution to this problem was proposed by Balbus & Hawley (1991), who claim that weak magnetic fields can cause an instability, which in turn leads to turbulent mixing. This mechanism that is known as *magnetorotational instability* (MRI) was originally diskovered by Velikhov (1959) and Chandrasekhar (1960) independently and only many years later applied to astrophysical systems.
Assume a differentially rotating accretion disk has a weak magnetic field, which penetrates the disk perpendicularly. Two fluid elements that lie directly next to each other are connected by a magnetic field line. If there is, however, a small initial displacement, the inner fluid element has a larger angular velocity due to differential rotation. This leads to an increase of the displacement and thus to an increase of magnetic tension. Magnetic tension force can be compared to a string that connects to two fluid elements. Consequently, the inner fluid element slows down, while the outer one speeds up, which is equivalent to a transport of angular momentum from the inner to the outer fluid element. The loss of angular momentum slows down the inner parcel further, leading to a further increase of the displacement. Now the magnetic tension increases again and a runaway process, i.e. an instability, sets in. It has been shown in numerical simulations of the multi-phase interstellar medium that the MRI is a significant source of turbulence, especially at low densities, for example in the outer regions of the galaxy (see, e.g. Piontek & Ostriker, 2005).

2.2.3 Star Formation in Clusters

So far the diskussion has been focused to the effects of magnetic fields on individual star formation. Typically stars form, however, in large clusters. For completeness we report here selected results found for magnetized star formation in clusters, where the effects of the single mechanisms described above are combined.
In complex numerical simulations Price & Bate (2008) test the influence of magnetic fields on star formation in turbulent molecular clouds. Interestingly, they find different results in comparison to the pure hydrodynamical runs even for very weak magnetic fields. The presence of weak fields leads to lower accretion rates and different star formation sequences. While in the hydrodynamical case after 1.5 free-fall times about 16 % of the gas is converted into stars, it is only 4 % in the run with a slightly supercritical magnetic field. Price & Bate (2008) find, moreover, that the structure of the molecular clouds changes drastically, when the pressure is dominated by magnetic fields. They observe in their simulations magnetically supported voids and column density striations. The presence of strong magnetic fields is expected to have also important consequences on the initial mass function, as typically fewer low mass objects are formed.

As numerical simulations are always limited by resolution the total effect of magnetic fields on star formation still yields many open questions. For example in the large-scale simulations discussed above, small-scale effects like the fragmentation of cores and stellar jets cannot be included. Stellar jets, however, reach length scales up to a few parsec (Goodman & Arce, 2004) and thus penetrate deep into the environmental ISM. In order to overcome the resolution problem Federrath et al. (2014) apply a subgrid model to study the effects of stellar jets. They find that the star formation rate is reduced by a factor of roughly two, when jets are included, and that the average stellar mass decreases by factor of 3. Thus, jets might influence the initial stellar mass function drastically.

2.3 Magnetic Fields in Galaxies

One of the main findings of astronomy in the 20th century was that magnetic fields are omnipresent in the Universe. Observations show that strong magnetic fields are even present on galactic scales. We summarize the main characteristics of galactic magnetic fields in different types of galaxies in this section and also discuss their role in the dynamics of the large-scale interstellar medium.

2.3.1 Observational Results for Galactic Magnetic Fields

Observational Techniques

For observations of galactic magnetic fields a variety of techniques is used leading to information not only about the field strength, but also about the structure of the field (see for example the recent review article by Beck & Wielebinski, 2013). The total synchrotron radiation, which is emitted by cosmic rays spiraling around the magnetic field lines and lies typically in the radio regime, gives the total magnetic field strength. Polarized emission, which results from the alignment of non-spherical dust particles along the magnetic field, traces the ordered (or better regular) magnetic field component.

Strength and Structure of Galactic Magnetic Fields

In a spiral galaxy the turbulent field strength is of the order of 20-30 μG in the optical spiral arms and bars and up to 50-100 μG in the central starburst region. This exceeds the strength of the ordered fields, which are strongest in the interarm region with typical values 10-15 μG (Beck, 2011). In grand design galaxies, like for example in M51 shown in figure 2.3, the ordered field component follows the spiral pattern. Interestingly, the magnetic spiral arms are observed in all disk galaxies even when there are no optical arms (Soida et al., 2002). Observations show that there are also large-scale ordered magnetic fields in disk galaxies that are seen edge-on. Here the field is typically parallel to the disk near the disk plan (Dumke et al., 1995) and follows a X-shape in the radio halo (e.g. Krause et al., 2006). Comparison with

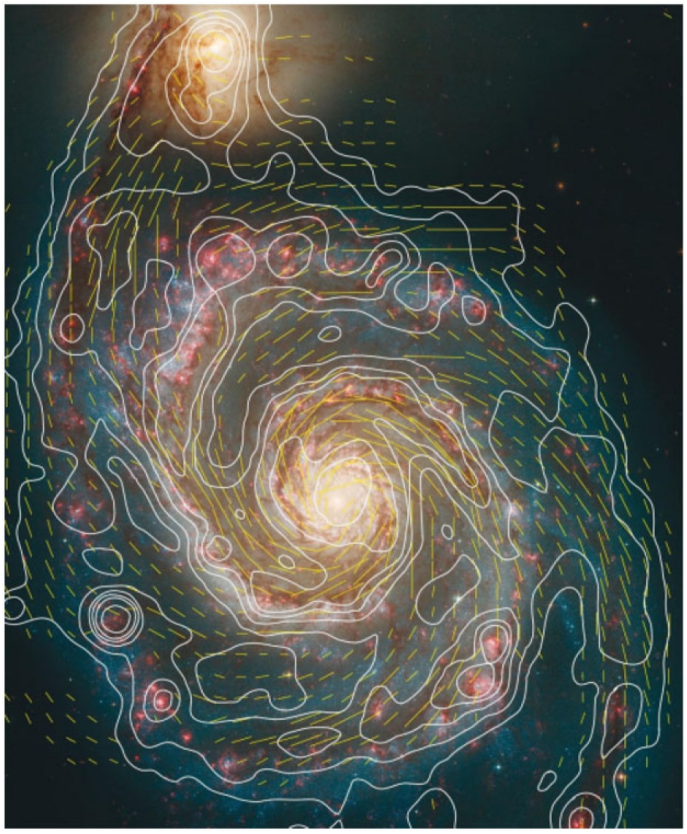

Figure 2.3:
The magnetic field of the spiral galaxy M51. The figure shows an optical image from the Hubble telescope, overlaid with contours indicating the synchrotron emission and lines indicating the polarization measurements.
image credit: Beck (2011)

other forms of energy implies the importance of the galactic magnetic field. In fact, the magnetic energy density in galaxies is typically of the same order of magnitude as the thermal and turbulent energy density as well as the one of cosmic rays (Heiles & Crutcher, 2005; Beck, 2007; Draine, 2011).
Observations of magnetic fields in elliptical galaxies are more difficult. Without significant star formation and without an active galactic nucleus, the latter do not produce cosmic rays, which trace the magnetic fields by their synchrotron emission. Hopefully, future telescopes like SKA can detect magnetic fields in ellipticals by observing polarized background sources.
Magnetic fields are better observable in irregular galaxies by using radio continuum maps. Here field strengths of a few μG and spiral pattern are detected (Beck & Wielebinski, 2013). The total field strength in starburst dwarfs is of the order of 10-15 μG, leading to an energy density that is comparable to the one of chaotic gas rotation. We thus can expect that the evolution of the entire system is influenced by the magnetic field.

The Far-Infrared-Radio Correlation

One of the most remarkable correlations in astronomy is the *far-infrared(FIR)-radio correlation*, which is observed in galaxies (van der Kruit, 1971, 1973). The tight correlation holds over five orders of magnitude in luminosity (Price & Duric, 1992).

A detailed study by Yun et al. (2001), who identify approximately 1800 radio counterparts to the *IRAS Redshift Survey* galaxies (Neugebauer et al., 1984) in the *NRAO VLA Sky Survey* data set (Condon et al., 1998), results in the following correlation:

$$\log\left(L_{1.4\ \mathrm{GHz}}\right) \propto (0.99 \pm 0.01)\ \log\left(L_{60\ \mu\mathrm{m}}\right). \tag{2.11}$$

The linear nature of the FIR-radio correlation has been interpreted as a direct relation between star formation and cosmic ray production (Harwit & Pacini, 1975). While the FIR radiation can be associated with thermal emission from HII regions around massive stars, and by this traces the star formation in a galaxy, the radio emission is expected to be synchrotron radiation from cosmic rays traveling in the galactic magnetic field. With massive stars being the common origin of HII regions as well as cosmic rays, which are accelerated in the final phases of massive stars, the supernova remnants, the tight correlation can be explained.
The FIR-radio correlation has not only been tested in the local Universe with global galaxy properties, but also in high-resolution observations of individual galaxies (e.g. Tabatabaei et al., 2013). New studies explore the relation between the FIR and the radio flux also as a function of redshift. For example Bourne et al. (2011) did not find a significant evolution of the FIR-radio correlation with redshift up to $z \approx 2$. Depending on the global properties of a galaxy Schleicher & Beck (2013) predict, however, a breakdown of the correlation at higher redshifts, where the cosmic rays lose their energy not predominantly via synchrotron radiation, but also via inverse Compton scattering (see also chapter 8 of this thesis).

2.3.2 Impact on the Large-scale Interstellar Medium

Dynamics of the ISM

Magnetic fields act as an additional pressure in the gas. In fact, Dobbs & Price (2008) find in their three-dimensional magnetohydrodynamical (MHD) simulations of a galactic disk, that the magnetic field has similar effects as an increase in thermal pressure, which suppresses structure formation and overall smooths out the gas. With increasing magnetic field strength they find, moreover, a reduction of the strength of the spiral shocks. This in turn leads to a decrease of the density in the spiral arms and to a suppression of spur formation. However, unlike in the 2D MHD simulations without self-gravity of Shetty & Ostriker (2006), Dobbs & Price (2008) find that some interarm structure remains also with magnetic fields.

Magnetohydrodynamical Instabilities as a Generator of Molecular Clouds

The inclusion of magnetic fields in a galaxy model can initiate some instabilities, which may help to understand the formation of giant molecular clouds.
One obvious trigger for the condensation of giant, star-forming clumps is the *Parker*

instability (Parker, 1966). This instability origins in a disk with uniformly distributed gas and a magnetic field parallel to the disk. If there is a small perturbation in the magnetic field, a part of the field lines bulges up. The gas, which is frozen into the magnetic field, is effected by the gravity pointing to the disk. However, it can only move along the field lines, which leads to an accumulation of gas in the field line valleys away from the bulge. The flux of gas makes the bulge lighter and it rises further, resulting in an instability. The molecular clouds then form within the field line valleys. Numerical studies of Kim et al. (2002), however, suggest that the Parker instability plays only a secondary role in the formation of giant molecular clouds.
A more important effect for the generation of giant molecular clouds probably has the *magneto-rotational instability* (MRI) (Kim et al.; Piontek & Ostriker, 2005), which has already been diskussed in the context of accretion disks above. Numerical simulations (Kim et al.) show that MRI-driven turbulence develops rapidly and, with strong self-gravity, high-amplitude density perturbations form massive bound clouds.
Another possible instability that might lead to the formation of large-scale cloud complexes is the *magneto-Jeans instability* (MJI). In a rotating disk self-gravity needs to overcome Coriolis forces. This can be achieved via magnetic tension forces resulting in an instability (Elmegreen, 1987). In simulations by Kim et al. (2002) MJI turns out to be the most powerful instability to form high-mass clouds from non-axisymmetric perturbations.

Confinement of Cosmic Rays

A further consequence of magnetic fields in galaxies is the confinement of *cosmic rays*. These particles are presumably accelerated in shock fronts (we refer to the pioneering work by Bell, 1978a,b) and reach energies up to 10^{21} eV[1]. However, with a power-law distribution in energy that decreases with a slope around -2.7, the majority of cosmic rays have energies around 10^9 eV. The energy density of cosmic rays in a typical galaxy is roughly 1.39 eV cm^{-3} and thus comparable to the kinetic one of the gas 0.49 eV cm^{-3} and one of the magnetic field 0.89 eV cm^{-3} (Draine, 2011).
Cosmic rays are charged particles and thus underlie the Lorenz force. When traveling in a magnetized plasma, they spiral around the field lines. By comparing the typical gyroradius

$$r_{\mathrm{g}} = \frac{pc}{eB} \approx \frac{E}{eB} \tag{2.12}$$

of a particle with the scale height of the galaxy h_{gal}, one can estimate if cosmic rays are confined. Here $p = E/c$ is the relativistic momentum, E the total energy of a particle with charge e and c the speed of light. When we assume $h_{\mathrm{gal}} = 100$ pc and

[1] For comparison the energy protons reach in the *Large Hadron Collider* is of the order of 10^{13} eV.

a $B = 10^{-5}$ G, which are typical values for the Milky Way disk, we find that cosmic rays up to an energy of 10^{18} eV are confined within the disk. Thus, except for the ultra energetic particles, most of the high-energy cosmic rays are confined within the galaxy by the magnetic field.
The presence of cosmic rays influences the interstellar medium crucially. They significantly change the chemistry by ionizing the gas. Observations by Indriolo & McCall (2012) indicate an ionization rate as high as 10^{-16} s^{-1} in translucent clouds, while the rate in local ISM is still an open question. A very important consequence of cosmic ray propagation in the ISM is the additional (and often domininat) source of heating (Glassgold et al., 2012). The heating proceeds via chemical reactions that lead to ionization or excitation of molecules. Heating results from the energy of electrons that origin from ionized atoms and from Coulomb collisions between the cosmic rays and charged particles (Field et al., 1969).

Galactic Outflows

The cosmic rays can couple to the a magnetized plasma by the emission of MHD-waves. Ipavich (1975) shows that coupled dynamics of cosmic rays and magnetic fields can lead to outflows from galaxies, i.e. to a *galactic wind*. These winds cause a loss of mass and energy to the galaxy.
Recent simulations of disk galaxies by Pakmor & Springel (2013) show that magnetic fields can produce significant outflows with large mass losses. Supernova feedback can in their case be excluded as the origin of the outflows, however they are qualitatively similar to ones purely driven by supernovae in other simulations.
Galactic outflows may play an important role in magnetizing the intergalactic medium. Kronberg et al. (1999) show that a large fraction of the intergalactic medium can be polluted with magnetic fields due to outflows from young starburst galaxies. Magnetic diffusion may have spread these fields over great volumes within a Hubble time. We shortly discuss the current state of intergalactic magnetic fields in the next section.

2.4 Intergalactic Magnetic Fields

As we will discuss in the following chapters, any model for magnetic field amplification requires the existence of a seed field. One of the best places to look for these seed fields is the *intergalactic medium* (IGM), because any primordial field is probably the least unaffected within this region.
Up to now there is no direct detection of intergalactic magnetic fields. Only estimates of upper and lower limits of the field strength and the coherence length scale can be found in the literature. These limits are nicely summarized in figure 2.4, which is taken from Neronov & Vovk (2010). There is a natural lower limit on the coherence length resulting from the comparison of the magnetic diffusion time scale and the age of the Universe, while the upper bound on the coherence length

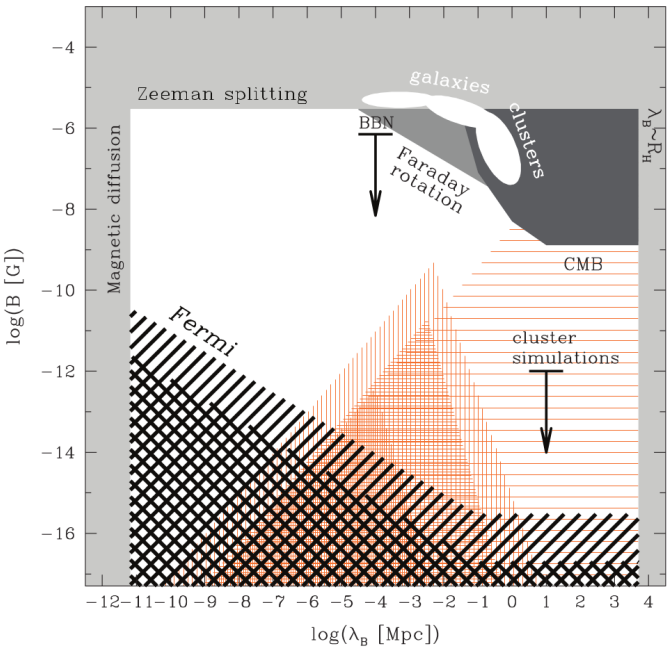

Figure 2.4:
Limits on the strength and coherence length of the intergalactic magnetic field as summarized in Neronov & Vovk (2010). The lower hatched region is suggested from observations of TeV blazers. The orange hatched regions give the allowed ranges of cosmic magnetic fields generated in the early Universe.
image credit: Neronov & Vovk (2010)

is given by the size of the visible Universe. An upper limit on the field strength is easily found from Zeemann splitting of the 21 cm absorption line in the spectra of distant quasars. Here the detection of the μG galactic fields rules out stronger fields in the IGM. Further upper bounds of the field strength are gained from Faraday rotation of polarized light from quasars (Kronberg, 1994) , distortions and polarization properties of the cosmic microwave background (Seshadri & Subramanian, 2009; Trivedi et al., 2012) and from Big Bang nucleosynthesis (Grasso & Rubinstein, 2001). Neronov & Vovk (2010) claim the detection of a lower bound of 3×10^{-16} G for the intergalactic magnetic field strength. For this result they use the γ-ray emission from distant blazars. These TeV γ-rays decay into electron-positron pairs, the trajectories of which are influenced by an intergalactic magnetic field. Thus, an extended γ-ray emission of the initial blazar point source would indicate a line of sight magnetic field and one expects no observations of GeV γ-ray emission. We note, however, that there are alternative explanations for the non-detection of GeV-γ rays from blazar sources, which include plasma beam instabilities (Chang et al., 2012).
Studying the possible existence of magnetic fields in the intergalactic medium is very important, as these could be of primordial origin. This means that, due to a lake of dynamics in the IGM, these fields did probably not evolve significantly and could still be of the same kind as the original magnetic seed fields.

CHAPTER 3

Principles of Magnetic Field Amplification

The aim of this chapter is to provide the relevant theoretical basics for understanding magnetohydrodynamical dynamos. We start with a broad discussion of the theory of hydrodynamics, which is step by step extended to magnetohydrodynamics. The origin of the first magnetic fields in the Universe is discussed, the so-called seed fields, which are later amplified by magnetohydrodynamical dynamos. The chapter ends with a phenomenological description of dynamos.

3.1 Dynamics of Neutral and Ionized Fluids

3.1.1 Hydrodynamics

A complete description of the state of a fluid needs to predict the position and the velocity of every single fluid particle at every time. In the astrophysical context, with for example molecular clouds containing about 10^{63} particles, this is impossible. Thus, a statistical ansatz is necessary. In this section we sketch an elegant derivation of the hydrodynamic equations by using the Boltzmann equation. For this purpose we mainly follow the textbook of Choudhuri (1998).

The Boltzmann Equation

For the description of a fluid that consists of N particles we have to consider a (6+1)-dimensional coordinate space (3 coordinates for the position, 3 for the velocity vector and one for the time). In this space we can introduce a distribution function

$$f(\boldsymbol{x}, \boldsymbol{u}, t) \equiv \lim_{\delta V \to 0} \frac{\delta N}{\delta V}. \tag{3.1}$$

The volume δV in this limit needs to be small compared to the extension of the points in space, but still large enough to contain many particles δN.

If we now consider a fluid, in which the particles do not interact with each other, the time derivation of the distribution function in our (6+1)-dimensional space along any trajectory needs to vanish,

$$\begin{aligned} \frac{\mathrm{D}f}{\mathrm{D}t} &= 0 \\ \leftrightarrow \frac{\partial f}{\partial t} + \dot{\boldsymbol{x}} \cdot \nabla f + \dot{\boldsymbol{u}} \cdot \nabla_{\boldsymbol{u}} f &= 0, \end{aligned} \tag{3.2}$$

where we define the velocity gradient as

$$\nabla_{\boldsymbol{u}} \equiv \sum_{i=1}^{3} \frac{\partial}{\partial u_i} \boldsymbol{e}_i. \tag{3.3}$$

Equation (3.2) tells us how the distribution function $f(\boldsymbol{x}, \boldsymbol{u}, t)$ evolves in time. A fluid without particle interactions is called collisionless and is described by the *collisionless Boltzmann equation* (3.2).

Now we go one step further and consider the more realistic case of a fluid, in which the particles interact with each other. Due to collisions particles can change their velocities. This means that a particle, which has a velocity $\boldsymbol{u}$ before a collision, can change its velocity leading to a decrease of the distribution function $f(\boldsymbol{x}, \boldsymbol{u}, t)$. On the other hand, a velocity of a particle which is initially different can be changed to $\boldsymbol{u}$ and by this increases $f(\boldsymbol{x}, \boldsymbol{u}, t)$. So the general form of the evolution of $f(\boldsymbol{x}, \boldsymbol{u}, t)$ is given by

$$\frac{\mathrm{D}f}{\mathrm{D}t} \mathrm{d}x^3 \mathrm{d}u^3 = C_{\mathrm{in}} - C_{\mathrm{out}}, \tag{3.4}$$

where C_{in} and C_{out} describe the number of particles that change their velocity to and from $\boldsymbol{u}$, respectively.

These two quantities can be determined for example for a dilute gas, in which only binary collisions take place. Choudhuri (1998) finds for this special case

$$C_{\mathrm{in}} = \mathrm{d}x^3 \mathrm{d}u^3 \int \mathrm{d}\tilde{u}^3 \int \mathrm{d}\boldsymbol{\Omega}\, \sigma(\boldsymbol{u}, \tilde{\boldsymbol{u}} | \boldsymbol{u}', \tilde{\boldsymbol{u}}') \, |\boldsymbol{u} - \tilde{\boldsymbol{u}}| \, f(\boldsymbol{x}, \boldsymbol{u}', t) f(\boldsymbol{x}, \tilde{\boldsymbol{u}}', t), \tag{3.5}$$

$$C_{\mathrm{out}} = \mathrm{d}x^3 \mathrm{d}u^3 \int \mathrm{d}\tilde{u}^3 \int \mathrm{d}\boldsymbol{\Omega}\, \sigma(\boldsymbol{u}, \tilde{\boldsymbol{u}} | \boldsymbol{u}', \tilde{\boldsymbol{u}}') \, |\boldsymbol{u} - \tilde{\boldsymbol{u}}| \, f(\boldsymbol{x}, \boldsymbol{u}, t) f(\boldsymbol{x}, \tilde{\boldsymbol{u}}, t). \tag{3.6}$$

In the above expressions $\boldsymbol{u}$ and $\tilde{\boldsymbol{u}}$ are the velocities of the two particles before the collision, $\boldsymbol{u}'$ and $\tilde{\boldsymbol{u}}'$ the ones afterwards, $\boldsymbol{\Omega}$ is the scattering angle and $\sigma(\boldsymbol{u}, \tilde{\boldsymbol{u}} | \boldsymbol{u}', \tilde{\boldsymbol{u}})$ the cross section for the collision. The full *Boltzmann equation* for a dilute gas follows as

$$\begin{aligned} \frac{\partial f}{\partial t} + \dot{\boldsymbol{x}} \cdot \nabla f + \dot{\boldsymbol{u}} \cdot \nabla_{\boldsymbol{u}} f &= \int \mathrm{d}\tilde{u}^3 \int \mathrm{d}\boldsymbol{\Omega}\, \sigma(\boldsymbol{\Omega}) \, |\boldsymbol{u} - \tilde{\boldsymbol{u}}| \cdot \\ &\quad \times \left(f(\boldsymbol{x}, \boldsymbol{u}', t) f(\boldsymbol{x}, \tilde{\boldsymbol{u}}', t) - f(\boldsymbol{x}, \boldsymbol{u}, t) f(\boldsymbol{x}, \tilde{\boldsymbol{u}}, t) \right). \end{aligned} \tag{3.7}$$

The Boltzmann equation governs the time evolution of the distribution function of the gas.

The Moment Equations

Now let us consider a quantity χ that is conserved in a binary collision, i.e.

$$\chi + \tilde{\chi} = \chi' + \tilde{\chi}', \tag{3.8}$$

where the $'$ denotes a later time. If we multiply the Boltzmann equation with this quantity χ and integrate over d^3u we find

$$\begin{aligned} \int \mathrm{d}^3u\ \chi \frac{\mathrm{D}f}{\mathrm{D}t} &= \int \mathrm{d}^3u \int \mathrm{d}^3\tilde{u} \int \mathrm{d}\boldsymbol{\Omega}\ \sigma(\boldsymbol{\Omega})|\boldsymbol{u} - \tilde{\boldsymbol{u}}| \cdot \\ &\quad \times \left(f(\boldsymbol{x}, \boldsymbol{u}', t) f(\boldsymbol{x}, \tilde{\boldsymbol{u}}', t) - f(\boldsymbol{x}, \boldsymbol{u}, t) f(\boldsymbol{x}, \tilde{\boldsymbol{u}}, t)\right) \chi. \end{aligned} \tag{3.9}$$

One can show that the right hand side equals zero (Choudhuri, 1998). Thus, we are left with

$$\int \mathrm{d}^3u\ \chi \left(\frac{\partial f}{\partial t} + u_\mathrm{i} \frac{\partial f}{\partial x_\mathrm{i}} + \frac{F_\mathrm{i}}{m} \frac{\partial f}{\partial u_\mathrm{i}} \right) = 0, \tag{3.10}$$

where we have used equation (3.2) and the relations $\dot{\boldsymbol{x}} = \boldsymbol{u}$ and $\dot{\boldsymbol{u}} = \boldsymbol{F}/m$ with $\boldsymbol{F}$ being a force acting on a particle with mass m. We can rewrite equation (3.10) as

$$\begin{aligned} &\frac{\partial}{\partial t} \int \mathrm{d}^3u\ \chi f + \frac{\partial}{\partial x_\mathrm{i}} \int \mathrm{d}^3u\ \chi u_\mathrm{i} f - \int \mathrm{d}^3u\ u_\mathrm{i} f \frac{\partial \chi}{\partial x_\mathrm{i}} \\ &\qquad - \frac{1}{m} \int \mathrm{d}^3u\ \frac{\partial \chi}{\partial u_\mathrm{i}} F_\mathrm{i} f - \frac{1}{m} \int \mathrm{d}^3u\ \chi \frac{\partial F_\mathrm{i}}{\partial u_\mathrm{i}} f = 0. \end{aligned} \tag{3.11}$$

This equation simplifies when we introduce the definition of the average. Given a quantity Q we define its average $\langle Q \rangle$ by

$$\langle Q \rangle \equiv \frac{1}{n} \int \mathrm{d}^3u\ Q f, \tag{3.12}$$

where the number density is

$$n \equiv \int \mathrm{d}^3u\ f. \tag{3.13}$$

Using the definition of the average we can modify equation (3.11) and end up with

$$\frac{\partial}{\partial t} \left(n \langle \chi \rangle\right) + \frac{\partial}{\partial x_\mathrm{i}} \left(n \langle u_\mathrm{i} \chi \rangle\right) - n \left\langle u_\mathrm{i} \frac{\partial \chi}{\partial x_\mathrm{i}} \right\rangle - \frac{n}{m} \left\langle F_\mathrm{i} \frac{\partial \chi}{\partial u_\mathrm{i}} \right\rangle - \frac{n}{m} \left\langle \frac{\partial F_\mathrm{i}}{\partial u_\mathrm{i}} \chi \right\rangle = 0. \tag{3.14}$$

This is the so-called *conservation equation*, which describes how the volume density $n \langle \chi \rangle$ of a conserved quantity χ changes in time. It is of crucial importance for hydrodynamics. Evaluation of (3.14) for the conserved quantities in a fluid, the mass, the momentum and the energy, results in the three central equations of hydrodynamics.

Conservation of Mass Let us start with substituting the particle mass m, which is conserved in a binary collision, into the conservation equation (3.14). The value of the mass does not depend on the position of the particle nor on its velocity (in the non-relativistic limit at least). If we additionally consider the force $\boldsymbol{F}$ to be independent of velocity, we end up with

$$\frac{\partial}{\partial t}(nm) + \frac{\partial}{\partial x_\mathrm{i}}(nm\langle u_\mathrm{i}\rangle) = 0. \tag{3.15}$$

$$\rho \equiv nm \tag{3.16}$$

and the average velocity

$$\boldsymbol{v} \equiv \langle \boldsymbol{u} \rangle \tag{3.17}$$

we can rewrite equation (3.15) as

$$\begin{aligned} \frac{\partial \rho}{\partial t} + \frac{\partial}{\partial x_\mathrm{i}}(\rho v_\mathrm{i}) &= 0 \\ \rightarrow \frac{\partial \rho}{\partial t} + \nabla(\rho \boldsymbol{v}) &= 0. \end{aligned} \tag{3.18}$$

This is the first moment of the Boltzmann equation and also known as the *continuity equation*.

Conservation of Momentum For deriving the second moment equation we substitute χ in (3.14) by the momentum mu_j. This leads to

$$\begin{aligned} \frac{\partial}{\partial t}(nm\langle u_\mathrm{j}\rangle) + \frac{\partial}{\partial x_\mathrm{i}}(nm\langle u_\mathrm{i}u_\mathrm{j}\rangle) - n\langle F_\mathrm{i}\delta_\mathrm{ij}\rangle &= 0 \\ \rightarrow \frac{\partial}{\partial t}(\rho v_\mathrm{j}) + \frac{\partial}{\partial x_\mathrm{i}}(\rho\langle u_\mathrm{i}u_\mathrm{j}\rangle) - \frac{\rho}{m}F_\mathrm{j} &= 0. \end{aligned} \tag{3.19}$$

We can simplify this further by defining a tensor

$$\begin{aligned} P_\mathrm{ij} &\equiv nm\langle (u_\mathrm{i} - v_\mathrm{i})(u_\mathrm{j} - v_\mathrm{j})\rangle \\ &= nm(\langle u_\mathrm{i}u_\mathrm{j}\rangle - v_\mathrm{i}v_\mathrm{j}). \end{aligned} \tag{3.20}$$

With P_ij we can bring equation (3.19) into the form

$$\frac{\partial}{\partial t}(\rho v_\mathrm{j}) + \frac{\partial}{\partial x_\mathrm{i}}(\rho v_\mathrm{i}v_\mathrm{j}) = \frac{\rho}{m}F_\mathrm{j} - \frac{\partial P_\mathrm{ij}}{\partial x_\mathrm{i}}. \tag{3.21}$$

Using the continuity equation (3.18) we can simplify the left hand side and get

$$\rho\left(\frac{\partial v_\mathrm{j}}{\partial t} + v_\mathrm{i}\frac{\partial v_\mathrm{j}}{\partial x_\mathrm{i}}\right) = \frac{\rho}{m}F_\mathrm{j} - \frac{\partial P_\mathrm{ij}}{\partial x_\mathrm{i}}. \tag{3.22}$$

Conservation of Energy Finally, we calculate the third moment of the conservation equation. For this we assume the translational kinetic energy $1/2m|\boldsymbol{u}-\boldsymbol{v}|^2$ to be a conserved quantity in a monoatomic gas. Substituting this quantity into the conservation equation (3.14) we find

$$\frac{\partial}{\partial t}(\rho\epsilon)+\frac{\partial}{\partial x_\mathrm{i}}(\rho\epsilon v_\mathrm{i})+\frac{\partial q_\mathrm{i}}{\partial x_\mathrm{i}}+P_\mathrm{ij}\Lambda_\mathrm{ij}=0, \tag{3.23}$$

with the internal energy per unit mass

$$\epsilon=\frac{1}{2}\left\langle|\boldsymbol{u}-\boldsymbol{v}|^2\right\rangle, \tag{3.24}$$

the energy flux

$$\boldsymbol{q}=\frac{1}{2}\rho\left\langle(\boldsymbol{u}-\boldsymbol{v})\,|\boldsymbol{u}+\boldsymbol{v}|^2\right\rangle, \tag{3.25}$$

and

$$\Lambda_\mathrm{ij}=\frac{1}{2}\left(\frac{\partial v_\mathrm{i}}{\partial x_\mathrm{j}}-\frac{\partial v_\mathrm{j}}{\partial x_\mathrm{i}}\right). \tag{3.26}$$

We can simplify equation (3.23) by using the continuity equation (3.18) and end up with

$$\rho\left(\frac{\partial\epsilon}{\partial t}+v_\mathrm{i}\frac{\partial\epsilon}{\partial x_\mathrm{i}}\right)+\frac{\partial q_\mathrm{i}}{\partial x_\mathrm{i}}+P_\mathrm{ij}\Lambda_\mathrm{ij}=0. \tag{3.27}$$

The moment equations describe the evolution of the conserved quantities in a fluid. However, the equations (3.18), (3.22) and (3.27) do not provide a dynamical theory, as there are to many independent variables. We will solve this problem in the next subsection, where we derive expressions for $\boldsymbol{q}$ and P_ij by taking into account transport phenomena.

Transport Phenomena

In the equilibrium case we expect the velocity distribution function f to be a *Maxwellian*, i.e.

$$\begin{aligned} f(\boldsymbol{x},\boldsymbol{u},t) &= f^{(0)}(\boldsymbol{x},\boldsymbol{u},t) \\ &= n(\boldsymbol{x},t)\left(\frac{m}{2\pi kT(\boldsymbol{x},t)}\right)^{3/2}\exp\left(-\frac{m(\boldsymbol{u}-\boldsymbol{v}(\boldsymbol{x},t))^2}{2kT(\boldsymbol{x},t)}\right). \end{aligned} \tag{3.28}$$

In case there are, however, strong gradients of temperature or velocity in the fluid, particles with higher velocity will stream into regions that are described by velocity distributions with lower velocities. We expect then a deviation from the local

Maxwellian distribution function. In this case we can write the distribution function as

$$f(\boldsymbol{x}, \boldsymbol{u}, t) = f^{(0)}(\boldsymbol{x}, \boldsymbol{u}, t) + g(\boldsymbol{x}, \boldsymbol{u}, t), \tag{3.29}$$

where $g(\boldsymbol{x}, \boldsymbol{u}, t)$ is the deviation from the Maxwellian $f^{(0)}(\boldsymbol{x}, \boldsymbol{u}, t)$. Inserting this ansatz into the collisional Boltzmann equation (3.7) yields in first order of g

$$\frac{\partial f}{\partial t} + \dot{\boldsymbol{x}} \cdot \nabla f + \dot{\boldsymbol{u}} \cdot \nabla_{\boldsymbol{u}} f = -\frac{f - f^{(0)}}{\tau}. \tag{3.30}$$

We have introduced here the collision time τ, which equals approximately the inverse of the collision integral. For a strong spatial gradient the second term on the left hand side of (3.30) is dominant. In this case we can approximate equation (3.30) by

$$\frac{|u| f^{(0)}}{L} \approx \frac{|g|}{\tau} \tag{3.31}$$

with $|u|$ being the typical particle velocity and L being the macroscopic size of the system. Expressing τ by the mean free path $\lambda = \tau |u|$ yields

$$\frac{|g|}{f^{(0)}} \approx \frac{\lambda}{L}. \tag{3.32}$$

Thus, if the mean free path is small compared to the macroscopic scale the distribution function will be almost Maxwellian. In this case f can be expanded in terms of λ / L:

$$f = f^{(0)} + \frac{\lambda}{L} f^{(1)} + \left(\frac{\lambda}{L}\right)^2 f^{(1)} + \dots . \tag{3.33}$$

This series is known as the *Chapman-Enskop expansion* (see Chapman et al. (1953) for more details).
When using only the first-order corrections, i.e. using $f \approx f^{(0)}$ on the left hand side of (3.30), one can show that

$$g = -\tau \left[\frac{1}{T} \frac{\partial T}{\partial x_i} U_i \left(\frac{m}{2kT} U^2 - \frac{5}{2} \right) + \frac{m}{kT} \Lambda_{ij} \left(U_i U_j - \frac{1}{3} \delta_{ij} U^2 \right) \right] f^{(0)}, \tag{3.34}$$

with $\boldsymbol{U} \equiv \boldsymbol{u} - \boldsymbol{v}$. Using this expression of g the quantities P_{ij} given in (3.20) and $\boldsymbol{q}$ given in (3.25) can be calculated. Integration yields

$$P_{ij} = p \delta_{ij} - 2 \nu \rho \left(\Lambda_{ij} - \frac{1}{3} \delta_{ij} \nabla \cdot \boldsymbol{v} \right) \tag{3.35}$$

with the *viscosity*

$$\nu = \frac{\tau k T}{m}. \tag{3.36}$$

For the quantity $\boldsymbol{q}$ one finds

$$\boldsymbol{q} = -K\nabla T \tag{3.37}$$

with the coefficient of *thermal conductivity*

$$K = \frac{5}{2}\frac{\tau n k^2 T}{m}. \tag{3.38}$$

A main conclusion of this section is that, both transport coefficients ν as K depend on the collision time τ. Under the assumption that the particles are rigid spheres with radius a Choudhuri (1998) finds

$$\tau = \frac{1}{4na^2}\left(\frac{m}{\pi kT}\right)^{1/2}. \tag{3.39}$$

The dependence of the transport coefficients on τ is intuitively clear as momentum and temperature are transported in collisions. For higher τ the coefficients ν and K become larger. In this case particles can stream into a region from further away without colliding leading to stronger deviations of the local distribution function from the Maxwellian.
We note here that more rigorous calculations for the transport coefficients have been performed by Braginskii (1965), who takes into account higher orders of the Chapman-Enskop expansion. He finds the following expression for the viscosity

$$\nu = 0.406\frac{(kT)^{5/2}}{e^4 m^{1/2} n \ln\Lambda}. \tag{3.40}$$

The result from this method yields a value of ν that is smaller by only a factor of roughly 3 compared to the one in equation (3.36). Also the result for K from the Chapman-Enskop method differs only be a factor of 3/2 compared to the result given in (3.38).

The Set of the Hydrodynamical Equations

Inserting the expressions (3.35) and (3.37) into the equation for momentum conservation (3.22) and the energy equation (3.27) simplifies these drastically. The set of the hydrodynamical equations is then given as: the *continuity equation*

$$\frac{\partial \rho}{\partial t} + \nabla(\rho \boldsymbol{v}) = 0, \tag{3.41}$$

the *Navier-Stokes equation*

$$\frac{\partial \boldsymbol{v}}{\partial t} + (\boldsymbol{v}\cdot\nabla)\boldsymbol{v} = -\frac{1}{\rho}\nabla p + \frac{1}{m}\boldsymbol{F} + \nu\left(\nabla^2\boldsymbol{v} + \frac{1}{3}\nabla(\nabla\cdot\boldsymbol{v})\right) \tag{3.42}$$

and the *energy conservation equation*

$$\rho\left(\frac{\partial \epsilon}{\partial t} + \boldsymbol{v}\cdot\nabla\epsilon\right) = \nabla\cdot(K\nabla T) - p\nabla\cdot\boldsymbol{v}. \tag{3.43}$$

These three equations constitute a dynamical theory of the fluid, yielding the time evolution of the variables $\boldsymbol{v}$, ρ, p, T and ϵ. Note, however, that the thermodynamical quantities ρ, p, T and ϵ are connected via equations of state and only two out of the four are independent. Thus, for a given viscosity ν, thermal conductivity K and external force $\boldsymbol{F}$ we have five independent variables, the evolution of which is described by the five hydrodynamical equations[1].
We have arrived at a theory that describes the dynamics of a neutral fluid. Interactions between the individual particles take place only via direct collisions, while the trajectories of the particles in between collisions are straight lines. The situation becomes more complicated when the particles carry charges. Here long-range interactions via electromagnetic forces occur and the particle trajectories become more complex. We continue our discussion now with the theoretical description of the electromagnetic field.

3.1.2 The Maxwell Equations

When a fluid is not made of neutral particles, but of ions and electrons, it reacts to electromagnetic fields. The electromagnetic field, i.e. the electric field $\boldsymbol{E}$ and the magnetic field $\boldsymbol{B}$, is described by the four *Maxwell equations* that we will discuss in the following.

Maxwell Equations of the Electric Field

The electric flux Φ appearing from an arbitrary charge distribution $\rho_{\mathrm{el}}(\boldsymbol{x})$ with total charge Q is given as

$$\begin{aligned}\Phi &= \int_{\partial \mathrm{V}} \boldsymbol{E}\ \mathrm{d}\boldsymbol{f} \\ &= \int_{\partial \mathrm{V}} \int_{\mathrm{V}} \rho_{\mathrm{el}}(\boldsymbol{x'}) \frac{\boldsymbol{r}^3}{r}\ \mathrm{d}^3x' \mathrm{d}\boldsymbol{f} \\ &= 4\pi \int_{\mathrm{V}} \rho_{\mathrm{el}}(\boldsymbol{x'})\ \mathrm{d}^3x' \\ &= 4\pi Q, \end{aligned} \tag{3.44}$$

where we have used Coulombs law for the electric field $\boldsymbol{E}$. The second step in this calculation can be rewritten with Gauss' theorem, which leads to

$$\begin{aligned}\int_{\partial \mathrm{V}} \boldsymbol{E}\ \mathrm{d}\boldsymbol{f} &= \int_{\mathrm{V}} \nabla \cdot \boldsymbol{E}\ \mathrm{d}V \\ &= 4\pi \int_{\mathrm{V}} \rho_{\mathrm{el}}(\boldsymbol{x'})\ \mathrm{d}V. \end{aligned} \tag{3.45}$$

The relation found here,

$$\nabla \cdot \boldsymbol{E} = 4\pi \rho_{\mathrm{el}}, \tag{3.46}$$

[1] Note, that the Navier-Stokes equation (3.42) is a vector equation, which has three components.

is the first Maxwell equation.
The second Maxwell equation can be derived from *Faraday's law of induction*, which claims that the electric voltage is proportional to the change of the magnetic flux,

$$\int_{\mathrm{c}} \boldsymbol{E}\ \mathrm{d}s = -\frac{1}{c}\frac{\mathrm{d}}{\mathrm{c}t}\int_{\partial \mathrm{V}} \boldsymbol{B}\ \mathrm{d}\boldsymbol{f}. \tag{3.47}$$

With Stokes' theorem we find

$$\int_{\partial \mathrm{V}} \nabla \times \boldsymbol{E}\ \mathrm{d}\boldsymbol{f} = -\frac{1}{c}\int_{\partial \mathrm{V}} \frac{\partial \boldsymbol{B}}{\partial t}\ \mathrm{d}\boldsymbol{f} \tag{3.48}$$

Thus, we find the second Maxwell equation to be

$$\nabla \times \boldsymbol{E} + \frac{1}{c}\frac{\partial \boldsymbol{B}}{\partial \mathrm{t}} = 0. \tag{3.49}$$

Maxwell Equations of the Magnetic Field

The derivation of the divergence of the magnetic field is simple, when we use our experience that there are no magnetic charges. So the magnetic flux through a closed area always vanishes,

$$\begin{aligned} \int_{\partial \mathrm{V}} \boldsymbol{B}\ \mathrm{d}\boldsymbol{f} &= \int_{\mathrm{V}} \nabla \cdot \boldsymbol{B}\ \mathrm{d}V \\ &= 0, \end{aligned} \tag{3.50}$$

and we find the third Maxwell equation

$$\nabla \cdot \boldsymbol{B} = 0. \tag{3.51}$$

For the last Maxwell equation we have to rewrite *Ampere's law*, which is given as

$$\oint_{\mathrm{c}} \boldsymbol{B}\ \mathrm{d}\boldsymbol{x} = \frac{4\pi}{c} I, \tag{3.52}$$

where $I = \int_{\partial \mathrm{V}} \boldsymbol{j} \mathrm{d}\boldsymbol{f}$ is the electric current. With Stokes law we find

$$\begin{aligned} \oint_{\mathrm{c}} \boldsymbol{B}\ \mathrm{d}\boldsymbol{x} &= \int_{\partial \mathrm{V}} \nabla \times \boldsymbol{B}\ \mathrm{d}\boldsymbol{f} \\ &= \int_{\partial \mathrm{V}} \frac{4\pi}{c}\boldsymbol{j}\ \mathrm{d}\boldsymbol{f}. \end{aligned} \tag{3.53}$$

The equation

$$\nabla \times \boldsymbol{B} = \frac{4\pi}{\mathrm{c}}\boldsymbol{j} \tag{3.54}$$

does not fulfill the continuity equation for the charge. For this reason an additional term, the so-called displacement current $c^{-1}\partial \boldsymbol{E}/\partial \mathrm{t}$, needs to be included. Thus, we end up with the fourth Maxwell equation

$$\nabla \times \boldsymbol{B} - \frac{1}{c}\frac{\partial \boldsymbol{E}}{\partial \mathrm{t}} = \frac{4\pi}{\mathrm{c}}\boldsymbol{j}. \tag{3.55}$$

We found a set of four equations describing the divergence and the rotation of the electric and the magnetic field. According to the *fundamental theorem of vector analysis* these equations determine the electromagnetic field completely as long as $\boldsymbol{E}$ and $\boldsymbol{B}$ decrease fast enough for large distances.

3.1.3 A Single Charged Particle in an Electromagnetic Field

A particle with the charge q and a velocity $\boldsymbol{v}$ in an electromagnetic field is exposed to the *Lorentz force*

$$\boldsymbol{F}_{\mathrm{L}} = q\left(\boldsymbol{E} + \frac{1}{c}\,\boldsymbol{v} \times \boldsymbol{B}\right). \tag{3.56}$$

With the definition of the current density

$$\boldsymbol{j} = q\boldsymbol{v} \tag{3.57}$$

the Lorentz force can be rewritten as

$$\boldsymbol{F}_{\mathrm{L}} = q\boldsymbol{E} + \frac{1}{c}\,\boldsymbol{j} \times \boldsymbol{B}. \tag{3.58}$$

By replacing the current density with the magnetic field according to Amperes law (3.55), we find[2]

$$\boldsymbol{F}_{\mathrm{L}} = q\boldsymbol{E} + \frac{1}{4\pi}\,(\boldsymbol{B}\cdot\nabla)\,\boldsymbol{B} - \nabla\frac{B^2}{8\pi}. \tag{3.59}$$

This form of the Lorentz force shows that the magnetic part consists of two components: a force resulting from the gradient of $B^2/(8\pi)$ and a *magnetic tension* $1/(4\pi)\,(\boldsymbol{B}\cdot\nabla)\,\boldsymbol{B}$. The term $B^2/(8\pi)$ acts like the thermal pressure and is thus labeled *magnetic pressure*. The magnetic tension force, which directs to the center of field line curvature, tends to straighten the field lines and behaves like the force in an elastic spring.
When solving the equation of motion $\boldsymbol{F}_{\mathrm{L}} = m\,\mathrm{d}\boldsymbol{u}/\mathrm{d}t$ with the Lorentz force (3.56) one finds, that charged particles of mass m move in spirals around magnetic field lines if they have a velocity component perpendicular to the magnetic field. The characteristic frequency of this motion is the *gyro-frequency*

$$\omega_{\mathrm{c}} = \frac{|q|B}{mc}. \tag{3.60}$$

[2]Here we use the vector identity $\nabla(\boldsymbol{X}\cdot\boldsymbol{Y}) = \boldsymbol{X}\times(\nabla\times\boldsymbol{Y})+\boldsymbol{Y}\times(\nabla\times\boldsymbol{X})+(\boldsymbol{X}\cdot\nabla)\boldsymbol{Y}+(\boldsymbol{Y}\cdot\nabla)\boldsymbol{X}$.

3.1.4 One-Fluid Magnetohydrodynamical Equations

The evolution of a magnetized fluid is described by the magnetohydrodynamical (MHD) equations. We present these equations in the following and discuss their nature.

Continuity Equation The continuity equation (3.41) that has been derived from the Boltzmann equation in the hydrodynamical case still holds when an electromagnetic fields is involved. For completeness we write it down again:

$$\frac{\partial \rho}{\partial t} + \nabla \cdot (\rho \boldsymbol{v}) = 0. \tag{3.61}$$

An important special case is a fluid the density of which is constant in time. In this case we the continuity equation simplifies to

$$\nabla \cdot (\rho \boldsymbol{v}) = 0. \tag{3.62}$$

If the density is also constant in space we find

$$\nabla \cdot \boldsymbol{v} = 0. \tag{3.63}$$

We speak of an incompressible fluid in this case.

Momentum Equation In absence of a magnetic field the time evolution of momentum is described by the Navier-Stokes equation (3.42). Now let us assume that the plasma is magnetized. This means that we have to consider an additional magnetic force. The Lorentz force (3.56) for a continuous system is $1/c\ \boldsymbol{j} \times \boldsymbol{B}$. Thus, we have to include the term

$$\begin{aligned} \frac{1}{c\rho}\boldsymbol{j} \times \boldsymbol{B} &= \frac{1}{4\pi\rho} (\nabla \times \boldsymbol{B}) \times \boldsymbol{B} \\ &= \frac{1}{4\pi\rho} (\boldsymbol{B} \cdot \nabla) \boldsymbol{B} - \frac{1}{\rho} \nabla \frac{B^2}{8\pi}, \end{aligned} \tag{3.64}$$

where we have used Ampere's law (3.55). Altogether, in MHD we have to use the following momentum equation

$$\frac{\partial \boldsymbol{v}}{\partial t} + (\boldsymbol{v} \cdot \nabla)\boldsymbol{v} = -\frac{1}{\rho} \nabla \left(p + \frac{B^2}{8\pi} \right) + \frac{1}{m}\boldsymbol{F} + \frac{1}{4\pi\rho} (\boldsymbol{B} \cdot \nabla) \boldsymbol{B} + \frac{\mu}{\rho} \left(\nabla^2 \boldsymbol{v} + \frac{1}{3} \nabla (\nabla \cdot \boldsymbol{v}) \right). \tag{3.65}$$

One can easily see, that the magnetic field leads to an additional magnetic pressure $B^2/(8\pi)$. Furthermore, one can show, that the second term including $\boldsymbol{B}$ is responsible for a tension along the magnetic field lines (see, e.g. Choudhuri, 1998).

Energy Equation The equation of the internal energy is in MHD almost the same as it is in hydrodynamics,

$$\rho\left(\frac{\partial\epsilon}{\partial t}+\boldsymbol{v}\cdot\nabla\epsilon\right)=\nabla\cdot(K\nabla T)+\frac{\boldsymbol{j}^2}{\sigma}-p\nabla\cdot\boldsymbol{v}. \tag{3.66}$$

There is only one additional term, $\boldsymbol{j}^2/\sigma$, which describes the *Ohmic heating*.

3.1.5 Collisions and Transport Phenomena in Magnetohydrodynamics

Collisions play a central role in the dynamics a fluid, as should be clear from the discussion within neutral fluids in section 3.1.1. The situation becomes more complex when the particles are charged. Not only do we have to treat collisions between different species, we also need to take into account forces from the electromagnetic field that act on the particles. The mathematical treatment of collisions is very complicated and we summarize here only the most important results. For detailed calculations we refer to the textbook by Spitzer (1956).

Resistivity and Ohm's Law

In order to treat collisions between electrons and ions[3] we need to use a two fluid approximation (see, e.g. Choudhuri, 1998). The equation of motion is given by the Navier-Stokes equation (3.42), in which we assume the viscosity term to vanish. Then for the electrons holds

$$m_\mathrm{e}n\frac{\partial\boldsymbol{v}_\mathbf{e}}{\partial t}=-\nabla p_\mathrm{e}-ne\left(\boldsymbol{E}+\frac{\boldsymbol{v}_\mathbf{e}}{c}\times\boldsymbol{B}\right)-m_\mathrm{e}n\nu_\mathrm{ie}\left(\boldsymbol{v}_\mathbf{e}-\boldsymbol{v}_\mathbf{i}\right), \tag{3.67}$$

where the additional last term describes the energy loss in collisions with ions at a collision frequency ν_ie. The force that is used here is the Lorentz force (3.56). With the definition of the electric current

$$\boldsymbol{j}=ne\left(\boldsymbol{v}_\mathbf{i}-\boldsymbol{v}_\mathbf{e}\right), \tag{3.68}$$

equation (3.67) becomes

$$m_\mathrm{i}n\frac{\partial\boldsymbol{v}_\mathbf{i}}{\partial t}=-\nabla p_\mathrm{i}-ne\left(\boldsymbol{E}+\frac{\boldsymbol{v}_\mathbf{i}}{c}\times\boldsymbol{B}\right)+\frac{m_\mathrm{e}\nu_\mathrm{ie}}{e}\boldsymbol{j}. \tag{3.69}$$

The corresponding equation of motion for the ions is

$$m_\mathrm{e}n\frac{\partial\boldsymbol{v}_\mathbf{e}}{\partial t}=-\nabla p_\mathrm{e}+ne\left(\boldsymbol{E}+\frac{\boldsymbol{v}_\mathbf{e}}{c}\times\boldsymbol{B}\right)-\frac{m_\mathrm{e}\nu_\mathrm{ie}}{e}\boldsymbol{j}. \tag{3.70}$$

[3]For simplicity we assume here an ionized hydrogen gas, i.e. the ions are protons.

Combination of equations (3.69) and (3.70) leads to

$$\boldsymbol{E} + \frac{1}{c}\boldsymbol{v} \times \boldsymbol{B} - \frac{1}{\sigma}\boldsymbol{j} = \frac{1}{ne}\left(\frac{1}{c}\boldsymbol{j} \times \boldsymbol{B} - \nabla p_{\mathrm{e}}\right), \tag{3.71}$$

where we have used the fact that $m_{\mathrm{e}} \ll m_{\mathrm{i}}$. We further have defined the *electric conductivity*

$$\sigma = \frac{ne^2}{m_{\mathrm{e}}\nu_{\mathrm{ie}}} \tag{3.72}$$

and the single-fluid velocity

$$\boldsymbol{v} = \frac{m_{\mathrm{i}}\boldsymbol{v}_{\mathrm{i}} + m_{\mathrm{e}}\boldsymbol{v}_{\mathrm{e}}}{m_{\mathrm{i}} + m_{\mathrm{e}}}. \tag{3.73}$$

Equation (3.71) is known as the *generalized Ohm's law*. Typically the terms $\boldsymbol{j} \times \boldsymbol{B}$, which corresponds to the Hall effect, and ∇p_{e} are small and we only have to deal with *Ohm's law*

$$\boldsymbol{j} = \sigma\left(\boldsymbol{E} + \frac{1}{c}\boldsymbol{v} \times \boldsymbol{B}\right). \tag{3.74}$$

The electrical conductivity σ is related to the *electrical resistivity* by

$$\eta = \frac{c^2}{4\pi\sigma} \tag{3.75}$$

The resistivity (3.75), which depends on the collision frequency between ions and electrons ν_{ie}, can be derived in general way (see the book of Spitzer, 1956). The result of the closure scheme is found to be

$$\eta = \frac{\pi^{3/2} m_{\mathrm{e}}^{1/2} e^2 c^2 \ln\Lambda}{2\gamma_{\mathrm{E}}\,(2kT)^{3/2}}, \tag{3.76}$$

where

$$\Lambda = \frac{3}{2e^3}\left(\frac{k^3T^3}{\pi n}\right)^{1/2}, \tag{3.77}$$

and the numerical factor γ_{E} is roughly 0.582 for an ionic charge of 1. The factor $\ln\Lambda$ is called Coulomb logarithm has a typical value of the order of 10.

Ambipolar Diffusion

In many astrophysical environments, like for example in the interstellar medium, the gas is not fully ionized. In this case MHD can only be applied, when there is a strong coupling between the electron-ion component and the neutral component due the collisions. There are, however, cases where this coupling is not perfect.

An important consequence of this decoupling is *ambipolar diffusion*, which might play a crucial role in the initial phase of star formation. With a typical collision rate between the charged and the neutral particles, one can show that there is a diffusion process between the two components. In case of a collapsing molecular cloud, the ionized gas is tied to the interstellar magnetic field. A decoupling of the charged from the neutral component makes gravitational collapse possible. The resulting flux is given by

$$n\boldsymbol{v} = -D_{\mathrm{AD}}\nabla n, \tag{3.78}$$

with D_{AD} being the coefficient of ambipolar diffusion (see, e.g. Choudhuri, 1998).

The Presence of a Strong Magnetic Field

In the transition from an unmagnetized to a magnetized state, the plasma becomes anisotropic, i.e. certain physical quantities depend on their relative orientation to the magnetic field direction.
We have discussed the closure of the hydrodynamical equations in subsection 3.1.1. The main assumption was that the mean free path is much smaller than the macroscopic scales of the system. In presence of a magnetic field, a third typical length scales enters, the gyro-radius of the charged particles

$$r_{\mathrm{c}} = \frac{(2m_s kT)^{1/2} c}{eB}. \tag{3.79}$$

The index s refers here to the different charged species, i.e. the ions and the electrons. If the magnetic field is very strong the gyro-radius becomes smaller than the mean free path and one uses the latter for closing the set of equations.
With a strong ordered magnetic field the medium becomes anisotropic and one has to distinguish between the viscosity along (parallel to) and the one perpendicular to the magnetic field lines. The motion of charged particles along the field is still determined by the mean free path and the transport coefficients are the same as in the unmagnetized case (see equations 3.36 and 3.75).
Thus the parallel viscosity is given by equation (3.40):

$$\nu_{\parallel} = 0.406 \frac{(kT)^{5/2}}{e^4 m^{1/2} n \ \ln\Lambda}. \tag{3.80}$$

Braginskii (1965) shows that the viscosity perpendicular to the field is given by

$$\nu_{\perp} = \frac{2}{5}\left(\frac{\pi}{kT}\right)^{1/2} \frac{e^4 \ \ln\Lambda}{m^{3/2}\omega_{\mathrm{c}}^2} \tag{3.81}$$

with the gyro-frequency of the ions from equation (3.60).
For the electric resistivity and the conductivity, the situation is similar. The component along the field lines is given by the Spitzer expression (3.76):

$$\eta_{\parallel} = \frac{\pi^{3/2} m_{\mathrm{e}}^{1/2} e^2 c^2 \ \ln\Lambda}{2\gamma_{\mathrm{E}}(2kT)^{3/2}} \tag{3.82}$$

and the one perpendicular to the field lines by

$$\eta_\perp = \frac{\pi^{3/2} m_\mathrm{e}^{1/2} e^2 c^2 \ln\Lambda}{2\gamma_\mathrm{EB}(2kT)^{3/2}} \tag{3.83}$$

with $\gamma_\mathrm{E} \approx 0.582$ and $\gamma_\mathrm{EB} = 3\pi/32$. Note, that $\eta_\perp$ is, contrary to the case of the perpendicular viscosity, no function of the magnetic field strength and the difference between the parallel and the perpendicular components is just approximately a factor of two.

3.1.6 The Induction Equation

For a full dynamical theory of MHD we have to find one more equation in addition to the fluid equations discussed in subsection 3.1.4, because there are more independent variables. We require an equation describing the magnetic field $\boldsymbol{B}$, which we can derive from the Maxwell equations and Ohm's law (3.74).
By combinating Faraday's law (3.49) with Ohm's law (3.74) we can eliminate the electric field $\boldsymbol{E}$,

$$\frac{1}{c}\frac{\partial \boldsymbol{B}}{\partial t} = -\nabla \times \left(\frac{\boldsymbol{j}}{\sigma} - \boldsymbol{v} \times \boldsymbol{B} \right). \tag{3.84}$$

When we neglect Maxwell's displacement current $c^{-1}\partial \boldsymbol{E}/\partial t$ in Ampere's law (3.55) and substitute the current density $\boldsymbol{j}$ into the upper equation we find the *induction equation*

$$\frac{\partial \boldsymbol{B}}{\partial t} = \nabla \times (\boldsymbol{v} \times \boldsymbol{B} - \eta \nabla \times \boldsymbol{B}), \tag{3.85}$$

which describes the evolution of the magnetic field.
We can make the induction equation dimensionless by introducing the typical quantities of our system: B is the typical field strength, L the typical length scale, V the typical velocity and T the typical timescale. With $\boldsymbol{B} = B\tilde{\boldsymbol{B}}$, $\nabla = 1/L\tilde{\nabla}$, $\boldsymbol{v} = V\tilde{\boldsymbol{v}}$ and $\boldsymbol{t} = T\tilde{\boldsymbol{t}}$ we find

$$\frac{\partial \tilde{\boldsymbol{B}}}{\partial t} = \tilde{\nabla} \times \left(\tilde{\boldsymbol{v}} \times \tilde{\boldsymbol{B}} - \frac{1}{\mathrm{Rm}} \nabla \times \tilde{\boldsymbol{B}} \right). \tag{3.86}$$

We defined here the *magnetic Reynolds number*

$$\mathrm{Rm} \equiv \frac{VL}{\eta}, \tag{3.87}$$

which is an indicator for the importance of the two terms on the right hand side of equation (3.85). The limit of $\mathrm{Rm} \ll 1$ leads to a diffusion equation. In this case the magnetic field can only decay. The other limit, $\mathrm{Rm} \gg 1$, is the limit of perfect conduction, where the electric conductivity $\sigma \gg 1$. Only in this case the magnetic energy can increase.

3.1.7 The Full Set of Magnetohydrodynamical Equations

In presence of a strong magnetic field the fluid equations are given by the continuity equation (3.61), the momentum equation (3.65) and the energy equation (3.66). In addition to the three components of the velocity $\boldsymbol{v}$ and the thermodynamical quantities ρ, p, T and ϵ (only two of which are independent), the three components of the magnetic field strength $\boldsymbol{B}$ need to be included. The five modified hydrodynamical equations are thus not enough for the description of the fluid. In order to have a full dynamical system of equations we need to include the induction equation (3.85).
In conclusion, the complete set of the MHD equations is given by

$$\frac{\partial \rho}{\partial t} + \nabla \cdot (\rho \boldsymbol{v}) = 0 \tag{3.88}$$

$$\frac{\partial \boldsymbol{v}}{\partial t} + (\boldsymbol{v} \cdot \nabla)\boldsymbol{v} = -\frac{1}{\rho}\nabla\left(p + \frac{B^2}{8\pi}\right) + \frac{1}{m}\boldsymbol{F} + \frac{1}{4\pi\rho}(\boldsymbol{B} \cdot \nabla)\boldsymbol{B} + \frac{\mu}{\rho}\left(\nabla^2 \boldsymbol{v} + \frac{1}{3}\nabla(\nabla \cdot \boldsymbol{v})\right) \tag{3.89}$$

$$\rho\left(\frac{\partial \epsilon}{\partial t} + \boldsymbol{v} \cdot \nabla \epsilon\right) = \nabla \cdot (K \nabla T) + \frac{\boldsymbol{j}^2}{\sigma} - p \nabla \cdot \boldsymbol{v} \tag{3.90}$$

$$\frac{\partial \boldsymbol{B}}{\partial t} = \nabla \times (\boldsymbol{v} \times \boldsymbol{B} - \eta \nabla \times \boldsymbol{B}). \tag{3.91}$$

In the case of ideal MHD the transport coefficients vanish and the upper set of equations is reduced to

$$\frac{\partial \rho}{\partial t} + \nabla \cdot (\rho \boldsymbol{v}) = 0 \tag{3.92}$$

$$\frac{\partial \boldsymbol{v}}{\partial t} + (\boldsymbol{v} \cdot \nabla)\boldsymbol{v} = -\frac{1}{\rho}\nabla\left(p + \frac{B^2}{8\pi}\right) + \frac{1}{m}\boldsymbol{F} + \frac{1}{4\pi\rho}(\boldsymbol{B} \cdot \nabla)\boldsymbol{B} \tag{3.93}$$

$$\rho\left(\frac{\partial \epsilon}{\partial t} + \boldsymbol{v} \cdot \nabla \epsilon\right) = \frac{\boldsymbol{j}^2}{\sigma} - p \nabla \cdot \boldsymbol{v} \tag{3.94}$$

$$\frac{\partial \boldsymbol{B}}{\partial t} = \nabla \times (\boldsymbol{v} \times \boldsymbol{B}). \tag{3.95}$$

We note, that in order to close the system of MHD equations an equation of state is required that connects two of the thermodynamic quantities.

3.2 Magnetic Seed Fields

The induction equation (3.85) describes the evolution of a magnetic field, i.e. the amplification and the dissipation of magnetic energy. With $\boldsymbol{B} = \boldsymbol{0}$ being a solution of the induction equation, it provides no explanation for the real origin of the fields. In our further analysis we thus need to assume the existence of a magnetic seed field. We discuss possible generation mechanisms of these seed fields in this section.

3.2.1 Origin within the First Minutes of the Universe

Different mechanisms are proposed in literature, which describe the generation of magnetic fields in the very early Universe. These exotic theories predict large-scale magnetic fields of various strengths, but are obviously hard to confirm by observations. Nevertheless, we shortly discuss the field generation in inflation and cosmological phase transitions in this section. For more details on that topic we refer to the reviews by Widrow (2002) and Widrow et al. (2012).

Magnetic Field Inhomogeneities in Inflation

Theoretically, the first seed fields might already have been generated in the very early Universe during inflation. In this era of the Universe, where the scale factor increases exponentially leading to an spatial increase by a factor of roughly 10^{30}, small spatial quantum fluctuations expand into the large-scale seeds of which stars and galaxies form.
In the same way magnetic fluctuations could expand into large-scale magnetic fields during inflation. However, under the assumption of conformal invariance of electromagnetism the product of the magnetic field strength and the scale factor squared, Ba^2, stays constant. With an increase by a factor of 10^{30}, the field strength would decrease by a factor of 10^{60} and become extremely weak.
Turner & Widrow (1988) find that conformal invariance can be broken for example through gravitational coupling of the photon. The resulting field strengths depend strongly on the model. Typical magnetic fields that generated in inflation can be as strong as $B_0 \approx 10^{-10}$ G on a Mpc scale. We note, however, that alternative models predict considerably weaker fields, which are of the order of $B_0 \approx 10^{-40}$ G.

Magnetic Field Generation in Phase Transitions

With the expansion of the Universe the temperature decreases. This leads to a series important phase transitions, i.e. symmetry brakings, in the early Universe changing the appearance of forces and particles crucially. In these phase transitions typically a large amount of energy is released and currents of the charged particles are driven. The generation of electric and magnetic fields is a natural consequence.
Mostly discussed in this context are first-order phase transitions. Here a regime of mixed phases occurs, in which bubbles of the new phase expand into regions of

the former phase until they fill the whole space. Especially the bubble walls, where energy is released into heat, play an important role. Let us for example consider the QCD phase transition. As the differently charged quarks in the quark-gluon plasma have different masses, it is has a net positive charge, while the lepton sector has a net negative charge. This leads to the generation of electric currents on the bubble walls, which separate the quark sectors from the baryon sectors. Quashnock et al. (1989) show that this currents can generate magnetic fields in the QCD phase transition with a strength of 5 G on a scale of 100 cm. This leads to a typical field strength of 10^{-17} G on a scale of 10^{11} cm at the time of recombination, when an inverse cascade of the magnetic energy to larger scales is assumed. Cheng & Olinto (1994) and Sigl et al. (1997) show that baryons concentrate on the bubble walls during the phase transition. This effect leads to magnetic fields that are approximately seven orders of magnitude stronger than the ones predicted without this effect.

3.2.2 Origin from Plasma Phenomena

Battery Mechanisms

Besides a cosmological origin of magnetic fields there are so-called battery mechanisms, which can continuously work in the Universe. We have seen, that the normal induction equation (3.85) provides no way of creating a magnetic field. Every term of this equation includes $\boldsymbol{B}$ and thus $\boldsymbol{B} = 0$ is a valid solution. However, we have so far used the one-fluid approximation for magnetohydrodynamics. We will see that additional terms will appear in our equations if we go one step further and use a two-fluid approximation, including two differently charged species.
For simplicity we consider a partially ionized hydrogen gas, which consists of electrons, protons and neutrals. In the two-fluid approximation the generalized Ohm's law is given in equation (3.71). The first term on the right hand side of this equation is responsible for the Hall effect. The last term in (3.71), $\nabla p_\mathrm{e}/(ne)$ is the so-called *Biermann term*, which provides a way to generate a magnetic field. Deriving the induction equation in the same way like we did in Section 3.1.6, but now using the generalized Ohm's law, results in (Spitzer, 1956)

$$\frac{\partial \boldsymbol{B}}{\partial t} = \nabla \times (v_\mathrm{i} \times \boldsymbol{B}) - \frac{\eta}{4\pi} \nabla \times (\nabla \times \boldsymbol{B}) - \frac{ck}{e} \frac{\nabla n_\mathrm{e}}{n_\mathrm{e}} \times \nabla T, \tag{3.96}$$

where we use $p_\mathrm{e} = n_\mathrm{e} kT$. This generalized induction equation has, compared to equation (3.85), one additional term $ck/(en_\mathrm{e})\nabla n_\mathrm{e} \times \nabla T$, which is independent of the magnetic field $\boldsymbol{B}$. Thus, this source term can generate a field under the condition that there is a pressure and a temperature gradient that are not parallel.
The descriptive explanation of this generation mechanism, which is also illustrated in figure 3.1, uses the fact that our two charged species have very different masses, i.e. $m_\mathrm{e} \ll m_\mathrm{p}$. If there is a pressure gradient in the plasma the particles get accelerated. The electrons are more strongly accelerated than the protons, because they have a smaller mass. This leads to a separation of charge and an electric field is

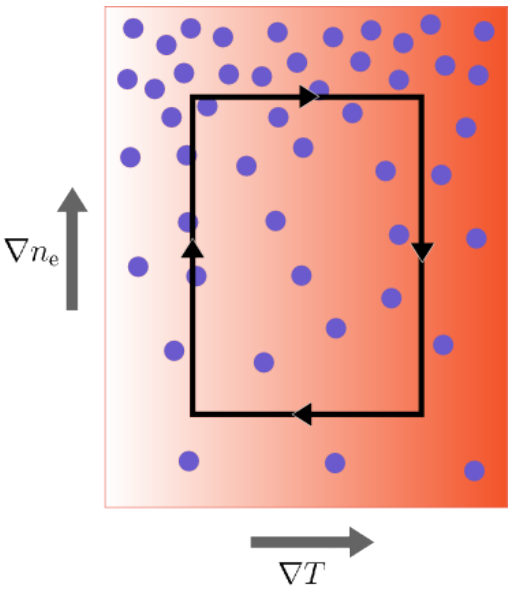

Figure 3.1:
The principle of the Biermann battery: Non-parallel gradients in density (∇n_e)and temperature (∇T) lead to a charge separation, by which in turn a magnetic field is generated.

generated. If now the electron density n_e is constant in space the electric field is static. But a spatial dependence of n_e gives rise to an electric current and thus to the generation of a magnetic field (Biermann, 1950; Kulsrud & Zweibel, 2008).
Let us now estimate how strong the fields produced by the Biermann battery are (Kulsrud & Zweibel, 2008). In a system that is formed by gravity, the energy that can be transformed into magnetic energy is the gravitational energy. The typical timescale on which the magnetic field is generated is then given by the free-fall time $T_{ff} = 1/\sqrt{Gmn}$, where G is the gravitational constant and m the mean partial mass. From the generalized induction equation (3.96) we find

$$\begin{aligned} \frac{B}{T_{ff}} &\approx \frac{ck}{e} \frac{L^{-1} n_e}{n_e} L^{-1} T \\ &= \frac{ckT}{L^2 e}. \end{aligned} \tag{3.97}$$

The typical length scale L of a gravitationally formed system is the Jeans length L_J, which is determined by the Jeans mass (2.5) with $M_J = 4/3\pi\rho L_J^3$. Hence we set $L \approx c_s(\rho G)^{1/2}$, where $c_s = (kT/m)^{1/2}$ is the thermal sound speed. Thus, we find for the typical magnetic field strength generated by a Biermann battery:

$$B \approx \frac{c}{e} m^{3/2} (nG)^{1/2}. \tag{3.98}$$

For the typical intergalactic medium with $m \approx 1.67 \times 10^{-24}$ g and $n \approx 1$ cm^{-3} the Biermann battery can generate a magnetic field of roughly 10^{-20} G.
On the numerical side, there are a number of MHD simulations including the Biermann battery effect. For example Xu et al. (2008) study magnetic fields in primordial star formation with a self-consistent three-dimensional adaptive mesh refinement simulation. They find that the Biermann battery is most important in the early

evolution of a primordial halo. The generated magnetic field gets further amplified in the collapse through gravitational compression. Xu et al. (2008) find a peak magnetic field strength of 10^{-19} G at a redshift of 17.55.

Aperiodic Plasma Fluctuations

Recently, Schlickeiser (2012) has shown that a turbulent magnetic field can be generated in plasma fluctuations within an unmagnetized non-relativistic medium. He analyses a special kind of plasma fluctuations, so-called *aperiodic fluctuations*. These fluctuations do not propagate in space, but can permanently grow or decrease in time. Schlickeiser (2012) shows that aperiodic fluctuations can generate a random magnetic field with a typical field strength of

$$B \approx 4.7 \times 10^{-16} \text{ G } \left(\frac{T}{10^4 \text{ K}}\right)^{1/2} \left(\frac{n}{10^{-7} \text{ cm}^{-3}}\right)^{2/3}. \tag{3.99}$$

This formula is expressed in terms of the properties of the intergalactic medium, which is being photoionized by the first stars leading to typical temperatures of $T \approx 10^4$ K and densities of $n \approx 10^{-7}$ cm^{-3}. Applying the same formula (3.99) to a protogalaxy with $T \approx 5 \times 10^3$ K and $n \approx 10$ cm^{-3} leads to a seed field strength of the order of 10^{-10} G.

3.3 Simple Models for Magnetic Field Amplification

3.3.1 Ideal Magnetohydrodynamics and the Concept of Flux Freezing

In order to amplify a magnetic field by dynamical motions of the gas, it needs to be frozen into the gas, i.e. the field lines need to be dragged along with the fluid elements. This condition is called *flux freezing* and is provided in the case of ideal MHD. Strictly speaking, a system can only be described by ideal MHD if all of the following conditions are fulfilled:

- The collision rate between the ions and neutrals in an ionized gas needs to be very high. This ensures that the neutral and the charged particles are coupled perfectly and behave as one fluid. If there is, for example, a strong external magnetic field the whole fluid feels the Lorentz force and not only the ions.
- The viscosity needs to vanish ($\nu \to 0$), i.e. the hydrodynamic Reynolds number is infinite (Re $\propto 1/\nu \to \infty$).
- The resistivity needs to vanish ($\eta \to 0$), i.e. the electric conductivity and the magnetic Reynolds number become infinite ($\sigma \propto 1/\eta \to \infty$ and Rm $\propto 1/\eta \to \infty$). Because of this condition ideal MHD is also known as non-resistive MHD.

Let us now define the magnetic flux Ψ as

$$\Psi = \int_S \boldsymbol{B}\ \mathrm{d}\boldsymbol{S}, \tag{3.100}$$

with $\boldsymbol{S}$ being an area through which a magnetic field $\boldsymbol{B}$ flows. Both, $\boldsymbol{B}$ and S, can change in time. The first term of the time derivative of Ψ is

$$\begin{aligned}\left(\frac{\partial\Psi}{\partial t}\right)_1 &= \int_S \frac{\partial \boldsymbol{B}}{\partial t}\ \mathrm{d}\boldsymbol{S} \\ &= -c\int_S \nabla\times\boldsymbol{E}\ \mathrm{d}\boldsymbol{S},\end{aligned} \tag{3.101}$$

where we used the Maxwell equation (3.49). With $\partial\mathrm{d}\boldsymbol{S}/\partial t = \boldsymbol{u}\times\mathrm{d}\boldsymbol{l}$, the second term of $\partial\Psi/\partial t$ becomes

$$\begin{aligned}\left(\frac{\partial\Psi}{\partial t}\right)_2 &= \oint_c \boldsymbol{B}\cdot(\boldsymbol{u}\times\mathrm{d}\boldsymbol{l}) \\ &= -c\oint_c(\boldsymbol{B}\times\boldsymbol{u})\cdot\mathrm{d}\boldsymbol{l} \\ &= -\int_S \nabla\times(\boldsymbol{B}\times\boldsymbol{u})\ \mathrm{d}\boldsymbol{S},\end{aligned} \tag{3.102}$$

Here we use Stoke's law of integration in the last step. In total, this yields a time derivative of the magnetic flux of

$$\frac{\partial\Psi}{\partial t} = -\int_S \nabla\times(\boldsymbol{u}\times\boldsymbol{B} + c\boldsymbol{E})\ \mathrm{d}\boldsymbol{S}, \tag{3.103}$$

Comparison with Ohm's law (3.74) results in

$$\frac{\partial\Psi}{\partial t} = -\int_S \nabla\times(c\eta\boldsymbol{j})\ \mathrm{d}\boldsymbol{S}. \tag{3.104}$$

As the resistivity vanishes in ideal MHD, the value under the integral becomes zero and we find

$$\frac{\partial\Psi}{\partial t} = 0. \tag{3.105}$$

Thus, the magnetic flux is a conserved quantity in ideal MHD and the magnetic field is virtually frozen into the fluid. This behavior is also known as *Alvén's theorem of flux freezing* (Alvén, 1942).
We point out that flux freezing is only ensured for weak magnetic fields. With increasing magnetic energy, magnetic back reactions become more important and at some point the neutrals will not follow the magnetic field any more.

3.3.2 Compression of Field Lines in Different Geometries

When the magnetic field follows the motion of the plasma, i.e. the magnetic flux is frozen into the fluid, it can be amplified when the density increases. If and by how much the field strength increases depends on the geometry of the collapse. We present here derivations for parallel, perpendicular and spherical compression from the book of Frank-Kamenezki (1967).
A mathematical treatment of amplification by gravitational compression starts with the continuity and the induction equation, as these describe the evolution of the density and the magnetic field strength. In Lagrangian notation, they are

$$\begin{aligned} \frac{\mathrm{d}\rho}{\mathrm{d}t} &= -\rho\nabla\cdot\boldsymbol{v}, \\ \frac{\mathrm{d}\boldsymbol{B}}{\mathrm{d}t} &= (\boldsymbol{B}\cdot\nabla)\,\boldsymbol{v} - \boldsymbol{B}\,(\nabla\cdot\boldsymbol{v})\,. \end{aligned} \tag{3.106}$$

Elimination of $\nabla\cdot\boldsymbol{v}$ leads to

$$\begin{aligned} \frac{\mathrm{d}\boldsymbol{B}}{\mathrm{d}t} &= (\boldsymbol{B}\cdot\nabla)\,\boldsymbol{v} + \frac{\boldsymbol{B}}{\rho}\frac{\mathrm{d}\rho}{\mathrm{d}t} \\ \leftrightarrow \frac{\mathrm{d}}{\mathrm{d}t}\left(\frac{\boldsymbol{B}}{\rho}\right) &= \left(\frac{\boldsymbol{B}}{\rho}\cdot\nabla\right)\boldsymbol{v}. \end{aligned} \tag{3.107}$$

We now aim to study the evolution of a frozen-in field line in a plasma that is compressed arbitrarily. For this purpose we consider two fluid elements and connect them through a fluid line $\boldsymbol{l}$. If these elements have the velocities $\boldsymbol{v}_1$ and $\boldsymbol{v}_2$, the length of the fluid line $\boldsymbol{l}$ changes as

$$\frac{\mathrm{d}\boldsymbol{l}}{\mathrm{d}t} = (\boldsymbol{v}_2 - \boldsymbol{v}_1)_l, \tag{3.108}$$

where the index l indicates the protection of the velocities on the fluid line. For an infinitesimal fluid line $\delta\boldsymbol{l}$ this expression becomes

$$\frac{\mathrm{d}\delta\boldsymbol{l}}{\mathrm{d}t} = (\delta\boldsymbol{l}\nabla)\boldsymbol{v}. \tag{3.109}$$

By comparing the upper equation with equation (3.107), we directly find

$$\frac{B}{\rho} \propto \delta l. \tag{3.110}$$

This means that the ratio of the magnetic field strength over the density changes proportional to the length of the fluid line. We can consider some special cases of this result.
When the compression of the fluid is, for example, perpendicular to the magnetic field lines, the length of the field line δl does not change (see Figure 3.2). With $\delta l = const$, we find

$$B \propto \rho. \tag{3.111}$$

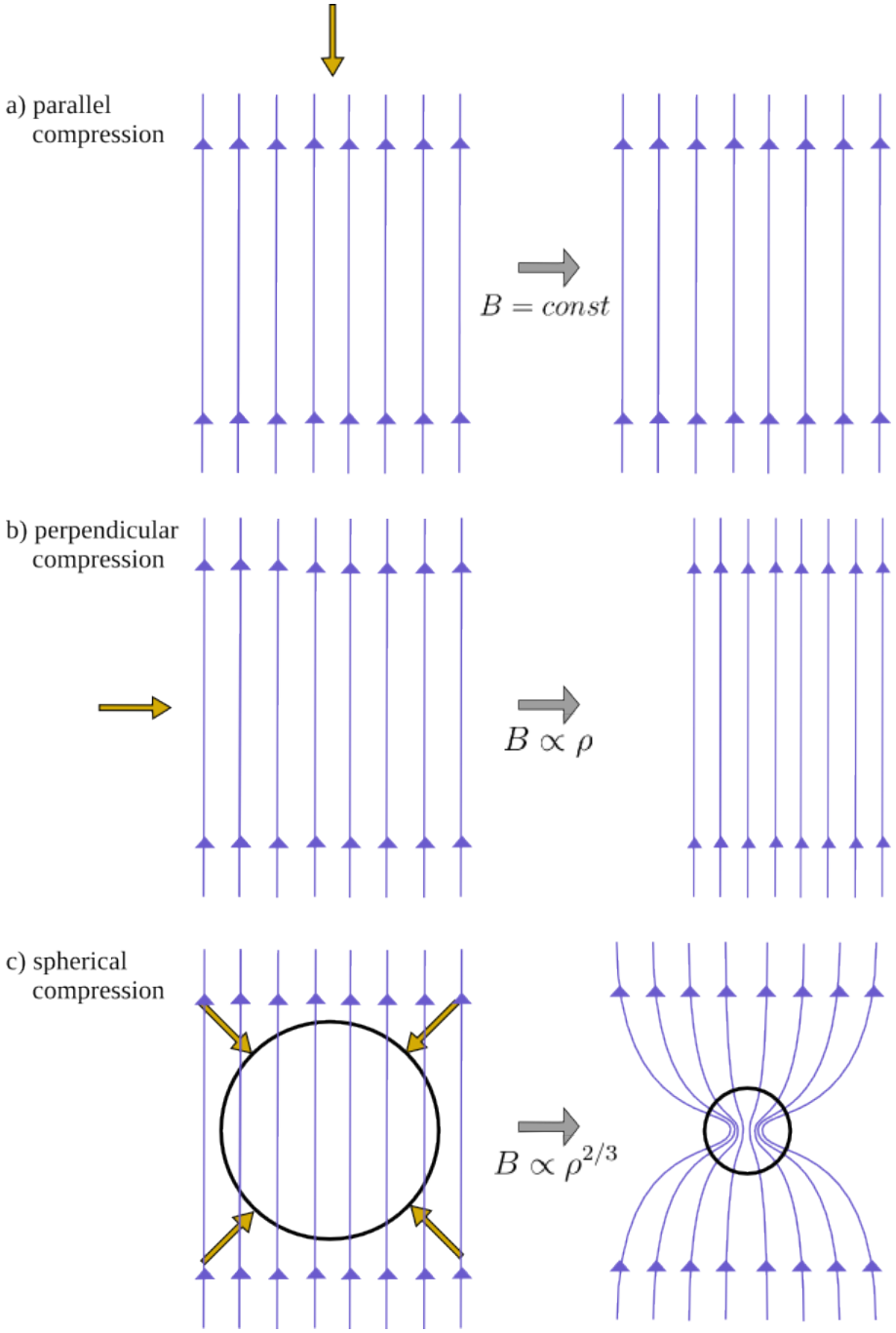

Figure 3.2:
Compression of magnetic field lines in different force fields. A force acting parallel to the field lines does not affect the field strength, as indicated in part a). Perpendicular compression, illustrated in picture b), leads to compaction of the field lines and thus to an amplification of the field strength. Also the spherical compression in picture c) leads to an increase of the field strength, leaving behind a characteristic hourglass shaped magnetic field.

In this case the magnetic field strength increases proportional to the density, because the magnetic field lines move closer together.
When, on the other hand, the compression takes place parallel to the field lines, the single fluid lines get shorter, but the distance between the fluid lines does not change (see figure 3.2). In this change δl changes inversely proportional to ρ, and we find

$$B = const. \tag{3.112}$$

In astrophysics the most important case is spherical compression, where $\rho \propto \delta l^{-3}$. With equation (3.110) we find for this case

$$B \propto \rho^{2/3}. \tag{3.113}$$

The geometry of a magnetic field that has been compressed spherically is shown in part (c) of figure 3.2. The shape is usually refereed to as an hourglass shape, which has in fact been detected in molecular clouds (see the observation in figure 2.2).
The effect of magnetic field amplification due to gravitational compression is also seen in numerical simulations. Xu et al. (2008) find in their simulation of population III star formation, besides the field generation due to the Biermann battery, an amplification of the field roughly proportional to $\rho^{2/3}$. Also Federrath et al. (2011) test the amplification due to spherical compression in their MHD simulations. They start with a weak field in z-direction and analyse the magnetic field strength during the collapse. The field grows less than proportional to $\rho^{2/3}$ at the beginning, as the field is not yet isotropic. Due to the collapse, the field lines get stretched and the typical hour-glass shape is generated (see figure 3.2). Then the field becomes isotropic and grows almost[4] proportional to $\rho^{2/3}$.

3.3.3 Field Amplification in the Spherical Collapse of a Galaxy

In the astrophysical context we often find a spherical collapse for example during the formation of a galaxy. We now estimate the typical timescale for amplifying a Biermann seed field of $B_1 = 10^{-20}$ G to $B_2 = 10^{-6}$ G, which is observed in the Milky Way, in gravitational compression. With conservation of flux we find in spherical compression

$$B_1 \rho_1^{-2/3} = B_2 \rho_2^{-2/3}, \tag{3.114}$$

where we take $\rho_2 = 10^{-24}$ g as the density of the Milky Way. We now assume that the galaxy forms from the collapse of a cloud of density ρ_1 within the free-fall time

[4]However, Federrath et al. (2011) find in a test of the ideal MHD-approximation small derivations from $B \propto \rho^{2/3}$, which depend on the resolution of the simulation. This is caused by non-ideal magnetohydrodynamical effects due to small numerical diffusivity.

$T = 1/\sqrt{G\rho_1}$. Thus, we result in

$$\begin{aligned} B_1 G^{2/3} T^{4/3} &= B_2 \rho_2^{-2/3} \\ \leftrightarrow T &= \left(\frac{B_2}{B_1}\right)^{3/4} \frac{1}{\sqrt{G\rho_2}}. \end{aligned} \tag{3.115}$$

For our example, we find a typical timescale for amplification by gravitational compression of 10^{18} years, which is many orders higher than the Hubble time. We thus conclude that gravitational compression alone cannot explain the strong magnetic fields observed in galaxies. Mechanisms that can increase the magnetic field strength more efficiently are MHD dynamos, which will be discussed phenomenologically in the next section.

3.4 Overview of Magnetohydrodynamical Dynamos

3.4.1 The Mean-Field Dynamo

In the 20th century various observations of the Sun indicated the complex structure and time dependency of the solar magnetic field. We reported already the discovery of high field strengths in sunspots by Hale (1908). A further important observation is the variation of the number of sunspots in time with a period of roughly 22 years (see the *butterfly diagram* by Maunder, 1904). Any theory of stellar magnetism needs to explain these properties of sunspots.

Qualitative Description

The first theoretical interpretation for the solar magnetic field was published by Parker (1955a,b). Today that mechanism is referred to as the α-Ω *dynamo*, a qualitative picture of which is shown in figure 3.3. The Parker dynamo starts with an initially poloidal field $\boldsymbol{B}_\mathrm{p} = B_\mathrm{r}\hat{\boldsymbol{e}}_\mathrm{r} + B_\theta \hat{\boldsymbol{e}}_\theta$, which results for instance from gravitational compression during the formation of the Sun[5]. The poloidal field is shown in part (a) of figure 3.3. As the Sun rotates differentially, i.e. it rotates faster on the equator than on the poles, the poloidal field lines get stretched on the sphere (see (b) in figure 3.3). By coiling up the poloidal field a torodial magnetic field component $B_\phi \hat{\boldsymbol{e}}_\phi$ is generated. The torodial field lines become denser and denser (part (c)) until a full toroidal field is created by magnetic reconnection (part (d)). The process of making a toroidal field from a poloidal one by differential rotation is known as the Ω-*effect*.
There is still a poloidal component in figure (d), but has been omitted now in the figure for simplicity. If there was no mechanism that generates a poloidal field it would decay and thus also the production of the toroidal field would stop. Parker

[5]Poloidal magnetic fields are fields with an hourglass shape. These geometries of magnetic fields are commonly observed in gravitationally collapsing molecular clouds (see figure 2.2).

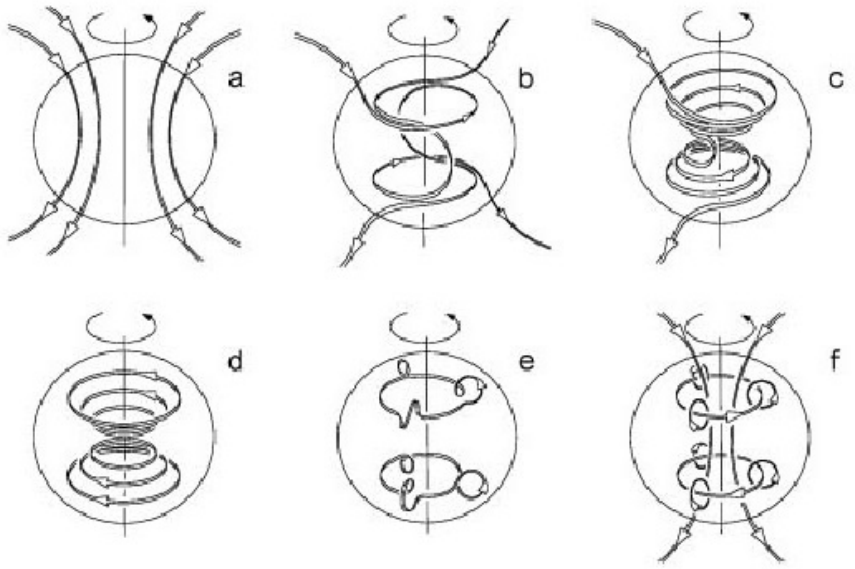

Figure 3.3:
The schematic evolution of the α-Ω dynamo as given in Love (1999). The illustration shows how a toroidal magnetic field is build up from an initially poloidal field (Ω-effect). The toroidal field in turn is converted to a poloidal field in the α-effect.
image credit: Love (1999)

(1955a) solves this problem by including the convective motions inside the Sun into the model. He assumed that, with partial flux freezing, the field lines of the torodial field are stretched (see (e)) in the helical turbulence initiated by convection. As the whole process takes place in a rotating system, the Coriolis force leads to vorticity of the field lines and a poloidal field is build up again (see part (f) of figure 3.3). Turbulent diffusion, in turn, gives rise to a large-scale poloidal magnetic field. The mechanism of converting a toroidal field into a poloidal field is labeled *α-effect*.

Mean-Field Magnetohydrodynamics

The systematic mathematical description of this large-scale dynamo was formulated by Steenbeck et al. (1966). It is based on the separation of the mean fields from the fluctuating fields, i.e.

$$\boldsymbol{B} = \langle \boldsymbol{B} \rangle + \delta \boldsymbol{B} \tag{3.116}$$

$$\boldsymbol{v} = \langle \boldsymbol{v} \rangle + \delta \boldsymbol{v}. \tag{3.117}$$

Here $\langle ... \rangle$ indicates an ensemble average, while $\delta ...$ refers to the fluctuating parts of the magnetic and the velocity field, respectively. Substituting this decomposition into the induction equation (3.85) and using the facts that the mean value of a mean is again the mean and the mean of a fluctuating quantity vanishes, leads to

the following equation

$$\frac{\mathrm{d}\langle \boldsymbol{B}\rangle}{\mathrm{d}t} = \nabla \times (\langle \boldsymbol{v}\rangle + \langle \boldsymbol{B}\rangle) + \nabla \times (\langle \boldsymbol{v}' \times \boldsymbol{B}'\rangle) + \eta \nabla^2 \langle \boldsymbol{B}\rangle \,. \tag{3.118}$$

This equation for the averaged magnetic field $\langle \boldsymbol{B}\rangle$ is identical to the induction equation except for the additional term $\nabla \times (\langle \boldsymbol{v}' \times \boldsymbol{B}'\rangle)$. It can be shown that (see, e.g. Choudhuri, 1998)

$$\langle \boldsymbol{v}' \times \boldsymbol{B}'\rangle = \alpha \langle \boldsymbol{B}\rangle - \eta_{\mathrm{turb}} \nabla \times \langle \boldsymbol{B}\rangle \tag{3.119}$$

with

$$\alpha = -\frac{1}{3} \langle \boldsymbol{v}' \cdot (\nabla \times \boldsymbol{v}')\rangle \ \tau \tag{3.120}$$

$$\eta_{\mathrm{turb}} = \frac{1}{3} \langle \boldsymbol{v}' \cdot \boldsymbol{v}'\rangle \ \tau. \tag{3.121}$$

Here we have introduced a correlation time τ. The evolution equation for the mean magnetic field can hence be written as

$$\frac{\mathrm{d}\langle \boldsymbol{B}\rangle}{\mathrm{d}t} = \nabla \times (\langle \boldsymbol{v}\rangle + \langle \boldsymbol{B}\rangle) + \nabla \times (\alpha \boldsymbol{B}) + (\eta + \eta_{\mathrm{turb}}) \nabla^2 \langle \boldsymbol{B}\rangle \,. \tag{3.122}$$

It is clear from the upper equation that η_{turb} provides a turbulent diffusion. In astrophysical environments η_{turb} is actually often much larger the the molecular diffusivity η. The quantity α is proportional to $\langle \boldsymbol{v}' \cdot (\nabla \times \boldsymbol{v}')\rangle$, which quantifies the helicity of the turbulent motion. It is this effect of helicity that twists the toroidal magnetic field lines and by this produces a poloidal field component.
For more details about the mathematical description of large-scale dynamos we refer to the reviews by Roberts & Soward (1992) and Brandenburg & Subramanian (2005) and the textbook by Krause & Raedler (1980).

3.4.2 The Small-Scale Turbulent Dynamo

As indicated by its name the *turbulent dynamo* converts kinetic energy from turbulence into magnetic energy. The amplification process is fastest on small length scales, which leads to the alternative name *small-scale dynamo*. This type of MHD dynamo amplifies a magnetic seed field by randomly stretching, twisting and folding the field lines. The different stages of field amplification are explained in this section phenomenologically, while we postpone the mathematical description of the turbulent dynamo to the next chapter.

Kinematic Dynamo Regime

A schematic model describing the conversion of turbulent kinetic energy into magnetic energy is the *stretch-twist-fold dynamo* (Vainshtein & Zeldovich, 1972). We illustrate this model in figure 3.4, which shows the evolution of closed magnetic flux

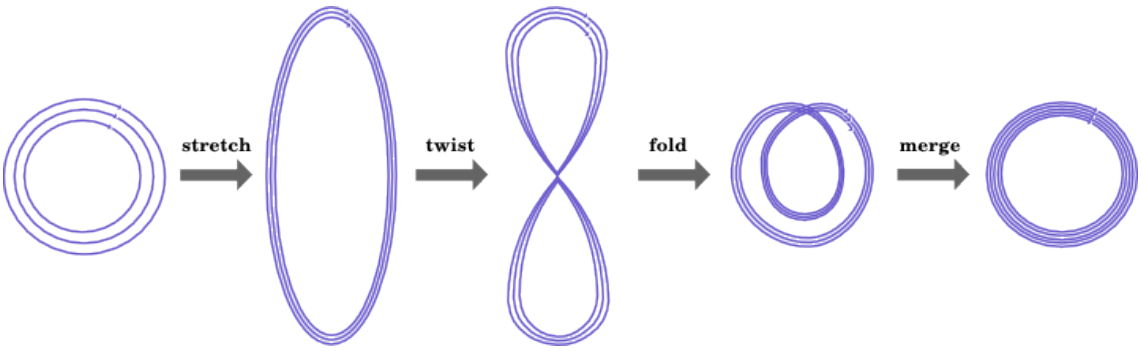

Figure 3.4:
The stretch-twist fold dynamo as a toy model for the turbulent dynamo. The illustration shows the time evolution a closed magnetic flux rope. First, it gets stretched, with a simultaneous increase of the field strength. Subsequent twisting, folding and merging of the flux rope regains the original shape. The process can now continue in the same fashion.

rope. Starting on the left hand side, the flux tube with a cross section A is stretched. This leads to amplification of the magnetic field strength, as the magnetic flux BA is a conserved quantity. Afterwards the rope is twisted, folded and merged such that the original shape is regained. After one circle the cross section is the same as the initial one, but the field strength has increased, which is indicated by the denser magnetic field lines in the right hand side of figure 3.4.
It is intuitively clear that the shorter the turnover time of the turbulent eddies is, the faster the stretch-twist-fold mechanism proceeds and thus the faster the magnetic field is amplified. The turnover time decreases with decreasing eddy size. Thus, in the limit of high magnetic Prandtl numbers, which are defined as ν/η, the amplification rate of the dynamo is most efficient on the smallest scale of the inertial range, i.e. the viscous scale ℓ_ν, of the turbulent velocity spectrum.
During the transition from large to small magnetic Prandtl numbers, the resistive scale ℓ_η becomes larger than the viscous one. The amplification then takes place at roughly ℓ_η, which lies within the inertial range of the turbulent velocity spectrum. Due to larger time scales of the turbulent eddies in the inertial range, we expect the small-scale dynamo to be less efficient at low magnetic Prandtl numbers. While in the large Prandtl regime the hydrodynamical Reynolds number regulates the dynamo, here the magnetic Reynolds number is the relevant quantity.

Non-linear Dynamo Regime

When the magnetic field gets strong enough back reactions from the field onto the fluid dynamics cannot be neglected anymore. The so-called *non-linear dynamo* phase sets in. In theoretical models of the turbulent dynamo it usually is assumed that this phase begins when saturation on the viscous scale is reached. The magnetic spectrum then peaks at the viscous scale (for large magnetic Prandtl numbers) and decreases to larger length scales.

Even though the dynamo is saturated on the viscous scale of the turbulence spectrum, amplification continues on larger scales. Here the stretching, twisting, and folding proceeds, however with a reduced growth rate. As the equipartition field strength is larger on larger scales, the peak of the spectrum moves to larger scales in the non-linear phase. A typical assumption is that the peak moves on the local eddy turn-over time. This inverse cascade of magnetic energy continues until the dynamo is saturated on all scales.

Saturation

With the increasing magnetic field strength the electric resistivity increases. This leads to a decrease of the magnetic Reynolds number Rm. As will be discussed in the next chapter Rm needs to be larger than a critical value $\mathrm{Rm}_{\mathrm{crit}}$ for the small-scale dynamo to operate. When Rm reaches this critical number the dynamo is saturated and the amplification comes to an end.

CHAPTER 4

Theoretical Description of the Turbulent Dynamo

In this chapter we discuss the theoretical modeling of the turbulent dynamo. As the energy input of the dynamo comes from turbulent motions we begin the chapter with a short review on turbulence and how it can be described mathematically. We develop a model for the turbulent flow which we can use as an input for the dynamo equations. In the kinematic phase the dynamo can be explained within the Kazantsev theory. We review the main predictions of this theory and apply it to calculate the growth rate of the dynamo for different types of turbulence.
The analytical results for the turbulent dynamo presented in this chapter are published in Schober et al. (2012c) and Schober et al. (2012a), while we summarize also the numerical solutions for the dynamo from Bovino et al. (2013). Our discussion continues with a model of the non-linear dynamo phase as published in Schleicher et al. (2013) and a toy model for the saturation of the turbulent dynamo. Finally, we compare the analytical results with predictions from numerical simulations as published in Federrath et al. (2011).

4.1 Turbulence as the Initial Form of Energy

As stressed in the previous chapter the turbulent dynamo converts the kinetic energy from turbulence into magnetic energy. It is thus crucial to have a suitable model for turbulence.
Turbulence is chaotic motion of a fluid. We speak of turbulence when the velocity fluctuates randomly on different scales as a function of space and time. A totally deterministic description of this phenomenon is not possible and there is no full theory describing it. The best way to handle turbulence is by using statistical tools, some of which we will introduce in this section. For more details we refer to the textbooks on turbulence by Davidson (2004), Pope (2000) and Frisch (1995).

4.1.1 Chaotic Motion and the Closure Problem of Turbulence

Under certain conditions a fluid can be come unstable and the amplitude of the perturbations grows. The situation can be illustrated in the phase space of the fluid. If there is a point P in phase space that is stable, but all the points within the direct environment of this point are end points of trajectories leading away from P, one speaks of an unstable equilibrium. A system that lies initially exactly on P is stable and remains unchanged. However, if the system lies only slightly away from P its final state can differ significantly. In measurements of fluids one is always limited by resolution. If one can resolve only a finite region in phase space that includes an point of instability, it is impossible to predict the time evolution of the fluid theoretically. The dynamics of this fluid are chaotic.
Let us now analyze, where this unpredictability appears when starting a theoretical description from the hydrodynamical equations that have been derived in section 3.1.1. The evolution of the velocity in a fluid is determined by the Navier-Stokes equation (3.42). Without an external force $\boldsymbol{F}$ and for an incompressible fluid ($\nabla \cdot \boldsymbol{v} = 0$) this equation reduces to

$$\begin{aligned} \frac{\partial \boldsymbol{v}}{\partial t} &= -(\boldsymbol{v} \cdot \nabla)\boldsymbol{v} - \frac{1}{\rho}\nabla p + \nu \nabla^2 \boldsymbol{v} \\ &\equiv f_1(\boldsymbol{v}, p). \end{aligned} \tag{4.1}$$

The time evolutions of the velocity $\boldsymbol{v}$ is thus expressed by some function $f_1(\boldsymbol{v}, p)$. With the incompressibility of the fluid one finds

$$\nabla^2 \left(\frac{p}{\rho} \right) = -\nabla \cdot (\boldsymbol{v} \cdot \nabla \boldsymbol{v}), \tag{4.2}$$

when taking the curl of (4.1). Thus, the pressure depends on the velocity field and we can write

$$\frac{\partial \boldsymbol{v}}{\partial t} = f_2(\boldsymbol{v}). \tag{4.3}$$

This shows that the evolution of the velocity field is a function of $\boldsymbol{v}$. The evolution equation (4.3) is a deterministic equation that can, in principle, be integrated. In practice, however, a solution of (4.3) is very difficult to gain due to the complexity of the velocity field and one can do this only numerically.
It turns out that the statistical properties, like $\langle \boldsymbol{v} \rangle$ and $\langle \boldsymbol{v}^2 \rangle$[1], provide a more practical description of the turbulent motions and are moreover easier to handle. We can calculate the first moment of equation (4.1) in order to find an evolution equation for $\langle \boldsymbol{v} \rangle$. It turns out, due to the non-linear term in (4.1), that this equation depends also on the second moment $\langle \boldsymbol{v}^2 \rangle$:

$$\frac{\partial \langle \boldsymbol{v} \rangle}{\partial t} = f_3(\langle \boldsymbol{v} \rangle, \langle \boldsymbol{v}^2 \rangle). \tag{4.4}$$

[1] For simplifying the notation in this subsection, we use here only one-point statistics. Turbulent flows are, however, better described by two-point correlation functions, like $\langle \boldsymbol{v}(\boldsymbol{r})\boldsymbol{v}(\boldsymbol{r}+\boldsymbol{l}) \rangle$, which contain information about the spatial structure.

When writing down the evolution equation for $\langle \boldsymbol{v}^2 \rangle$ we find

$$\frac{\partial \langle \boldsymbol{v}^2 \rangle}{\partial t} = f_4(\langle \boldsymbol{v}^2 \rangle, < \boldsymbol{v}^3 >). \tag{4.5}$$

This can be continued. The evolution of a velocity moment of the order n always depends on the velocity moment of the order (n+1). This is called the *closure problem of turbulence* and arises from the non-linear term $\nu\nabla^2\boldsymbol{v}$ in the Navier-Stokes equation.
A diagnostic tool for checking whether a fluid system is turbulent or laminar is the hydrodynamical Reynolds number Re, which indicates how important the non-linear term is compared to the linear terms in the Navier-Stokes equation. Let us rewrite the Navier-Stokes equation (4.1) by taking the curl[2]:

$$\frac{\partial \boldsymbol{\omega}}{\partial t} = \nabla \times (\boldsymbol{v} \times \boldsymbol{\omega}) + \nu\nabla^2\boldsymbol{v}, \tag{4.6}$$

where we have defined the *vorticity*

$$\boldsymbol{\omega} = \nabla \times \boldsymbol{v}. \tag{4.7}$$

The vorticity equation (4.6) can be written down dimensionlessly by defining the quantities $\tilde{\boldsymbol{x}} = \boldsymbol{x}/L$, $\tilde{\boldsymbol{v}} = \boldsymbol{v}/V$, $\tilde{t} = t\ V/L$, $\tilde{\boldsymbol{\omega}} = \boldsymbol{\omega}\ L/V$, which yields

$$\frac{\partial \tilde{\boldsymbol{\omega}}}{\partial \tilde{t}} = \tilde{\nabla} \times (\tilde{\boldsymbol{v}} \times \tilde{\boldsymbol{\omega}}) + \mathrm{Re}^{-1}\tilde{\nabla}^2\tilde{\boldsymbol{v}}. \tag{4.8}$$

Here the hydrodynamic Reynolds number

$$\mathrm{Re} = \frac{VL}{\nu} \tag{4.9}$$

is defined, where V is the velocity on the turbulent forcing scale L. The Reynolds number represents the ratio of vorticity generation and viscous dissipation. For a large Re the term of vortex generation in (4.8) dominates and chaotic motions are generated easily, while for small Re the viscous term becomes important and the flow is laminar.

4.1.2 Phenomenological Description of Turbulence

Kolomogorov's Theory of Incompressible Turbulence

Kolmogorov (1941) constructs a phenomenological model of incompressible turbulence, which works surprisingly well when the density remains constant. His main assumption is that energy is transported from large to small scales at a constant

[2]In (4.1) the external force is neglected. Note, however, that a conservative force would drop out anyway, when taking the curl of the equation.

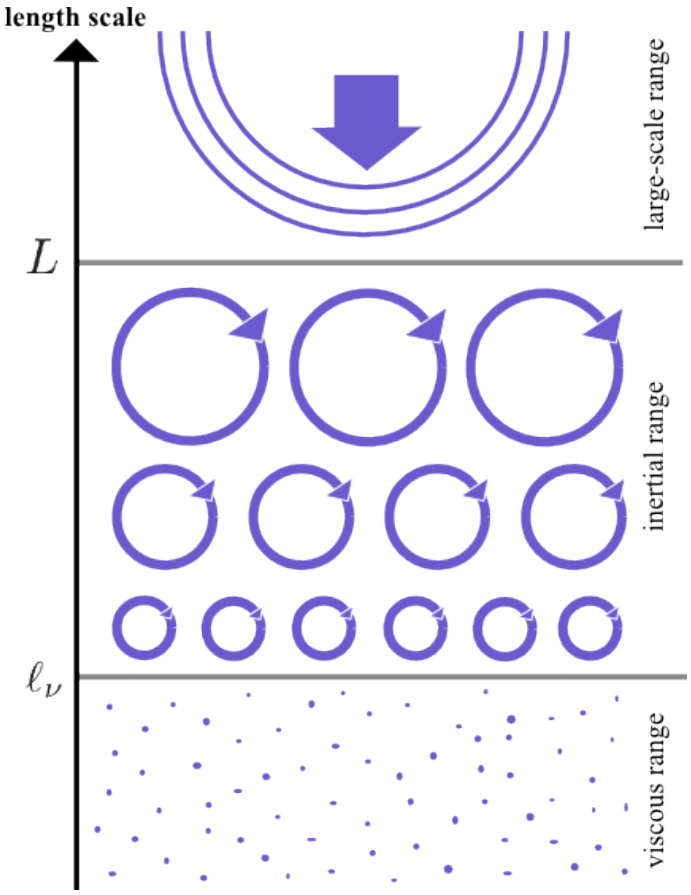

Figure 4.1:
Illustration of the turbulent energy cascade in the Kolmogorov model. The forcing of turbulence takes place on a scale L. In the inertial range the turbulent eddies cascades into smaller and smaller eddies down to a scale ℓ_ν below which energy is dissipated.

rate ϵ. The transport takes place via turbulent eddies, which are driven on a forcing scale L. These eddies interact and decay into smaller and smaller eddies until their length scale reaches the viscous scale ℓ_ν, below which the energy is dissipated. This concept is known as the *turbulent energy cascade*. We illustrate the forcing of turbulence, the decay of the turbulent eddies in the so-called *inertial range*, and the energy dissipation in figure 4.1.
In fact, the viscous scale ℓ_ν is given as the scale where the viscosity ν equals roughly the product of velocity and length scale $v_\nu \ell_\nu$. From this definition follows that the Reynolds number on ℓ_ν is unity:

$$\mathrm{Re}_\nu = \frac{v_\nu \ell_\nu}{\nu} \approx 1. \tag{4.10}$$

The Reynolds number on the forcing scale of a turbulent flow, which we usually refer to if not indicated otherwise, is

$$\mathrm{Re} = \frac{VL}{\nu} \gg 1. \tag{4.11}$$

By dimensional analysis (Kolmogorov, 1941) finds that the energy transfer rate needs to be of the order of

$$\epsilon \approx \frac{v^3}{\ell}, \tag{4.12}$$

where v is the turbulent velocity on a scale ℓ. From the conservation of energy follows that this rate needs to be the same on all scales. This directly leads to

$$\frac{V^3}{L} = \frac{v_\nu^3}{\ell_\nu}. \tag{4.13}$$

Thus, the velocity in the inertial range scales with the size of the eddies as

$$v(\ell) \propto \ell^{1/3}. \tag{4.14}$$

The viscous scale in Kolmogorov type turbulence is determined by

$$\begin{aligned} & \ell_\nu = \frac{v_\nu^3 L}{V^3} = \frac{v_\nu^3 \ell_\nu^3}{\nu^3} \frac{\nu^3}{V^3} \frac{1}{\ell_\nu^3} L = \mathrm{Re}_\nu^3 \frac{\nu^3}{V^3 L^3} \frac{1}{\ell_\nu^3} L^4 = \mathrm{Re}^{-3} \frac{L^4}{\ell_\nu^3} \\ \rightarrow \quad & \ell_\nu = \mathrm{Re}^{-3/4} L, \end{aligned} \tag{4.15}$$

which is also called the *Kolmogorov microscale*.
In the Kolmogorov picture the energy spectrum in Fourier space is determined by

$$\begin{aligned} & E(k)\mathrm{d}k \approx E(k)k \approx \frac{1}{2} v(\ell)^2 \approx \frac{1}{2} (\epsilon \ell)^{2/3} \approx \epsilon^{2/3} k^{-2/3} \\ \rightarrow \quad & E(k) \approx \epsilon^{2/3} k^{-5/3}. \end{aligned} \tag{4.16}$$

We used here (4.12) and $\ell = 2\pi/k$. This spectrum of turbulent kinetic energy is known as *Kolmogorov's* 5/3*-law*. In Kolmogorov turbulence most of the energy is located at the largest scales, i.e. the driving scale, while energy dissipation occurs on the smallest scale of the inertial range ℓ_ν

Highly Compressible Turbulence

The assumption of incompressibility is often not applicable in astrophysics. In the ISM turbulence is driven by shocks with high Mach numbers of the order of 10, leading to a high compressibility of the gas. The classical Kolmogorov theory of turbulence is thus strictly speaking not applicable.
Burgers (1948) describes the extreme case of highly compressible turbulence by assuming that the momentum flux $\dot{p}$ in the inertial range is constant. He then results in

$$\begin{aligned} p &\propto v \\ \rightarrow \dot{p} &\propto \dot{v} \propto \frac{v}{t} = \frac{v^2}{\ell} \equiv const. \\ \rightarrow v &\propto \ell^{1/2}, \end{aligned} \tag{4.17}$$

where p is the momentum. The viscous scale in Burgers turbulence is

$$\ell_\nu = \mathrm{Re}^{-2/3} L, \tag{4.18}$$

and thus for a fixed Reynolds number larger than for Kolmogorov turbulence.

Turbulence in Observations and Simulations

So far we have discussed the two extreme and idealized cases of incompressible Kolmogorov turbulence and highly compressible Burgers turbulence. Real astrophysical objects like the ISM are, however, of higher complexity (see figure 4.2 for an exemplary observation of the filamentary structure in the ISM). First, the interstellar gas is highly compressible and gas motions are often supersonic with the typical Mach number in the warm diffuse ISM being of the order of unity and the one in cold dense molecular clouds up to 50. High Mach numbers in compressible gas lead to strong density perturbations. In supersonic turbulence energy dissipation takes not only place on the smallest scales of the inertial range, but also within shocks, which destroys the local nature of turbulence. In addition, the driving of turbulence in galaxies is very complex. The energy input is, for example, a result of supernova blastwaves and other inhomogeneous processes. A uniform model for the driving of turbulence is, thus, an additional simplification of the problem.
In reality, we expect the turbulence spectrum to be somewhere between the two extreme cases of incompressible and highly compressible turbulence. We can model the scaling of the velocity in the inertial range as

$$v \propto \ell^\vartheta. \tag{4.19}$$

The scaling exponent for Kolmogorov is $\vartheta = 1/3$ and for Burgers turbulence $\vartheta = 1/2$. Thus, we use the parameter range of $1/3 \leq \vartheta \leq 1/2$.
One of the first observational hints towards turbulence in the ISM comes from von Hoerner (1951), who notes that the rms velocity in the Orion nebula increases with

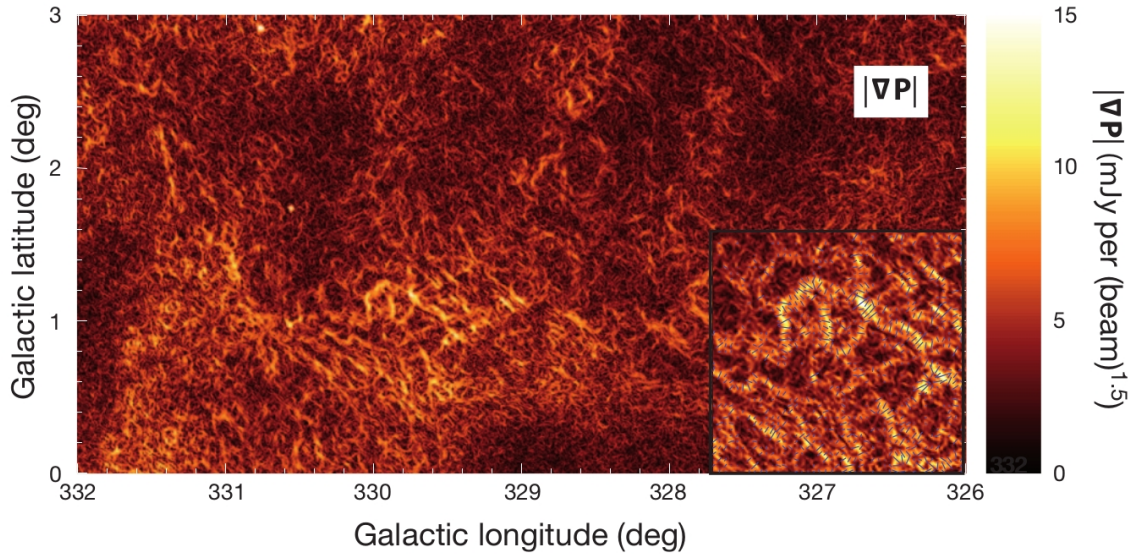

Figure 4.2:
Turbulence in the interstellar medium observed in terms of the complex filamentary structure of discontinuities in gas density. Shown here are radio polarization gradients for an 18-deg^2 region from the Southern Galactic Plane Survey.
image credit: Gaensler et al. (2011)

the projected separation as a power law. The measured slope in these early observations is, however, very imprecise, but initially Kolmogorov type turbulence was suggested as an explanation. In later observations Wilson et al. (1959) finds considerable steeper slopes and argues for compressible turbulence. Larson (1981) uses a combination of different data sets of several molecular cloud surveys and finds scaling relations between the velocity dispersion and the cloud sizes. He finds a scaling exponent of $\vartheta \approx 0.38$, which has also been reported by several independent authors (e.g. Myers & Goodman, 1988; Caselli & Myers, 1995). Ossenkopf & Mac Low (2002) find in their analysis of the velocity structure of molecular clouds a slightly steeper slope of $\vartheta \approx 0.47$. Overall, observations indicate the interstellar turbulence to be highly compressive.
An important tool for studying the nature of turbulence are numerical simulations. For example Boldyrev et al. (2002) set up direct numerical simulations of driven supersonic turbulence and analyze the statistical properties of the velocity field. The typical scaling exponent they find is $\vartheta \approx 0.42$. Federrath et al. (2010) investigate the effect of different types of forcing in their numerical experiments, in which they solve the hydrodynamical equations on a grid. For the two extreme cases, solenoidal (divergence-free) and compressive (rotation-free) forcing, they find characteristic scaling exponents of $\vartheta \approx 0.43$ and $\vartheta \approx 0.47$, respectively.

4.1.3 Statistical Description of Turbulence

As has been motivated above, one of the best methods to study turbulence is via its statistical properties. We provide in this section only the most important definitions and concepts. For detailed discussions on the topic we refer to the standard textbooks (Frisch, 1995; Pope, 2000; Davidson, 2004).

Three-Dimensional Correlations and the Power Spectrum

A statistical description of turbulence starts with the decomposition of the velocity field $\boldsymbol{v}$ into a mean field $\langle \boldsymbol{v} \rangle$ and a turbulent component $\delta \boldsymbol{v}$:

$$\boldsymbol{v} = \langle \boldsymbol{v} \rangle + \delta \boldsymbol{v}. \tag{4.20}$$

From this equation it is clear that the mean of the fluctuations $\delta \boldsymbol{v}$ vanishes. For a description of the statistical properties of a fluctuating field, we thus need to go to higher moments. Following the work of Taylor (1935), we model the spatial appearance of turbulence via the two-point correlation function. The spatial cross correlation of two turbulent velocity components at the positions $\boldsymbol{r}_1$ and $\boldsymbol{r}_2$ is given by

$$\langle \delta v_i(\boldsymbol{r}_1, t) \delta v_j(\boldsymbol{r}_2, s) \rangle \equiv T_{ij}(\boldsymbol{r}) \tag{4.21}$$

with the two-point correlation function $T_{ij}(\boldsymbol{r})$, where $\boldsymbol{r} \equiv \boldsymbol{r}_2 - \boldsymbol{r}_1$.
We can define energy spectrum tensor $E_{ij}(\boldsymbol{k})$ as

$$E_{ij}(\boldsymbol{k}) = \frac{1}{(2\pi)^3} \int_{-\infty}^{\infty} T_{ij}(\boldsymbol{r}) \mathrm{e}^{-i\boldsymbol{k}\boldsymbol{r}} \, \mathrm{d}\boldsymbol{r} \tag{4.22}$$

with the Fourier back transform

$$T_{ij}(\boldsymbol{r}) = \int_{-\infty}^{\infty} E_{ij}(\boldsymbol{k}) \mathrm{e}^{i\boldsymbol{k}\boldsymbol{r}} \, \mathrm{d}\boldsymbol{k}. \tag{4.23}$$

The turbulent kinetic energy E_{kin} per mass can be expressed via the correlation tensor with $i = j$ and $\boldsymbol{r} = 0$:

$$\begin{aligned} E_{\mathrm{kin}} &= \frac{1}{2} \left\langle \delta v_i^2 \right\rangle \\ &= \int_{-\infty}^{\infty} \frac{1}{2} E_{ii}(\boldsymbol{k}) \, \mathrm{d}\boldsymbol{k} \\ &= \int_0^{\infty} \int \frac{1}{2} E_{ii}(\boldsymbol{k}) \, \mathrm{d}S(k) \mathrm{d}k, \end{aligned} \tag{4.24}$$

where $S(k)$ is the surface of a sphere with radius $k = (k_i^2)^{1/2}$. With the definition of the energy power spectrum

$$E(k) \equiv \int \frac{1}{2} E_{ii}(\boldsymbol{k}) \, \mathrm{d}S(k) \tag{4.25}$$

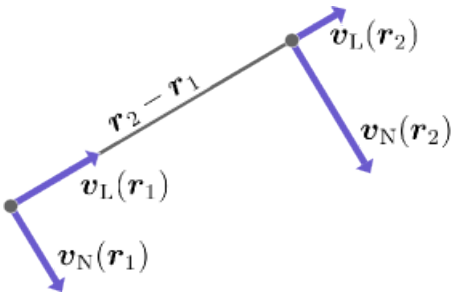

Figure 4.3:
Longitudinal ($\boldsymbol{v}_\mathrm{L}$) and transversal ($\boldsymbol{v}_\mathrm{N}$) velocity components at two points in space, $\boldsymbol{r}_1$ and $\boldsymbol{r}_2$.

we can express the kinetic energy per mass as

$$E_\mathrm{kin} = \int_0^\infty E(k)\ \mathrm{d}k. \tag{4.26}$$

The power spectrum, thus, contains information about the spectral distribution of the turbulent kinetic energy. This makes it an extremely important tool for studying the properties of turbulence. For Kolmogorov turbulence, for example, $E(k)$ is given in equation (4.16).

Longitudinal and Transversal Correlation Function

Let us now assume that turbulence is an isotropic and homogeneous Gaussian random field. It is clear that in this case T_{ij} does not depend on the direction of $\boldsymbol{r}$ any more, but only on the distance $r = |\boldsymbol{r}|$. Batchelor (1953) has shown that the correlation function can then be divided into a transverse part T_N and a longitudinal part T_L in the following way:

$$T_{ij}(r) = \left(\delta_{ij} - \frac{r_i r_j}{r^2}\right) T_\mathrm{N}(r) + \frac{r_i r_j}{r^2} T_\mathrm{L}(r). \tag{4.27}$$

We neglect here the effect of helicity, which would appear as an additional term in T_{ij}. The decomposition of the velocity is illustrated in figure 4.3.
In the special case of a divergence-free turbulent velocity field ($\nabla \cdot \delta\boldsymbol{v} = 0$), which is characteristic for incompressible fluids, we find that the transverse correlation function is connected to the longitudinal one by

$$T_\mathrm{N}(r) = \frac{1}{2r}\frac{\mathrm{d}}{\mathrm{d}r}\left(r^2 T_\mathrm{L}(r)\right). \tag{4.28}$$

For the other extreme case, an irrotational turbulent velocity field ($\nabla \times \delta\boldsymbol{v} = 0$), as it is expected for purely shock-dominated flows, we find the relation

$$T_\mathrm{L}(r) = r\frac{\mathrm{d}T_\mathrm{N}(r)}{\mathrm{d}r} + T_\mathrm{N}(r). \tag{4.29}$$

One can easily show that the longitudinal power spectrum can be expressed by the longitudinal correlation function:

$$E_\mathrm{L}(k) = \frac{1}{\pi}\int_{-\infty}^{\infty} T_\mathrm{L}(r)\ \mathrm{e}^{-kr}\ \mathrm{d}r \tag{4.30}$$

and the transversal power spectrum by the transversal correlation function:

$$E_{\mathrm{T}}(k) = \frac{1}{\pi} \int_{-\infty}^{\infty} T_{\mathrm{T}}(r)\ \mathrm{e}^{-kr}\ \mathrm{d}r. \tag{4.31}$$

4.2 Description of the Kinematic Turbulent Dynamo within the Kazantsev Theory

Kazantsev (1968) develops a theory for the time evolution of the magnetic energy that grows due to turbulent motions in a conducting fluid. The mechanism of converting kinetic energy into magnetic energy in this way is known as the turbulent or small-scale dynamo.
In this section we sketch the derivation of the Kazantsev theory following mainly the formalism proposed by Subramanian (1997) and used in Brandenburg & Subramanian (2005). We use a model for the turbulence spectrum that takes into account the effects of compressibility as an input for the Kazantsev theory. The results from this approach are published in Schober et al. (2012c), Schober et al. (2012a) and Bovino et al. (2013).

4.2.1 The Kazantsev Equation

Like the velocity field, the magnetic field can be separated into a mean field $\langle \boldsymbol{B} \rangle$ and a fluctuating field $\delta \boldsymbol{B}$:

$$\boldsymbol{B} = \langle \boldsymbol{B} \rangle + \delta \boldsymbol{B}. \tag{4.32}$$

Now let us assume that the fluctuating component $\delta \boldsymbol{B}$, like the velocity field, is a homogeneous, isotropic Gaussian random field with zero mean. Then we can write the correlation function as

$$\langle \delta B_i(\boldsymbol{r}_1, t) \delta B_j(\boldsymbol{r}_2, t) \rangle = M_{ij}(r, t) \tag{4.33}$$

with the two-point correlation function

$$M_{ij}(r,t) = \left(\delta_{ij} - \frac{r_i r_j}{r^2} \right) M_{\mathrm{N}}(r,t) + \frac{r_i r_j}{r^2} M_{\mathrm{L}}(r,t). \tag{4.34}$$

We will omit the time and space dependencies for a better overview in most of the following equations.
As the magnetic field is always divergence-free, i.e. $\partial M_{ij}/\partial r_{1i} = \partial M_{ij}/\partial r_{1j} = 0$, we can derive a relation between the transverse and the longitudinal correlation function similar to equation (4.28):

$$M_{\mathrm{N}} = \frac{1}{2r} \frac{\mathrm{d}}{\mathrm{d}r} \left(r^2 M_{\mathrm{L}} \right). \tag{4.35}$$

Here we have used that $(r_i r_j/r^2)M_{ij} = M_{\mathrm{L}}$ and $(r_i/r_j)M_{ij} = M_{\mathrm{N}}$. The time derivative of $\langle \delta B_i \delta B_j \rangle$ is

$$\begin{aligned}\frac{\partial M_{ij}}{\partial t} &= \frac{\partial}{\partial t}\left(\langle \delta B_i \delta B_j \rangle\right) \\ &= \frac{\partial}{\partial t}\left(\langle B_i B_j \rangle - \langle B_i \rangle \langle B_j \rangle\right) \\ &= \left\langle \frac{\partial B_i}{\partial t} B_j \right\rangle + \left\langle B_i \frac{\partial B_j}{\partial t} \right\rangle - \frac{\partial}{\partial t}\left(\langle B_i \rangle \langle B_j \rangle\right). \end{aligned} \tag{4.36}$$

We can now substitute the induction equation (3.85) and the evolution equation of the magnetic mean field

$$\frac{\partial \langle \boldsymbol{B} \rangle}{\partial t} = \boldsymbol{\nabla} \times \left[\langle \boldsymbol{v} \rangle \times \langle \boldsymbol{B} \rangle - \eta_{\mathrm{eff}} \boldsymbol{\nabla} \times \langle \boldsymbol{B} \rangle\right] \tag{4.37}$$

with the effective parameter $\eta_{\mathrm{eff}} = \eta + T_{\mathrm{L}}(0)$, into equation (4.36). A lengthy calculation (see appendix A for a derivation) leads to

$$\frac{\partial M_{\mathrm{L}}}{\partial t} = 2\kappa_{\mathrm{diff}} M_{\mathrm{L}}'' + 2\left(\frac{4\kappa_{\mathrm{diff}}}{r} + \kappa_{\mathrm{diff}}'\right) M_{\mathrm{L}}' + \frac{4}{r}\left(\frac{T_{\mathrm{N}}}{r} - \frac{T_{\mathrm{L}}}{r} - T_{\mathrm{N}}' - T_{\mathrm{L}}'\right) M_{\mathrm{L}} \tag{4.38}$$

with

$$\kappa_{\mathrm{diff}}(r) \equiv \eta + T_{\mathrm{L}}(0) - T_{\mathrm{L}}(r). \tag{4.39}$$

The prime denotes differentiation with respect to r. The diffusion of the magnetic correlations, κ_{diff}, contains in addition to the magnetic diffusivity η the scale-dependent turbulent diffusion $T_{\mathrm{L}}(0) - T_{\mathrm{L}}(r)$.
Once we found a solution for M_{L} from equation (4.38) we can determine M_{N} by using the relation (4.35) and thus have the total correlation function of the magnetic field fluctuations M_{ij}. We note that this quantity is proportional to the energy density of the magnetic field, $B^2/(8\pi)$.
In order to separate the time from the spatial coordinates in equation (4.38) we use the ansatz

$$M_{\mathrm{L}}(r,t) \equiv \frac{1}{r^2\sqrt{\kappa_{\mathrm{diff}}}} \psi(r) \mathrm{e}^{2\Gamma t}. \tag{4.40}$$

This yields the so-called *Kazantsev equation*

$$-\kappa_{\mathrm{diff}}(r)\frac{\mathrm{d}^2\psi(r)}{\mathrm{d}^2 r} + U(r)\psi(r) = -\Gamma\psi(r). \tag{4.41}$$

The Kazantsev equation formally looks like the quantum-mechanical Schrödinger equation with a "mass" $\hbar^2/(2\kappa_{\mathrm{diff}})$ and the "potential"

$$U(r) \equiv \frac{\kappa_{\mathrm{diff}}''}{2} - \frac{(\kappa_{\mathrm{diff}}')^2}{4\kappa_{\mathrm{diff}}} + \frac{2\kappa_{\mathrm{diff}}}{r^2} + \frac{2T_{\mathrm{N}}'}{r} + \frac{2(T_{\mathrm{L}} - T_{\mathrm{N}})}{r^2}. \tag{4.42}$$

It describes the *kinematic limit* of the turbulent dynamo and is only applicable when the back reaction from the magnetic field on the velocity field are negligible.

4.2.2 WKB Approximation

We can use common methods from quantum mechanics, like the WKB approximation, to solve the Kazantsev equation (4.41). WKB stands for Wentzel, Kramers, and Brillouin, who have developed this method (Kramers, 1926).

Solution of the Kazantsev Equation in the WKB Approximation

In order to use the standard WKB method, we have to make some substitutions. Let us first introduce a new radial coordinate x by defining $r \equiv \mathrm{e}^x$. By this (4.41) changes to

$$\frac{\kappa_{\mathrm{diff}}(x)}{\mathrm{e}^x}\frac{\mathrm{d}}{\mathrm{d}x}\left(\frac{1}{\mathrm{e}^x}\frac{\mathrm{d}\psi(x)}{\mathrm{d}x}\right) - (\Gamma + U(x))\,\psi(x) = 0. \tag{4.43}$$

Next we eliminate the first-derivative terms through the substitution

$$\psi(x) \equiv \mathrm{e}^{x/2}\theta(x), \tag{4.44}$$

to obtain

$$\frac{\mathrm{d}^2\theta(x)}{\mathrm{d}x^2} + p(x)\theta(x) = 0 \tag{4.45}$$

with the definition

$$p(x) \equiv -\frac{[\Gamma + U(x)]\mathrm{e}^{2x}}{\kappa_{\mathrm{diff}}(x)} - \frac{1}{4}. \tag{4.46}$$

The WKB solutions of equation (4.45) are linear combinations of

$$\theta(x) = \frac{1}{p^{1/4}}\exp\left(\pm i\int\sqrt{p(x')}\mathrm{d}x'\right) \tag{4.47}$$

with the boundary conditions for $\psi(r)$ and $\theta(x)$

$$\begin{aligned} \psi(r) &\xrightarrow{r\to 0,\infty} 0 \\ \to \theta(x) &\xrightarrow{x\to\pm\infty} 0. \end{aligned} \tag{4.48}$$

We can make some predictions about the shape of the function $\theta(x)$. For very small x ($x \to -\infty$), $p(x)$ goes to $-1/4 < 0$, which leads to exponentially growing and decaying solutions of θ. In the other limit ($x \to \infty$), $p(x) \to -\Gamma/\eta\ \mathrm{e}^{2x}$, we have growing mode solutions only for positive Γ. The boundary conditions require θ to grow exponentially for $x \to -\infty$ and decay exponentially at $x \to \infty$. In order to arrange this, $p(x)$ must go through zero, thus $U(x)$ needs to become negative for some r. From now on we label the roots of $U(x)$ as x_1 and $x_2 > x_1$. As $U(r)$ becomes negative for some r, $p(r)$ becomes positive for certain values of r. This means that

we have oscillatory solutions for $x_1 < x < x_2$. The condition for the eigenvalues Γ in this case is (Mestel & Subramanian, 1991)

$$\int_{x_1}^{x_2} \sqrt{p(x')}\mathrm{d}x' = \frac{2n+1}{2}\pi \tag{4.49}$$

for different excitation levels $n \in \mathbb{N}$. In this work we concentrate on the lowest mode $n = 0$, which refers to the largest growth rates of the turbulent dynamo.

Validity of the WKB Approximation

In order to find the limits in which the WKB method provides valid solutions of the Kazantsev equation, we derive the differential equation that is solved exactly by

$$\theta(x) = \frac{1}{p^{1/4}} \exp\left(\pm i \int_{x_1}^{x_2} \sqrt{p(x')}\mathrm{d}x'\right). \tag{4.50}$$

The second derivative of $\theta(x)$ with respect to x can be written as

$$\theta''(x) + \left(1 + \frac{p''}{4p^2} - \frac{3}{16}\frac{(p')^2}{p^3}\right) p\ \theta(x) = 0, \tag{4.51}$$

where now the prime denotes $\mathrm{d}/\mathrm{d}x$. This equation results in the Kazantsev equation (4.45) if

$$|f(x)| \ll 1, \tag{4.52}$$

with

$$f(x) \equiv \frac{p''}{4p^2} - \frac{3}{16}\frac{(p')^2}{p^3}. \tag{4.53}$$

We use this result in the appendix B to check the range of parameters in which the WKB method produces accurate solutions of the Kazantsev equation. The main result of this analysis is that the WKB approximation is valid for very large and very small magnetic Prandtl numbers.

4.2.3 Modeling the Turbulent Correlation Function

We aim to analyze the case of general types of turbulence, which can be described by the relation between the velocity $v(\ell)$ and the size ℓ of a turbulent fluctuation,

$$v(\ell) \propto \ell^{\vartheta}. \tag{4.54}$$

The power-law index ϑ varies for the different types (see also section 4.1.2). It attains its minimal value of $\vartheta = 1/3$ for Kolmogorov theory (Kolmogorov, 1941),

i.e. incompressible turbulence. For Burgers turbulence, i.e. highly compressible turbulence, ϑ gets its maximal value of 1/2 (Burgers, 1948). The viscous scale for this generalized turbulence spectrum is given by

$$\ell_\nu = \mathrm{Re}^{-1/(1+\vartheta)} L. \tag{4.55}$$

Motivated by the definition of the scale-dependent turbulent diffusion coefficient in the last section,

$$\eta_{\mathrm{turb}}(r) = T_{\mathrm{L}}(0) - T_{\mathrm{L}}(r), \tag{4.56}$$

we construct a model for the longitudinal correlation function of the turbulent velocity field $T_{\mathrm{L}}(r)$. The diffusion coefficient is calculated from the power law (4.54) in the following way:

$$\eta_{\mathrm{turb}}(r) \propto v_\ell \ell \propto \ell^\vartheta \ell = \ell^{\vartheta+1}. \tag{4.57}$$

So we assume the correlation function in the inertial range to be (Vainshtein, 1982; Subramanian, 1997)

$$T_{\mathrm{L}}(r) = \frac{VL}{3}\left(1 - (r/L)^{\vartheta+1}\right). \tag{4.58}$$

The pre-factor VL fixes the units, which should be the same as for magnetic diffusivity. V and L are the velocity and the length scale of the largest eddies. On the diffusive scale the correlation function should be steadily continued and satisfy the condition that its derivative $T'_{\mathrm{L}}(0)$ vanishes at $r = 0$. This is accomplished, for example, for $T_{\mathrm{L}} \propto r^2$. The exact form of T_{L} in the diffusive range does not affect the results crucially (Subramanian, 1997). Furthermore, we expect no correlation on scales larger than the largest eddies, so T_{L} should vanish there.
Taken all together, we can set up a general turbulence model for the longitudinal correlation function on the different length scales as follows:

$$T_{\mathrm{L}}(r) = \begin{cases} \dfrac{VL}{3}\left(1 - \mathrm{Re}^{(1-\vartheta)/(1+\vartheta)}\left(\dfrac{r}{L}\right)^2\right) & \text{for } 0 < r < \ell_\nu \\ \dfrac{VL}{3}\left(1 - \left(\dfrac{r}{L}\right)^{\vartheta+1}\right) & \text{for } \ell_\nu < r < L \\ 0 & \text{for } L < r. \end{cases} \tag{4.59}$$

The transverse correlation functions T_{N} for a divergence-free (i.e. Kolmogorov turbulence) and for an irrotational (i.e. Burgers turbulence) turbulent velocity field can be derived from the relations (4.28) and (4.29). Notice, however, that a turbulent velocity field that is divergence free or irrotational in the inertial range does not have to be this in the diffusive range. We calculate for the extreme cases in the inertial range ($\ell_\nu < r < L$)

$$T_{\mathrm{N}}^{\mathrm{K}}(r) = \frac{VL}{3}\left(1 - \frac{5}{3}\left(\frac{r}{L}\right)^{4/3}\right), \tag{4.60}$$

$$T_{\mathrm{N}}^{\mathrm{B}}(r) = \frac{VL}{3}\left(1 - \frac{2}{5}\left(\frac{r}{L}\right)^{3/2}\right). \tag{4.61}$$

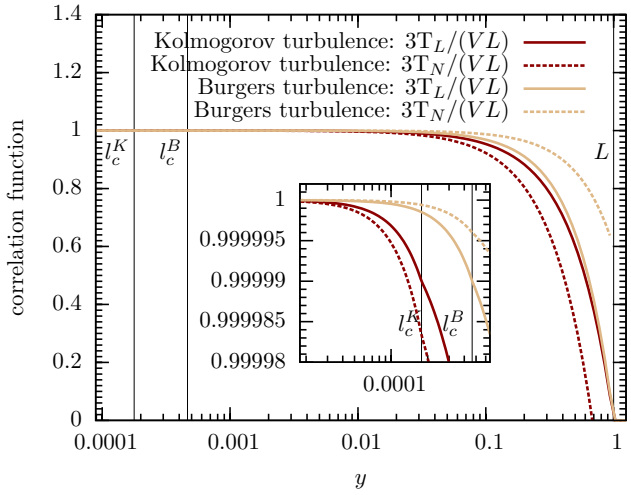

Figure 4.4:
Dependence of the longitudinal and transverse correlation functions T_L and T_N on the dimensionless parameter $y \equiv r/L$ for Kolmogorov ($\vartheta = 1/3$) and Burgers ($\vartheta = 1/2$) turbulence. We choose a fixed Reynolds number of 10^5. The vertical lines indicate the viscous scale ℓ_ν and the forcing scale L. Notice that the viscous scale for Kolmogorov turbulence ($\ell_\nu^\mathrm{K} = \mathrm{Re}^{-3/4}L$) is different from the one for Burgers turbulence ($\ell_\nu^\mathrm{B} = \mathrm{Re}^{-2/3}L$). The inset shows a zoom of the dissipative range.
image credit: Schober et al. (2012c)

In order to find a general expression for T_N we make the ansatz

$$T_\mathrm{N}(r) = \frac{VL}{3}\left(1 - t(\vartheta)\left(\frac{r}{L}\right)^{\vartheta+1}\right), \tag{4.62}$$

where $t(\vartheta) = a - b\vartheta$. With equations (4.60) and (4.61) we find that $a = 21/5$ and $b = 38/5$. Furthermore, we calculate the small-scale transverse correlation (i.e. $0 < r < \ell_\nu$) by steady continuation. Thus, we end up with the following model for the transverse correlation function for a general slope of the turbulent velocity spectrum:

$$T_\mathrm{N}(r) = \begin{cases} \dfrac{VL}{3}\left(1 - t(\vartheta)\mathrm{Re}^{(1-\vartheta)/(1+\vartheta)}\left(\dfrac{r}{L}\right)^2\right) & \text{for } 0 < r < \ell_\nu \\ \dfrac{VL}{3}\left(1 - t(\vartheta)\left(\dfrac{r}{L}\right)^{\vartheta+1}\right) & \text{for } \ell_\nu < r < L \\ 0 & \text{for } L < r, \end{cases} \tag{4.63}$$

with $t(\vartheta) = (21 - 38\vartheta)/5$.
The longitudinal and transverse correlation functions depend on the dimensionless parameter $y \equiv r/L$ as shown in figure 4.4 for Kolmogorov and Burgers turbulence. We choose here a fixed hydrodynamical Reynolds number of 10^5. In the inset of figure 4.4 we show a zoom into the dissipative range ($0 < r < \ell_\nu$). Furthermore, we plot the potential of the Kazantsev equation, resulting from our models for T_L and T_N for Kolmogorov and Burgers turbulence in figure 4.5. We choose two different values for the Reynolds number Re and different magnetic Prandtl numbers. The

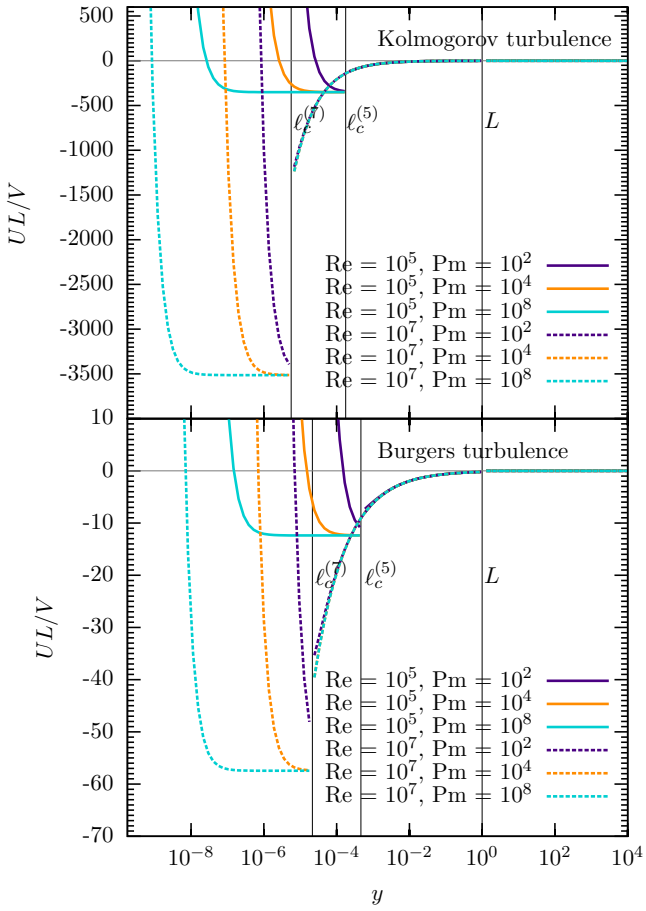

Figure 4.5:
Dependence of the potential on the dimensionless parameter $y \equiv r/L$ for Kolmogorov ($\vartheta = 1/3$) and Burgers ($\vartheta = 1/2$) turbulence. We choose two different Reynolds numbers $\mathrm{Re} = 10^5$ and $\mathrm{Re} = 10^7$, and different Prandtl numbers $\mathrm{Pm} = 10^2$, $\mathrm{Pm} = 10^4$ and $\mathrm{Pm} = 10^8$. The viscous scale ℓ_ν depends on the turbulence model and the Reynolds number. For Kolmogorov turbulence $\ell_\nu = \mathrm{Re}^{-3/4}L$; for Burgers turbulence $\ell_\nu = \mathrm{Re}^{-2/3}L$. A Reynolds number 10^x is indicated in the viscous scale as $\ell_\nu^{(\mathrm{x})}$.
image credit: Schober et al. (2012c)

magnetic Prandtl number is defined as the ratio of the magnetic Reynolds number Rm and the hydrodynamical Reynolds number Re:

$$\mathrm{Pm} = \frac{\mathrm{Rm}}{\mathrm{Re}} = \frac{\nu}{\eta}. \tag{4.64}$$

The potential at fixed Re and Pm is deeper in the small-scale range in the Kolmogorov case than in the Burgers case. For higher Re the potential gets deeper and the viscous scale ℓ_ν decreases. For higher Pm the potential in the small-scale range gets broader. From the look on the potential we already see that the magnetic Prandtl number plays an important role for the turbulent dynamo. In the next two sections we will learn that the growth rates of the dynamo are very different in the limit of small Pm and large Pm.

4.2.4 The Turbulent Dynamo at Large Magnetic Prandtl Numbers[3]

In this section we use our model of the turbulent velocity correlation function, given in (4.59) and (4.63), as the input for the Kazantsev theory. We solve the Kazantsev equation in order to obtain the characteristic properties of the small-scale dynamo. We employ the WKB method, which gives a good approximate solution for large magnetic Prandtl numbers. In fact, in the limit of infinite Pm the WKB approximation is an exact solution of the Kazantsev equation. For more details about the validity of this approximation see the appendix B.

Critical Magnetic Reynolds Number for Small-scale Dynamo Action

Intuitively, one expects that the high magnetic diffusivity for very low magnetic Reynolds numbers prevents amplification of the magnetic field. Even higher diffusivity eventually results in a net decrease of the field strength. In this section we calculate the critical magnetic Reynolds number $\mathrm{Rm}_{\mathrm{crit}}$ for small-scale dynamo action. To accomplish this we set the growth in our equations at zero.
It should be noted that we use the inertial range ($\ell_\nu < r < L$) for determining $\mathrm{Rm}_{\mathrm{crit}}$ as the potential is always negative in this range and for that the growth rate is positive (see figure 4.5). In this range with our turbulence spectrum and $\Gamma = 0$ we get for the p-function (4.46)

$$p(y) = \frac{-9/4 - a(\vartheta)\mathrm{Rm}_{\mathrm{crit}} y^{\vartheta+1} + b(\vartheta)\mathrm{Rm}_{\mathrm{crit}}^2 y^{2(\vartheta+1)}}{\left(1 + \frac{1}{3}\mathrm{Rm}_{\mathrm{crit}} y^{\vartheta+1}\right)^2} \tag{4.65}$$

with $a(\vartheta) \equiv 5/6 - (79/30)\ \vartheta + (157/30)\ \vartheta^2$ and $b(\vartheta) \equiv (14/15)\ \vartheta - (103/60)\ \vartheta^2$.
Now we can evaluate the eigenvalue condition (4.49) for this $p(y)$ in the ground state $n = 0$:

$$\int_{y_{0_1}}^{y_{0_2}} \frac{\sqrt{p(y)}}{y}\, \mathrm{d}y = \frac{\pi}{2}, \tag{4.66}$$

where the additional y comes from the substitution $y = r/L = e^x/L$. The limits of the integral are the roots of $p(y)$. There is only one real and positive root of $p(y)$, which we label y_1. For the upper limit we have to realize that the potential (4.42) changes for $y > 1$ to $2\eta/(yL)^2$, which is clearly always positive. Furthermore, also the diffusion coefficient $\kappa_{\mathrm{diff}} = \eta + T_{\mathrm{L}}(0) > 0$ for $y > 1$. With U and κ_{diff} being positive $p(y)$ is negative in this range, which means that $p(y)$ needs to go through zero during this transition. Thus we have our second root at roughly $r \approx L$ and $y_2 = 1$.
We can solve equation (4.66) numerically for the critical magnetic Reynolds number $\mathrm{Rm}_{\mathrm{crit}}$ if we put in a fixed value of ϑ. Recall that ϑ was defined in the inertial range of the turbulence via the relation $v(\ell) \propto \ell^\vartheta$. Results for common models in the

[3]This section follows closely Schober et al. (2012c).

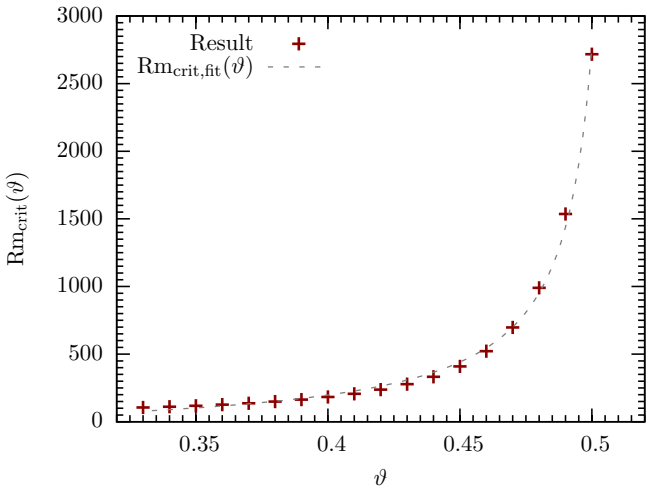

Figure 4.6:
Dependence of the critical magnetic Reynolds number $\mathrm{Rm}_{\mathrm{crit}}$ on the slope of the turbulent velocity spectrum ϑ. The dashed line is an empirical fit to our results. *image credit: Schober et al. (2012c)*

literature can be found in Table 4.1. In figure 4.6 we show how $\mathrm{Rm}_{\mathrm{crit}}$ depends on ϑ. Here one can see that the critical magnetic Reynolds number increases rapidly as ϑ gets closer to its maximum value of 1/2. An empirical fit $\mathrm{Rm}_{\mathrm{crit,fit}}(\vartheta)$ through these data in the range $0.33 < \vartheta < 0.5$ is

$$\mathrm{Rm}_{\mathrm{crit,fit}}(\vartheta) = 88\,[\tan(2.68\vartheta + 0.2) - 1]\,. \tag{4.67}$$

We find that the small-scale dynamo is easiest excited in the case of a purely rotational turbulent velocity field, i.e. for Kolmogorov turbulence, where we find $\mathrm{Rm}_{\mathrm{crit}} \approx 110$. The critical magnetic Reynolds number for a turbulent field with a vanishing rotational component, i.e. Burgers turbulence, is roughly 2700 in our model.
From our results for $\mathrm{Rm}_{\mathrm{crit}}$ we see that for all types of turbulence a high magnetic Reynolds number needs to be exceeded for small-scale dynamo action. In astrophysical objects we often find very high magnetic Reynolds numbers (we refer to the compilation in Childress & Gilbert, 1995). The core of Jupiter, for example, has $\mathrm{Rm} \approx 10^6$, the solar convection zone has $\mathrm{Rm} \approx 10^8$, and the solar corona $\mathrm{Rm} \approx 10^{12}$. In the interstellar medium we find $\mathrm{Rm} \approx 10^{17}$. Consequently, the critical magnetic Reynolds number is exceeded by far in nature, and we expect that a small-scale dynamo is excited in typical astrophysical objects.
There are different ways to obtain approximate solutions of the Kazantsev equation. In addition to the WKB method there is also an asymptotic solution, which uses the separation of scales (Zeldovich et al., 1990). The potential $U(r)$ and the mass $m(r)$ are estimated on different scales, such that a solution of the Kazantsev equation can be found. Rogachevskii & Kleeorin (1997) use this method to determine $\mathrm{Rm}_{\mathrm{crit}}$ for different compressibilities of turbulence. They find that, in the limit of small magnetic Prandtl numbers Rm needs to be larger than roughly 400 for excitation of a small-scale dynamo in the case of Kolmogorov turbulence. For a larger compressibility, i.e. toward Burgers turbulence, they find that $\mathrm{Rm}_{\mathrm{crit}}$ increases sharply. We see the same trend of increasing $\mathrm{Rm}_{\mathrm{crit}}$ for higher compressibility.

The determination of the critical magnetic Reynolds number is, moreover, the first step to understanding the saturation of the small-scale dynamo. For if the magnetic field in a system increases, back reactions from the gas become more important. Then processes like ambipolar diffusion can change the properties of the gas and the magnetic Reynolds number can decrease. If the magnetic Reynolds number becomes smaller than the critical magnetic Reynolds number, the magnetic field stops growing and the small-scale dynamo is saturated.

Growth Rate of the Small-Scale Magnetic Field

Growth Rate in the Limit $\mathrm{Pm} \to \infty$ In this section we derive a general analytical solution for the growth rate Γ for an arbitrary slope of the turbulent velocity spectrum, in the limit of infinite Prandtl number.
As the potential has its minimum in the small-scale range, i.e. the dissipative range of the turbulence (see figure 4.5), the growth rate, which is the eigenvalue of the Kazantsev equation, takes its maximal value there. So we expect the fastest growing mode to be in the small-scale range.
In order to have scale-independent equations, we introduce the substitution

$$z \equiv \left(\frac{V\sqrt{\mathrm{Re}}}{3L\eta}\right)^{1/2} r = \left(\frac{\mathrm{Re}^{3/2}\mathrm{Pm}}{3}\right)^{1/2} y, \tag{4.68}$$

The p-function (4.46) in z space for the general turbulence spectrum, defined by (4.59) and (4.63), in the dissipative range is

$$p(z) = \frac{A_0 z^4 - B_0 z^2 - 45\mathrm{Re}^{(3+7\vartheta)/(2+2\vartheta)}}{20\mathrm{Re}^{1/2}\left(\mathrm{Re}^{(1+3\vartheta)/(2+2\vartheta)} + \mathrm{Re}^{1/(1+\vartheta)} z^2\right)^2} \tag{4.69}$$

with the definitions

$$A_0 = \mathrm{Re}^{(5+\vartheta)/(2+2\vartheta)}\,(163 - 304\vartheta) - \frac{20}{3}\mathrm{Re}^{5/2}\bar{\Gamma}, \tag{4.70}$$

$$B_0 = (304\vartheta - 98)\,\mathrm{Re}^2 + \frac{20}{3}\mathrm{Re}^{(2+8\vartheta)/(1+\vartheta)}\bar{\Gamma}, \tag{4.71}$$

and the normalized growth rate

$$\bar{\Gamma} \equiv \frac{L}{V}\,\Gamma. \tag{4.72}$$

In the limit of large Prandtl number z is large, too, and we can neglect the constant terms. We obtain

$$p(z) = \frac{\mathrm{Re}^{-(5+\vartheta)/(2+2\vartheta)}}{20}\,\frac{A_0 z^2 - B_0}{z^2}. \tag{4.73}$$

The one real and positive root of this function is $z_1 = \sqrt{B_0/A_0}$. At the viscous scale of the turbulence the p-function changes its sign. We take this as our second

root and find $z_2 = \sqrt{\mathrm{Pm}/3}\ \mathrm{Re}^{(3\vartheta-3)/(4\vartheta+4)}$. Thus we get for the general eigenvalue condition

$$\frac{\mathrm{Re}^{-(5+\vartheta)/(4+4\vartheta)}}{2\sqrt{5}} \int_{z_1}^{z_2} \sqrt{\frac{A_0 z^2 - B_0}{z^4}} \mathrm{d}z = \frac{\pi}{2}, \tag{4.74}$$

resulting in the analytical solution of the integral

$$\frac{\mathrm{Re}^{-(5+\vartheta)/(4+4\vartheta)}}{2\sqrt{5}z} \left[\sqrt{A_0}\ln\left(2\left(\sqrt{A_0}z + \sqrt{A_0 z^2 - B_0}\right)\right) - \sqrt{A_0 z^2 - B_0}\right]\Big|_{z_1}^{z_2} = \frac{\pi}{2}. \tag{4.75}$$

For $z_2 \gg 1$ this becomes

$$\frac{\mathrm{Re}^{-(5+\vartheta)/(4+4\vartheta)}}{2\sqrt{5}} \sqrt{A_0} \left[1 - \ln\left(4\sqrt{A_0}z_2\right) + \frac{1}{2}\ln\left(4B_0\right)\right] = \frac{\pi}{2}. \tag{4.76}$$

A zero-order iterative solution for $\bar{\Gamma}$ gives us

$$\bar{\Gamma} = \frac{163 - 304\vartheta}{60}\mathrm{Re}^{(1-\vartheta)/(1+\vartheta)} - \left(\frac{\pi\sqrt{5}\ \mathrm{Re}^{(5+\vartheta)/(4+4\vartheta)}}{1 - \ln\left(4\sqrt{A_0}z_2\right) + 1/2\ \ln\left(4B_0\right)}\right)^2, \tag{4.77}$$

which becomes for large Prandtl number

$$\bar{\Gamma} = \frac{163 - 304\vartheta}{60}\ \mathrm{Re}^{(1-\vartheta)/(1+\vartheta)}. \tag{4.78}$$

As a result we get for the absolute growth rate Γ for a general slope of the turbulent velocity spectrum

$$\Gamma = \frac{163 - 304\vartheta}{60}\frac{V}{L}\ \mathrm{Re}^{(1-\vartheta)/(1+\vartheta)} \tag{4.79}$$

in the limit $\mathrm{Pm} \to \infty$.
In figure 4.7 we show the dependency of the normalized growth rate $\bar{\Gamma}$ on the Reynolds number for different types of turbulence. One extreme case is incompressible turbulence, i.e. Kolmogorov turbulence, with $\bar{\Gamma} \propto \mathrm{Re}^{1/2}$. In the other extreme case, highly compressible turbulence, i.e. Burgers turbulence, the growth rate increases only as $\mathrm{Re}^{1/3}$. Altogether we find that the growth rate increases faster with the Reynolds number when the compressibility is lower.

Growth Rate as a Function of the Prandtl Number In this section we discard the assumption of infinite Prandtl number. In this case we have to solve the full equation resulting from the WKB method (4.49),

$$\int \frac{\sqrt{p(z)}}{z}\ \mathrm{d}z = \frac{\pi}{2}, \tag{4.80}$$

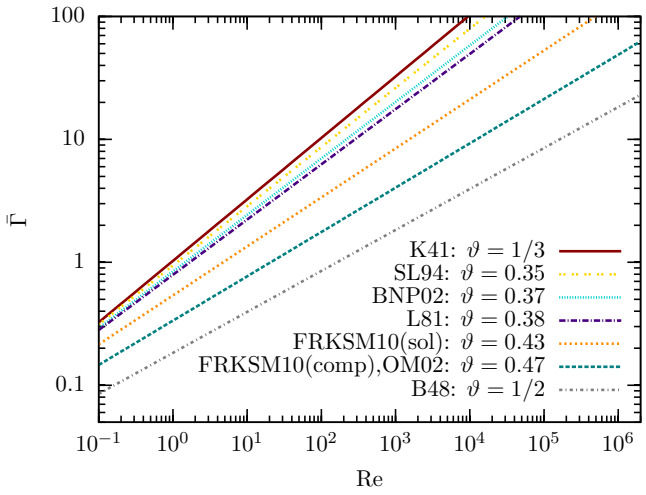

Figure 4.7:
The normalized growth rate of the small-scale dynamo $\bar{\Gamma}$ as a function of the Reynolds number Re in the limit $\mathrm{Pm} \to \infty$. For the slopes of the turbulent velocity spectrum ϑ we choose common values from the literature: K41 (Kolmogorov, 1941), SL94 (She & Leveque, 1994), BNP02 (Boldyrev et al., 2002), L81 (Larson, 1981), FRKSM10 (Federrath et al., 2010) (sol: solenoidal forcing; comp: compressive forcing), OM02 (Ossenkopf & Mac Low, 2002) and B48 (Burgers, 1948). *image credit: Schober et al. (2012c)*

with $p(z)$ from (4.69). There is no analytical solution of this integral equation. The numerical results of the normalized growth rate are shown in figure 4.8 for Kolmogorov turbulence and in figure 4.9 for Burgers turbulence. We plot the normalized growth rate as a function of the Prandtl number for different values of the Reynolds number.

In figure 4.7 as well as in table 4.1, we present our results for the growth rate of the small-scale dynamo in the limit of infinite magnetic Prandtl number. Our results show that the growth rate is proportional to the velocity V of the largest eddy divided by its length L. The ratio V/L is the reciprovcal of the turnover time of an eddy. Thus, the growth rate increases with decreasing turnover time, and the smallest modes grow at the highest rate. This is expected, because smaller turnover times lead to a faster tangling of the magnetic field lines.
Furthermore, the growth rate increases with increasing hydrodynamical Reynolds number for all types of turbulence, characterized by $v(\ell) \propto \ell^{\vartheta}$. In order to achieve the same growth rate for Kolmogorov and Burgers turbulence we have to provide a larger Reynolds number in the latter case. Assuming a fixed Reynolds numbers in both extreme cases, Re^{K} and Re^{B}, the growth rates of the two different turbulence types are the same for $\mathrm{Re}^{\mathrm{K}} \approx 0.18(\mathrm{Re}^{\mathrm{B}})^{3/2}$. This fact can again be explained with the stretch-twist-fold model (see section 3.4.2). We need solenoidal modes, i.e. divergence-free modes, of the turbulence for this process (Federrath et al., 2011), which explains why incompressible turbulence amplifies the magnetic field more effectively.
With the asymptotic solution of the Kazantsev equation, Rogachevskii & Kleeorin (1997) find in the limit of small magnetic Prandtl number $\Gamma \propto \ln(\mathrm{Rm}/\mathrm{Rm}_{\mathrm{crit}})$.

Figure 4.8:
Dependence of the normalized growth rate $\bar{\Gamma}$ of the small-scale dynamo on the magnetic Prandtl number Pm for Kolmogorov turbulence. We choose different values for the Reynolds number Re. In the limit $\mathrm{Pm} \to \infty$ the normalized growth rates are $\bar{\Gamma} = 10.28$ for $\mathrm{Re} = 10^2$, $\bar{\Gamma} = 102.78$ for $\mathrm{Re} = 10^4$, and $\bar{\Gamma} = 10277.78$ for $\mathrm{Re} = 10^8$. These limits are indicated in the plot as horizontal lines.
image credit: Schober et al. (2012c)

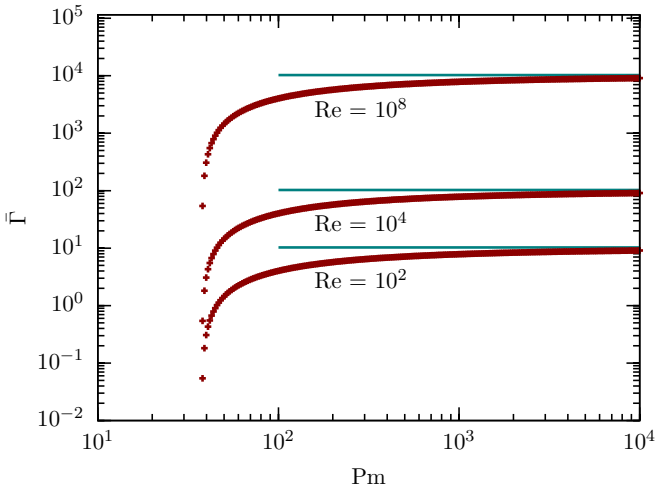

Figure 4.9:
The same plot as 4.8, but for Burgers turbulence. In the limit $\mathrm{Pm} \to \infty$ the normalized growth rates are $\bar{\Gamma} = 0.85$ for $\mathrm{Re} = 10^2$, $\bar{\Gamma} = 3.95$ for $\mathrm{Re} = 10^4$, and $\bar{\Gamma} = 85.1$ for $\mathrm{Re} = 10^8$. These limits are indicated in the plot as horizontal lines.
image credit: Schober et al. (2012c)

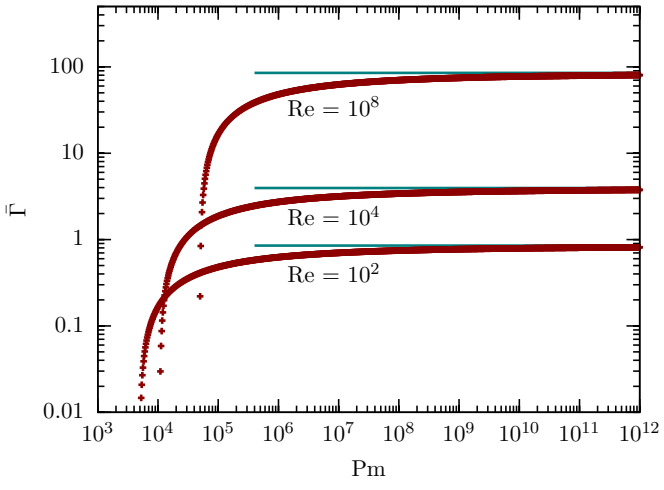

The constant of proportionality depends on the amount of compressibility. In a later work Kleeorin & Rogachevskii (2012) find that this logarithmic scaling of the growth rate is valid only in the vicinity of the threshold of small-scale dynamo excitation. For magnetic Reynolds numbers much larger than $\mathrm{Rm}_{\mathrm{crit}}$, they found in the limit of small magnetic Prandtl number $\Gamma \propto \mathrm{Rm}^{1/2}$ for Kolmogorov turbulence. As for a constant magnetic Prandtl number $\mathrm{Rm} \propto \mathrm{Re}$, this agrees with our result.

4.2.5 The Turbulent Dynamo at Small Magnetic Prandtl Numbers[4]

In this section we investigate the limit of small magnetic Prandtl numbers. While the derivation of the dynamo properties from the Kazantsev theory proceeds in a similar way, the results found differ significantly from those of large magnetic Prandtl numbers.

Critical Magnetic Reynolds Number

For the onset of the small-scale dynamo the magnetic Reynolds number needs to exceed a critical value $\mathrm{Rm}_{\mathrm{crit}}$. We determine the latter by setting the growth rate in (4.46) equal to zero and solving equation (4.49) for Rm. As the p-function in the inertial range only depends on Rm, but not on Re, it is independent of the magnetic Prandtl number. We list the numerical results for $\mathrm{Rm}_{\mathrm{crit}}$ in table 4.1. The critical magnetic Reynolds number increases with increasing compressibility.
In the limit of large Pm the critical magnetic Reynolds number is not necessarily the dominant restriction, as $\mathrm{Re} > 10^3$ is required for turbulent flows. As $\mathrm{Rm} \gg \mathrm{Re}$ for large Pm, Rm needs to be much larger than 10^3, which is larger than the critical magnetic Reynolds number. In the opposite limit of small Pm we have the case of $\mathrm{Rm} \ll \mathrm{Re}$. For low hydrodynamic Reynolds numbers, the magnetic Reynolds number can fall below $\mathrm{Rm}_{\mathrm{crit}}$, and the small-scale dynamo can not operate.
We note that, contrary to our results presented here, Iskakov et al. (2007) found a weak dependence of the critical magnetic Reynolds number on the magnetic Prandtl number. Therefore, it needs to be explored further whether the discrepancy in our results is due to approximations in the Kazantsev model or if it is a result of the relatively narrow inertial range in numerical simulations. The latter provides a restriction on the number of turbulent eddies resolved in the box, and thus on the overall statistical sampling of the dynamics. In future studies, it would thus be desirable to explore this behavior at higher resolution in numerical simulations, and by relaxing the assumption of the Kazantsev theory in analytical studies.

Growth Rate

We are interested in bound eigenfunctions of the Kazantsev equation (4.45), which have corresponding real eigenvalues, i.e. growth rates. For this we require part of

[4]This section follows closely Schober et al. (2012a).

Model and reference	ϑ	$\bar{\Gamma}$ (Pm$\ll$1)	$\bar{\Gamma}$ (Pm$\gg$1)	$\mathrm{Rm}_{\mathrm{crit}}$
Incompressible turbulence (Kolmogorov, 1941)	1/3	$0.027\,\mathrm{Rm}^{1/2}$	$1.03\,\mathrm{Re}^{1/2}$	≈ 107
Intermittency of Kolmogorov turbulence (She & Leveque, 1994)	0.35	$0.027\,\mathrm{Rm}^{0.48}$	$0.94\,\mathrm{Re}^{0.48}$	≈ 118
Driven supersonic MHD-turbulence (Boldyrev et al., 2002)	0.37	$0.026\,\mathrm{Rm}^{0.46}$	$0.84\,\mathrm{Re}^{0.46}$	≈ 137
Observation in molecular clouds (Larson, 1981)	0.38	$0.025\,\mathrm{Rm}^{0.45}$	$0.79\,\mathrm{Re}^{0.45}$	≈ 149
Solenoidal forcing of the turbulence (Federrath et al., 2010)	0.43	$0.019\,\mathrm{Rm}^{0.40}$	$0.54\,\mathrm{Re}^{0.40}$	≈ 227
Compressive forcing of the turbulence (Federrath et al., 2010)	0.47	$0.012\,\mathrm{Rm}^{0.36}$	$0.34\,\mathrm{Re}^{0.36}$	≈ 697
Observations in molecular clouds (Ossenkopf & Mac Low, 2002)	0.47	$0.012\,\mathrm{Rm}^{0.36}$	$0.34\,\mathrm{Re}^{0.36}$	≈ 697
Highly compressible turbulence (Burgers, 1948)	1/2	$0.0054\,\mathrm{Rm}^{1/3}$	$0.18\,\mathrm{Re}^{1/3}$	≈ 2718

Table 4.1:
The normalized growth rate of the small-scale dynamo $\bar{\Gamma}$ in the limit of small (Rm$\ll$Re) and large magnetic Prandtl numbers (Rm$\gg$Re). We show our results for different types of turbulence, which are characterized by the exponent ϑ of the slope of the turbulent velocity spectrum, $v(\ell) \propto \ell^{\vartheta}$. The extreme values of ϑ are 1/3 for Kolmogorov turbulence and 1/2 for Burgers turbulence. Also listed are the results found for the critical magnetic Reynolds number $\mathrm{Rm}_{\mathrm{crit}}$.

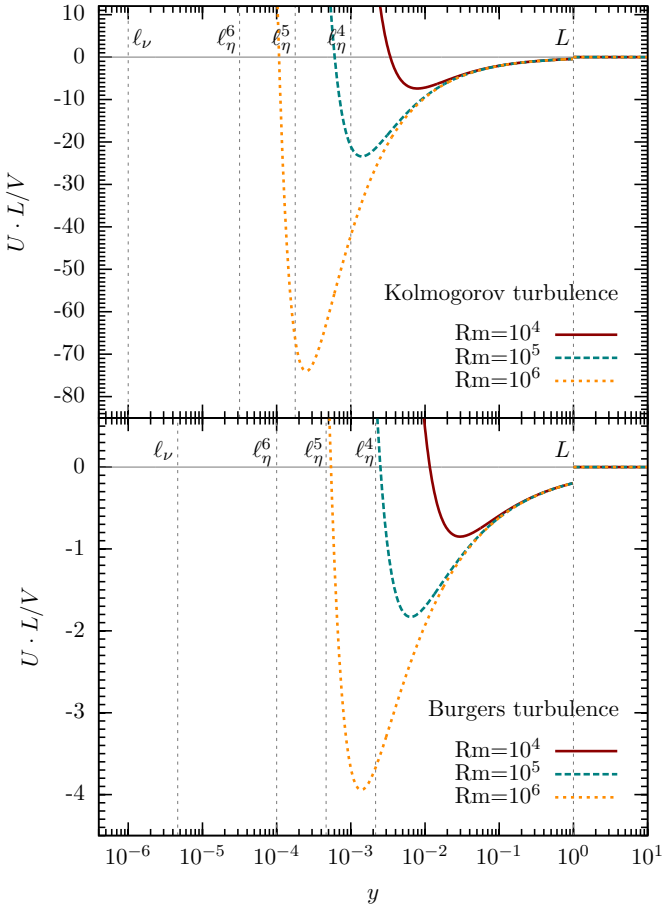

Figure 4.10:
Dependence of the potential on the dimensionless parameter $y \equiv r/L$ for Kolmogorov ($\vartheta = 1/3$) and Burgers ($\vartheta = 1/2$) turbulence at $\mathrm{Re} = 10^8$. We choose different magnetic Reynolds numbers $\mathrm{Rm} = 10^4$, $\mathrm{Rm} = 10^5$ and $\mathrm{Rm} = 10^6$, resulting in the Prandtl numbers $\mathrm{Pm} = 10^{-4}$, $\mathrm{Pm} = 10^{-3}$ and $\mathrm{Pm} = 10^{-2}$. The viscous scale ℓ_ν depends on the type of turbulence and the Reynolds number. For Kolmogorov turbulence $\ell_\nu = \mathrm{Re}^{-3/4}L$; for Burgers turbulence $\ell_\nu = \mathrm{Re}^{-2/3}L$. The resistive scale is $\ell_\eta = \mathrm{Rm}^{-3/4}L$ for Kolmogorov and $\ell_\eta = \mathrm{Rm}^{-2/3}L$ for Burgers turbulence. A magnetic Reynolds number 10^x is indicated in the resistive scale as $\ell_\eta^{(\mathrm{x})}$. (Re appears only in the viscous range.)
image credit: Schober et al. (2012a)

the potential (4.42) to be negative.
In figure 4.10 we show the normalized potential (4.42) as a function of $y = r/L$ for Kolmogorov and Burgers turbulence. We choose a Reynolds number of 10^8, which is a typical value for example for the interior of planets (Roberts & Glatzmaier, 2000) and primordial halos (Schober et al., 2012b). The different lines correspond to different magnetic Reynolds numbers of 10^4, 10^5 and 10^6 and hence represent magnetic Prandtl numbers of 10^{-4}, 10^{-3} and 10^{-2}, respectively. The crucial discrepancy to the contrary limit of large Pm is that the potential only has a negative part in the inertial range. Thus, there are only real positive eigenvalues of the Kazantsev equation (4.41) within this range.
With our model for the correlation function of the turbulent velocity field, equations (4.59) and (4.63), the p-function (4.46) in the inertial range is

$$\begin{aligned} p(y) &= \frac{-3}{20\left(3+\mathrm{Rm}\, y^{1+\vartheta}\right)^2}\left(135+\mathrm{Rm}\, y\,\left(60\, y\,\bar{\Gamma}-a(\vartheta)\,\mathrm{Rm}\, y^{1+2\,\vartheta}\right.\right. \\ &\quad \left.\left.+2\, y^{\vartheta}\,\left(25-b(\vartheta)+10\,\mathrm{Rm}\, y^2\,\bar{\Gamma}\right)\right)\right), \end{aligned} \tag{4.81}$$

where we use the abbreviations

$$a(\vartheta) = \vartheta(56-103\vartheta) \tag{4.82}$$

$$b(\vartheta) = \vartheta(79-157\vartheta). \tag{4.83}$$

For the analytical determination of the zeros of $p(y)$ we use the approximations

$$p_1(y) = \frac{3\,\mathrm{Rm}\, y^{1+\vartheta}\,\left(a(\vartheta)\,\mathrm{Rm}\, y^{1+\vartheta}+2\, b(\vartheta)-50\right)-405}{20\left(3+\mathrm{Rm}\, y^{1+\vartheta}\right)^2}, \tag{4.84}$$

which is valid for $\bar{\Gamma} \to 0$, and

$$p_2(y) = \frac{3\, a(\vartheta)}{20} - 3\, y^{1-\vartheta}\,\bar{\Gamma}, \tag{4.85}$$

where we leave out the constant terms in (4.81). We show $p(y)$ as well as the two approximations in figure 4.11 for the exemplary case of $\mathrm{Re} = 10^8$ and $\mathrm{Rm} = 10^5$.
By using $p_1(y)$ we find for the first zero of $p(y)$ approximately

$$y_1 = \left(\frac{c(\vartheta)}{\mathrm{Rm}}\right)^{1/(1+\vartheta)}, \tag{4.86}$$

where we defined

$$c(\vartheta) = \frac{25+\sqrt{135\, a(\vartheta)+\left(b(\vartheta)-25\right)^2}-b(\vartheta)}{a(\vartheta)}. \tag{4.87}$$

With $p_2(y)$ we find the second zero

$$y_2 = \left(\frac{a(\vartheta)}{20\,\bar{\Gamma}}\right)^{1/(1-\vartheta)}. \tag{4.88}$$

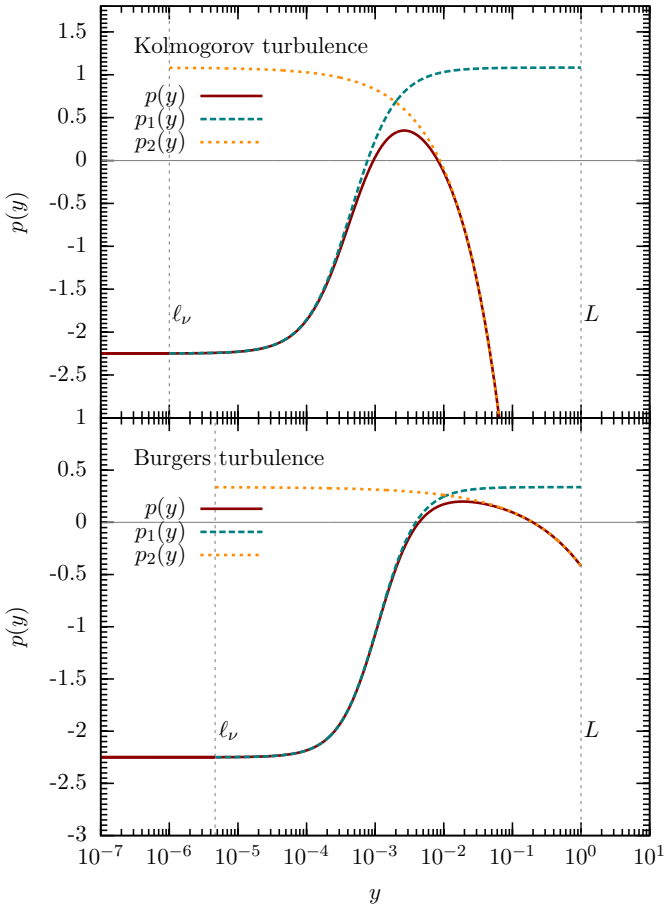

Figure 4.11:
The p-function (red curve) as a function of the normalized scale parameter $y = r/L$ in the viscous, inertial and large-scale range. We indicate the viscous scale ℓ_ν and the forcing scale L as vertical lines. For the plot, we use our result for the growth rate in the limit of small Pm, $\mathrm{Re} = 10^8$ and $\mathrm{Rm} = 10^5$. The dashed green line reefers to the approximation function p_1 and the dotted purple line to p_2. The upper panel shows $p(y)$ for Kolmogorov turbulence, the lower panel for Burgers turbulence.
image credit: Schober et al. (2012a)

The eigenvalue can be determined approximately by the equation

$$\int_{y_1}^{y_2} \frac{\sqrt{p_2(y)}}{y}\,\mathrm{d}y = \frac{\pi}{2}. \tag{4.89}$$

Here we use the approximative function $p_2(y)$ instead of the full function $p(y)$ in order to find an analytical solution of the integral. Note that the scaling of the abscissa in figure 4.11 is logarithmic and thus $p_2(y)$ is a good approximation of $p(y)$ for $y > y_1$. The value of the integral does not change by much due to this simplification.
We can solve the resulting equation from (4.89) with the ansatz

$$\bar{\Gamma} = \alpha\ \mathrm{Rm}^{(1-\vartheta)/(1+\vartheta)}. \tag{4.90}$$

This is motivated by the result of Schober et al. (2012c) in the limit of large magnetic Prandtl numbers: $\bar{\Gamma} \propto Re^{(1-\vartheta)/(1+\vartheta)}$. Here the amplification process takes place at the viscous scale, which depends on the hydrodynamical Reynolds number. As mentioned above in the limit of low magnetic Prandtl numbers the dynamo operates mainly on the resistive scale, which depends on Rm. Thus, our ansatz is to replace the hydrodynamic Reynolds number by the magnetic one (see also e.g. Boldyrev & Cattaneo, 2004).
With (4.90) we find for the solution of (4.89):

$$\begin{aligned}\frac{1}{\vartheta-1}\sqrt{\frac{3}{5}}\Bigg(&\sqrt{a(\vartheta)-20\,c(\vartheta)^{(1-\vartheta)/(1+\vartheta)}\,\alpha}+\log\left(4\,\sqrt{5\mathrm{Rm}^{(1-\vartheta)/(1+\vartheta)}\,\alpha}\right)^{\sqrt{a(\vartheta)}}\\ &-\log\left(2\sqrt{\frac{c(\vartheta)}{\mathrm{Rm}}}^{(\vartheta-1)/(\vartheta+1)}\left(\sqrt{a(\vartheta)}+\sqrt{a(\vartheta)-20\,c(\vartheta)^{(1-\vartheta)/(1+\vartheta)}\,\alpha}\right)\right)^{\sqrt{a(\vartheta)}}\Bigg) \;=\; \frac{\pi}{2}.\end{aligned} \tag{4.91}$$

As we assume the pre-factor of the growth rate to be very small, i.e. $\alpha \ll 1$, we use $a(\vartheta) \gg 20\,c(\vartheta)^{(1-\vartheta)/(1+\vartheta)}\,\alpha$ to approximate (4.91) as

$$\begin{aligned}\frac{\sqrt{a(\vartheta)}}{\vartheta-1}\sqrt{\frac{3}{5}}\Bigg(1-\log\Bigg(&4\sqrt{\frac{a(\vartheta)c(\vartheta)}{\mathrm{Rm}}}^{(\vartheta-1)/((1+\vartheta))}\Bigg)\\ &+\log\left(4\,\sqrt{5\mathrm{Rm}^{(1-\vartheta)/(1+\vartheta)}\,\alpha}\right)\Bigg) \;=\; \frac{\pi}{2}.\end{aligned} \tag{4.92}$$

The solution of this equation can easily be found:

$$\alpha = \frac{a(\vartheta)}{5}\,c(\vartheta)^{(1-\vartheta)/(1+\vartheta)}\,\exp\left(\sqrt{\frac{5}{3\,a(\vartheta)}}\,\pi\,(\vartheta-1)-2\right). \tag{4.93}$$

We list results for the normalized growth rate of the small-scale dynamo in the limit of low magnetic Prandtl numbers for exemplary types of turbulence in table

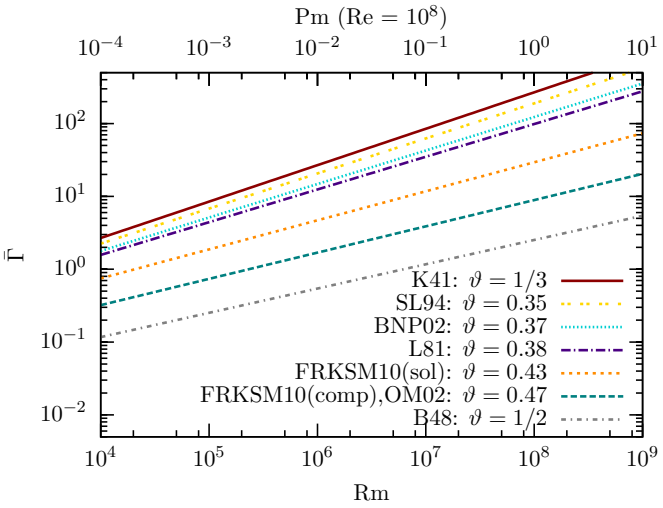

Figure 4.12:
The normalized growth rate $\bar{\Gamma}$ as a function of the magnetic Reynolds number Rm (lower x axes) and the magnetic Prandtl number Pm (upper x axes). The results shown for the lower abscissa are only valid for small Pm, while we used a fixed Re of 10^8 for the upper abscissa. We present results for slopes of the turbulent velocity spectrum ϑ: K41 (Kolmogorov, 1941), SL94 (She & Leveque, 1994), BNP02 (Boldyrev et al., 2002), L81 (Larson, 1981), FRKSM10 (Federrath et al., 2010) (sol: solenoidal forcing; comp: compressive forcing), OM02 (Ossenkopf & Mac Low, 2002) and B48 (Burgers, 1948). *image credit: Schober et al. (2012a)*

4.1. For comparison we also list the results for Pm $\to \infty$ from Schober et al. (2012c). Moreover, we present the normalized growth rate in figure 4.12. The lower abscissa shows the dependency on the magnetic Reynolds number, which is valid for any hydrodynamic Reynolds number Re $\gg$ Rm. The upper abscissa in figure 4.12 shows the dependency on the magnetic Prandtl number for a fixed Re of 10^8. We present the results for different types of turbulence reported in the astrophysical literature (Kolmogorov, 1941; She & Leveque, 1994; Boldyrev et al., 2002; Larson, 1981; Federrath et al., 2010; Ossenkopf & Mac Low, 2002; Burgers, 1948).

4.2.6 Numerical Solution of the Kazantsev Equation[5]

The Growth Rate in the Full Prandtl Number Regime

Bovino et al. (2013) solve the Kazantsev equation (4.41) numerically by using the Numerov algorithm. The turbulent correlation function they use is identical to the one used in the analytical calculations presented above, i.e. equations (4.59) and (4.63). A comparison of the numerical results with our analytical solution is shown in figure 4.13 at a fixed Reynolds number of 10^{14}. The comparison shows excellent agreement between the numerical and the analytical solutions in the limit of small ($\bar{\Gamma} \propto \mathrm{Rm}^{(1-\vartheta)/(1+\vartheta)}$ Schober et al., 2012a) and large magnetic Prandtl numbers ($\bar{\Gamma} \propto \mathrm{Re}^{(1-\vartheta)/(1+\vartheta)}$ Schober et al., 2012c). We find that the range where

[5]This section follows closely Bovino et al. (2013).

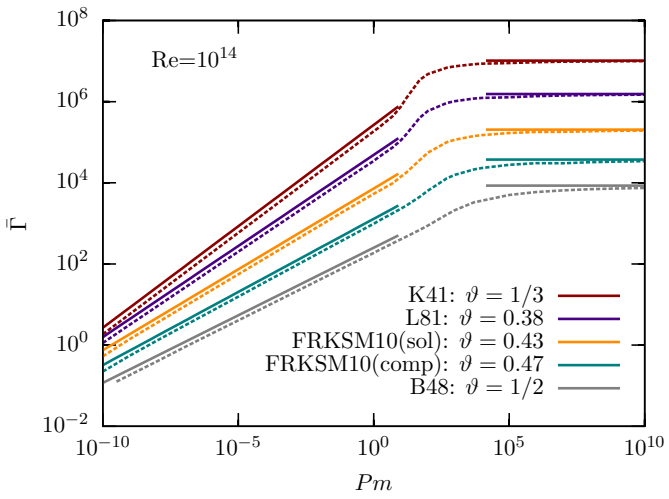

Figure 4.13:
The normalized growth rate $\bar{\Gamma}$ as a function of the magnetic Prandtl number Pm for a fixed Reynolds number $\mathrm{Re} = 10^{14}$. The solutions from numerical integration of the Kazantsev equation by Bovino et al. (2013) are indicated as dashed lines, while the analytical solutions in the limits of small (Schober et al., 2012a) and large Prandtl numbers (Schober et al., 2012c) are shown by the solid lines. We present different types for turbulence, indicated by the slope of the turbulent velocity spectrum ϑ: K41 (Kolmogorov, 1941), L81 (Larson, 1981), FRKSM10 (Federrath et al., 2010) (sol: solenoidal forcing; comp: compressive forcing), and B48 (Burgers, 1948).
image credit: Schober et al. (2012a)

our analytical solution (4.90) can be used is not restricted to $\mathrm{Pm} \ll 1$ but is also applicable in the regime $\mathrm{Pm} \approx 1$ for all types of turbulence at $\mathrm{Re} = 10^{14}$. We see a minor offset between our solutions and the numerical ones for small Pm. This is probably caused by the approximations we made in equations (4.91) and (4.92).

Numerical Solutions for Higher Modes of the Growth Rate

In figure 4.14 we show the normalised growth rate $\bar{\Gamma}$ found by Bovino et al. (2013) for different modes and $\mathrm{Re} = 10^{14}$ for the case of Kolmogorov turbulence small to large magnetic Prandtl . For a narrow range of Pm they find a strong increase of the growth rate, in particular for the fastest growing mode, which depends on the fact that for $5 \leq \mathrm{Pm} \leq 10^5$ the potential is negative both in the inertial and in the viscous range yielding two contributions (see figures 4.10 and 4.5). We note that the additional contribution coming from the viscous range is marked only for $\mathrm{Pm} > 10$, even if it starts to appear for $\mathrm{Pm} \geq 5$. The higher modes shown in the figure clearly depend on the depth of the potential $U(x)$, and only the main growing mode (the larger in magnitude) was found to exist in the whole range of Pm. It is worth noting that the small-scale dynamo amplification can occur also for $\mathrm{Pm} \ll 1$. The presence of the higher growing modes is important since it gives an additional contribution to

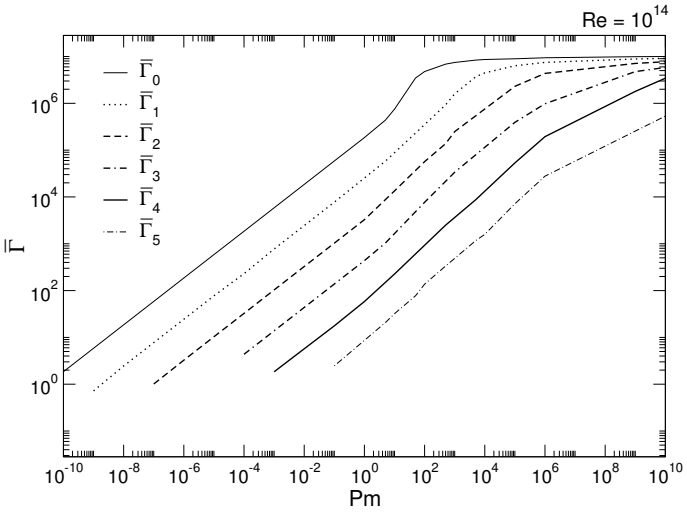

Figure 4.14:
Log-Log plot of the computed fastest and slower modes of the normalized growth rate $\bar{\Gamma}$ as a function of Pm for incompressible Kolmogorov turbulence and for Re = 10^{14}.
image credit: Bovino et al. (2013)

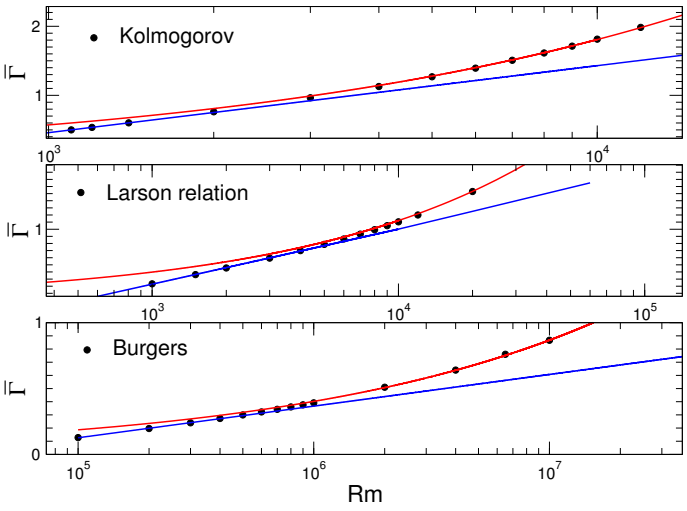

Figure 4.15:
Computed normalized growth rate $\bar{\Gamma}$ as a function of Rm for three different types of turbulence and for Pm ≈ 1. Fitting curves are also reported in the panels. $\bar{\Gamma}$ scales as Rm^{α} (red line) when far from the threshold, and $\propto \beta \ln(\mathrm{Rm})$ in the vicinity of the threshold.
image credit: Bovino et al. (2013)

the magnetic field amplification that becomes more marked for Pm $\gg 1$, where the $\bar{\Gamma}$ values are 6 orders of magnitude larger than for Pm $\ll 1$ (for the same Reynolds number). Especially for Pm $\gg 1$, a large number of higher modes has been found. By taking in consideration Burgers turbulence Bovino et al. (2013) find a small number of modes going to a maximum of 3 ($\bar{\Gamma}_0$, $\bar{\Gamma}_1$, and $\bar{\Gamma}_2$) for Pm $\to \infty$ up to only 1 mode for intermediate and small Pm. This provides a further confirmation of the fact that for Kolmogorov turbulence there is a larger amplification of the magnetic field.

Dynamo Thresholds

An important criterion for small-scale dynamo action is that the magnetic Reynolds number needs to exceed a threshold $\mathrm{Rm}_{\mathrm{crit}}$. Bovino et al. (2013) have evaluated $\mathrm{Rm}_{\mathrm{crit}}$ for all types of turbulence considered here. An asymptotic value of $\mathrm{Rm}_{\mathrm{crit}} = 320$ has been found for Kolmogorov turbulence and Re=10^{14}, which is in good agreement with other analytical (Kleeorin & Rogachevskii, 2012) and numerical dynamo

ϑ	$\mathrm{Pm} \ll 1$	$\mathrm{Pm} \gg 1$
1/3	$1.85\times10^{-2}\ \mathrm{Rm}^{1/2}$	$9.98\times10^{-1}\ \mathrm{Re}^{1/2}$
0.38	$1.80\times10^{-2}\ \mathrm{Rm}^{0.45}$	$7.62\times10^{-1}\ \mathrm{Re}^{0.45}$
0.43	$1.31\times10^{-2}\ \mathrm{Rm}^{0.40}$	$5.09\times10^{-1}\ \mathrm{Re}^{0.40}$
0.47	$8.91\times10^{-3}\ \mathrm{Rm}^{0.36}$	$3.07\times10^{-1}\ \mathrm{Re}^{0.36}$
1/2	$3.69\times10^{-3}\ \mathrm{Rm}^{1/3}$	$1.54\times10^{-1}\ \mathrm{Re}^{1/3}$

Table 4.2:
The normalized growth rate of the small-scale dynamo $\bar{\Gamma}$ as a function of Re and Rm for five different types of turbulence. The results from the work of Bovino et al. (2013) for $\mathrm{Pm} \ll 1$ and $\mathrm{Pm} \gg 1$ are reported.

studies (Schekochihin et al., 2005; Haugen et al., 2004a; Malyshkin & Boldyrev, 2010), which report a $\mathrm{Rm_{crit}}$ value of 410, 500, 210, and ≈500, respectively. Furthermore, Bovino et al. (2013) confirm that the threshold for the generation of magnetic fluctuations by highly compressible turbulent flows is considerably larger ($\mathrm{Rm_{crit}} = 32000$) than for the case of an incompressible fluid. This trend is also mentioned in Rogachevskii & Kleeorin (1997). It is worth noting that Leorat et al. (1981) obtained a critical magnetic Reynolds number for compressible Kolmogorov turbulence of the order of a few tens. In figure 4.15, Bovino et al. (2013) explore the dependence of the fastest growing mode on the magnetic Reynolds number for values in the vicinity of the threshold $\mathrm{Rm_{crit}}$ for turbulence based on Kolmogorov, Burgers and the Larson relation. We adopt $\mathrm{Pm} \approxeq 1$ and analyse the scaling of the growth rate in the vicinity and far away from the threshold ($\mathrm{Rm_{crit}}$). For all cases considered here, the growth rate far from the threshold scales as $\propto \mathrm{Re}^{\alpha}$ for $\mathrm{Pm} \gg 1$ (or $\propto \mathrm{Rm}^{\alpha}$ for $\mathrm{Pm} \ll 1$), with α=1/2 for Kolmogorov and 1/3 for Burgers. In the vicinity of the threshold, the growth rate becomes a function of $\mathrm{Re\text{-}Rm_{crit}}$. Here Bovino et al. (2013) perform a fit with a logarithmic function, $\bar{\Gamma} = \beta \ln(\mathrm{Rm}) + \gamma$, with β equal to 0.4214, 0.3356, and 0.10438, and $\gamma = \beta \ln(\mathrm{Rm_{crit}})$ to be -2.4516, -2.0901, and -1.0754 for Kolmogorov, Larson and Burgers turbulence, respectively[6]. Table 4.2 reports the fitted growth rate as a function of Re and Rm for magnetic Reynolds numbers far from the threshold for the different types of turbulence, confirming the most efficient dynamo growth for the case of Kolmogorov turbulence.

[6]We note that the functional form near the threshold is not necessarily logarithmic, and a fit proportional to ($\mathrm{Rm}^{1/2}$-$\mathrm{Rm}_c^{1/2}$) also provides a valid description of the data (S. Boldyrev, private communication).

4.3 Non-linear Turbulent Dynamo[7]

The exponential growth phase will come to an end when in the Navier-Stokes equation (3.42) the tension force of the magnetic field, $\boldsymbol{B} \cdot \nabla \boldsymbol{B}$, becomes comparable to the inertial term of the flow, $\boldsymbol{u} \cdot \nabla \boldsymbol{u}$. At this point, magnetic field amplification will stop on the scales that fulfill this condition, and continue to proceed on larger scales. As discussed by Schekochihin et al. (2002), this condition translates to

$$\frac{B_{\ell_a}^2}{\ell_a} \approx \frac{u_{\ell_a}^2}{\ell_a}, \tag{4.94}$$

where ℓ_a denotes the smallest scale where amplification still occurs. In this regime, a linear growth of the magnetic energy has been reported in previous studies, based on the assumption of Kolmogorov turbulence (e.g. Schekochihin et al., 2002; Cho et al., 2009; Beresnyak, 2012). In the following, we will present a generalization of these investigations from Schleicher et al. (2013), who employ a simplified toy model as well as a more sophisticated Fokker-Planck model previously suggested by Schekochihin et al. (2002). As a result, one can show that different types of power-law growth can be expected depending on the adopted type of turbulence.
It further is important to point out that in the non-linear regime, we expect the magnetic Prandtl number to play a less critical role, as the amplification scale of the magnetic field is now expected to be larger than both the viscous and the resistive scale, such that no strong dependence on Re or Rm can be expected.
We note that the models considered in this section have previously been motivated in the context of the incompressible induction equation, given as

$$\partial_t \boldsymbol{B} + (\boldsymbol{v} \cdot \nabla)\, \boldsymbol{B} = (\boldsymbol{B} \cdot \nabla)\, \boldsymbol{v} + \eta \Delta \boldsymbol{B}. \tag{4.95}$$

However, they can be naturally extended into the compressible regime with the replacement

$$\boldsymbol{B} \rightarrow \frac{\boldsymbol{B}}{\rho}. \tag{4.96}$$

Inserting this replacement as well as the continuity equation,

$$\dot{\rho} = -\nabla \cdot (\rho \boldsymbol{v})\,, \tag{4.97}$$

it is straightforward to show that one obtains the compressible form of the induction equation,

$$\partial_t \boldsymbol{B} + (\boldsymbol{v} \cdot \nabla)\, \boldsymbol{B} = (\boldsymbol{B} \cdot \nabla)\, \boldsymbol{v} - \boldsymbol{B}\,(\nabla \cdot \boldsymbol{v}) + \eta \Delta \boldsymbol{B}. \tag{4.98}$$

As long as the mean density $\langle \rho \rangle$ in the box is constant, a significant growth of the quantity $\langle B/\rho \rangle$ nevertheless implies a corresponding growth of the magnetic energy, assuming that the density distribution function will not change significantly

[7] This section follows closely Schleicher et al. (2013).

over time. In the case of well-developed driven turbulence, one indeed expects a characteristic log-normal density probability distribution function, which naturally complies with these requirements (Vázquez-Semadeni, 1994; Passot & Vázquez-Semadeni, 1998; Federrath et al., 2008). Strictly speaking, the following considerations apply to the quantity $\tilde{B} = B/\rho$ and $\tilde{W} = W/\rho^2$, with W the magnetic energy. In the following, the $\tilde{}$ is however dropped for simplicity.

4.3.1 Non-Linear Magnetic Field Evolution in a Toy Model

In the toy model previously proposed by Schekochihin et al. (2002), the dominant fraction of the magnetic energy resides on the scale ℓ_a, the smallest scale where magnetic field amplification still occurs (thus yielding the shortest amplification timescale). On that scale, the magnetic energy is expected to be already close to saturation. The magnetic energy $E_{\rm mag}(t)$ can thus be related to the amplification scale ℓ_a by the approximate relation

$$E_{\rm mag}(t) \approx \frac{1}{2}\langle\rho\rangle u^2_{\ell_a(t)}. \tag{4.99}$$

The magnetic energy is evaluated here at the mean density $\langle\rho\rangle$ of the turbulent box, as we are interested only in the magnetic field amplification by shear. Adopting the eddy-turnover rate on the scale ℓ_a as the growth rate for the magnetic field, i.e.

$$\Gamma(t) \approx \frac{u_{\ell_a(t)}}{\ell_a(t)}, \tag{4.100}$$

the magnetic energy evolves as

$$\frac{\mathrm{d}}{\mathrm{d}t}E_{\rm mag} = \Gamma(t)E_{\rm mag}(t) - 2\eta k^2_{rms}E_{\rm mag}(t) \tag{4.101}$$

with

$$k^2_{rms}(t) = \frac{1}{E_{\rm mag}}\int_0^\infty k^2 M(t,k)\ \mathrm{d}k \tag{4.102}$$

and

$$M(t,k) = \frac{1}{2}\int \langle|\boldsymbol{B}(t,\boldsymbol{k})|^2\rangle\ \mathrm{d}\Omega_{\boldsymbol{k}}. \tag{4.103}$$

Now, we have $\Gamma(t)E_{\rm mag}(t) \approx \langle\rho\rangle u^3_{\ell_a(t)}/\ell_a(t) =: \epsilon(t)$. Inserting in equation (4.101) yields

$$\frac{\mathrm{d}}{\mathrm{d}t}E_{\rm mag} = \chi\epsilon(t) - 2\eta k^2_{rms}(t)E_{\rm mag}(t), \tag{4.104}$$

where χ is a constant of order unity. For Kolmogorov turbulence, the quantity $\epsilon(t) = \langle\rho\rangle u^3_{\ell_a(t)}/\ell_a(t)$ is a constant (Kolmogorov, 1941). In this case, and as long

as magnetic energy dissipation is negligible, $\mathrm{d}E_{\mathrm{mag}}/\mathrm{d}t = \mathrm{const}$, implying a phase of linear growth. In this limit, we obtain the result of Beresnyak (2012), where a constant fraction of the turbulence dissipation rate is converted into magnetic energy.
In the general case with $u_{\ell_a} \propto \ell_a^{\vartheta}$, $\epsilon(t)$ is however not constant, but varies as $\ell_a^{3\vartheta-1}$. In the case of Burgers turbulence, we thus obtain $\epsilon \propto \ell_a^{0.5}$. In this case, the growth of the magnetic energy is no longer linear, as the turbulent energy dissipation rate is not independent of scale!
For comparison, we note that the quantity $\tilde{\epsilon} = \rho e_{\mathrm{SGS}}^{3/2}/\ell$, with e_{SGS} the specific energy density of subgrid-scale turbulence, is practically independent of ℓ. It however has a weak dependence on the Mach number, and a strong dependence on the type of forcing (Schmidt & Federrath, 2011). As the density fluctuations will however not contribute to the shearing, we will adopt ϵ as the quantity of interest here.
To quantify the expected behavior, we need to solve equation (4.99) for ℓ_a. For this purpose, we recall that u_{ℓ_a} is related to the turbulence driving scale L and the velocity V on that scale via

$$u_{\ell_a} = V \left(\frac{\ell_a}{L} \right)^{\vartheta}. \tag{4.105}$$

From (4.99), we thus obtain

$$\ell_a = L \left(\frac{2E_{\mathrm{mag}}}{\langle\rho\rangle V^2} \right)^{1/(2\vartheta)}. \tag{4.106}$$

We can now evaluate (4.100) and (4.101), yielding

$$\frac{\mathrm{d}}{\mathrm{d}t} E_{\mathrm{mag}} \approx E_{\mathrm{mag}} V L^{-\vartheta} \left[L \left(\frac{2E_{\mathrm{mag}}}{\langle\rho\rangle V^2} \right)^{1/(2\vartheta)} \right]^{\vartheta-1} \propto E_{\mathrm{mag}}^{(3\vartheta-1)/(2\vartheta)}. \tag{4.107}$$

For Kolmogorov turbulence ($\vartheta = 1/3$), we confirm that $\mathrm{d}E_{\mathrm{mag}}/\mathrm{d}t = \mathrm{const}$, while in the more general case, this quantity will increase with increasing E_{mag}. This can be intuitively understood, as the steep spectra for $\vartheta > 1/3$ imply a more modest increase of the eddy-timescale with length scale, suggesting that the amplification rate remains larger when increasing the scale. We re-assess these results with the Fokker-Planck model below and explore the physical implications in more detail.

4.3.2 Non-Linear Magnetic Field Evolution in a Fokker-Planck Model

The starting point for our investigations is the Fokker-Planck model of Schekochihin et al. (2002). Here, the time-evolution of the magnetic-energy spectrum is given as

$$\partial_t M = \frac{\partial}{\partial k} \left[D(k) \frac{\partial M}{\partial k} - V(k) M \right] + 2\Gamma(t) M - 2\eta k^2 M, \tag{4.108}$$

with the diffusion coefficient $D(k) = \Gamma(t)k^2/5$ and the drift velocity in k-space $V(k) = 4\Gamma(t)k/5$. We recall that the magnetic-energy spectrum M is related to the magnetic energy E_{mag} via

$$E_{\mathrm{mag}}(t) = \int_0^\infty M(t,k)\ \mathrm{d}k. \tag{4.109}$$

To describe the evolution in the nonlinear regime, Schekochihin et al. (2002) postulated the following expressions:

$$\Gamma(t) = c_1 \left[\int_0^{k_s(t)} k^2 E(k)\ \mathrm{d}k\right]^{1/2}, \tag{4.110}$$

$$E_{\mathrm{mag}}(t) = c_2 \int_{k_s(t)}^\infty E(k)\ \mathrm{d}k. \tag{4.111}$$

The constants c_1 and c_2 are of order unity, $E(k)$ is the hydrodynamic energy spectrum neglecting the influence of the magnetic field, and the wave vector $k_s(t)$ is defined via equation (4.111). It corresponds to the smallest scale where amplification efficiently occurs. As input for the Fokker-Planck model, we require an energy spectrum of the turbulence. As before, we assume that the velocity in the inertial range scales as

$$u_\ell \propto \ell^\vartheta. \tag{4.112}$$

The hydrodynamic energy spectrum is then approximately given as

$$E(k) = \begin{cases} C_t \epsilon^{2/3} k^{-2\vartheta-1} & \text{for } k \in [k_f, k_\nu] \\ 0 & \text{elsewhere,} \end{cases} \tag{4.113}$$

with C_t a constant which depends on the type of turbulence, k_f and k_ν the wave vectors describing the injection scale of turbulence and the viscous scale, respectively. The value of k_ν is set to enforce the condition $\epsilon = 2\nu \int_0^\infty k^2 E(k)\ \mathrm{d}k$. Unlikely in (4.59) and (4.63), we do not explicitly model the turbulent spectra in the viscous regime, as these no longer contribute during the non-linear stage. With these input data, equation (4.111) can be evaluated as

$$E_{\mathrm{mag}}(t) = \frac{c_2 C_t \epsilon^{2/3}}{2\vartheta} \left[k_s^{-2\vartheta} - k_\nu^{-2\vartheta}\right]. \tag{4.114}$$

We further introduce the quantities

$$E_{\mathrm{mag},0} = c_2 \int_0^\infty E(k)\ \mathrm{d}k = \frac{c_2 C_t \epsilon^{2/3}}{2\vartheta} \left[k_f^{-2\vartheta} - k_\nu^{-2\vartheta}\right], \tag{4.115}$$

$$E_{\mathrm{mag},\nu} = \frac{c_2 C_t \epsilon^{2/3}}{2\vartheta} k_\nu^{-2\vartheta}. \tag{4.116}$$

We note that in the above expressions, the integral $\int_0^\infty dk$ corresponds to an integration from k_f to k_ν, as the turbulent energy is non-zero only in this regime (see 4.113). Using these definitions, the wave vectors k_ν, k_s and k_f can be expressed as

$$k_s = \left(\frac{2\vartheta}{c_2 C_t \epsilon^{2/3}}\right)^{-1/(2\vartheta)} \left[E_{\rm mag}(t) + E_{{\rm mag},\nu}\right]^{-1/(2\vartheta)}, \tag{4.117}$$

$$k_f = \left(\frac{2\vartheta}{c_2 C_t \epsilon^{2/3}}\right)^{-1/(2\vartheta)} \left[E_{\rm mag,0} + E_{{\rm mag},\nu}\right]^{-1/(2\vartheta)}, \tag{4.118}$$

$$k_\nu = \left(\frac{2\vartheta}{c_2 C_t \epsilon^{2/3}}\right)^{-1/(2\vartheta)} E_{{\rm mag},\nu}^{-1/(2\vartheta)}. \tag{4.119}$$

Integrating equation (4.110) now yields the following:

$$\Gamma(t) = c_1 \left[\left(\frac{C_t \epsilon^{2/3}}{2-2\vartheta}\right)\left(k_s^{2-2\vartheta}(t) - k_f^{2-2\vartheta}\right)\right]^{1/2}. \tag{4.120}$$

Substituting equations (4.117)-(4.119) into (4.120) yields the expression

$$\begin{aligned}\Gamma(t) &= c_1 \left(\frac{C_t \epsilon^{2/3}}{2-2\vartheta}\right)^{1/2} \left(\frac{c_2 C_t \epsilon^{2/3}}{2\vartheta}\right)^{(1-\vartheta)/(2\vartheta)} \\ &\quad \times \left[\left(E_{\rm mag}(t) + E_{{\rm mag},\nu}\right)^{(\vartheta-1)/\vartheta} - \left(E_{\rm mag,0} + E_{{\rm mag},\nu}\right)^{(\vartheta-1)/\vartheta}\right]^{1/2}. \end{aligned} \tag{4.121}$$

Considering turbulence models between Kolmogorov and Burgers, we have $1/3 \leq \vartheta \leq 1/2$. We further assume that $E_{\rm mag}(t) \ll E_{\rm mag,0}$, implying that the magnetic field is far from saturation on the current amplification scale. In this case, we can neglect the second term in the square brackets. As we focus here on the non-linear regime, we can further neglect $E_{{\rm mag},\nu}$ compared to $E_{\rm mag}(t)$, and obtain the expression

$$\Gamma(t) = c_1 \left(\frac{C_t \epsilon^{2/3}}{2-2\vartheta}\right)^{1/2} \left(\frac{c_2 C_t \epsilon^{2/3}}{2\vartheta}\right)^{(1-\vartheta)/(2\vartheta)} W^{(\vartheta-1)/(2\vartheta)}(t). \tag{4.122}$$

As in our toy model, the growth of the magnetic energy thus scales as

$$\frac{\mathrm{d}}{\mathrm{d}t} W \approx E_{\rm mag}(t)\Gamma(t) \propto W^{(3\vartheta-1)/(2\vartheta)}. \tag{4.123}$$

For Kolmogorov turbulence, the growth is thus linear, while it grows faster than linear for $\vartheta > 1/3$. Integrating equation (4.123), we obtain

$$E_{\rm mag}(t) = \left(\tilde{C} t\right)^{2\vartheta/(1-\vartheta)}, \tag{4.124}$$

with

$$\tilde{C} = c_1 \left(\frac{C_t \epsilon^{2/3}}{2-2\vartheta}\right)^{1/2} \left(\frac{c_2 C_t \epsilon^{2/3}}{2\vartheta}\right)^{(1-\vartheta)/(2\vartheta)} \left(\frac{1-\vartheta}{2\vartheta}\right). \tag{4.125}$$

From this expression, we already see that the energy grows linearly in t for Kolmogorov, while it grows as t^2 for Burgers turbulence. For a physical interpretation, the normalization in terms of the eddy-turnover time T_{ed} on the forcing scale is still required, which we perform below.

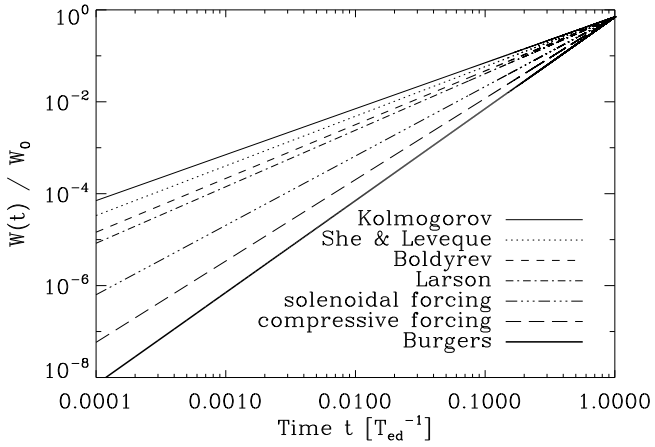

Figure 4.16:
The power-law growth of magnetic energy for different types of turbulence in the non-linear regime, following the evolution equation (4.129).
image credit: Schleicher et al. (2013)

4.3.3 Physical Implications of the Non-Linear Dynamo

To explore the physical implications of the above-mentioned results, we now perform a normalization in terms of the eddy-turnover time T_{ed} on the forcing scale k_f^{-1}. For this purpose, we note that the expression within the central brackets of equation (4.125) is identical to $E_{\mathrm{mag},\nu} k_\nu^{2\vartheta}$, and it is straightforward to show that

$$E_{\mathrm{mag},\nu} k_\nu^{2\vartheta} \approx E_{\mathrm{mag},0} k_f^{2\vartheta}. \tag{4.126}$$

If we normalize equation (4.124) in terms of $T_{ed} \approx (k_f \sqrt{E_{\mathrm{mag},0}})^{-1}$, we thus obtain

$$E_{\mathrm{mag}}(t) = \left(C \frac{t}{T_{ed}} \right)^{2\vartheta/(1-\vartheta)}, \tag{4.127}$$

$$C = c_1 E_{\mathrm{mag},0}^{(1-\vartheta)/(2\vartheta)} \left(\frac{\vartheta}{c_2(1-\vartheta)} \right)^{1/2} \left(\frac{1-\vartheta}{2\vartheta} \right). \tag{4.128}$$

Adopting a system of units with $E_{\mathrm{mag},0} = 1$ and $k_f = 1$, it is evident that $E_f \approx 1$, $v(k_f) \approx 1$ and thus $T_{ed} \approx 1$. We also assume $c_1 \approx 1$. From equation (4.113), we also expect $\epsilon \approx 1$. In these units, our evolution equations simplifies as

$$C = \frac{1}{2} \sqrt{\frac{1-\vartheta}{\vartheta}}. \tag{4.129}$$

We illustrate the behaviour for the different types of turbulence in Fig. 4.16 for $\mathrm{Re} = 10^4$, and summarize the power-law behaviour in Table 4.3. We thus obtain a steeper power-law growth for steeper turbulent spectra, implying that saturation can be reached in approximately the same time, in spite of the initially lower saturation level on smaller scales. The latter is fully consistent with our expectations for the kinematic regime, where the growth rates are higher for Kolmogorov turbulence, and a larger amount of magnetic energy may build up before the non-linear regime is reached (due to the increased amount of turbulent energy that is available on the

Model and reference	ϑ	$W \propto$	$\ell_a \propto$
Kolmogorov turbulence (Kolmogorov, 1941)	1/3	t^1	$t^{3/2}$
Intermittency of Kolmogorov turbulence (She & Leveque, 1994)	0.35	$t^{1.077}$	$t^{1.54}$
Driven supersonic MHD turbulence (Boldyrev et al., 2002)	0.37	$t^{1.17}$	$t^{1.59}$
Observation in molecular clouds (Larson, 1981)	0.38	$t^{1.23}$	$t^{1.61}$
Solenoidal forcing of turbulence (Federrath et al., 2010)	0.43	$t^{1.51}$	$t^{1.75}$
Compressive forcing of turbulence (Federrath et al., 2010)	0.47	$t^{1.77}$	$t^{1.89}$
Observation in molecular clouds (Ossenkopf & Mac Low, 2002)	0.47	$t^{1.77}$	$t^{1.89}$
Burgers turbulence (Burgers, 1948)	1/2	t^2	t^2

Table 4.3:
The power-law behavior of the small-scale dynamo for different types of turbulence in the non-linear regime taken from Schleicher et al. (2013)

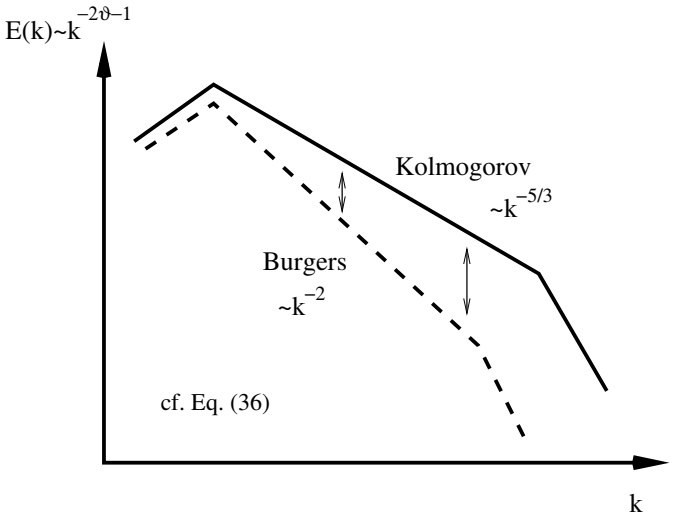

Figure 4.17:
A sketch of Kolmogorov vs. Burgers turbulence. While the turbulent energy is considerably smaller for Burgers spectra ($\vartheta = 1/2$) on small scales, it approaches the values for Kolmogorov turbulence ($\vartheta = 1/3$) on larger scales. As a result, the magnetic energy grows faster than linear for Burgers turbulence, as the growth rates gradually approach the Kolmogorov values at later times.
image credit: Schleicher et al. (2013)

same scale). We note that in the final stage close to saturation, the evolution may start to deviate from the power-law behavior reported here, providing a transition to the regime where $E_{\rm mag}(t) = \text{const}$.
From the relation derived above, we further calculate the characteristic scaling of the current amplification scale l_s as a function of time t. Adopting equation (4.99), we have $E_{\rm mag}(t) \approx \langle\rho\rangle u^2_{\ell_a(t)} \propto \ell_a^{2\vartheta}$, thus

$$\ell_a(t) \propto E_{\rm mag}^{1/(2\vartheta)}(t) \propto t^{1/(1-\vartheta)}. \tag{4.130}$$

For Kolmogorov turbulence, the characteristic length scale of the magnetic field thus grows as $t^{3/2}$, while it grows as t^2 for Burgers turbulence. The results are summarized for all types of turbulence in table 4.3.
The power-laws derived here depend on the type of turbulence due to the different eddy-turnover timescales as a function of scale, as we sketch in figure 4.17. We summarize the main ingredients based on the toy model developed in section 4.3.1:

Considering a driving scale L with a turbulence velocity V on that scale, the ratio of the eddy-turnover times on scale $l \ll L$ for Kolmogorov and Burgers turbulence is given as

$$\frac{t_K}{t_B} = \frac{(\ell/L)^{1-1/3}}{(\ell/L)^{1-1/2}} = \left(\frac{l}{L}\right)^{1/6}. \tag{4.131}$$

During the growth of the magnetic energy, the relevant length scale however shifts to larger scales. According to equation (4.131), the ratio of the eddy timescales approaches unity for $\ell \to L$. For Burgers turbulence, the magnetic field amplification is thus initially delayed with respect to Kolmogorov, and catches up later, resulting into the non-linear behaviour and the power-law growth described here.
Due to these results, it is clear that the growth rate of the dynamo is not a fixed fraction of the global turbulence dissipation rate, as previously proposed by Beresnyak

(2012). Due to the dependence on the turbulent spectrum, such a consideration may only hold locally, i.e. on a given scale, where the growth rate of the field is indeed related to the local eddy timescale. From a more global perspective, however, the turbulence dissipation rate changes as a function of scale for models different from Kolmogorov, such that the previously postulated universal behaviour cannot be expected. From equation (4.129), it is further evident that the evolution depends on the Reynolds number of the gas, and that larger Reynolds numbers imply stronger magnetic fields at earlier times.

4.4 Saturation of the Turbulent Dynamo

At some point the strength of the magnetic back reactions on the velocity field via the Lorentz force is comparable to the dynamo amplification. When this is the case on all scales of the system, the magnetic field amplification comes to an end, i.e. the turbulent dynamo is saturated.

4.4.1 Modification of the Magnetic Diffusivity for Strong Fields

Subramanian (1999) suggests a model for calculating the saturation energy density of the magnetic field, which is based on describing the change of the velocity field. In fact, he introduces an effective magnetic diffusivity

$$\eta_{\mathrm{sat}} = \eta + 2aM_{\mathrm{L}}(0,t), \tag{4.132}$$

where the parameter $a = \tau/(4\pi\rho)$ with τ being the response time of the system and ρ being the fluid density. With the effective diffusivity (4.132) one can, moreover, define an effective magnetic Reynolds number

$$\mathrm{Rm}_{\mathrm{sat}} = \frac{VL}{\eta + 2aM_{\mathrm{L}}(0,t)}, \tag{4.133}$$

which decreases with increasing magnetic energy density E_{mag}. For large E_{mag}, i.e. $\eta \ll 2aM_{\mathrm{L}}(0,t)$, this becomes

$$\mathrm{Rm}_{\mathrm{sat}} \approx \frac{VL}{2aM_{\mathrm{L}}(0,t)} = \frac{3VL}{16a\pi E_{\mathrm{mag}}}. \tag{4.134}$$

The decrease of $\mathrm{Rm}_{\mathrm{sat}}$ continues until the critical magnetic Reynolds number is reached and consequently the dynamo amplification stops. For $\mathrm{Rm}_{\mathrm{sat}} = \mathrm{Rm}_{\mathrm{crit}}$ saturation occurs and we find a final magnetic energy density of

$$E_{\mathrm{mag,sat}} \approx \frac{3}{2}\,\frac{1}{2}\rho V^2\,\frac{L/V}{\tau}\frac{1}{\mathrm{Rm}_{\mathrm{crit}}}. \tag{4.135}$$

The response time τ is a free parameter of the model, which should depend on the nature of turbulence.

4.4.2 Model for the Response Time

In the model for saturation described above a parameter τ enters, which will be estimated in this section. The timescale τ on which the fluid reacts to the magnetic field generated by the dynamo should be similar to the timescale of the turbulent eddies. As the eddy turnover time is different on different length scales, also the saturation process should be scale dependent.
We model here the response time on a scale ℓ as

$$\tau(\ell) = \frac{\ell}{v_\ell} = \frac{L^\vartheta}{V}\ell^{1-\vartheta}, \tag{4.136}$$

where we used equation (4.54) to find a dependency on the forcing length scale and velocity, L and V. We remind the reader that ϑ is the slope of the turbulence spectrum. The saturation energy on a scale ℓ is then given as

$$E_{\mathrm{mag,sat}}(\ell) \approx -\frac{3}{2}\,\frac{1}{2}\rho V^2\,\frac{L/V}{\tau(\ell)}\frac{1}{\mathrm{Rm}_{\mathrm{crit}}}, \tag{4.137}$$

where we have introduced a minus sign for resulting into a positive power spectrum.

4.4.3 Magnetic Field Spectrum at Saturation

The magnetic energy spectrum at saturation in our model of the scale-dependent response time (4.136) can be defined as

$$\epsilon_{\mathrm{mag,sat}}(\ell) = \frac{\mathrm{d}E_{\mathrm{mag,sat}}(\ell)}{\mathrm{d}\ell}. \tag{4.138}$$

When we compare this with the initial power spectrum of the turbulent kinetic energy

$$\epsilon_{\mathrm{kin},0}(\ell) = \frac{\mathrm{d}E_{\mathrm{kin},0}(\ell)}{\mathrm{d}\ell}, \tag{4.139}$$

with

$$E_{\mathrm{kin},0}(\ell) = \frac{1}{2}\rho v(\ell)^2 \tag{4.140}$$

we find a scale ℓ_{crit} for which $\epsilon_{\mathrm{mag,sat}}(\ell_{\mathrm{crit}}) > \epsilon_{\mathrm{kin},0}(\ell_{\mathrm{crit}})$. For scales $\ell < \ell_{\mathrm{crit}}$ the magnetic energy spectrum exceeds the turbulence spectrum, i.e. $\epsilon_{\mathrm{mag,sat}} > \epsilon_{\mathrm{kin},0}$. Comparison between the expressions (4.138) and (4.139) yields the critical scale

$$\ell_{\mathrm{crit}} = \left(\frac{3(1-\vartheta)}{4\vartheta \mathrm{Rm}_{\mathrm{crit}}}\right)^{1/(1+\vartheta)} L. \tag{4.141}$$

For the viscous scale $\ell_\nu > \ell_{\mathrm{crit}}$ the saturation value of the magnetic field decreases with scale ℓ according to equation (4.138) in the complete inertial range. For large hydrodynamical Reynolds numbers, however, the usual situation is $\ell_\nu < \ell_{\mathrm{crit}}$. Here

the response time at scales $\ell < \ell_{\rm crit}$ is very small, such that the term $2aM_{\rm L}(0,t)$ in equation (4.132) becomes insignificant compared to the normal magnetic diffusivity η. In order to ensure energy conservation in our model, we set (4.139) as an upper limit for the turbulence spectrum at saturation. The latter then takes the following form:

$$E_{\rm mag,sat}(\ell) = \begin{cases} \frac{1}{2}\rho v(\ell)^2 & , \ell_\nu < \ell \leq \ell_{\rm crit} \\ -\frac{3}{2}\,\frac{1}{2}\rho V^2\,\frac{L/V}{\tau(\ell)}\frac{1}{{\rm Rm}_{\rm crit}} & , \ell_{\rm crit} < \ell < L. \end{cases} \tag{4.142}$$

We note, that for small Reynolds numbers, which are for instance characteristic of turbulence simulations, the case $\ell_\nu > \ell_{\rm crit}$ can occur. Then we have to replace $\ell_{\rm crit}$ by ℓ_ν in equation (4.142), which means that we only have to integrate over $\epsilon_{\rm mag,sat}$ in the range $\ell_\nu < \ell < L$.
In the general case, the total magnetic energy at saturation on all scales is calculated in our model as

$$\begin{aligned} E_{\rm mag,sat} &= \int_{\ell_\nu}^{\ell_{\rm crit}} \epsilon_{\rm kin}(\ell)\ {\rm d}\ell + \int_{\ell_{\rm crit}}^{L} \epsilon_{\rm mag,sat}(\ell)\ {\rm d}\ell \\ &= E_{\rm kin,0}(\ell_{\rm crit}) - E_{\rm kin,0}(\ell_\nu) + E_{\rm mag,sat}(L) - E_{\rm mag,sat}(\ell_{\rm crit}) \\ &= \frac{1}{2}\rho V^2\left[\left(\frac{\ell_{\rm crit}}{L}\right)^{2\vartheta} - \left(\frac{\ell_\nu}{L}\right)^{2\vartheta} + \frac{3}{2}\,\frac{1}{{\rm Rm}_{\rm crit}}\left(\left(\frac{L}{\ell_{\rm crit}}\right)^{1-\vartheta} - 1\right)\right] \end{aligned} \tag{4.143}$$

In typical astrophysical environments the Reynolds numbers are very high, leading to a large separation between the viscous and the forcing scale, i.e. $\ell_\nu \ll L$. This means we can approximate (4.143) by

$$E_{\rm mag,sat} \approx \frac{1}{2}\rho V^2\left[\left(\frac{\ell_{\rm crit}}{L}\right)^{2\vartheta} + \frac{3}{2}\,\frac{1}{{\rm Rm}_{\rm crit}}\left(\left(\frac{L}{\ell_{\rm crit}}\right)^{1-\vartheta} - 1\right)\right] \tag{4.144}$$

The expression for the total magnetic energy at saturation derived above yields an important piece of information: The magnetic energy produced by a small-scale dynamo depends strongly on the critical magnetic Reynolds number, which determines also the onset of the dynamo in the first place.
The evolution of the magnetic energy spectrum is shown schematically in figure 4.18, where the gradient in blue colors represents different times. Initially, the field grows fastest on the viscous scale ℓ_ν in the kinematic dynamo phase. When saturation on ℓ_ν is reached, the peak of the spectrum moves to larger scales in the non-linear phase until saturation on the critical length scale $\ell_{\rm crit}$ occurs. Up to this scale, according to our model the turbulent kinetic energy is completely converted into magnetic energy. This is of course a simplified assumption, however, simulations show that the magnetic energy dominates the spectrum on small scales very soon after the onset of the dynamo (Brandenburg & Subramanian, 2005). For scales $\ell > \ell_{\rm crit}$ the saturation

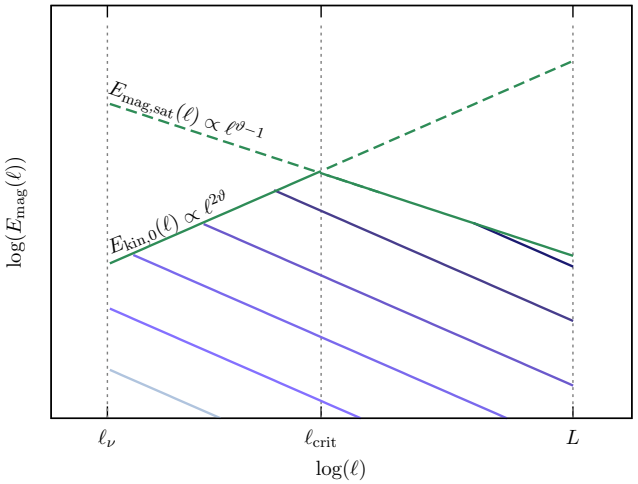

Figure 4.18:
The schematic spectrum of the magnetic energy $E_{\mathrm{mag}}(\ell)$ and its evolution in time. The gradient in blue color indicates the time evolution, from light blue for the initial spectrum to dark blue for the (almost) final saturation spectrum. The saturation values are limited by the kinetic energy of the turbulence E_{kin} up to a scale ℓ_{crit}. For $\ell > \ell_{\mathrm{crit}}$ the second green line $E_{\mathrm{mag,sat}}(\ell)$ indicates the upper limit of $E_{\mathrm{mag}}(\ell)$. Note, that the shape of the kinetic energy spectrum is expected also to change slightly with increasing magnetic energy due to back reaction on the fluid.

energy decreases again according to equation (4.138). Thus, the magnetic energy spectrum has a kink at the scale ℓ_{crit}. The field continues to increase by dynamo amplification on larger scales, but the saturation value decreases with ℓ. The whole dynamo process comes to an end, when the energy reaches the saturation value on the forcing scale L.

4.4.4 Turbulence Spectrum at Saturation

Under the assumption of constant forcing of turbulence and a constant flux of energy through the inertial range, the turbulent energy spectrum stays constant if there are no additional energy losses or gains. With a dynamo operating, a certain fraction of the kinetic energy is, however, converted into magnetic energy. As energy is conserved, the kinetic spectrum should change when the dynamo reaches saturation. The evolution of the kinetic energy spectrum, which we expect from our phenomenological model, is shown schematically in figure 4.19. The initial energy distribution scales as $E_{\mathrm{kin},0}(\ell) \propto \ell^{2\vartheta-1}$. With the dynamo converting turbulent energy into magnetic energy this spectrum decreases with $E_{\mathrm{kin}}(\ell) = E_{\mathrm{kin},0}(\ell) - E_{\mathrm{mag,sat}}(\ell)$, which is indicated by several blue lines. The time increases from light blue lines to dark blue lines. The kinetic energy decreases and, at the smallest scales of the inertial range, vanishes during dynamo saturation. For scales larger than ℓ_{crit} the magnetic energy at saturation is below the equipartition value. Thus for $\ell > \ell_{\mathrm{crit}}$ the kinetic energy dominates. The solid green line represents the turbulence spectrum, when the dynamo is saturated on all scales.

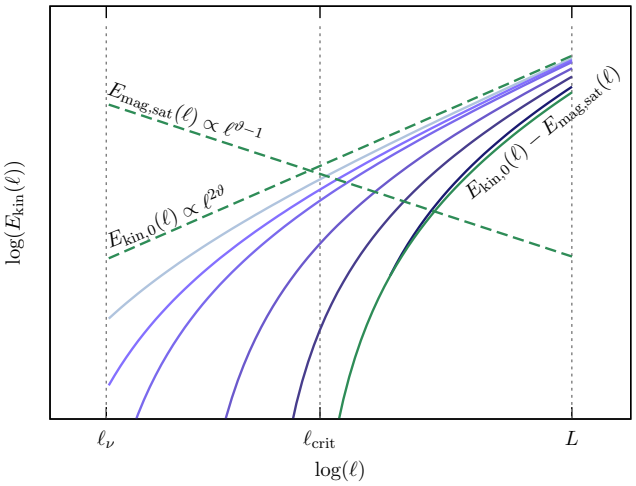

Figure 4.19:
The schematic spectrum of the kinetic energy $E_{\mathrm{kin}}(\ell)$ and its evolution in time. The time increases from the light blue lines to dark blue lines.

The integrated kinetic energy at dynamo saturation can then be calculated as

$$\begin{aligned} E_{\mathrm{kin,sat}} &= \int_L^{\ell_{\mathrm{crit}}} (\epsilon_{\mathrm{kin}}(\ell) - \epsilon_{\mathrm{mag,sat}}(\ell)) \ \mathrm{d}\ell \\ &= E_{\mathrm{kin}}(L) - E_{\mathrm{mag,sat}}(L) - E_{\mathrm{kin}}(\ell_{\mathrm{crit}}) - E_{\mathrm{mag,sat}}(\ell_{\mathrm{crit}}) \\ &= \frac{1}{2}\rho V^2 \left[1 - \left(\frac{\ell_{\mathrm{crit}}}{L} \right)^{2\vartheta} + \frac{3}{2} \frac{1}{\mathrm{Rm}_{\mathrm{crit}}} \left(\left(\frac{L}{\ell_{\mathrm{crit}}} \right)^{2\vartheta} - 1 \right) \right]. \end{aligned} \tag{4.145}$$

4.4.5 Energy Ratios

The most interesting quantities to calculate from our model are the ratio of the magnetic energy and kinetic energy at saturation

$$\mathcal{R}_1 = \frac{E_{\mathrm{mag,sat}}}{E_{\mathrm{kin,sat}}} \tag{4.146}$$

and the ratio of kinetic energy at saturation and initial kinetic energy

$$\mathcal{R}_2 = \frac{E_{\mathrm{kin,sat}}}{E_{\mathrm{kin},0}}. \tag{4.147}$$

The total initial turbulent energy is calculated from the integral over the initial turbulence power spectrum:

$$E_{\mathrm{kin},0} = \int_{\ell_\nu}^{L} \epsilon_{\mathrm{kin},0}(\ell) \ \mathrm{d}\ell = \frac{1}{2}\rho V^2 \left(1 - \left(\frac{\ell_\nu}{L} \right)^{2\vartheta} \right). \tag{4.148}$$

Both ratios, $\mathcal{R}_1$ and $\mathcal{R}_2$, include information about the efficiency of the turbulent dynamo. The ratio $\mathcal{R}_1$ tells us which fraction of energy equipartition can be reached, while the ratio $\mathcal{R}_2$ tells us how much of the initial turbulent energy is used for the

ϑ	$\mathrm{Rm}_{\mathrm{crit}}$	$\mathcal{R}_1$ ($\mathrm{Re} \to \infty$)	$\mathcal{R}_1$ ($\mathrm{Re} = 1500$)	$\mathcal{R}_2$ ($\mathrm{Re} \to \infty$)	$\mathcal{R}_2$ ($\mathrm{Re} = 1500$)
1/3	≈ 107	0.350	0.253	0.741	0.798
0.35	≈ 118	0.297	0.214	0.771	0.823
0.37	≈ 137	0.240	0.172	0.806	0.853
0.38	≈ 149	0.215	0.153	0.823	0.867
0.43	≈ 227	0.123	0.084	0.891	0.922
0.47	≈ 697	0.047	0.027	0.955	0.973
1/2	≈ 2718	0.016	0.005	0.985	0.994

Table 4.4:
Listed are the slopes of the turbulence spectrum ϑ for different types of turbulence (see the discussion in the text) and the corresponding critical magnetic Reynolds number $\mathrm{Rm}_{\mathrm{crit}}$ from (Schober et al., 2012c). For the different turbulence models we present the ratio of magnetic to turbulent energy at saturation $\mathcal{R}_1$ and the ratio of turbulent kinetic energy at saturation over the initial turbulent kinetic energy $\mathcal{R}_2$. Both quantities are given for $\mathrm{Re} \to \infty$ and $\mathrm{Re} = 1500$.

magnetic field amplification.
The resulting numerical values for $\mathcal{R}_1$ and $\mathcal{R}_2$ for a low Re and for the limit $\mathrm{Re} \to \infty$ are listed in table 4.4. We use here different types of turbulence, which have different critical magnetic Reynolds numbers $\mathrm{Rm}_{\mathrm{crit}}$. The slopes given in the table originate from the following works: incompressible turbulence (Kolmogorov, 1941, $\vartheta = 1/3$), observations of molecular clouds (Larson, 1981, $\vartheta \approx 0.38$), theoretical model of intermittency (She & Leveque, 1994, $\vartheta \approx 0.35$), simulations of supersonic magnetohydrodynamical turbulence (Boldyrev et al., 2002, $\vartheta \approx 0.37$), simulations with solenoidal (Federrath et al., 2010, $\vartheta \approx 0.43$) and compressive forcing (Federrath et al., 2010, $\vartheta \approx 0.47$), further molecular cloud oversations (Ossenkopf & Mac Low, 2002, $\vartheta \approx 0.47$) and Burgers turbulence (Burgers, 1948, $\vartheta = 1/2$).

4.4.6 Comparison with Numerical Simulations

The turbulent dynamo has also been studied in numerical simulations (Meneguzzi et al., 1981; Haugen et al., 2004a; Schekochihin et al., 2004, e.g.) yielding important results for comparison with analytical theory. Federrath et al. (2011) test the influence of different types of turbulent forcings on the small-scale dynamo. We will discuss their simulations in more detail in the next section. Here we refer to their

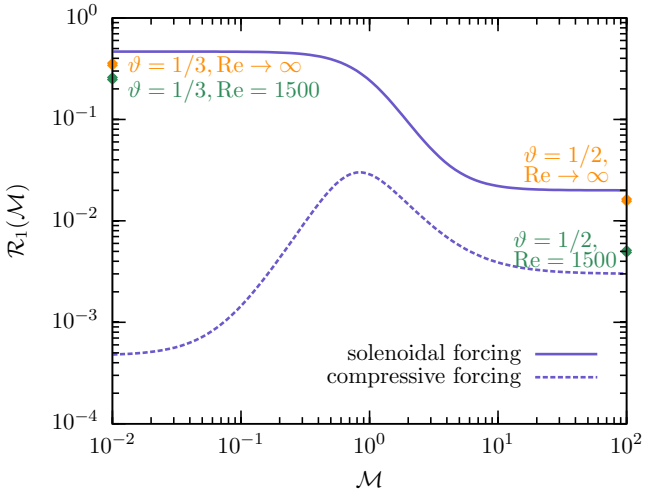

Figure 4.20:
The ratio of magnetic over kinetic energy $\mathcal{R}$ as a function of the Mach number M. The lines show fits to the data points measured in simulations of Federrath et al. (2011), where the solid line indicates solenoidal forcing and the dashed line compressive forcing. Also indicated by dots are the theoretically expected values of $\mathcal{R}$ for $\vartheta = 1/3$ and $\vartheta = 1/2$ and $\mathrm{Re} \to \infty$ and $\mathrm{Re} = 1500$.

results for the dynamo saturation level which, as they show, depends strongly on the turbulent forcing and the Mach number $\mathcal{M}$.
A fit to the ratio of magnetic over kinetic energy $\mathcal{R}_1$ measured by Federrath et al. (2011) is shown in figure 4.20. The value of $\mathcal{R}_1$ for solenoidal (divergence-free) exceeds the one of compressive (curl-free) forcing for all Mach numbers. This can be intuitively explained by the fact that the stretching, twisting and folding by the dynamo works better in divergence-free turbulence. The saturation level for soleniodal forcing is highest in the subsonic regime. For Mach numbers $\mathcal{M} > 1$ it decreases by a factor of more than 20 as here shocks become more and more dominant, leading to strongly compressible flows. The curve for compressive forcing behaves differently. In compressively driven turbulence the saturation level is very low, it peaks at $\mathcal{M} \approx 1$, where shocks appear, and seems to become constant in the highly supersonic regime.
The hydrodynamic Reynolds number in the simulations of Federrath et al. (2011) can be roughly estimated as $\mathrm{Re} \approx 1500$. For this value the critical length scale (4.141) is below the viscous scale ℓ_ν for high compressibility, which simplifies our equations and the saturation level can significantly differ from the one for $\mathrm{Re} \to \infty$. In general, we expect a slight dependence of $\mathcal{R}_1$ on Re, which should be investigated in future simulations. The resulting theoretical values of $\mathcal{R}_1$ and $\mathcal{R}_2$ for $\mathrm{Re} \approx 1500$ are listed in table 4.4. It is found that $\mathcal{R}_1$ for the large Re differs from the case of $\mathrm{Re} = 1500$ by a factor of 1.4 for Kolmogorov turbulence and by a factor of 3.2 for Burgers turbulence. We also indicate the theoretical values of $\mathcal{R}_1$ obtained from our model in figure 4.20. Here the solenoidal driven case is similar to Kolmogorov turbulence for very low Mach numbers, where there is a difference of roughly a factor 3 between theory and simulation. For Burgers turbulence, which is realized at very high Mach numbers, this difference is less than 4.
The differences between the numerical simulations and the theoretical are still tolerable, as we expect an error in the simulations of a factor of roughly 2. Also the determination of the hydrodynamical Reynolds number in simulations is difficult

and leaves some space for discussion. However, the trend of smaller saturation levels predicted from our theoretical model compared to the simulations, suggests that we might have overestimated the response time $\tau(\ell)$ in equation (4.136). The response from the magnetic field on the velocity fields seems to occur in a fraction of the eddy turnover time.
The mechanism of saturation of the dynamo in case of compressible forcing of the turbulence, especially in the subsonic regime, can not be predicted by our model. Here further analytical investigations are crucial for understanding the underlying physics.

4.5 The Small-Scale Dynamo in Numerical Simulations[8]

Besides with the analytical calculations, magnetic field amplification can be explored in numerical simulations. This approach has the advantage that it is not based on very simplified assumptions, which enter the theoretical model for example in the turbulence spectrum. On the other hand, in simulations, the power of the turbulent dynamo is not visible in full glory, as the scales, on which the fastest amplification takes place, are typically not resolved well.
In this section we concentrate on the simulations of Federrath et al. (2011). We describe the basic numerical methods and summarized their numerical results for the properties of the turbulent dynamo.

4.5.1 Dynamo Experiment in a Box - Numerical Setup

Federrath et al. (2011) perform numerical experiments with the grid-based magnetohydrodynamical code FLASH[9]. They solve the three-dimensional non-ideal MHD equations namely

$$\partial_t \rho + \nabla \cdot (\rho \mathbf{u}) = 0, \tag{4.149}$$

$$\partial_t (\rho \mathbf{u}) + \nabla \cdot \left[\rho \mathbf{u} \otimes \mathbf{u} + \left(p + \frac{1}{2} |\mathbf{B}|^2 \right) \mathbf{I}_3 - \mathbf{B} \otimes \mathbf{B} \right] = \rho \boldsymbol{\mathcal{F}}, \tag{4.150}$$

$$\partial_t \epsilon + \nabla \cdot \left[\left(\epsilon + p + \frac{1}{2} |\mathbf{B}|^2 \right) \mathbf{u} - (\mathbf{B} \cdot \mathbf{u}) \mathbf{B} \right] = 0, \tag{4.151}$$

$$\partial_t \mathbf{B} + \nabla \cdot (\mathbf{u} \otimes \mathbf{B} - \mathbf{B} \otimes \mathbf{u}) = 0, \tag{4.152}$$

$$\nabla \cdot \mathbf{B} = 0, \tag{4.153}$$

where $\mathbf{u}$ is the velocity, $p_\star = p + (1/2)|\mathbf{B}|^2$ is the total pressure with the thermal pressure $p = c_\mathrm{s}^2 \rho$ and $\epsilon = \rho e_\mathrm{int} + (1/2)\rho |\mathbf{u}|^2 + (1/2) |\mathbf{B}|^2$ is the total energy density. The turbulent forcing is included in $\boldsymbol{\mathcal{F}}$. Further, $\mathbf{I}_3$ is the 3×3 identity matrix, and

[8] This section follows closely Federrath et al. (2011).
[9] FLASH webpage: http://flash.uchicago.edu/site/flashcode/

$\otimes$ the dyadic product. Hydrodynamic diffusion is included via the traceless rate of strain tensor $S_{\rm ij} = (1/2)(\partial_{\rm i} u_{\rm j} + \partial_{\rm j} u_{\rm i}) - (1/3)\delta_{\rm ij}\nabla \cdot \mathbf{u}$ and via the kinematic viscosity ν. The magnetic diffusion is controlled by an explicit magnetic diffusivity η.
In their simulations Federrath et al. (2011) test the effect of different driving mechanisms of turbulence. For this purpose they model the forcing $\boldsymbol{\mathcal{F}}$ by an Ornstein-Uhlenbeck process (Schmidt et al., 2009; Federrath et al., 2010). In a box with the size L, $\boldsymbol{\mathcal{F}}$ has an autocorrelation time equal to the turnover time of turbulent eddies at the largest scales $t_{\rm ed} = L/(2\mathcal{M}c_{\rm s})$, where $\mathcal{M} = u_{\rm rms}/c_{\rm s}$ is the root-mean square Mach number. As turbulent forcing in astrophysical environments usually takes place on large scales, $\boldsymbol{\mathcal{F}}$ is modeled in Fourier space such that the kinetic energy is injected on the $1 < |\mathbf{k}|\, L/2\pi < 3$. The force field is decomposed into a solenoidal ($\mathcal{P}_{ij}^{\perp}$) and a compressive part ($\mathcal{P}_{ij}^{\parallel}$) by the projection operator

$$\mathcal{P}_{ij}^{\zeta}(\mathbf{k}) = \zeta\, \mathcal{P}_{ij}^{\perp} + (1-\zeta)\, \mathcal{P}_{ij}^{\parallel} = \zeta\, \delta_{ij} + (1-2\zeta)\, \frac{k_i k_j}{|k|^2}. \tag{4.154}$$

The free parameter ζ allows for applying a purely solenoidal force field with $\zeta = 1$, a purely compressive force field with $\zeta = 0$ and mixtures of both with $0 < \zeta < 1$. This way various types of turbulence can be realized.

4.5.2 Mach Number Dependence of the Growth Rate and the Saturation Level

With the numerical setup described above the dynamo amplification is tested for dependency on the Mach number $\mathcal{M}$ and the type of turbulent forcing.

Initial Conditions

The initial conditions of the simulation are motivated from previous studies of the small-scale dynamo in astrophysical environments. The initial velocity in the box with a size of $L = 1.24 \times 10^{19}$ cm is $\mathbf{u_0} = \mathbf{0}$, the initial density is $\rho_0 = 1.24 \times 10^{19}$ g cm^{-3} and the sound speed is $c_{\rm s} = 2 \times 10^4$ cm s^{-1}. The initial magnetic field is uniform and directed along the z-axes, e.g. $\mathbf{B} = (0, 0, B_{0,z})$ with a field strength of $B_{0,z} = 4.4 \times 10^{-16}$ G.

Results from the Simulations

After an initial transient phase that lasts for roughly $2\, t_{\rm ed}$, turbulence is fully developed and the Mach number reaches its present value, fluctuating on a 10% level. Figure 4.22 shows the time evolution of the Mach number in all runs. Note the drop in $\mathcal{M}$ for the solenoidally driven runs with $\mathcal{M} \lesssim 1$ as soon as the dynamo reaches saturation. For all subsonic, solenoidal runs the magnetic energy has increased to a dynamically significant level, causing the Mach number to drop. In contrast, all supersonic runs and all runs with compressive forcing have saturation levels significantly below 10%, such that the magnetic field has very little dynamical impact

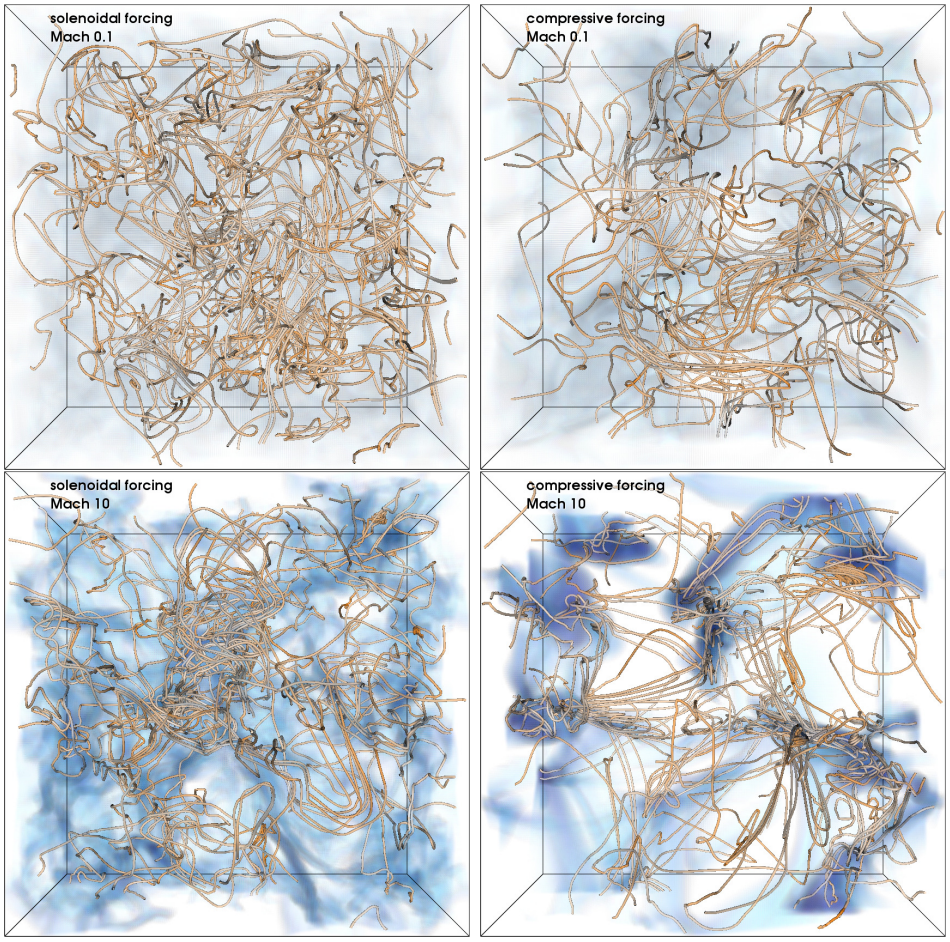

Figure 4.21:
Three-dimensional plots of the density on a logarithmic scale in the range $\rho = [0.5\rho_0, 50\rho_0]$, and magnetic field lines for solenoidal forcing (left) and compressive forcing (right) with $\mathcal{M} = 0.1$ (top), and $\mathcal{M} = 10$ (bottom). The stretch-twist-fold mechanism of the dynamo (Brandenburg & Subramanian, 2005) is evident in all models, but operates with different efficiency due to varying field geometries.
image credit: Federrath et al. (2011)

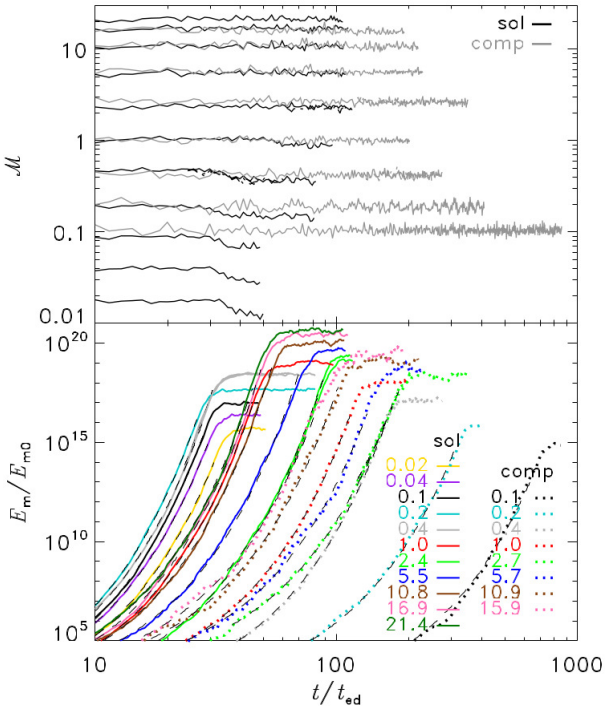

Figure 4.22:
Mach number $\mathcal{M}$ (top) and magnetic energy $E_{\rm mag}/E_{\rm mag,0}$ (bottom, here labeled as $E_{\rm m}/E_{\rm m,0}$) as a function of eddy-turnover time $t_{\rm ed}$ for all runs with solenoidal (sol) and compressive (comp) forcing. The Mach number is indicated in the legend. We also add non-ideal MHD models with $\mathcal{M} \approx 0.4, 2.5$ for solenoidal and compressive forcing, evolved on 2563, and 5123 grid cells. These models are hardly distinguishable from the corresponding ideal MHD models. Thin dashed lines show fits in the exponential growth phase.
image credit: Federrath et al. (2011)

on the turbulent flow, and hence the Mach number is unaffected. Although the dynamics of the flow are not strongly altered by the magnetic field in those cases, the fragmentation behavior of the gas might still be affected by the magnetic field (Hennebelle & Teyssier, 2008).

Figure 4.22 (bottom) shows that the magnetic energy grows exponentially over at least 10 orders of magnitude in each model and reaches saturation at different levels, which is discussed in detail below. First, the growth occurs only on small scales (small-scale dynamo). At later stages, i.e. close to saturation, the magnetic energy cascades to large scales, thus driving the amplification of the mean field component (large-scale dynamo) (Brandenburg & Subramanian, 2005).

Figure 4.21 shows that the high Mach number runs are dominated by shocks. Compressive forcing yields stronger density enhancements for similar Mach numbers. The magnetic field occupies large volume fractions with rather unfolded, straight field lines in the compressively driven cases, while solenoidal forcing produces more wound-up, tangled field configurations, suggesting that the dynamo is more efficiently excited by solenoidal forcing. This is quantitatively shown in figure 4.23, where we plot the growth rates, Γ, in the relation $E_{\rm mag} = E_{\rm mag,0}\exp(\Gamma t)$, and the saturation level, $(E_{\rm mag}/E_{\rm kin})_{\rm sat}$ with the magnetic and kinetic energies $E_{\rm mag}$ and $E_{\rm kin}$ as a function of Mach number. Both Γ and $(E_{\rm mag}/E_{\rm kin})_{\rm sat}$ depend on $\mathcal{M}$. Solenoidal forcing gives growth rates and saturation levels that are always higher than in compressive forcing, as indicted by the different field geometries shown in figure 4.21. Both Γ and $(E_{\rm mag}/E_{\rm kin})_{\rm sat}$ change significantly at the transition from subsonic to supersonic turbulence.

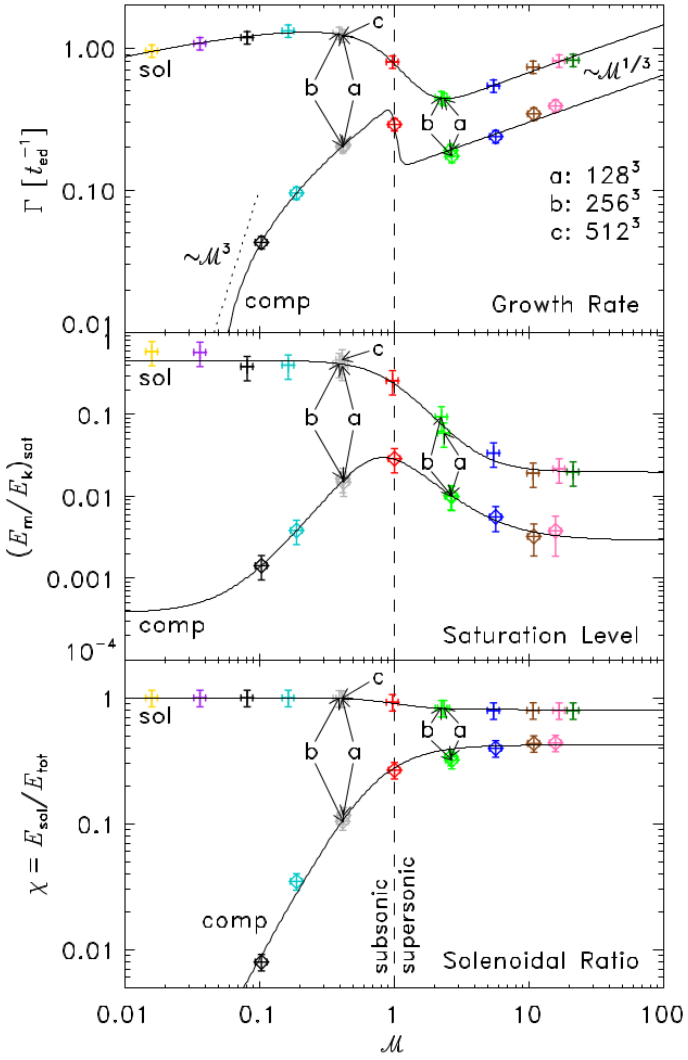

Figure 4.23:
Growth rate (top), saturation level (middle, here labeled as $(E_m/E_k)_{sat}$), and solenoidal ratio (bottom) as a function of Mach number, for all runs with solenoidal (crosses) and compressive forcing (diamonds). The solid lines show empirical fits with equation (4.155); see table 4.5. The arrows indicate four models ($\mathcal{M} \approx 0.4, 2.5$ for solenoidal and compressive forcing), using ideal MHD on 1283 grid cells (a), non-ideal MHD on 2563 (b), and 5123 grid cells (c), demonstrating convergence for the given magnetic Prandtl, Pm ≈ 2, and kinematic Reynolds number, Re ≈ 1500.
image credit: Federrath et al. (2011)

	$\Gamma\ [t_{\rm ed}^{-1}]$		$(E_{\rm mag}/E_{\rm kin})_{\rm sat}$		$(E_{\rm sol}/E_{\rm tot})$	
	(sol)	(comp)	(sol)	(comp)	(sol)	(comp)
p_0	-18.84	2.251	0.020	0.037	0.808	0.423
p_1	0.051	0.119	2.340	1.982	2.850	1.970
p_2	-1.059	-0.802	23.33	-0.027	1.238	0
p_3	2.921	25.53	2.340	3.601	2.850	1.970
p_4	1.350	1.686	1	0.395	1	0.535
p_5	0.313	0.139	0	0.003	0	0
p_6	1/3	1/3	0	0	0	0

Table 4.5:
Parameters in equation (4.155) for the fits in figure 4.23 as given in Federrath et al. (2011).

Discussion and Interpretation of the Results

We conclude that the development of shocks at $\mathcal{M} \approx 1$ is responsible for destroying some of the coherent vortical motions necessary to drive the dynamo (see also Haugen et al., 2004b). However, as $\mathcal{M}$ is increased further, vorticity generation in oblique, colliding shocks starts to dominate over the destruction. The very small growth rates of the subsonic, compressively driven models is due to the fact that hardly any solenoidal modes are excited in those cases, because of the absence of colliding, oblique shock fronts. The only way to introduce vorticity in this case is via viscous interactions and by the non-linear term in the vorticity equation in the absence of the baroclinic term (Moss & Shukurov, 1996; Mee & Brandenburg, 2006). This however, is such a slow process that dynamo action drops quickly with decreasing Mach number in compressively driven flows. Analytic estimates suggest that $\Gamma \propto \mathcal{M}^3$ for $\mathcal{M} \lesssim 1$ in compressively driven, acoustic turbulence (Moss & Shukurov, 1996)[10], indicated as dotted line in figure 4.23. The solid lines are fits with an empirical model function,

$$f(x) = \left(p_0 \, \frac{x^{p_1} + p_2}{x^{p_3} + p_4} + p_5 \right) x^{p_6}. \tag{4.155}$$

The fit parameters are given in table 4.5. We emphasize that the fits are empirical and do not necessarily reflect the true asymptotic behavior of Γ and $(E_{\rm mag}/E_{\rm kin})_{\rm sat}$. For the growth rate, we fixed p_6 such that $\Gamma \propto \mathcal{M}^{1/3}$ for $\mathcal{M} \gg 1$, in good agreement with our simulation data up to $\mathcal{M} \approx 20$. Even higher Mach numbers have to be investigated to see if $\Gamma \propto \mathcal{M}^{1/3}$ holds in this limit. For the saturation level, it

[10]Note that we define $t_{\rm ed} = L/(2\mathcal{M}c_{\rm s})$, while in Moss & Shukurov (1996), $t_{\rm ed} = L/(2c_{\rm s})$, differing by a factor $\mathcal{M}$.

is reasonable to assume that $(E_{\rm mag}/E_{\rm kin})_{\rm sat}$ approaches constants for $\mathcal{M} \ll 1$ and $\mathcal{M} \gg 1$, however, the physical saturation levels in these limits are quite uncertain and depend slightly on the Reynolds numbers (see Haugen et al., 2004a, and section 4.4). The subsonic, solenoidally driven models show high saturation levels, $(E_{\rm mag}/E_{\rm kin})_{\rm sat} \approx 40$–$60\%$, explaining the strong back reaction of the field on the flow, causing the Mach number to drop in the saturation regime (see figure 4.22). Federrath et al. (2011) find that Γ depends much less on $\mathcal{M}$ in the solenoidal forcing case than in the compressive one. Nevertheless, a drop at $\mathcal{M} \approx 1$ is noticeable in both cases. In contrast, theory predicts no dependence of Γ on $\mathcal{M}$.
We can compare the results from Federrath et al. (2011) with other high-resolution numerical simulations of the turbulent dynamo. As discussed above the extreme ways of driving turbulence are solenoidal and compressive forcing. Simulations typically show, in agreement with our analytical study, that solenoidally driven turbulence leads to larger growth rates of the small-scale dynamo. For example Waagan et al. (2011) find, using a Reynolds number of about 1500[11], and a magnetic Prandtl number of about 1, for totally solenoidal forcing of the turbulence $\bar{\Gamma}^{\rm sol} = 0.60$ and for totally compressive forcing $\bar{\Gamma}^{\rm comp} = 0.28$. These values of the growth rate are about a factor of 17 lower than those from our model (with Re = 1500), $\bar{\Gamma}^{\rm sol} = \bar{\Gamma}^{\vartheta=0.43} \approx 10.07$ and $\bar{\Gamma}^{\rm comp} = \bar{\Gamma}^{\vartheta=0.47} \approx 4.73$. This can be explained by the fact that the simulations have a very low magnetic Prandtl number of about 1. However, the result for the growth rate given in the third column of table 4.1 was derived under the assumption of infinite Prandtl numbers. Still the trend is that the growth rate decreases for lower Prandtl numbers, which can explain the lower growth rates from the simulations. Yet the ratio of the growth rate of turbulence driven by solenoidal and compressive forcing is in both cases about 2 (our analytical model: $\bar{\Gamma}^{\rm sol}/\bar{\Gamma}^{\rm comp} \approx 2.1$; Waagan et al. (2011): $\bar{\Gamma}^{\rm sol}/\bar{\Gamma}^{\rm comp} \approx 2.1$), which supports the analytical prediction that incompressible turbulence is more efficient in amplifying a magnetic field via the small-scale dynamo.

4.5.3 Critical Magnetic Reynolds Number

Recent high-resolution numerical studies confirm the existence of a critical magnetic Reynolds number for small-scale dynamo action. Haugen et al. (2004a) find $\mathrm{Rm}_{\rm crit} \approx 35$ for subsonic turbulence and $\mathrm{Rm}_{\rm crit} \approx 70$ for supersonic turbulence at a magnetic Prandtl number of about unity. In numerical simulations, the magnetic Reynolds number can be estimated by $\mathrm{Rm} \approx (\lambda/\ell_\nu)^{\vartheta+1}$, where λ is the typical size of turbulent structures and ℓ_ν is the viscous scale of turbulence. The latter can be estimated by $\ell_\nu \approx 0.5\ \Delta x$ with Δx the minimal resolved size in a simulation (Benzi et al., 2008). In resolution studies, Sur et al. (2010) and Federrath et al. (2011) find that the typical length of a turbulent fluctuation needs to be resolved with at least 30 grid cells in magnetohydrodynamic simulations of a self-gravitating gas. Only then the

[11] Waagan et al. (2011) gave a magnetic Reynolds number of about 200. However, these ideal MHD simulations were later calibrated with resistive non-ideal MHD-simulations in reference (Federrath et al., 2011), showing that the Reynolds number is about 1500.

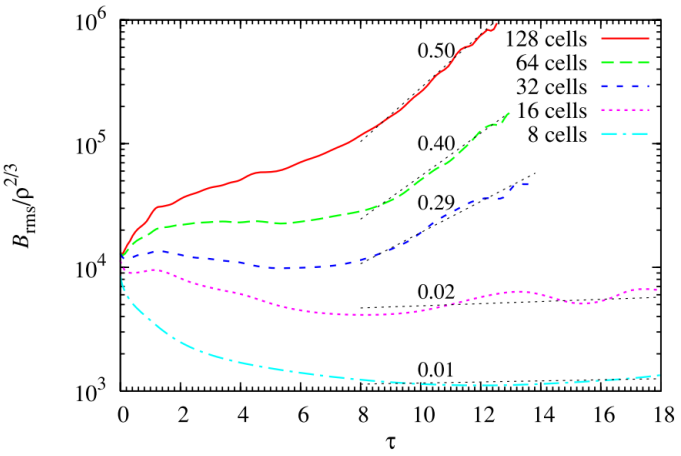

Figure 4.24:
The resolution criterion for small-scale dynamo action in numerical simulations. A resolution of at least 32 cells per Jeans length is necessary to see turbulent magnetic field amplification.
image credit: Federrath et al. (2011)

magnetic field is amplified exponentially, which is explained by the action of a small-scale dynamo. The time evolution of the magnetic field strength found by Federrath et al. (2011) is shown in figure 4.24. Note, that the field strength is divided by a factor $\rho^{2/3}$, which gives the increase of the magnetic field strength in spherical collapse (see section 3.3.2). Thus the presented curves show the pure turbulent dynamo amplification. An increase of the field strength is only found for runs with at least 32 cells per Jeans length.
For a physical interpretation of this result it is useful to take the stretch-twist-fold-dynamo as a toy-model of the turbulent dynamo (see subsection 3.4). This process works best in a purely rotational turbulent velocity field. Therefore, we expect the dynamo to be more easily excited in Kolmogorov turbulence. In order to see this process in simulations, one needs to resolve the stretching, twisting, and folding of the field lines, which explains the required high resolution.

4.6 The Main Theoretical Results for the Turbulent Dynamo

In this chapter we sketch a mathematical description of turbulence via the two-point correlation function. We model this function in the different regimes of the turbulence spectrum, the dissipation range, the inertial range and the large-scale forcing range. Our model is based on the slope of the fluctuating velocity in the inertial range ϑ. For this we assume that the turbulent velocity on a length scale ℓ is

$$v(\ell) \propto \ell^{\vartheta}. \tag{4.156}$$

We use our model for the turbulent velocity field as an input for the dynamo evolution equations. The basics of the Kazantsev theory, which describes the time evolution of the random magnetic field, are summarized. We generalize the Kazantsev equation (4.41) for different types of turbulence, which distinguish in their spectral

slope within the inertial range.
By solving the Kazantsev equation for a vanishing growth rate, we find a critical magnetic Reynolds number $\mathrm{Rm}_{\mathrm{crit}}$, which needs to be exceeded for small-scale dynamo action. The numerical value of $\mathrm{Rm}_{\mathrm{crit}}$ depends on the type of turbulence and ranges from ≈ 100 for Kolomogorov turbulence to ≈ 2700 for Burgers turbulence. We list the results for various slopes of the turbulence spectrum in table 4.1.
A central result from the Kazantsev theory is that the magnetic field strength grows exponentially in the kinematic phase:

$$B(t) = B_0 \exp(\Gamma t). \tag{4.157}$$

With our turbulence model, we found analytical solutions for the growth rate in the limit of large and small magnetic Prandtl numbers Pm:

$$\Gamma = \begin{cases} \dfrac{163 - 304\vartheta}{60} \dfrac{V}{L} \mathrm{Re}^{(1-\vartheta)/(1+\vartheta)} & \text{for } \mathrm{Pm} \gg 1 \\ \alpha \dfrac{V}{L} \mathrm{Rm}^{(1-\vartheta)/(1+\vartheta)} & \text{for } \mathrm{Pm} \ll 1 \end{cases} \tag{4.158}$$

with $\alpha \approx 0.027 - 0.0054$ depending on the slope of the turbulence spectrum ϑ. We refer to table 4.1, in which the growth rates for different types of turbulence are listed. These analytical results are reproduced the limits of large and small Pm by a numerical solution of the Kazantsev equation from Bovino et al. (2013) (see figure 4.13).
In the subsequent non-linear phase back reactions from the magnetic field on the velocity field become significant. Under the assumption that the magnetic energy is shifted towards larger scales on the local eddy timescale Schleicher et al. (2013) find that the magnetic field strength increases in this phase as

$$B(t) = (8\pi)^{1/2} (\tilde{C} t)^{\vartheta/(1-\vartheta)} \tag{4.159}$$

with the paramter $\tilde{C}$ given in equation (4.125).
When the magnetic energy reaches a certain fraction of the turbulent kinetic energy, saturation occurs. This can be modeled via an artificial drift in the velocity field, which leads to an increase of the resistivity η and likewise an decrease of the magnetic Reynolds numbers Rm. With a model that assumes the velocity to react to the magnetic field on a timescale comparable to the scale-dependent eddy timescale, we calculate the efficiency of the dynamo. For a large Reynolds number the fraction of magnetic energy to kinetic energy at saturation is ≈ 0.4 for Kolmogorov turbulence and ≈ 0.01 for Burgers turbulence.
The results of various numerical simulations have been discussed, with a focus on the work of Federrath et al. (2011). A typical observation that is made in simulations is that the small-scale dynamo amplification only takes place above a resolution of 32 cells per Jeans length. This criterion can be associated with the critical magnetic Reynolds number. The exponential growth of the field strength is confirmed in simulations, where the growth rates are lower for higher compressibility of the fluid. The saturation level of the turbulent dynamo is a function of the Mach number (see figure 4.23).

CHAPTER 5

The Turbulent Dynamo as the Most Important Magnetic Field Amplification Mechanism in the Early Universe

In this chapter we give short summary of the history of the Universe, which is nicely illustrated in figure 5.1, with a focus on the era of structure formation. In this epoch the dark ages end and the first stars and galaxies reionize the Universe and enrich it with heavy chemical elements. When these objects, which form in the centers of dark matter mini halos, accrete matter, turbulence is driven very efficiently. Supernova explosions of the first stars lead to further turbulent mixing of the primordial gas. With the onset of turbulence, the small-scale dynamo can for the first time efficiently amplify the previously generated magnetic seed fields up to dynamically important field strengths. This makes primordial star formation an important era in cosmic magnetogenesis.

5.1 Evolution of the Universe

5.1.1 From the Big Bang to the Dark Ages

Before the first stars formed the Universe was dark, expect for the cosmic microwave radiation (CMB). We summarize the cosmic evolution before the birth of stars in the following. See, for example, Liddle (2003) for an introductory cosmology textbook.

The Very Early Universe

The standard model of cosmology, i.e. the Λ Cold Dark Matter (ΛCDM) model, predicts that the Universe emerged from a singularity, the so-called *Big Bang*, roughly

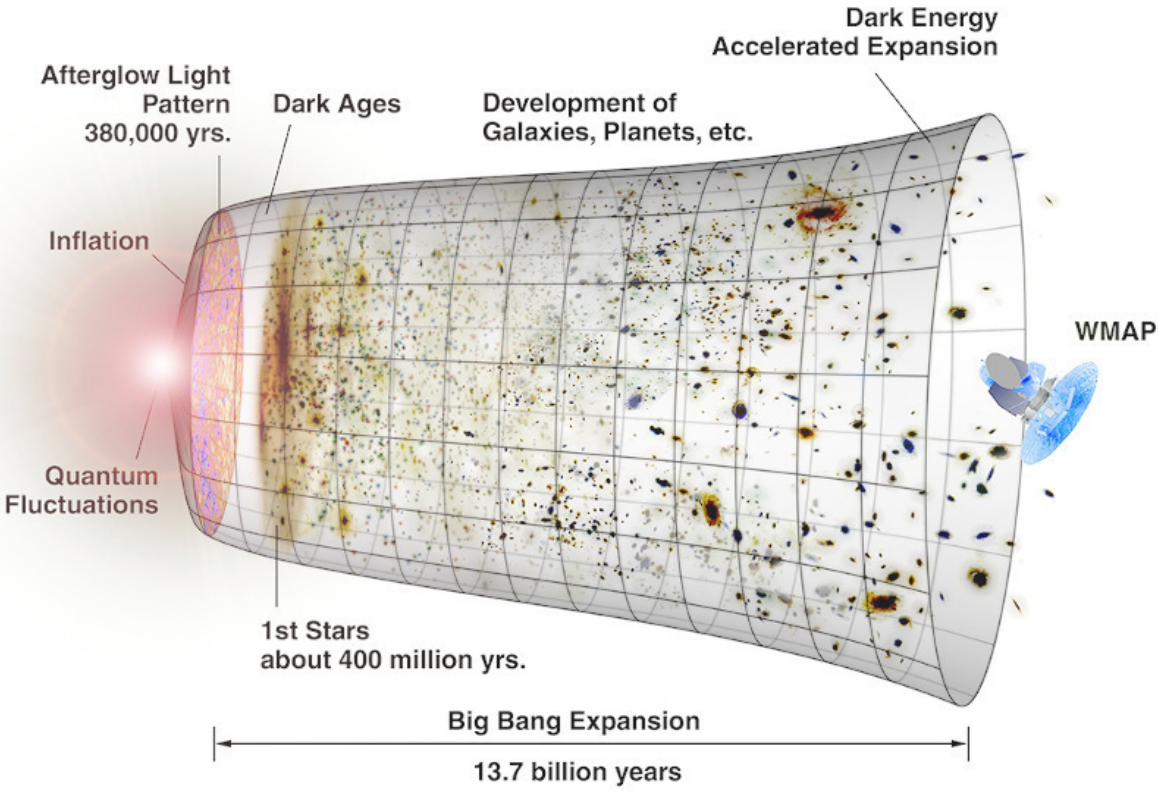

Figure 5.1:
The schematic evolution of the Universe from the Big Bang to present day.
image credit: http://www.wpclipart.com/space/stars_universe/universe_timeline_light.jpg.html

13.8 Gyr ago (Planck Collaboration et al., 2013b) and expands ever since. In the initial Planck epoch the temperature is so high that no matter particles exist and all four fundamental forces, the electromagnetic force, the weak and the strong force, and gravity, were combined in one unified force. The physics at these high energies is poorly understood, since we do not have a satisfying theory of quantum gravity at present. As the temperature decreases with the expansion of space, gravity separates at approximately $t = 10^{-43}$ s. The era in which all forces but gravity are unified is described by a *Grand Unified Theory* (GUT) and characterized by energies of the order of 10^{15} GeV. The GUT era ends at $t \approx 10^{-36}$ s, when the strong force separates.
From $t \approx 10^{-36}$ s to $t \approx 10^{-32}$ s probably *inflation* takes place, a phase of rapid exponential expansion, in which the scale factor of the Universe increases exponentially by a factor of roughly 10^{30}. This concept was originally suggested by (Guth, 1981) as a solution for the flatness and the horizon problem of cosmology[1]. During inflation small quantum fluctuations are blown up to cosmological scales. These density inhomogeneities are the seeds of structure formation, and the birth places of the first stars and galaxies (Hawking, 1982).
The extremely high potential energy released from the inflaton field goes into a hot dense mixture of quarks, antiquarks and gluons. The following epoch is the *electroweak era*, in which the weak and the electromagnetic force are still combined. The Universe is extremely hot with temperatures of the order of 10^{15} K and cools down adiabatically with the expansion. The high temperatures lead to the creation of W and Z bosons in energetic particle collisions until the temperature decreases to a critical value, below which no new particles are created and the W and Z bosons decay. The separation of the weak and the electromagnetic force marks the end of the electroweak phase. From $t \approx 10^{-12}$ s to $t \approx 10^{-6}$ s the temperature is still too high for quarks to combine into mesons and baryons. In this so-called *quark era* the Universe consists of a quark-gluon plasma. Eventually, the energy falls below the binding energy of quarks and they get confined into hadrons. In the initial stage of this *hadron era*, hadron-antihadron pairs are constantly created and annihilated. The matter is in thermal equilibrium with antimatter. At some point the temperature is too low to create hadron-antihadron pairs and matter and antimatter annihilates. An asymmetry, the origin of which is not satisfactorily understood, results in the predominance of matter over antimatter at present day. Roughly 1 s after the Big Bang the *lepton era* begins, in which the mass of the Universe is dominated by leptons. Lepton-antilepton pairs are created until the temperature falls below a certain point and the leptons only annihilate.
The Universe enters now the *radiation-dominated era* with most of the energy being stored in photons. These are interacting frequently with charged protons, electrons

[1]The flatness problem refers to the observations which find the Universe to be extremely flat, while the horizon problem rises from the fact, that the Universe seems to be extremely homogeneous over scales much larger than the cosmological horizon. These observational facts are found for example in WMAP data (Komatsu et al., 2009) and were recently confirmed in the *Planck* data (Planck Collaboration et al., 2013b).

and nuclei until recombination (see the next paragraph). In the radiation-dominated era the Big Bang nucleosynthesis takes place once the temperature falls below the point where protons and neutrons can be confined in nuclei. In nuclear fusion deuterium, helium and traces of other nuclei are formed. 70000 yrs after the Big Bang the density of non-relativistic matter, i.e. atoms, exceeds the one of photons and the Universe enters the *matter-dominated era*. In this era, small density perturbations are no longer wiped out by radiation and start to grow due to the Jeans instability.

Recombination and the Emergence of the Cosmic Microwave Background

Approximately 380000 yrs after the Big Bang, at a redshift of 1100, the Universe has cooled down to a temperature of roughly 4000 K. At this temperature the hydrogen ions recombine with the electrons and form neutral atoms[2]. As the photons were interacting with the gas by scattering with free electrons, at this point the photon gas decouples from matter and cools down with the further expansion of the Universe. This radiation field is called the *cosmic microwave background* (CMB) and has cooled down to a temperature of 2.7 K at present day. Except for the photons of the CMB, which dilute more and more with cosmic expansion, the Universe is for now dark. This epoch, which ended with the emergence of the first stars, is referred to as the *dark ages*.

Growth of the Dark Matter Halos

Even though the CMB is extremely uniform, it includes tiny spatial fluctuations of the order of 10^{-5}. These fluctuations grow due to gravitational instability and eventually form galaxies and the large-scale structure of the Universe (see, e.g. Barkana & Loeb, 2000).
The cosmic expansion can be modeled as an ideal pressureless fluid, which expands with the Hubble flow $\boldsymbol{v} = H(t)\boldsymbol{r}$, where $H(t) \equiv \dot{a(t)}/a(t)$ is the Hubble constant. Note that we refer in this section to $\boldsymbol{r}$ as the fixed coordinate and to $\boldsymbol{x} \equiv \boldsymbol{r}/a(t)$ as the comoving coordinate with the scale factor $a(t)$. The density perturbations are given by the function

$$\delta(\boldsymbol{x}) = \frac{\rho - \bar{\rho}}{\bar{\rho}}, \tag{5.1}$$

where ρ is the mass density and $\bar{\rho}$ its mean value. The evolution of the density fluctuations is given by the pressureless fluid equations. In the comoving framework

[2]Note, that according to the equation 13.6 eV $= kT$, we would expect hydrogen to recombine at a temperature of $T \approx 10^5$ K. The large fraction of the gas, however, recombines at significantly lower temperatures. This can be explained by the Boltzmann distribution of the atoms, which keeps many particles at higher energies then the mean energy.

the continuity and the Euler equation are given as

$$\begin{aligned} \frac{\partial \delta}{\partial t} + \frac{1}{a}\nabla \cdot [(1+\delta)\boldsymbol{u}] &= 0 \\ \frac{\partial \boldsymbol{u}}{\partial t} + H\boldsymbol{u} + \frac{1}{a}(\boldsymbol{u}\cdot\nabla)\,\boldsymbol{u} &= -\frac{1}{a}\nabla\Phi. \end{aligned} \tag{5.2}$$

The potential ϕ is governed by the Poisson equation $\nabla^2\phi = 4\pi G\bar{\rho}a^2\delta$. The fluid equations can be linearized for small perturbations $\delta \ll 1$, which results in an evolution equation for the fluctuations:

$$\frac{\partial^2\delta}{\partial t^2} + 2H\frac{\partial\delta}{\partial t} = 4\pi G\bar{\rho}\delta. \tag{5.3}$$

In case of a Universe that is matter-dominated the scaling factor evolves as $a(t) \propto t^{2/3}$. The solution of (5.3) is then given by $\delta(t) = c_1\ t^{2/3} + c_2\ t^{-1}$, where c_1 and c_2 are constants. Thus, there is a growing mode and a decaying mode, while only the first one is important for structure formation.
When the fluctuations reach $\delta \approx 1$[3] the linear perturbation theory is no longer applicable and the non-linear equations need to be solved. One needs to use the full Newtonian theory to describe the non-linear evolution of structure. This can be done analytically with certain approximations, for example with the Press-Schechter mechanism (Press & Schechter, 1974). A common approach to describe the non-linear structure formation is, however, to employ N-body simulations. These simulations are in principle very simple, but become very complicated due to the large number of particles. Springel et al. (2005) find in their *Millennium Simulation* that the present-day large-scale structure is characterized by voids and filaments connecting dense nodes, a structure that is known as the *cosmic web*. This fits perfectly to findings of large surveys such as the *2 degree Field Galaxy Redshift Survey* (2dFGRS) (Colless et al., 2001) and the *Sloan Digital Sky Survey* (SDSS) (Tegmark et al., 2004).

5.1.2 The Birth of the First Stars

The formation of the first stars marks an important transition in the Universe. The dark ages come to an end, the stellar radiation reionizes the baryonic gas and the medium is enriched with heavy chemical elements. We summarize here the current knowledge about primordial star formation. For a recent review on this topic we refer to Bromm (2013).

Dark Matter Minihalos

As discussed above, inflation increases microscopic quantum fluctuations up to cosmological scales, leading to large-scale spacial inhomogeneities. In regions with a

[3]For a comparison, the density fluctuations for galaxy clusters are of the order of $\delta = 10^3$, while they reach values of $\delta \approx 10^6$ for galaxies.

density that is enhanced compared to the mean density, gravity can increase these perturbations further. Eventually gravity dominates and decouples the region from the general Hubble flow of the background Universe. For a spherically symmetric perturbation in Einstein-de Sitter cosmology, the critical overdensity for gravitational collapse is roughly $\delta_{\mathrm{crit}} = 1.686$. The region then begins to collapse and a dark matter mini-halo forms. Collapse continues until a virial equilibrium is reached, where the virial density is larger than the background density by a factor of roughly 200 (Loeb, 2010).

Formation of the First Stars

Compared to star formation at present day, primordial star formation is at first sight a relatively simple and well defined problem. The reason for that is that the initial conditions can be directly inferred from the ΛCDM cosmology. The current standard model of cosmology includes the physics of gravity, of atomic and molecular hydrogen and helium and the particle physics of cold dark matter.
The birth places of the first stars are dark matter minihalos, which accrete baryonic gas. Due to adiabatic compression and shock heating the temperature of this gas increases to values of the order of 10^3 K at $z = 20$. This temperature is below the threshold of atomic hydrogen cooling, which is approximately 10^4 K. Cooling of the gas thus has to proceed via molecular hydrogen cooling, which makes it important to model the formation and destruction of H_2 carefully (Glover & Abel, 2008). Interestingly, it turns out that the fraction of H_2 increases with increasing virial temperature, thus only very hot halos can form sufficient H_2 to cool. If we now assume that stars do only form, when the cooling timescale is shorter than the dynamical timescale of the halo (Rees & Ostriker, 1977; Silk, 1977), we find a minimum halo mass of $10^6\ M_\odot$ for further collapse in a redshift regime $z \approx 20 - 30$. The collapse of a primordial gas cloud proceeds in distinct phases. First, the gas is heated adiabatically up to a density of $n = 1\ \mathrm{cm}^{-3}$, where the temperature reaches $T = 10^3$ K. While the gas at these densities is still mostly atomic, the small fraction of H_2 leads to cooling via rotational and vibrational modes. Thus the temperature decreases down to $T = 200$ K at a density of $n = 10^4\ \mathrm{cm}^{-3}$, above which the molecular cooling becomes less efficient and a quasi-hydrodynamical core forms, also refereed to as the *loitering state* (Bromm et al., 2002). In the subsequent collapse the temperature rises again due to compressional heating. At a particle density of roughly $n = 10^8\ \mathrm{cm}^{-3}$ H_2 can form efficiently in three-body reactions

$$\begin{aligned} \mathrm{H} + \mathrm{H} + \mathrm{H} &\rightarrow \mathrm{H}_2 + \mathrm{H} \\ \mathrm{H} + \mathrm{H} + \mathrm{H}_2 &\rightarrow \mathrm{H}_2 + \mathrm{H}_2. \end{aligned} \tag{5.4}$$

The gas becomes fully molecular at densities of $n = 10^{12}\ \mathrm{cm}^{-3}$. This leads to a sudden increase of the cooling rate. However, there is no net decrease of the temperature, as in the molecule formation binding energy is released. The consequence is a nearly isothermal collapse at a temperature of $T \approx 10^3$ K in addition to a softening of the equation of state induced by the additional degrees of freedom in the

molecules. With increasing density the ro-vibrational lines of H_2 become more and more optically thick and the temperature rises in the proceeding collapse.
The high temperatures during the collapse of a primordial gas cloud result in very high accretion rates, which in turn lead to the obsolete conclusion that the first stars were extremely massive with more than 100 $M_\odot$. Recent high resolution simulations paint, however, a different picture (Stacy et al., 2010; Clark et al., 2011; Greif et al., 2011, 2012). While it has been shown that the initial infall proceeds mostly spherically and a hydrostatic core builds up in the center, the material that falls in at later stages has non-negligible angular momentum. This gas does not fall on the core directly, but instead builds up a rotationally supported disk. The high-resolution simulations show further, that the disk fragments and instead of a single very massive star a multiple stellar system with individual stars of lower masses forms.
The current theory of primordial star formation, however, contains still many open questions. For example the growing evidence for the presence of strong primordial magnetic fields, which is discussed in this thesis. These fields could lead to effects very similar to the ones observed in present-day star formation, like the transport of angular momentum and additional pressure (see the discussion in section 2.2). Further uncertainties are the heating from dark matter annihilation and potentially cosmic rays.

5.1.3 Formation of the First Galaxies and Reionization

In hierarchical structure formation, initially small structures like stars form followed by a build up to larger structures like galaxies. The definition of the first galaxies is, however, not as clear as the one of the first star, which could be identified with the first object in which nuclear fusion sets in after the element synthesis in the very early Universe. A galaxy could for example be defined via its dark matter content, which should be sufficiently high to retain its stars. Its gravitational potential should further be deep enough to keep the baryonic gas contained such that star formation can proceed, even when the negative stellar feedback is taken into account.
The dark matter minihalos, in which the first stars form, are probably not the birthplace of the first galaxies. Here the negative feedback, i.e. the ionizing radiation (Alvarez et al., 2006) and the mechanical feedback from the supernova blast wave (Greif et al., 2007), is expected to lead to emptying of most of the baryonic gas from the halo. The situation could however be different in more massive ($\approx 10^7\ M_\odot$) minihalos and lower mass population III stars (Kitayama & Yoshida, 2005).
In their review article Bromm & Yoshida (2011) discuss the common model that the first galaxies form within atomic cooling halos. These objects have masses of typically $10^8\ M_\odot$ and build up at redshifts larger than $z \approx 10$. Their virial temperature, which is of the order of 10^4 K, exceeds the one in dark matter minihalos and makes cooling via atomic lines possible. Even though atomic cooling halos are small compared to present-day galaxies, they are massive enough to re-virialize gas that has been heated by the first generation of stars (Dijkstra et al., 2004).

Modeling the first galaxies is challenging as, opposed to the situation for the first stars, the initial conditions are not very clear. In fact, in young galaxies one could expect already some heavy elements from the very first stars, maybe also dust grains, a very turbulent environment, and in principle also magnetic fields, as well as complicated radiation fields. The formation of stars in the first galaxies, so-called population II stars, might thus be as complex as present-day star formation.
The appearance of the first stars and especial the first galaxies as strong sources of radiation leads to an important phase transition in the Universe known as *reionization* (Meiksin, 2009). The baryonic matter, that was neutral since recombination at a redshift of roughly 1100, becomes ionized again. While helium reionization was presumably completed at $z \approx 3.5$, the observational evidence for hydrogen reionization is less clear. The new data from *Planck* suggests that half of the Universe was reionized at a redshift of $z \approx 11.45$ (Planck Collaboration et al., 2013a). The exact value should be improved with future instruments like SKA, which will be able to measure the 21 cm line of hydrogen up to high redshifts. The exact time when reionization takes place and when it is completed provides crucial constraints of the formation of the first stars and galaxies.

5.2 Onset of Turbulence in Structure Formation

In the local Universe turbulence is an omnipresent phenomenon. We observe chaotic motions on various scales and in all phases of the interstellar medium. However, the origin of turbulent motions is not entirely clear. When turbulence is not driven, the kinetic energy is transported to smaller and smaller scales until it dissipates and the turbulence decays. This process turns out to be rather fast (Mac Low et al., 1998). So what is the driving mechanism of turbulence? And has there always been turbulence in these astrophysical objects? Might there even be a way to generate turbulent motions in early structure formation?
A mechanism that could answer the latter question is studied in Klessen & Hennebelle (2010). They propose that accretion, a process that continuously goes along with the formation of structure, can efficiently drive turbulence. An efficiency parameter of turbulence driving can be defined as

$$\epsilon = \left| \frac{\dot{E}_{\mathrm{decay}}}{\dot{E}_{\mathrm{in}}} \right|, \tag{5.5}$$

where the loss of turbulent energy is

$$\dot{E}_{\mathrm{decay}} = -\frac{M\sigma^2}{2\tau_{\mathrm{decay}}} \tag{5.6}$$

and the energy accreted per time is

$$\dot{E}_{\mathrm{in}} = -\frac{1}{2}\dot{M}_{\mathrm{in}} v_{\mathrm{in}}^2. \tag{5.7}$$

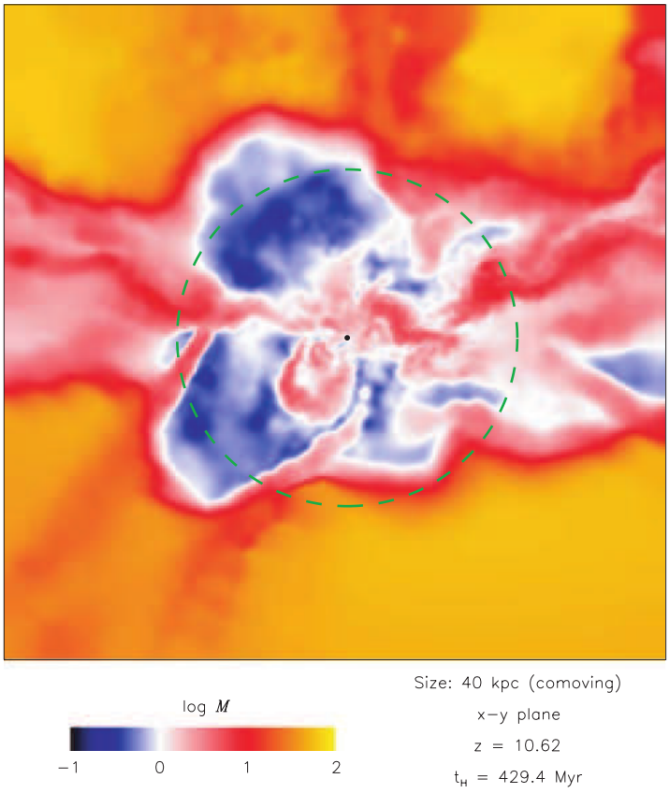

Figure 5.2:
The Mach number in the center of a primordial halo simulated by Greif et al. (2008). The virial radius is indicated by the dashed green line, where the Mach number approaches unity at the virial shock. Supersonic inflows of cold gas along filaments generate a high amount of turbulence in the center of the galaxy.
image credit: Greif et al. (2008)

Here M is the total mass of the system, σ the three-dimensional velocity dispersion, $\dot{M}_{\rm in}$ is the mass accretion rate and $\dot{v_{\rm in}}$ the infall velocity. The timescale for turbulence decay is roughly given as $\tau_{\rm decay} \approx L/\sigma$, when L is the forcing scale. It is clear that turbulence is only driven efficiently for $\epsilon < 1$. Klessen & Hennebelle (2010) estimate the efficiency factor for various astrophysical system by using colliding flow simulations and also analytical arguments. They find typical values of $\epsilon \approx 0.01 - 0.1$ and claim that accretion-driven turbulence is a universal concept in astrophysics.
Simulations by Greif et al. (2008) show indeed, that accretion flows lead to a highly turbulent environment already in atomic cooling halos, the birth places of the first galaxies. In their highly resolved simulations they analyze the velocity field of a galaxy during virialization in detail. They find that the accretion process can be divided in two phases: In the first *hot accretion phase* gas is accreted directly from the intergalactic medium and heated to the virial temperature in shocks. For the driving of turbulence the second phase, the so-called *cold accretion*, is important. Here the environmental gas cools in filaments before it enters the halo at high velocities. The Mach number in such a simulated halo is shown in figure 5.2, where the cold accretion flows are clearly visible. Typical Mach numbers in the filaments are of the order of 10, while they are still around 3 in the very center of the halo (Greif et al., 2008).
Further sources of turbulence in young galaxies are supernova explosions of the first generations of stars. Korpi et al. (1998) simulate a galactic disk with randomly distributed supernova explosions. They find that the first explosions give rise to

density fluctuations in the interstellar medium. The shock wave of a new supernova propagates through this clumpy medium, while its velocity changes with changing density. This way vorticity is generated.
With the evidence from analytical estimates as well as from simulations, there is no doubt about the presence of turbulent motion in primordial halos. The combination of turbulence with weak magnetic seed field makes turbulent dynamo action in these objects possible.

5.3 Dynamo Timescales

The typical time scale of the turbulent dynamo can be estimated by the inverse growth rate of the fluctuating magnetic field. In the limit of large magnetic Prandtl number we have determined the growth rate analytically from the Kazantsev theory (see section 4.2.4). In this limit the dynamo timescale is

$$t_{\mathrm{dynamo}} = \frac{60\ L}{(163 - 304\vartheta)\ V}\mathrm{Re}^{-(1-\vartheta)/(1+\vartheta)}. \tag{5.8}$$

Let us estimate the dynamo timescale for young galaxies. For this we assume for example a hydrodynamical Reynolds number of $\mathrm{Re} = 10^{11}$, a forcing scale of turbulence $L = 10^{21}$ cm and a large-scale turbulent velocity of $V = 10^5$ cm s^{-1}. With a slope of the turbulence spectrum of $\vartheta = 1/2$, which is valid for highly compressible turbulence, we find a typical timescale of

$$t_{\mathrm{dynamo}} \approx 10^{13}\ \mathrm{s} \approx 10^5\ \mathrm{yr}. \tag{5.9}$$

This very short compared to the Hubble time

$$t_{\mathrm{Hubble}} = \frac{1}{H_0} \approx 10^{10}\ \mathrm{yr}, \tag{5.10}$$

where $H_0 = 67.11$ km Mpc^{-1}s^{-1} is the Hubble constant.
Thus the turbulent dynamo can be expected to be a very fast process and should saturate shortly after the onset of turbulence. Consequently, the dynamo probably plays a more important role in the early Universe than it does today, as any seed field should have been amplified by the dynamo to a significant fraction of the turbulent energy up to now. Magnetic energy in galaxies can, of course, also be dissipated and under suitable circumstances the dynamo can set in again. However, we point out that the first glorious phase of the turbulent dynamo occurs, when turbulence comes into the game. We expect the first efficient driving of turbulence during the formation of structure, i.e. during the birth of the first stars and galaxies. Hence, it is worth exploring the role of the dynamo during structure formation in more detail, which will be the topic of the next chapters.

CHAPTER 6

The Turbulent Dynamo in the Formation of the First Stars[1]

Magnetic fields play an important role in star formation (we refere to the discussion in section 2.2). There is increasing evidence that dynamically important magnetic fields were also present in the early Universe (Banerjee & Jedamzik, 2004; Silk & Langer, 2006; Schleicher et al., 2010; Sur et al., 2010; Federrath et al., 2011; Turk et al., 2012). If this turns out to be true, current models for the formation of the first stars and galaxies need to be revisited.

The theory of primordial star formation has gone through a change recently, as has been discussed in section 5.1.2. It was previously assumed that the first stars were extremely massive and isolated (Abel et al., 2002; Bromm & Larson, 2004). However, new high-resolution calculations (Stacy et al., 2010; Clark et al., 2011; Smith et al., 2011; Greif et al., 2011, 2012) show that the accretion disk of a collapsing primordial halo fragments into multiple stars. The inclusion of magnetic fields could change this picture again. The magnetic pressure can stabilize an accretion disk and, depending on the field strength, suppress the fragmentation (Machida et al., 2004; Hennebelle & Teyssier, 2008; Price & Bate, 2007; Peters et al., 2011; Seifried et al., 2011). So far, there are only a few studies on primordial star formation that include magnetic fields (Tan & Blackman, 2004; Maki & Susa, 2004; Silk & Langer, 2006; Maki & Susa, 2007; Schleicher et al., 2010; Machida, 2010; Federrath et al., 2011; Sur et al., 2012; Turk et al., 2012). The magnetic field is expected to have similar effects to those seen in present-day star formation, such as the launching of winds and jets (Machida et al., 2006, 2008a). The latter eject gas from the accretion disk which could otherwise have collapsed onto the star. Thus, the star formation efficiency is reduced, especially for high-mass stars (Tan & Blackman, 2004; Machida, 2010). Strong jets can transport matter even out of the star-forming halo, leading to a magnetization of the intergalactic medium (Xu et al., 2011).

For developing primordial star formation theory further, we need to know structure

[1] This chapter follows closely Schober et al. (2012b).

and strength of the magnetic fields. The mechanism we suggest for producing strong fields is the small-scale dynamo, the theoretical description of which has been discussed in chapter 4 in detail. In this chapter we use the solution for large magnetic Prandlt numbers proposed by Schober et al. (2012c), which takes into account different types of turbulence.
We model the physical and chemical processes during the collapse of a primordial halo to quantitatively determine the properties of the small-scale dynamo. We calculate the magnetic Prandtl number and the magnetic Reynolds number. The latter is compared to the critical magnetic Reynolds number for small-scale dynamo action. Furthermore, we calculate the growth rate, which depends on the magnetic Prandtl number and the hydrodynamic Reynolds number. We assume a weak initial magnetic field of 10^{-20} G on the viscous scale produced by the Biermann battery (Biermann, 1950; Kulsrud et al., 1997; Xu et al., 2008). This allows us to determine the evolution of the magnetic field strength during the collapse.
The structure of this chapter, which closely follows Schober et al. (2012b), is as follows. In section 6.1 we review the properties of primordial gas. We present our numerical calculation of the chemistry and thermal evolution of the gas and discuss the characteristic magnetohydrodynamical quantities. Furthermore, we discuss the origin of turbulence and weak magnetic seed fields in primordial halos, which are essential for operation of the small-scale dynamo. In the section 6.2 we apply our theoretical results for the turbulent dynamo to our model for the collapse of a primordial halo. We present a simple model for the transport of the magnetic energy to larger scales in section 6.3. This allows us to calculate the magnetic energy on the Jeans scale of the primordial halo.

6.1 Properties of the Primordial Gas

6.1.1 Chemical and Thermal Evolution

We determine the chemical and thermal evolution of gravitationally collapsing primordial gas using the one-zone model of Glover & Savin (2009), together with a modification implemented by Schleicher et al. (2009) that relates the collapse time to the equation of state. Moreover, we have included additional Li^+ chemistry by using the reaction rates from Bovino et al. (2011b) and HeH^+ chemistry according to Bovino et al. (2011a). Glover & Savin (2009) model the chemistry of the gas with a chemical network that includes around 30 different atomic and molecular species linked by around 400 different chemical reactions. In our calculations, we use the same initial chemical abundances as in the default model in Glover & Savin (2009). The elemental abundances of helium, deuterium and lithium relative to hydrogen are taken to be 0.083 for helium, 2.6×10^{-5} for deuterium and 4.3×10^{-10} for lithium (Cyburt, 2004). The initial density and temperature of the gas were assumed to be $n_0 = 1\,\mathrm{cm}^{-3}$ and $T_0 = 1000$ K, respectively, but we have verified that our results are not sensitive to these values.

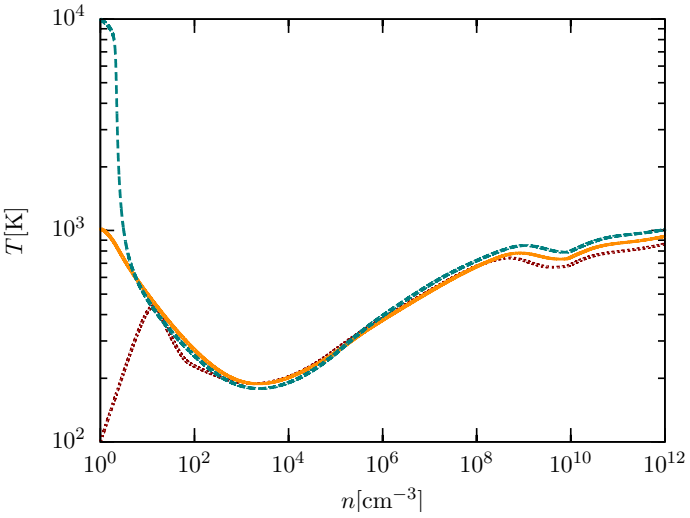

Figure 6.1:
The temperature as a function of the number density. The different lines indicate different initial conditions. The dashed green line corresponds to an initial temperature of 10^4 K, the dotted red line to 10^3 K and the solid orange line to 10^2 K.
image credit: Schober et al. (2012b)

In the one-zone model the mass density ρ evolves as

$$\frac{\mathrm{d}\rho}{\mathrm{d}t} \propto \frac{\rho}{t_{\mathrm{ff}}}, \tag{6.1}$$

where $t_{\mathrm{ff}} = \sqrt{3\pi/(32G\rho)}$ is the free-fall time. Moreover, the temperature evolution is determined by the energy equation,

$$\frac{\mathrm{d}\epsilon}{\mathrm{d}t} = \frac{p}{\rho^2}\frac{\mathrm{d}\rho}{\mathrm{d}t} - \Lambda_{\mathrm{cool}} + \Lambda_{\mathrm{heat}}, \tag{6.2}$$

where ϵ is the specific internal energy, p is the thermal pressure and Λ_{cool} and Λ_{heat} are the total cooling and the heating rate per unit mass, respectively. The resulting temperature evolution is shown in figure 6.1. Besides the initial temperature of 10^3 K, we also show in this figure the results for the initial temperatures 10^2 K and 10^4 K. Our calculations result in roughly the same evolution for all the initial temperatures after an increase of the density of about one order of magnitude.
In figure 6.2, the fractional abundances of H, He, H_2, H^+, Li^+ and free electrons vary with increasing density in our calculations. The abundance of H is constant at low densities, but decreases at densities higher than about 10^{10} cm^{-3} due to the formation of H_2. As there is no dust in primordial gas, large quantities of H_2 are produced only at high densities, via the three-body reactions:

$$\mathrm{H} + \mathrm{H} + \mathrm{H} \rightarrow \mathrm{H_2} + \mathrm{H}, \tag{6.3}$$
$$\mathrm{H} + \mathrm{H} + \mathrm{He} \rightarrow \mathrm{H_2} + \mathrm{He}, \tag{6.4}$$
$$\mathrm{H} + \mathrm{H} + \mathrm{H_2} \rightarrow \mathrm{H_2} + \mathrm{H_2}. \tag{6.5}$$

For the magnetic properties of the primordial gas the abundances of the charged species are especially important. They determine for example the conductivity, which is calculated in the next section. At densities $n < 10^8\,\mathrm{cm}^{-3}$, ionized hydrogen is the main positive ion, while at higher densities, Li^+ dominates. The sharp drop

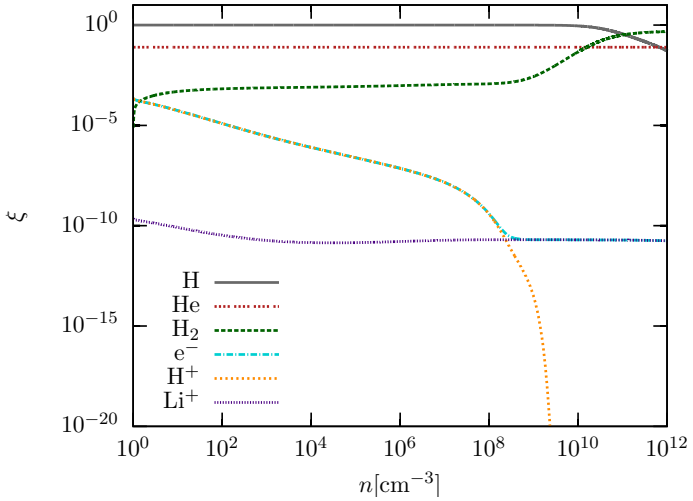

Figure 6.2:
The fractional abundances of different chemical species as a function of the number density.
image credit: Schober et al. (2012b)

in the H^+ abundance at densities $n > 10^8\,\mathrm{cm}^{-3}$ results from the removal of H^+ from the gas by the reaction chain (Glover & Savin, 2009),

$$H_2 + H^+ \rightarrow H_3^+ + \gamma, \tag{6.6}$$
$$H_3^+ + e^- \rightarrow H_2 + H. \tag{6.7}$$

6.1.2 Characteristic Magnetohydrodynamical Quantities

We have discussed the transport mechanisms in ionized fluids in sections 3.1.1 and 3.1.1. In this place we repeat the result for the viscosity given in section 3.1.5 and employ a more complex model for the magnetic diffusivity.

Viscosity It can be shown that the kinematic viscosity is

$$\nu = \frac{1}{4d^2 n}\left(\frac{kT}{\pi m}\right)^{1/2}, \tag{6.8}$$

if the molecules are assumed to be rigid spheres (Choudhuri, 1998). Here, $n = \rho/m$ is the number density, k the Boltzmann constant and T the temperature. Furthermore, $d = \sum_\mathrm{i} \xi_\mathrm{i} d_\mathrm{i}$ is the mean particle diameter and $m = \sum_\mathrm{i} \xi_\mathrm{i} m_\mathrm{i}$ the mean mass. ξ_i is the relative abundance of the species i, m_i and d_i are the masses and the Van-der-Waals diameters, respectively. The temperature as well as the abundances of the individual species are functions of the number density.

Diffusivity For calculating the magnetic diffusivity η we need the conductivity of the gas. In a plasma the three most important contributions to the conductivity of

a neutral species (indicated by index n) are (Wardle & Ng, 1999),

$$\sigma_{||,\mathrm{n}} = \frac{c}{B}\sum_{\mathrm{s}} \xi_{\mathrm{s}} n q_{\mathrm{s}} \beta_{\mathrm{ns}}, \tag{6.9}$$

$$\sigma_{\mathrm{P,n}} = \frac{c}{B}\sum_{\mathrm{s}} \xi_{\mathrm{s}} n q_{\mathrm{s}} \frac{\beta_{\mathrm{ns}}}{1+\beta_{\mathrm{ns}}^2}, \tag{6.10}$$

$$\sigma_{\mathrm{H,n}} = \frac{c}{B}\sum_{\mathrm{s}} \xi_{\mathrm{s}} n q_{\mathrm{s}} \frac{1}{1+\beta_{\mathrm{ns}}^2}, \tag{6.11}$$

as given in Pinto et al. (2008). The Hall-parameters β_{ns} are defined as

$$\beta_{\mathrm{ns}} = \frac{q_{\mathrm{s}} B}{m_{\mathrm{s}} c} \frac{m_{\mathrm{s}} + m_{\mathrm{n}}}{m_{\mathrm{n}} \xi_{\mathrm{n}} n \left\langle \sigma v \right\rangle_{\mathrm{sn}}}. \tag{6.12}$$

Here, m_{n} and m_{s} are the masses of the neutral and the charged particles, ξ_{n} and ξ_{s} are the abundance fractions of the species, and $\langle \sigma v \rangle_{\mathrm{sn}}$ is the momentum transfer rate coefficient. We take these coefficients, which are functions of the temperature, from Pinto & Galli (2008), where we use the polarisation approximation for Li^+.
The two dominant effects that lead to the dissipation of magnetic energy are the Ohmic resistivity and ambipolar diffusion. We can neglect the contribution of the Hall effect to the resistivity, as here the force acts perpendicular to the current and, thus, no energy is dissipated into heat. We calculate the distributions of the Ohmic resistivity and the ambipolar diffusion by

$$\eta_{\mathrm{Ohm,n}} = \frac{c^2}{4\pi \sigma_{||,\mathrm{n}}}, \tag{6.13}$$

$$\eta_{\mathrm{AD,n}} = \frac{c^2}{4\pi}\left(\frac{\sigma_{\mathrm{P,n}}}{\sigma_{\mathrm{P,n}}^2 + \sigma_{\mathrm{H,n}}^2} - \frac{1}{\sigma_{||,\mathrm{n}}} \right). \tag{6.14}$$

We focus on the most important neutral species H, He and $\mathrm{H_2}$ and the charged species H^+, e^- and Li^+. For each neutral species we calculate the resistivities $\eta_{\mathrm{Ohm,n}}$ and $\eta_{\mathrm{AD,n}}$. The magnetic field strength B drops out in the Ohmic case. Finally, the total Ohmic magnetic diffusivity is $\eta_{\mathrm{Ohm}} = \sum_{\mathrm{n}} \eta_{\mathrm{Ohm,n}}$ and the total resistivity due to ambipolar diffusion is $\eta_{\mathrm{AD}} = 1/(\sum_{\mathrm{n}} \eta_{\mathrm{AD,n}}^{-1})$.[2]

Reynolds Numbers The hydrodynamic and magnetic Reynolds numbers are defined as

$$\mathrm{Re} \equiv \frac{VL}{\nu} \tag{6.15}$$

$$\mathrm{Rm} \equiv \frac{VL}{\eta}, \tag{6.16}$$

where L is the length of the largest turbulent fluctuations and V the typical velocity on that scale. Notice, that we give these numbers on the forcing scale, i.e. the

[2]From private communication with Daniele Galli.

Jeans scale, which means $L = L_{\rm J}$ and $V = V_{\rm J}$. For the calculation of the magnetic Reynolds number we use the sum of $\eta_{\rm Ohm}$ and $\eta_{\rm AD}$. The resulting Reynolds numbers are shown in figure 6.3 as a function of the density.

Magnetic Prandtl Number The definition of the magnetic Prandtl number is

$$\mathrm{Pm} \equiv \frac{\mathrm{Rm}}{\mathrm{Re}} = \frac{\nu}{\eta}. \tag{6.17}$$

We can calculate this quantity by using the equations (6.8), (6.13) and (6.14). In figure 6.3 the density dependency of the magnetic Prandtl number is shown for both Kolmogorov and Burgers turbulence. For clarification we point out that the rapid decrease of the magnetic Reynolds and Prandtl number is caused by the dynamo amplification of the magnetic field. In the beginning of the collapse Ohmic resistivity is the dominant diffusion process. With increasing magnetic field $\eta_{\rm AD}$ increases proportional to B^2 (see equations 6.1.2 to 6.14) and becomes the main process for magnetic diffusion. Since Rm and Pm are both proportional to $1/\eta_{\rm AD}$, in the limit where $\eta_{\rm AD} \gg \eta_{\rm Ohm}$, both decrease rapidly with increasing magnetic field strength.
In addition, we tested the influence of varying the initial temperature on the evolution of the Reynolds numbers and the magnetic Prandtl number. For the initial temperature ranging from 10^2 K to 10^4 K we found only small variations in the Reynolds numbers and the magnetic Prandtl number, as illustrated in figure 6.3.

6.1.3 Turbulence

For the first star-forming halos considered here, we assume that turbulence is driven by virialisation (Wise & Abel, 2007; Greif et al., 2008) or by accretion of gas into the center of the halos (Klessen & Hennebelle, 2010; Elmegreen & Burkert, 2010; Federrath et al., 2011). The presence of turbulence affects star formation strongly, as the turbulent pressure works against the collapse to a star (Vazquez-Semadeni et al., 1998; Mac Low & Klessen, 2004; Krumholz & McKee, 2005; McKee & Ostriker, 2007). Moreover, Federrath et al. (2011) show in a Fourier analysis that the turbulence is effectively driven on the Jeans scale.
There are different types of turbulence (see also the discussion in section 4.1). In this paper we concentrate on the two extreme cases, Kolmogorov turbulence and highly compressible Burgers turbulence. The different types are described in the inertial range by the relation between the length scale ℓ and the velocity v on that scale,

$$v \propto \ell^{\vartheta}. \tag{6.18}$$

The exponent ϑ ranges from 1/3 for incompressible turbulence (Kolmogorov, 1941) to 1/2 for highly compressible turbulence (Burgers, 1948). In real astrophysical objects we expect the turbulence index ϑ to lie between these extreme cases (Kritsuk et al., 2007; Schmidt et al., 2008; Federrath et al., 2010).

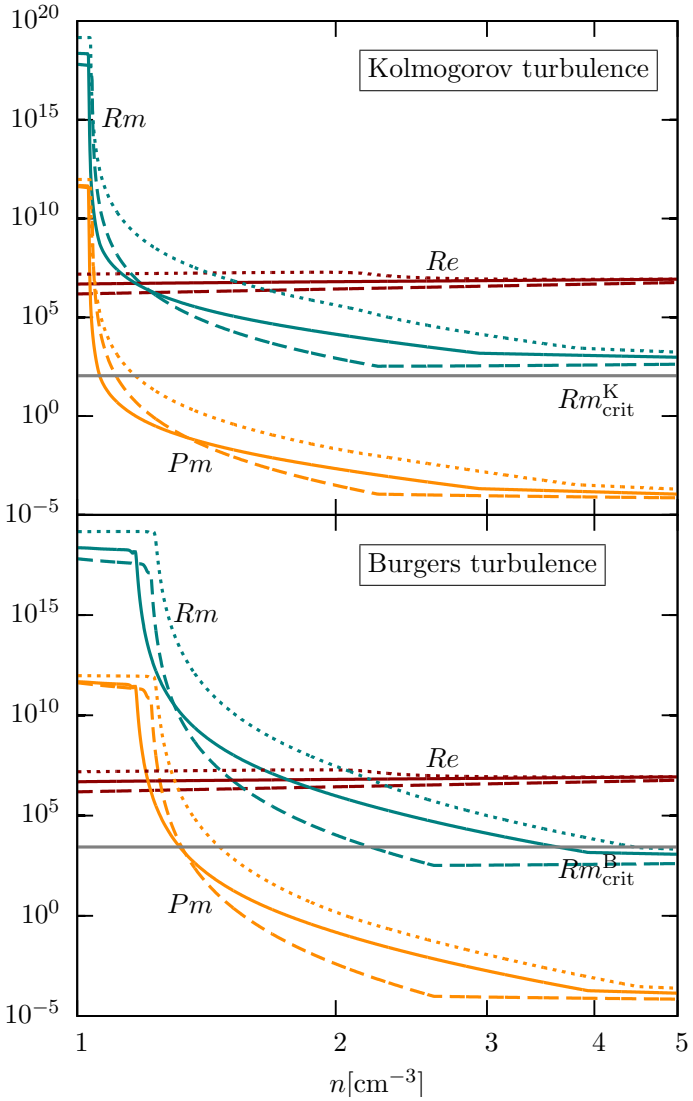

Figure 6.3:
The hydrodynamic and magnetic Reynolds numbers, Re and Rm, as well as the magnetic Prandtl numbers, Pm, on the current Jeans scale. The numbers are presented as a function of the hydrogen nuclei number density n. The solid lines represent an initial temperature of 10^3 K, the dashed lines 10^2 K and the dotted lines 10^4 K. Moreover, the horizontal lines indicate the critical magnetic Reynolds number for Kolmogorov and Burgers turbulence ($\mathrm{Rm}^{\mathrm{K}}_{\mathrm{crit}} = 107$ and $\mathrm{Rm}^{\mathrm{B}}_{\mathrm{crit}} = 2718$) as derived in Schober et al. (2012c). The rapid decrease of Rm and Pm from the very high starting values is caused by the exponential dynamo amplification of the magnetic field. We show the results for Kolmogorov turbulence in the upper plot and the results for Burgers turbulence in the lower plot.
image credit: Schober et al. (2012b)

6.1.4 Magnetic Seed Fields

The origin of magnetic seed fields has been discussed in section 3.2. The conclusion from this section is that these initial fields were extremely weak. Recall, that inflation models predict field strengths of the order of $B_0 \approx 10^{-40}$–10^{-10} G on a scale of 1 Mpc (Turner & Widrow, 1988) and models for cosmological phase transitions $B_0 \approx 10^{-20}$ G on a scale of 10 Mpc (Sigl et al., 1997). The typical fields strengths from a Biermann battery was also estimated to be $B_0 \approx 10^{-20}$ G. We chose the latter value as the initial field strength in our study of magnetized primordial star formation.

6.2 Magnetic Field Amplification on the Viscous Scale

In this section we analyse the evolution of the small-scale magnetic field. We outline the Kazantsev theory, which gives the growth rates of the magnetic field on the viscous scale. Together with the amplification due to gravitational compression and dissipation processes we can calculate the resulting small-scale magnetic field evolution.

6.2.1 Magnetic Field Amplification and Dissipation

Amplification by a Turbulent Dynamo With a model for the turbulent correlation function, Schober et al. (2012c) solve the Kazantsev equation (4.41) in the WKB approximation (see section 4.2.4 of this thesis). They find that the critical magnetic Reynolds number for dynamo action $Rm_{\rm crit}$ increases with compressibility. The values that Rm needs to exceed are

$$\mathrm{Rm}^{\mathrm{K}}_{\mathrm{crit}} \approx 107, \tag{6.19}$$

$$\mathrm{Rm}^{\mathrm{B}}_{\mathrm{crit}} \approx 2718, \tag{6.20}$$

for Kolmogorov and Burgers turbulence, respectively.
Moreover, Schober et al. (2012c) find different growth rates of the magnetic field for different turbulence models, with

$$\Gamma = \frac{(163 - 304\vartheta)}{60}\frac{V}{L}\mathrm{Re}^{(1-\vartheta)/(1+\vartheta)} \tag{6.21}$$

in the limit of infinite magnetic Prandtl numbers. Here V is the typical velocity on the largest scale of the turbulent eddies of size L and Re is the hydrodynamical Reynolds number.
In this paper we analyse the two extreme types of turbulence, Kolmogorov with $\vartheta = 1/3$ and Burgers turbulence with $\vartheta = 1/2$. We find in the limit of large

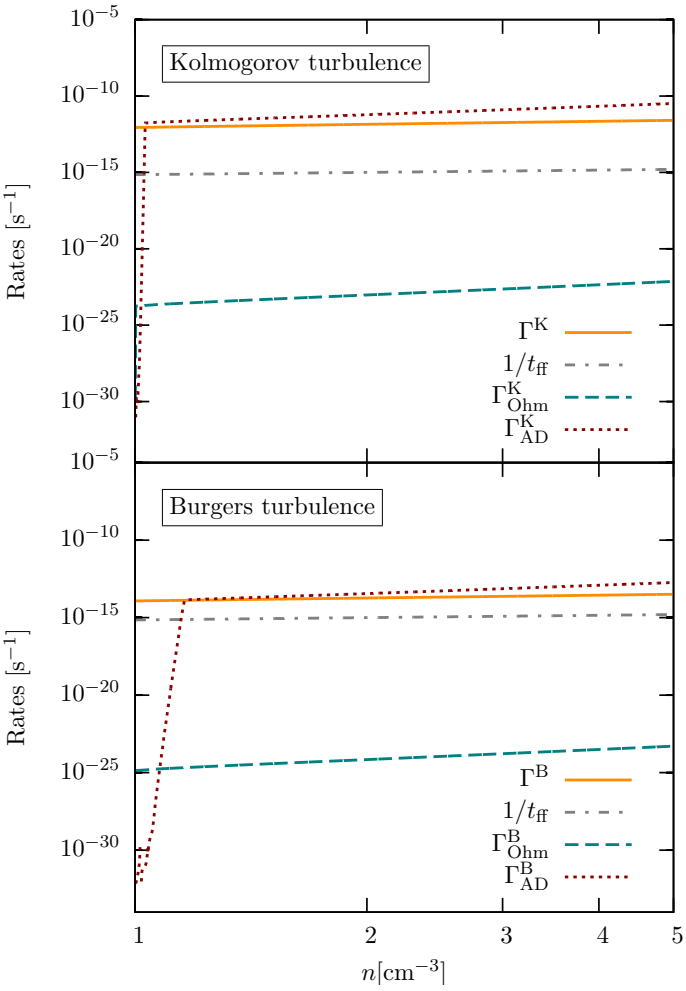

Figure 6.4:
Different characteristic rates on the viscous scale as a function of the density. We compare the growth rate of the magnetic field (solid orange line) to the inverse free fall time (dashed-dotted gray line) and the dissipation rates (Ohmic dissipation: dashed green line, ambipolar diffusion: dotted red line). We show the results for Kolmogorov turbulence in the upper plot and the results for Burgers turbulence in the lower plot. *image credit: Schober et al. (2012b)*

magnetic Prandtl numbers

$$\Gamma^{\rm K} = \frac{37}{36}\frac{V}{L}{\rm Re}^{1/2}, \tag{6.22}$$

$$\Gamma^{\rm B} = \frac{11}{60}\frac{V}{L}{\rm Re}^{1/3}. \tag{6.23}$$

For the typical velocity of the largest fluctuations we use the sound speed $V = V_{\rm J} \approx \sqrt{\gamma kT/m}$, as the Mach number in a primordial halo is roughly one (Greif et al., 2008). Here γ is the adiabatic index. We take L to be the Jeans length, as this is the effective driving scale for turbulence in a collapsing system (Schleicher et al., 2010; Federrath et al., 2011). Hence we set $L \approx L_{\rm J} = \sqrt{\gamma kT/(Gm^2n)}$, where G is the gravitational constant.
We compare the growth rate of the small-scale dynamo Γ on the viscous scale $\ell_\nu = L_{\rm J}{\rm Re}^{-1/(1+\vartheta)}$ to the inverse free-fall time $1/t_{\rm ff} = [3\pi/(32Gmn)]^{-1/2}$. The result is shown in figure 6.4. In our model the magnetic field on the fastest growing scale increases one to three orders of magnitude faster than the halo collapses. Note that the dynamo growth is exponential in time.

Amplification by Gravitational Compression The gravitational compression due to the collapse of the halo provides additional amplification of the magnetic field. As long as the condition of flux freezing is fulfilled, the magnetic field B increases with density like

$$B \propto n^{2/3} \tag{6.24}$$

for spherically symmetric collapse. Before the dynamo saturates, the amplification by gravitational compression is minor compared to the dynamo growth.

Dissipation of Magnetic Energy Part of the magnetic energy is converted into heat by dissipation processes. The dissipation term in the induction equation (3.85) is $\eta\nabla^2\mathbf{B}$. We consider Ohmic dissipation and ambipolar diffusion and approximate this by $\eta B/\ell^2$ and $\partial B/\partial t$ by $B\Gamma_{\rm Ohm}$ and $B\Gamma_{\rm AD}$ respectively. We get

$$\Gamma_{\rm Ohm} \approx \frac{\eta_{\rm Ohm}}{\ell^2}, \tag{6.25}$$

$$\Gamma_{\rm AD} \approx \frac{\eta_{\rm AD}}{\ell^2}. \tag{6.26}$$

$\Gamma_{\rm Ohm}$ and $\Gamma_{\rm AD}$ are the rates of magnetic energy dissipation by Ohmic resistivity and ambipolar diffusion.

6.2.2 Critical Magnetic Reynolds Number

The dependency of the magnetic Reynolds number Rm on the number density is shown in figure 6.3 for the two extreme types of turbulence. We also indicate the critical magnetic Reynolds number for small-scale dynamo action $\mathrm{Rm}_{\rm crit}$. One can see that the magnetic Reynolds number is larger than $\mathrm{Rm}_{\rm crit}$ at the onset of the collapse. For densities above roughly 4 cm^{-3} Rm becomes smaller than the critical value in the case of Burgers turbulence. For Kolmogorov turbulence Rm becomes also smaller than $\mathrm{Rm}_{\rm crit}$ for high densities, which are not shown in figure 6.3. However, as we see below, at this point the dynamo is already saturated on the small scale as well as on the large scale. Thus, in the density regimes where the small-scale dynamo operates, the condition $\mathrm{Rm} > \mathrm{Rm}_{\rm crit}$ is always fulfilled.

6.2.3 Resulting Small-Scale Magnetic Field

In principle, the magnetic energy density, $E_{\rm B} = B^2/(8\pi)$, evolves as

$$\frac{\mathrm{d}E_{\rm B}}{\mathrm{d}t} = \left[\Gamma + \frac{4}{3n}\frac{\mathrm{d}n}{\mathrm{d}t} - \Gamma_{\rm Ohm} - \Gamma_{\rm AD}(E_{\rm B})\right] E_{\rm B}, \tag{6.27}$$

where we assume spherically symmetric collapse.
By solving equation (6.27) numerically we find the evolution of the magnetic energy density on small scales. In figure 6.7 we show the resulting growth of the magnetic

field strength. As an initial field strength B_0 we use 10^{-20} G on the viscous scale, which is a conservative value for a field generated by a Biermann battery (Biermann, 1950; Xu et al., 2008). The field strength grows extremely rapidly as the density increases. However, we cannot trust the whole evolution of the magnetic field exactly as shown in figure 6.7. When the field has become strong enough, the magnetic Prandtl number becomes unity or less (see figure 6.3). Then the WKB-approximation breaks down and equations (6.2.1) are no longer valid. Complementary studies have shown, however, that the small-scale dynamo still operates for $\mathrm{Pm} < 1$ (Boldyrev & Cattaneo, 2004; Schekochihin et al., 2005, 2007; Eyink et al., 2011), although the growth rate may decrease by a factor of a few. We note that Boldyrev & Cattaneo (2004) find in their studies that the critical magnetic Reynolds number increases with decreasing magnetic Prandtl number. Furthermore, we see in figure 6.4 that the ambipolar diffusion rate becomes higher than the growth rate of the magnetic field. In this regime, equation (6.21) is no longer a solution of the Kazantsev equation. We expect that the field grows at the rate (6.21) almost until saturation, but then decreases and the field reaches saturation more slowly.

6.2.4 Validity of our Approximation

In figure 6.3 the magnetic Prandtl number Pm is shown as a function of the density. Pm starts with an extremely high value of roughly 10^{12} and then after a rather constant phase decreases rapidly. The magnetic Prandtl number is defined in equation (6.17) with $\eta = \eta_{\mathrm{Ohm}} + \eta_{\mathrm{AD}}$. For low densities the Ohmic resistivity dominates, which is independent of the magnetic field strength. With increasing density the magnetic field increases due to the dynamo amplification and with $\eta_{\mathrm{AD}} \propto B^2$ the ambipolar diffusion rate becomes dominant. In this regime the magnetic Prandtl number decreases proportional to B^{-2}. As the magnetic field increases exponentially during the small-scale dynamo amplification in the beginning of the collapse, the magnetic Prandtl number decreases rapidly.
The approximation of large magnetic Prandtl numbers (Schober et al., 2012c) is accurate during most of the dynamo growth. At the end of the dynamo phase, however, Pm reaches unity and decreases even further and our approximations eventually break down. Schober et al. (2012c) show that for decreasing Pm the growth rate decreases. However, they make no prediction for the regime $\mathrm{Pm} \approx 1$. But numerical simulations show that the dynamo operates also in this regime (e.g. Federrath et al., 2011). For $\mathrm{Pm} \ll 1$ there is again analytical evidence for small-scale dynamo action (e.g. Schekochihin et al., 2007). We note that this treatment concerns the viscous scale only.

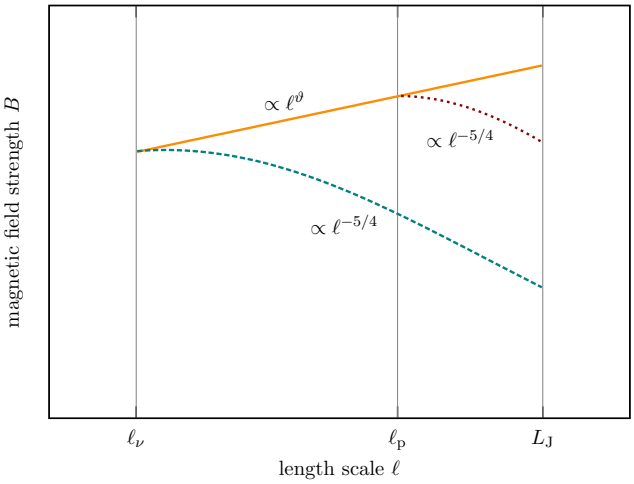

Figure 6.5:
Schematic time evolution of the magnetic spectrum in the inertial range of turbulence. The different colors and line types represent the spectrum at different times. The green dashed line shows the spectrum at saturation on the viscous scale ℓ_ν. To larger scales the spectrum decreases according to the Kazantsev slope ($B \propto \ell^{-5/4}$). At a time after saturation on the viscous scale the spectrum is indicated by the dotted red line. Finally, the solid orange line shows the spectrum at saturation on the Jeans scale L_J.
image credit: Schober et al. (2012b)

6.3 Magnetic Field Amplification on Larger Scales

6.3.1 Model for the Transport of Magnetic Energy to Larger Scales

After the magnetic field saturates on the viscous scale the peak of the magnetic energy spectrum moves to larger scales. In this section we present a model for the time evolution of the magnetic energy spectrum. The situation is illustrated schematically in figure 6.5. For simplicity we use a fixed frame of reference, where the viscous and the Jeans scale stay constant. Here we indicate three different curves, which represent different times. The dashed green line is the spectrum at the time of saturation on the viscous scale, the dotted red line shows a later time and the solid orange line represents an even later point in time at which the magnetic field has saturated on the Jeans scale.
During saturation, the coherence length of the magnetic field shifts towards larger scales, a well-known behavior for the small-scale dynamo (Schekochihin et al., 2002; Brandenburg & Subramanian, 2005), recently shown to be true also in a collapsing system (Sur et al., 2012). Analytical arguments suggest this occurs on the eddy-timescale of the current peak scale ℓ_p

$$\frac{\ell_\mathrm{p}}{v_\mathrm{p}} = \frac{L_\mathrm{J}}{V_\mathrm{J}} \left(\frac{\ell_\mathrm{p}}{L_\mathrm{J}} \right)^{1-\vartheta} , \tag{6.28}$$

where we used $v_\mathrm{p} = V_\mathrm{J}(\ell_\mathrm{p}/L_\mathrm{J})^{\vartheta}$. Considering that the peak scale moves from the viscous scale $\ell_\nu(t_\nu)$ towards larger scales, we find for the time-dependency of the

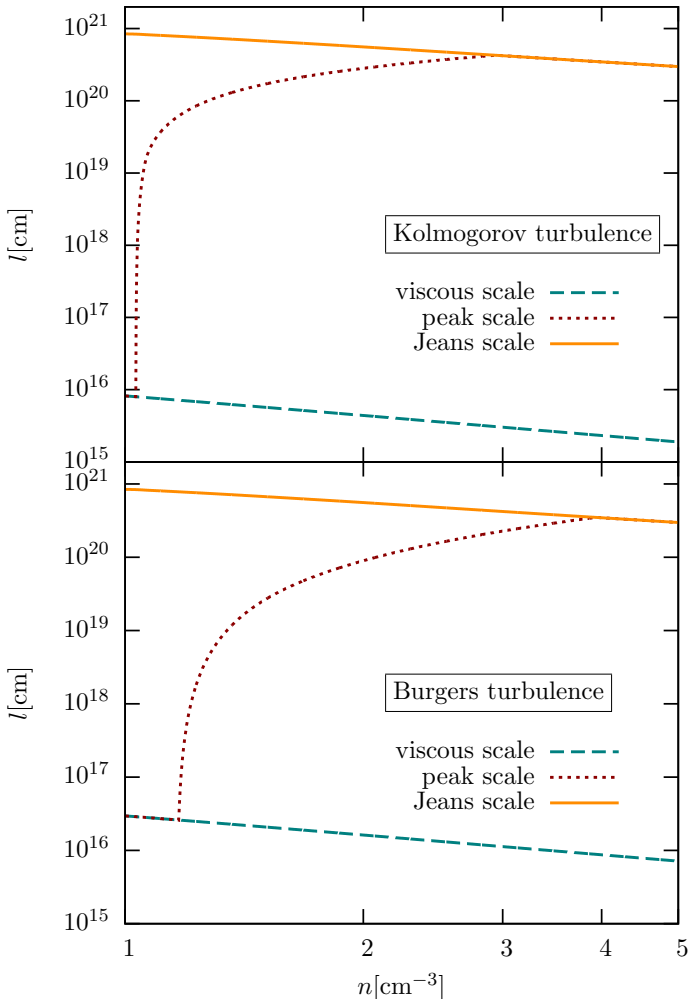

Figure 6.6:
Different characteristic scales as a function of the density. The dashed green line indicates the viscous scale, the dotted red line the scale corresponding to the peak of the magnetic energy spectrum, and the solid orange line the Jeans scale. We show the results for Kolmogorov turbulence in the upper plot and the results for Burgers turbulence in the lower plot.
image credit: Schober et al. (2012b)

peak scale

$$\ell_{\mathrm{p}}(t) = \ell_{\nu}(t_{\nu}) + \left(\frac{V_{\mathrm{J}}}{L_{\mathrm{J}}^{\vartheta}} (t - t_{\nu}) \right)^{1/(1-\vartheta)} , \tag{6.29}$$

where t_{ν} is the point in time, when saturation occurs on the viscous scale.
The slope of the curves proportional to $\ell^{-5/4}$ is known as the Kazantsev slope in real space[3], which can be derived from the Fourier-transformed Kazantsev equation (4.41) (Brandenburg & Subramanian, 2005). This characteristic slope is also observed in simulations (Federrath et al., 2011; Xu et al., 2011). The curve that connects the peak maxima at different times (red-colored curve) is a relic of the turbulence spectrum and thus is proportional to ℓ^{ϑ}.
At each time step we calculate the peak magnetic field strength by solving the stationary case of equation (6.27). However, we find that the magnetic field strength

[3]In many references the magnetic energy spectrum is given as a function of the wave number k, defined for example as $B^2/(8\pi\rho) = 1/2 \int M(k)\mathrm{d}k$. In this case the Kazantsev slope is $M(k) \propto k^{3/2}$. From this we find $B^2 \propto k^{5/2}$ and $B \propto \ell^{-5/4}$.

exceeds the equipartition field strength on scales larger than the viscous scale. The reason for this is that the ambipolar dissipation rate, which is proportional to B^2/ℓ^2, decreases rapidly in this regime. Thus, it cannot balance the growth rate any longer and we need to set the equipartition field strength as an upper limit $B_{\ell,\max}$. With $B^2_{\ell,\max}/(8\pi) = 1/2\rho v(\ell)^2$ we find the maximum magnetic field strength $B_{\ell,\max} = \sqrt{4\pi\rho}v(\ell)$.
Taking the typical turbulent velocity on the scale of the turbulence ℓ to be related to the sound-speed by $v(\ell) = (\ell/L_\mathrm{J})^\vartheta c_s \simeq (\gamma kT/m)^{1/2}(\ell/L_\mathrm{J})^\vartheta$, we find that

$$B_{\ell,\max} = \sqrt{4\pi\gamma kTn}\ (\ell/L_\mathrm{J})^\vartheta\,. \tag{6.30}$$

Using the Kazantsev slope, we can extrapolate the magnetic field strength onto the current Jeans length. By this we are able to determine the time evolution of the magnetic field on the Jeans scale.
For this process to be relevant during collapse, the eddy-timescale needs to be smaller than the collapse timescale. Thus, the small-scale dynamo is unlikely to produce magnetic fields on scales larger than the Jeans scale. Figure 6.6 shows the viscous, the peak, and the Jeans scale as a function of density. During the small-scale dynamo growth the spectrum of the magnetic energy peaks at the viscous scale. After saturation on the viscous scale the peak moves to larger scales according to equation (6.29) until it reaches the Jeans scale.

6.3.2 Resulting Jeans-Scale Magnetic Field

As described in the last section, we determine the magnetic field on the Jeans scale by extrapolation from the peak scale. The result of the large-scale magnetic field is shown in figure 6.7 together with the field on the current peak scale and the one on the viscous scale. One can see that the magnetic energy is shifted rapidly onto larger scales. For Kolmogorov turbulence the field on the Jeans scale saturates at a density of roughly 3 cm^{-3} and for Burgers at a density of roughly 4 cm^{-3}. At the end of dynamo growth on the Jeans scale we have a magnetic field strength of about 10^{-6} G throughout the entire inertial range of the turbulence, i.e. within the Jeans volume.
After the rapid initial dynamo amplification the only way to amplify the magnetic field on the Jeans scale further is gravitational compression, which leads to $B \propto n^{2/3}$. However, the field has already reached equipartition with the kinetic energy at the end of the dynamo amplification and, thus, increases only with $n^{1/2}$ (see equation 6.30). The growth rate of the magnetic field on the Jeans scale Γ_J is then

$$\Gamma_\mathrm{J} = \frac{1}{n}\frac{\mathrm{d}n}{\mathrm{d}t}. \tag{6.31}$$

In figure 6.8 we compare the growth rate Γ_J to the ambipolar and Ohmic diffusion rates on the Jeans scale, $\Gamma_\mathrm{AD,J}$ and $\Gamma_\mathrm{Ohm,J}$. As Γ_J is always larger than the diffusion rates in the shown density range, the magnetic energy on the Jeans scale is not dissipated again during the collapse. At a density of 10^{12} cm^{-3}, we determine with $B \propto n^{1/2}$ a magnetic field strength of 0.4 G.

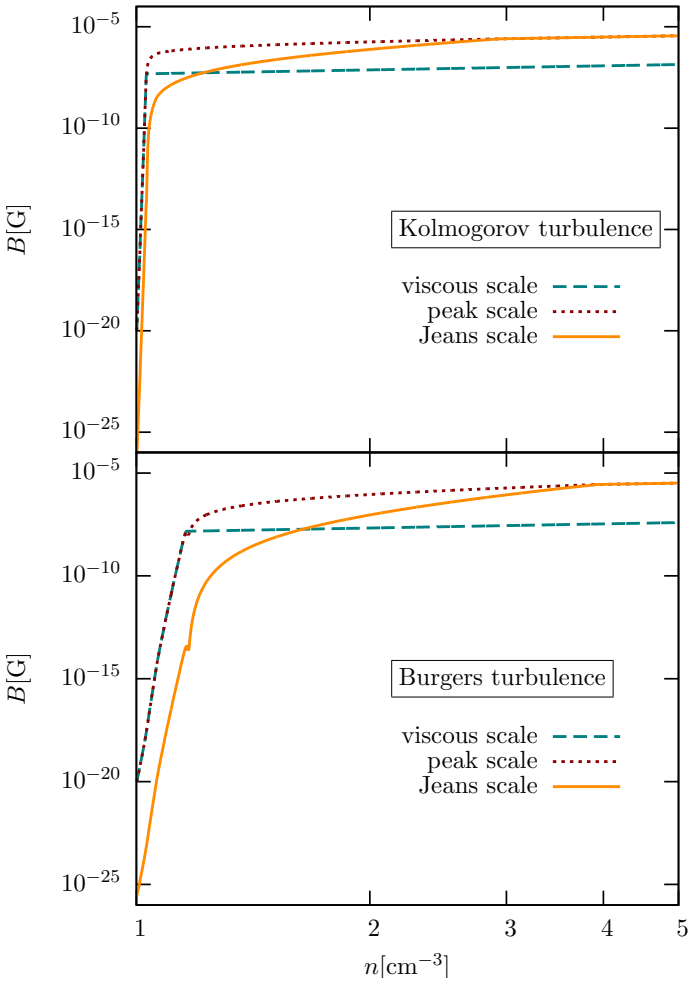

Figure 6.7:
The magnetic field strength as a function of the number density on different scales. The dashed green line corresponds to the field evolution on the viscous scale, the dotted red line to the peak scale and the solid orange line to the Jeans scale. We show the results for Kolmogorov turbulence in the upper plot and the results for Burgers turbulence in the lower plot.
image credit: Schober et al. (2012b)

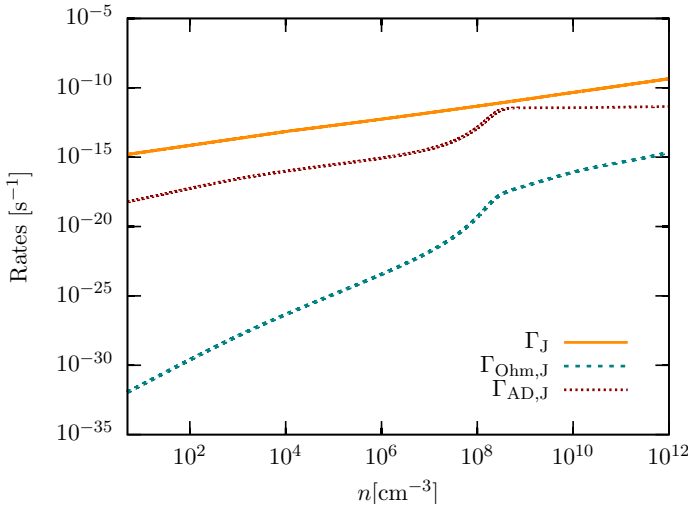

Figure 6.8:
The growth rate on the Jeans scale Γ_J after the dynamo amplification compared to the diffusion rates as a function of the number density. $\Gamma_{Ohm,J}$ and $\Gamma_{AD,J}$ are the Ohmic and ambipolar diffusion rate, respectively.
image credit: Schober et al. (2012b)

6.3.3 Implications for Numerical Simulations

Our calculations show that, due to the rather small viscosity and resistivity in primordial gas, the hydrodynamical Reynolds number, the magnetic Reynolds number and the magnetic Prandtl numbers have very high values as long as the magnetic field is not saturated. Such Reynolds numbers are well above what can be reached in numerical simulations, implying that the physical growth rate of the magnetic field largely exceeds the growth rate obtained in numerical simulations. Particularly important here is the fact that the typically unresolved viscous scales are highly relevant for magnetic field amplification even on larger scales. In this sense, numerical simulations can only show the presence of a dynamo, but will typically underestimate the magnetic field amplification rate. This behavior has also been demonstrated in pioneering studies by Sur et al. (2010) and Federrath et al. (2011). On the other hand, our results show that magnetic fields quickly saturate once turbulence forms, and the limiting timescale may thus be the timescale on which turbulence is generated. This is again an issue which can be addressed with numerical simulations, and indeed, simulations for instance by Turk et al. (2012) convincingly demonstrated the release of turbulence from the gravitational energy during primordial collapse. Overall, such simulations are thus relevant to explore the origin and generation of turbulence, while the strength of the magnetic field should rather be estimated based on the physical growth rates. As a net effect, we therefore expect that the magnetic energy is always close to saturation once turbulence is generated in the halo.

6.4 Summary of Our Dynamo Model in Primordial Star Formation

In this chapter we compute the evolution of the magnetic field and its saturation level in typical primordial halos based on the Kazantsev theory of the turbulent dynamo in combination with a detailed description of the physical and chemical processes in zero-metallicity gas. The model is, in principle, applicable only to magnetic field fluctuations on very small scales. However, when interested in the influence of the field on the overall dynamical evolution of the halo gas, it is most important to understand how saturation occurs on larger scales. To address this problem, we also consider the transport of magnetic energy from the viscous scale to the Jeans scale. Starting with a weak magnetic seed field of 10^{-20} G, as can be produced by the Biermann battery, we follow the evolution of magnetic field fluctuations on the viscous scale and find that they are amplified very rapidly on timescales much shorter than the free-fall time. As a consequence, the field saturates almost immediately after the onset of gravitational collapse in the halo. By extrapolating the small-scale magnetic field to larger scales and assuming the peak of the magnetic spectrum shifts on the local eddy timescale, we are able to follow the evolution of the magnetic field strength throughout the full inertial range within the Jeans volume. For typical

halo parameters, the dynamo growth of the magnetic energy saturates at a density of roughly 3 cm^{-3} for Kolmogorov turbulence and 4 cm^{-3} for Burgers turbulence. At this point in time the field has a strength of about 10^{-6} G. We point out, however, that the field continues to grow in the collapsing gas due to gravitational compression.

Our results show that the magnetic energy on small scales, and more importantly also on dynamically important large scales, can grow to very high values. In order to understand the influence of this strong field on the evolution of the halo gas, it is important to know whether the small-scale magnetic field can be transformed into a coherent large-scale field. One way to produce more coherent magnetic structures is by forming disks, which is suggested by Latif et al. (2012). Moreover, the saturation behavior of the small-scale dynamo should be explored further in the regime $\mathrm{Pm} < 1$, as we have shown that the magnetic Prandtl number is in this regime for high densities.

If indeed the processes discussed here can produce dynamically significant fields on large scales, then the magnetic field will influence the star formation process in high-redshift halos. For example, since recent high-resolution simulations indicate that the accretion disks around the very first stars were strongly susceptible to fragmentation (Turk et al., 2009; Stacy et al., 2010; Clark et al., 2011; Greif et al., 2011; Smith et al., 2011) it is expected that most primordial stars formed as members of binary or higher-order multiple systems with a wide range of masses rather than being isolated, high-mass stars. From studies of low-mass star formation at present day, however, we know that magnetic fields close to the equipartition value can effectively redistribute angular momentum via a process called magnetic braking (Mouschovias & Paleologou, 1979; Machida et al., 2008b) and can thereby reduce the fragmentation probability in the disk (Hennebelle & Ciardi, 2009; Peters et al., 2011; Hennebelle et al., 2011; Seifried et al., 2011). The correct treatment of magnetic fields in calculations of primordial star formation therefore seems critical to better understand the mass function and multiplicity of metal-free stars.

CHAPTER 7

The Turbulent Dynamo in Young Galaxies[1]

In section 2.3 the complex nature of magnetic fields in galaxies has been discussed. Local spiral galaxies have a typical turbulent field component of $(2-3)\times10^{-5}$ G within the arms and bars, while a field of $(5-10)\times10^{-5}$ G is observed in the central starburst regions. These fields appear to be coherent on scales larger than 10 kpc, which is the same order of magnitude as the size of the galaxy. In disk galaxies usually an ordered magnetic field component is found with its strength peaking at $(1-1.5)\times10^{-5}$ G in the interarm region (Beck, 2011). Also dwarf irregular galaxies have magnetic fields, however they appear not to be ordered on large scales and have a lower strength of $\leq 4\times10^{-6}$ G (Chyży et al., 2011). The origin of galactic magnetic fields is a highly debated problem in astrophysics.
Moreover, new observations indicate that even highly redshifted galaxies have magnetic field strengths comparable to present-day galaxies (Bernet et al., 2008). For instance the rotation measure, a quantity depending on the magnetic field along the line of sight, is constant up to redshifts of roughly 5 (Hammond et al., 2012). Observations of the intergalactic medium provide further information on primordial seed fields. Detailed analysis of the CMB temperature bispectrum using data from the PLANCK satellite gives an upper limit of the magnetic field strength of the order of a few nG on the Mpc scale (Shiraishi et al., 2012). The increasing evidence for magnetic fields in highly redshifted galaxies and the intergalactic medium indicates an early generation of the magnetic fields.
We suggest that a dynamo operates in young galaxies, which converts the kinetic energy from turbulence into magnetic energy. This mechanism provides a rapid amplification of weak magnetic seed fields (see section 3.2 of this thesis) up to dynamical important values. The origin of turbulence in dark matter halos is been discussed in section 4.1. In young galaxies accretion as well as the penetration of supernovae (SN) shocks through the gas generate turbulence initiating small-scale

[1] This chapter follows closely Schober et al. (2013).

dynamo action (Beck et al., 2012; Latif et al., 2013).
In order to follow the evolution of the magnetic field in an initially weakly magnetized young galaxy, we adopt two simplified complementary models: a spherical galaxy as well as a disk-like system, both with constant density and temperature. We model microphysical processes, such as the diffusion of the kinematic and magnetic energy, in order to find the magnetohydrodynamical (MHD) quantities, which determine the growth rate of the small-scale dynamo. Turbulence can be generated by accretion flows into the center of the halo, for which we estimate the typical Reynolds numbers. Then we follow the evolution of the magnetic field strength in the kinematic and the non-linear phase, until saturation on the driving scale of the turbulence is reached. Also stellar feedback, in particular SN explosions, influences the evolution of the magnetic field. On the one hand supernovae distribute stellar magnetic fields in the interstellar medium (ISM) (Rees, 1987), on the other hand they drive turbulence, which again leads to dynamo action (Balsara et al., 2004). We compare the resulting magnetic field strengths from both mechanisms with the field strength gained by an accretion-driven small-scale dynamo.
The outline of this chapter, which follows closely Schober et al. (2013), is as follows: In section 7.1 we describe our models for young galaxies. We determine the values of viscosity and magnetic diffusivity in the interstellar medium and estimate the evolution of SN explosions. Driving mechanisms of turbulence are discussed in general. We further provide the main theoretical predictions for the turbulent dynamo in the kinematic and the non-linear phase. In section 7.2 our results for the evolution of the magnetic field in the different types of models are presented. We discuss the generation of turbulence by accretion and the resulting efficiencies of the dynamo, i.e. the saturation magnetic field strength and the time until saturation occurs. Furthermore, we analyze the effect of stellar feedback. We compare the efficiency of distributing stellar magnetic fields by SNe with the one of the SN-driven turbulent dynamo.

7.1 Modeling Physical Processes in a Protogalaxy

7.1.1 General Aspects

The nature of young galaxies is still an active topic of research (see Bromm & Yoshida (2011) for a review). For our order of magnitude estimate of the magnetic field evolution we use a very simplified model, with the choice of parameters being motivated from numerical simulations (Greif et al., 2008; Bromm et al., 2009; Latif et al., 2013). We are interested in massive protogalactic objects at redshifts of roughly 10.
In our model we assume a mean particle density of

$$n = 10 \text{ cm}^{-3}, \tag{7.1}$$

and a temperature of

$$T = 5 \times 10^3 \text{ K}. \tag{7.2}$$

The density as well as the temperature are, as first approximation, constant throughout the whole galaxy. For simplicity we take a gas into account that only consists of hydrogen, which is at the given values of n and T mostly ionized.
The mean shape of the primordial galaxies differs most probably from the one of present-day galaxies. Due to a significant amount of angular momentum the protogalaxies may form in a spherical way and develop a more disk-like structure at later stages. To account for the unknown typical shape, we model two extreme cases, a spherical and a disk-like galaxy, which have the same gas mass.

Spherical Galaxy In the case of a spherical protogalaxy we assume the radius to be

$$R_{\text{sph}} = 10^3 \text{ pc}. \tag{7.3}$$

As within this radius the density as well as the temperature are constant we find a total mass of the baryonic gas of

$$M \approx 10^9 \ M_\odot. \tag{7.4}$$

Disk-like Galaxy As our second fiducial model we use a galaxy with disk scale height of ten percent of the radius, i.e.

$$H_{\text{disk}} = 0.1 \ R_{\text{disk}}. \tag{7.5}$$

With the condition that the gas mass of the disk needs to be the same as in the spherical case, the disk radius is

$$R_{\text{disk}} \approx 2.4 \times 10^3 \text{ pc}. \tag{7.6}$$

7.1.2 Microphysics in the ISM

As the temperature in the primordial ISM is very high, we can assume the gas to be (at least partially) ionized. We thus need to deal with the full plasma equations, i.e. the continuity, the momentum and the energy equations for both the ions and the electrons. Closures of these equations were found by Braginskii (1965), who used the Chapman-Enskog scheme (Chapman et al., 1953). The closure is based on the assumption that the macroscopic scale of the plasma is large compared to the mean-free path

$$\ell_{\text{mfp}} = \frac{1}{nd^2}, \tag{7.7}$$

or compared to the gyro-radii of the electrons and the ions

$$r_{\text{c}}(B) = \frac{(2m_{\text{s}}kT)^{1/2}c}{eB}. \tag{7.8}$$

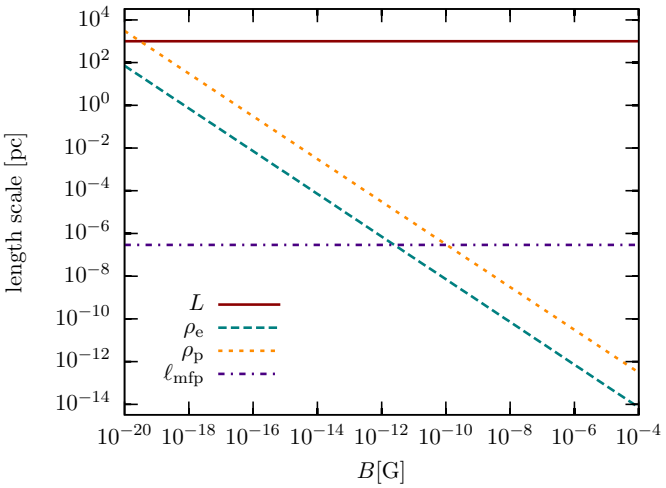

Figure 7.1:
The gyro-radii of electrons and ions ρ_e and ρ_p as a function of magnetic field strength compared to the typical macroscopic scale $L \approx 10^3$ pc and the mean-free path ℓ_{mfp}. Within our fiducial case for the density and the temperature the electron fluid becomes magnetized at a magnetic field strength of roughly 10^{-12} G, the ion fluid at 10^{-10} G.
image credit: Schober et al. (2013)

Here $d = e^2/(kT)$ is the distance of closest particle approach with e being the elementary charge and k the Boltzmann constant. The mass of the species is labeled m_s, where the s stands for electrons (e) or protons (p), and c is the speed of light. Further, we use here the thermal velocity $(2kT/m_s)^{1/2}$ and assume that the temperatures of the ions and electrons are equal ($T_e = T_p \equiv T$). In principle, the components of a plasma can have unequal temperatures as during plasma heating the different fluids are heated differently. However, after a certain time t_{eq}, an equilibrium will be reached. The electron-proton equilibrium time can be computed by (Spitzer, 1956)

$$t_{eq} = \frac{3 m_e m_p k^{3/2}}{8(2\pi)^{1/2} n Z_e^2 Z_p^2 e^4 \ln(\Lambda)} \left(\frac{T_{e,0}}{m_e} + \frac{T_{p,0}}{m_p} \right)^{3/2}, \tag{7.9}$$

where Z_s is the charge of species s, $T_{s,0}$ its initial temperature and the Coulomb logarithm is defined by

$$\ln(\Lambda) \approx 6.6 - 0.5 \ln\left(\frac{n}{10^{14}\ \mathrm{cm}^{-3}} \right) + 1.5 \ln\left(\frac{kT}{1.6 \times 10^{-12}\ \mathrm{erg}} \right). \tag{7.10}$$

If we assume $T_{e,0}$ and $T_{p,0}$ to be extremely different, e.g., $T_{e,0} = 10^3\ T_{p,0}$, the typical t_{eq} for our model is on the order of 440 yr. It will be shown later that this is way below the typical dynamo timescales, which can be up to many Myr. Thus, the electron and the proton temperature can be assumed to be equal in our calculation. A comparison of the length scales (7.7) and (7.8) in our model can be found in figure 7.1. When the gyro-radius becomes smaller than the mean-free path, the magnetic field dominates the dynamics of the plasma, i.e. it becomes "magnetized". In our model the electron fluid becomes magnetized at a magnetic field strength of roughly 10^{-12} G, the ion fluid at 10^{-10} G.

Viscosity

In the transition from an unmagnetized to a magnetized state, the plasma becomes anisotropic, i.e. certain physical quantities then depend on their relative orientation

to the magnetic field direction. This has been discussed in detail in section 3.1.5. On this place, we further analyze the different behaviors of electrons and ions.
In the unmagnetized case the kinematic viscosities for electrons and ions obtained from the Chapman-Enskog closure scheme are (Braginskii, 1965)

$$\nu_{\parallel,\mathrm{e}} = 0.73\frac{\tau_\mathrm{e} kT}{m_\mathrm{e}} = 1.4\times10^{14}\ \mathrm{cm^2 s^{-1}} \tag{7.11}$$

$$\nu_{\parallel,\mathrm{p}} = 0.96\frac{\tau_\mathrm{p} kT}{m_\mathrm{p}} = 8.7\times10^{15}\ \mathrm{cm^2 s^{-1}} \tag{7.12}$$

with the collision times for electrons and ions

$$\tau_\mathrm{e} = \frac{6\sqrt{2}\pi^{3/2}\sqrt{m_\mathrm{e}}(kT)^{3/2}}{16\pi^2\ln(\Lambda)e^4 n} \tag{7.13}$$

$$\tau_\mathrm{p} = \frac{12\pi^{3/2}\sqrt{m_\mathrm{p}}(kT)^{3/2}}{16\pi^2\ln(\Lambda)e^4 n}. \tag{7.14}$$

In the presence of a strong magnetic field the viscosity becomes anisotropic and one has to distinguish between the viscosity along (parallel to) and the one perpendicular to the magnetic field lines. While the parallel viscosity stays the same as in the unmagnetized case (e.g., equations 7.11 and 7.12), the viscosity perpendicular to the field is given by (Simon, 1955)

$$\nu_{\perp,\mathrm{e}}(B) = 0.51\frac{kT}{\omega_{\mathrm{c,e}}(B)^2\tau_\mathrm{e} m_\mathrm{e}} \tag{7.15}$$

$$\nu_{\perp,\mathrm{p}}(B) = \frac{3kT}{10\omega_{\mathrm{c,p}}(B)^2\tau_\mathrm{p} m_\mathrm{p}} \tag{7.16}$$

with the gyro-frequencies of the electrons and the protons $\omega_{\mathrm{c,e}}(B) = eB/(m_\mathrm{e}c)$ and $\omega_{\mathrm{c,p}}(B) = eB/(m_\mathrm{p}c)$.
The different viscosities as a function of density are shown in figure 7.2. Note that the perpendicular viscosity only becomes valid when the plasma is magnetized, i.e. when the gyro-radius becomes smaller than the mean-free path. According to figure 7.1 this is the case above a magnetic field strength of 10^{-11} G for the electrons and 10^{-9} G for the ions. Thus, the most important part of the viscosity is the parallel one and we will ignore the perpendicular part, which decreases proportional the $1/B^2$, from now on. Furthermore, the viscosity of the ions exceeds the electron viscosity by roughly two orders of magnitude. This is caused by the fact that the ions carry the largest part of the momentum. In total, the parallel viscosity of the ions is the crucial quantity and we will refer from now on to

$$\nu \equiv \nu_{\parallel,\mathrm{p}} \approx 8.7\times10^{15}\ \mathrm{cm^2 s^{-1}}. \tag{7.17}$$

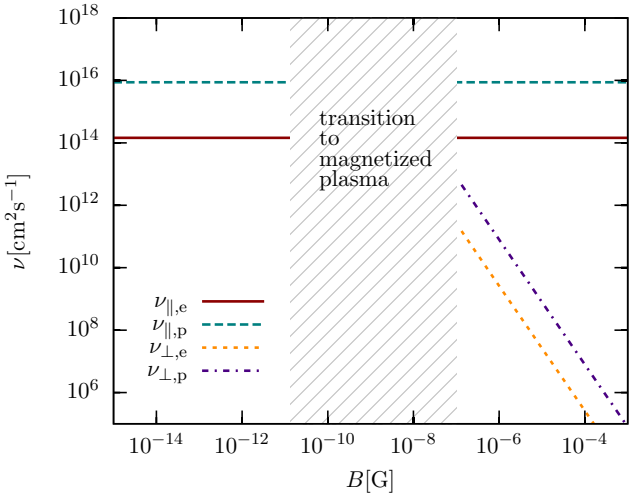

Figure 7.2:
The kinematic viscosity parallel ($\nu_\parallel$) and perpendicular to the magnetic field lines ($\nu_\perp$) as a function of magnetic field strength B. We show the results for the electron as well as for the ion fluid. The range between 10^{-11} G and 10^{-7} G is not shown, as here the transition from the unmagnetized to a magnetized plasma takes place.
image credit: Schober et al. (2013)

Magnetic Diffusivity

For the parallel conductivity the closure scheme yields (Spitzer, 1956)

$$\sigma_\parallel = 1.96 \frac{4\pi n e^2 \tau_\mathrm{e}}{m_\mathrm{e}} \tag{7.18}$$

and for the conductivity perpendicular to the magnetic field

$$\sigma_\perp = 0.51 \sigma_\parallel. \tag{7.19}$$

The conductivity perpendicular to the magnetic field lines is, contrary to the case of viscosity, no function of the magnetic field strength. The difference between the parallel and the perpendicular component of the conductivity is just approximately a factor of two. Usually, $\sigma_\parallel$ is used to determine the magnetic diffusivity η of a plasma. We thus find

$$\eta = \frac{c^2}{4\pi\sigma_\parallel} = 4.7 \times 10^9 \ \mathrm{cm^2 s^{-1}}. \tag{7.20}$$

Magnetic Prandtl Number

With these values of viscosity and resistivity the magnetic Prandtl number (4.64) is

$$\mathrm{Pm} = \frac{\nu}{\eta} \approx 2.3 \times 10^7. \tag{7.21}$$

Thus, in young galaxies we are clearly in the large Prandtl number regime. This implicates that we can use our analytical solutions for the growth rate of the small scale dynamo.

7.1.3 Turbulence

Generation of Turbulent Motions by Accretion

Structure formation is always associated with accretion. In order to build up the first stars and galaxies, gas flows into the potential wells of dark matter halos, where it gets compressed and cools. The potential energy released during that process in parts gets converted into turbulent kinetic energy (Klessen & Hennebelle, 2010), which has been discussed in more detail in section 5.2 of this thesis. Simulations by Greif et al. (2008) of atomic cooling halos confirm that accretion is an efficient driving mechanism of turbulence. They observe how gas is cooled down and flows into the central regions of the halo at high velocities in the cold accretion phase (Dekel et al., 2009; Nelson et al., 2013).

Generation of Turbulent Motions by Supernova Explosions

Once stars have formed, their feedback strongly influences the ISM in galaxies in terms of ionizing radiation and at later stages by SN explosions, which are especially important for the generation of turbulence.
In order to calculate the corresponding energy input, we need to estimate the rate of SN explosions. The star formation rate (SFR) is proportional to the mass density $\rho = nm$ over the free-fall time $t_{\rm ff} = (3\pi/(32G\rho))^{1/2}$ (Mac Low & Klessen, 2004; McKee & Ostriker, 2007):

$$SFR \propto \frac{\rho}{t_{\rm ff}}. \tag{7.22}$$

From the star formation rate we can estimate the supernova rate (SNR). For this we divide the star formation rate by the typical mass of a star that results in a SN ($10\ M_\odot$). As not all the gas goes into stars and not all the stars are massive enough to end in a SN we introduce an efficiency factor α:

$$SNR \approx \alpha \frac{\rho}{t_{\rm ff} \cdot 10\ M_\odot}. \tag{7.23}$$

The number of supernovae within the whole galaxy with a volume $V_{\rm gal}$ and a time interval t is then given by

$$N_{\rm SN}(t) = SNR\ V_{\rm gal}\ t, \tag{7.24}$$

where we assume that the SNR stays constant over time. In general the SN rate is expected to change with time, however, modeling this time dependency goes beyond the scope of this work.

7.1.4 Turbulent Magnetic Field Amplification

Kinematic Small-Scale Dynamo

The magnetic field grows exponentially in the kinematic phase of the turbulent dynamo (see section 4.2 for a discussion of the kinematic dynamo phase):

$$B \propto \exp(\Gamma t). \tag{7.25}$$

In our model we are in the limit of the very high Pm (see equation 7.21), where Schober et al. (2012c) find the growth rate

$$\Gamma = \frac{(163 - 304\vartheta)}{60} \frac{V}{L} Re^{(1-\vartheta)/(1+\vartheta)}. \tag{7.26}$$

Here V is the typical velocity on the largest scale of the turbulent eddies of size L. By solving the Kazantsev equation (4.41) numerically, Bovino et al. (2013) have recently confirmed that equation (7.26) describes the growth rate of the dynamo in the limit large Pm. For our fiducial model with $\vartheta = 0.4$ the growth rate thus scales with $\mathrm{Re}^{0.43}$.

Nonlinear Small-Scale Dynamo

As soon as the magnetic energy is comparable to the kinetic energy of the turbulence on the viscous scale the exponential growth comes to an end. We label this point in time t_ν. The dynamo is then saturated on the viscous scale and the nonlinear growth begins, which has been discussed in section 4.3 of this thesis. Schleicher et al. (2013) the magnetic energy in the non-linear phase scales as

$$\frac{\mathrm{d}}{\mathrm{d}t} E_{\mathrm{mag}} \propto E_{\mathrm{mag}}^{1+(\vartheta-1)/(2\vartheta)}. \tag{7.27}$$

Thus, in the case of Kolmogorov turbulence with $\vartheta = 1/3$ the magnetic energy grows linear in time, while it grows quadratically in case of Burgers turbulence with $\vartheta = 1/2$. In our fiducial model, where we assume $\vartheta = 0.4$, we find $E_{\mathrm{mag}} \propto t^{4/3}$ on ℓ_{a}.

In the nonlinear phase the dynamo process shifts the magnetic energy to larger scales with the peak scale evolving as

$$\ell_{\mathrm{p}}(t) = \ell_\nu + \left(\frac{V}{L^\vartheta} (t - t_\nu) \right)^{1/(1-\vartheta)}. \tag{7.28}$$

From the peak scale to larger scales we assume the spectrum to drop off with the Kazantsev slope. By this we can determine the magnetic field on the forcing scale L at each point in time as

$$B_{\mathrm{L}}(t) = B_{\ell_{\mathrm{p}}}(t) \left(\frac{\ell_{\mathrm{p}}(t)}{L} \right)^{5/4}. \tag{7.29}$$

The nonlinear growth phase comes to an end, when saturation on the turbulent forcing scale is achieved. Now the spectrum of the magnetic energy density scales as the one of the kinetic energy density.

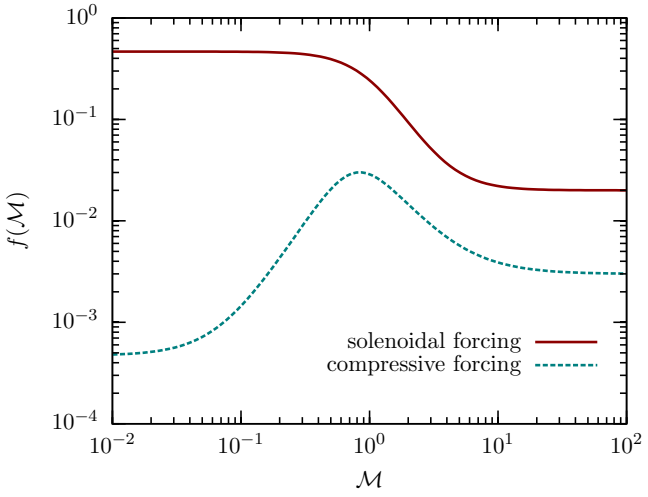

Figure 7.3:
The ratio of magnetic over turbulent kinetic energy at saturation $f(\mathcal{M})$ as a function of the Mach number $\mathcal{M}$. We present fits for solenoidal (solid line) and compressive forcing (dashed line) of the turbulence from the driven MHD simulations by Federrath et al. (2011).
image credit: Schober et al. (2013)

Saturation Magnetic Field Strength from Dynamo Amplification

A turbulent dynamo can amplify magnetic fields at most to equipartition with the turbulent kinetic energy. However, high-resolution simulations by Federrath et al. (2011) show that only a certain fraction f of the turbulent kinetic energy can be transformed into magnetic energy. This fraction depends on the type of forcing as well as on the Mach number $\mathcal{M}$. We show $f(\mathcal{M})$ for solenoidal and compressive forcing of turbulence in figure 7.3. Note, that the efficiency of the small-scale dynamo in case of compressive forcing peaks at a Mach number of 1, i.e. at the transition from the subsonic to the supersonic regime. At this point shocks appear, which generate solenoidal motions that are more efficient for dynamo amplification. At larger Mach numbers the efficiency decreases again and appears to become constant.
According to Federrath et al. (2010) solenoidal forcing leads to a slope of the turbulence spectrum of 0.43, while compressive forcing results in $\vartheta \approx 0.47$. For our fiducial model we choose the saturation efficiency of solenoidal driven turbulence, as we assume a spectrum with $\vartheta = 0.4$.
The resulting saturation magnetic field strength on the forcing scale is

$$B_{L,\mathrm{sat}} = (4\pi\rho)^{1/2} \; V \; f(\mathcal{M})^{1/2}, \tag{7.30}$$

where V is again the velocity at the forcing scale. If we scale down the turbulent velocity to the viscous scale by

$$v_\nu = \left(\frac{\ell_\nu}{L}\right)^{\vartheta} \; V \tag{7.31}$$

the saturation magnetic field strength on the viscous scale is

$$B_{\nu,\mathrm{sat}} = (4\pi\rho)^{1/2} \; \left(\frac{\ell_\nu}{L}\right)^{\vartheta} \; V \; f(\mathcal{M})^{1/2}. \tag{7.32}$$

Evolution of a Magnetic Field Amplified by the Small-Scale Dynamo

Summarizing the results of this section gives for the magnetic field evolution on the viscous scale

$$B_\nu(t) = \begin{cases} B_{\nu,0}\,\exp(\Gamma t) & t < t_\nu \\ B_{\nu,\mathrm{sat}} & t \geq t_\nu, \end{cases} \tag{7.33}$$

i.e. it grows exponentially with rate (7.26) until saturation on the viscous scale is reached at the time t_ν.
The field on the turbulent forcing scale evolves as

$$B_L(t) = \begin{cases} B_{\ell_\nu,0}\,\exp(\Gamma t)\,\left(\dfrac{\ell_\nu}{L}\right)^{5/4} & t < t_\nu \\ (4\pi\rho)^{1/2} V \left(\dfrac{\ell_\mathrm{p}(t)}{L}\right)^{\vartheta+5/4} f(\mathcal{M})^{1/2} & t_\nu \leq t < t_L \\ B_{L,\mathrm{sat}} & t \geq t_L. \end{cases} \tag{7.34}$$

Until the time t_ν the field grows exponentially in the kinematic phase. For $t \geq t_\nu$ the dynamo is in the nonlinear phase, in which the peak of the magnetic spectrum, which is given by equation (7.28), is shifted toward larger scales. The dynamo is saturated on all scales of the turbulent inertial range including the driving scale for times $t \geq t_L$.
The dynamo amplification of a weak magnetic seed field of 10^{-20} G is shown in figure 7.4. We choose here a forcing scale of 10^3 pc, which is the radius of the spherical halo considered here, and three different turbulent velocities: 1 km s^{-1}, 10 km s^{-1} and 100 km s^{-1}. The microphysical quantities are taken from the calculations in the previous sections. In the figure the dashed lines represent the magnetic field strength on the viscous scale, the solid lines the one on the forcing scale.

7.2 Magnetic Field Evolution in a Protogalaxy

7.2.1 Magnetic Fields from an Accretion-driven Small-scale Dynamo

Forcing Turbulence by Accretion

Accretion in a Spherical Galaxy During the formation of the primordial halo turbulence is generated by accretion (Birnboim & Dekel, 2003; Semelin & Combes, 2005; Wise et al., 2008; Vogelsberger et al., 2013). Simulations show that accretion flows have high Mach numbers with respect to the cold gas even in the central regions of the halo (Greif et al., 2008). The characteristic forcing scale in case of a spherical halo is the radius, where the accretion flow comes to a halt:

$$L_\mathrm{acc} \approx R_\mathrm{sph}. \tag{7.35}$$

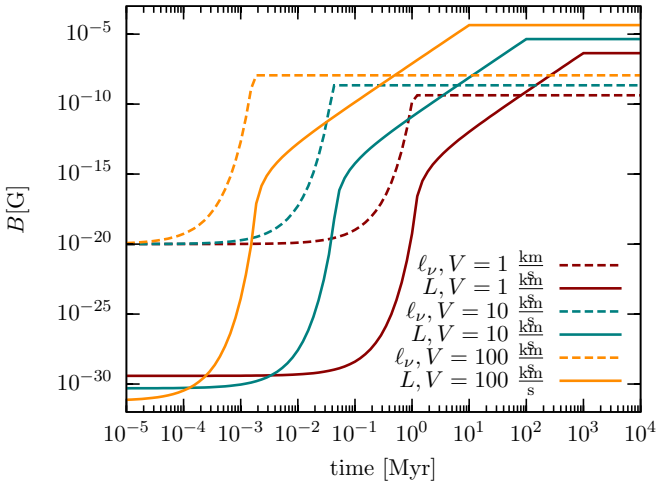

Figure 7.4:
The evolution of the magnetic field amplified by the small-scale dynamo. The dashed lines show the evolution on the viscous scale ℓ_ν, the solid lines the one on the forcing scale of the turbulence L. We use in this plot $L = 10^3$ pc and $\vartheta = 0.4$. The different colors indicate different turbulent velocities $V = 1 - 100$ km s^{-1}. The microphysical quantities are determined in section 7.1.2. The viscosity is $\nu = 4.7 \times 10^9$ cm^{2}s^{-1}, the magnetic resistivity $\eta = 37.8$ cm^{2}s^{-1}, the density is $n = 10$ cm^{-3} and the mean particle mass is $m = 1.6 \times 10^{-24}$ g. The initial magnetic field strength on the viscous scale in this plot is $B_0 = 10^{-20}$ G.
image credit: Schober et al. (2013)

Latif et al. (2013) show in their simulation of a nearly isothermal protogalaxy that the Mach number in such environment is roughly 2. Thus, the typical turbulent velocities from accretion are on the order of

$$V_{\rm acc} \approx 2\ c_{\rm s}\ \beta^{1/2}, \tag{7.36}$$

where $c_{\rm s} = (\gamma kT/m)^{1/2}$ is the sound speed and we use an adiabatic index γ of 5/3. Further, we assume here that only a certain fraction β of the kinetic energy of the accretion flows goes into turbulence, with β typically depending on the density contrast between the accretion flows and the halo (Klessen & Hennebelle, 2010). Simulations (Latif et al., 2013) indicate that about five percent of the kinetic energy are in turbulent motions, i.e. $\beta \approx 0.05$.
The resulting turbulent length scales, velocities and Reynolds numbers for a spherical galaxy are given in table 7.1.

Accretion in a Disk-like Galaxy In the case of a disk-like galaxy we adopt the typical forcing scale of the turbulence by accretion flows to be the scale height

$$L_{\rm acc} \approx H_{\rm disk}. \tag{7.37}$$

We further estimate the typical velocity for accretion flows to be on the order of the Kepler velocity in a disk

$$V_{\rm Kepler} \approx (G\ n\ m\ \pi\ R_{\rm disk}\ H_{\rm disk})^{1/2}\ . \tag{7.38}$$

If a percentage β of the kinetic energy goes into turbulence, the resulting turbulent velocity is given by

$$V_{\rm acc} \approx V_{\rm Kepler}\ \beta^{1/2}. \tag{7.39}$$

Typical values of the length scale, the velocity scales and the Reynolds numbers with a value of $\beta = 0.05$ are summarized in table 7.1.

Accretion-driven Small-scale Dynamo

Based on the discussion of the strength of magnetic seed fields in the introduction, we assume the initial magnetic field strength on the viscous scale to be

$$B_{\nu,0} = 10^{-20}\ \text{G}. \tag{7.40}$$

This is a rather conservative estimate.
The small-scale dynamo amplifies this seed field as soon as sufficient turbulence has evolved. The typical growth rates in the kinematic phase are summarized in table 7.1. We find 150 Myr^{-1} for the case of a spherical galaxy and 1400 Myr^{-1} for a disk. A fraction of the magnetic energy can be dissipated again by Ohmic diffusion. The dissipation rate on the viscous scale ℓ_ν is given by

$$\Gamma_{\text{Ohm},\nu} = \frac{\eta}{\ell_\nu^2}. \tag{7.41}$$

In our model $\Gamma_{\text{Ohm},\nu}$ is on the order of $10^{-12} - 10^{-10}$ Myr^{-1} and thus can be neglected compared the growth rate of the magnetic field.
With these relatively large growth rates, the small-scale dynamo amplification works on very short timescales. We find that in a spherical galaxy a magnetic field of 1.6×10^{-6} G and be reached on a scale of 10^3 pc after 270 Myr. In a disk the saturation field strength is larger by a factor of more than 2. However, the field is only on a scale of 240 pc, but it is saturated after already 24 Myr.
The efficiency of the small-scale dynamo, i.e. the saturation magnetic field strength ($B_{\text{sat},\nu}$ or $B_{\text{sat},L}$) that can be achieved and the time on which saturation occurs (t_ν or t_L), depends strongly on the amount of turbulent kinetic energy, controlled by the parameter β (see equations 7.36 and 7.39). In our fiducial model we use $\beta = 0.05$, however, this is a rough assumption. We test how the dynamo efficiency changes when varying β in figure 7.5.
In the upper panel of figure 7.5 we show the dependency of the viscous scale ℓ_ν and the forcing scale L on β. Of course L is not effected by β, while ℓ_ν, which is a function of the Reynolds number and thus of the turbulent velocity, decreases with increasing β. The time until saturation of the dynamo, which is shown in the middle panel of figure 7.5, also decreases with increasing β. This is a natural consequence of the larger amount of turbulent kinetic energy. In the same way the plot in the lower panel can be understood: the more turbulent energy, i.e. the higher β, the higher is the saturation field strength. The magnetic field strength on the forcing scale $B_{\text{sat},L}$ increases as

$$B_{\text{sat},L} \propto \beta^{1/2}. \tag{7.42}$$

	Accretion-Driven Dynamo		SN-Driven Dynamo	
	sphere	disk	sphere	disk
L	10^3 pc	2.4×10^2 pc	7.0×10^2 pc	2.4×10^2 pc
V	3.7 km s^{-1}	9.7 km s^{-1}	47 km s^{-1}	61 km s^{-1}
Re	1.3×10^{11}	8.1×10^{10}	1.2×10^{12}	5.1×10^{11}
Rm	2.4×10^{17}	1.5×10^{17}	2.2×10^{18}	9.6×10^{17}
ℓ_ν	1.1×10^{-5} pc	3.8×10^{-6} pc	1.7×10^{-6} pc	1.0×10^{-6} pc
Γ	1.5×10^2 Myr^{-1}	1.4×10^3 Myr^{-1}	7.1×10^3 Myr^{-1}	1.9×10^4 Myr^{-1}
t_ν	1.7×10^{-1} Myr	1.9×10^{-2} Myr	3.8×10^{-3} Myr	1.5×10^{-3} Myr
t_L	2.7×10^2 Myr	24 Myr	15 Myr	3.8 Myr
$B_{\mathrm{sat},\nu}$	1.1×10^{-9} G	3.3×10^{-9} G	7.5×10^{-9} G	1.2×10^{-8} G
$B_{\mathrm{sat},L}$	1.6×10^{-6} G	4.3×10^{-6} G	2.1×10^{-5} G	2.7×10^{-5} G

Table 7.1:
The characteristic quantities of the small-scale dynamo for accretion-driven turbulence (left hand side) and for SN-driven turbulence (right hand side). In each case we present results for a spherical galaxy and a disk-shaped galaxy. We list the forcing scale of the turbulence L, the typical turbulent velocity on that scale V, the hydrodynamic and magnetic Reynolds numbers Re and Rm, the viscous scale ℓ_ν, the kinematic growth rate of the dynamo Γ, the time until saturation on the viscous and the forcing scale occurs t_ℓ and t_L and the saturation field strengths on those scales $B_{\mathrm{sat},\nu}$ and $B_{\mathrm{sat},L}$. All the given values in this table are for the fiducial model with a factor $\beta = 0.05$ of kinetic energy that goes into turbulent motions and a SN efficiency of $\alpha = 0.01$.

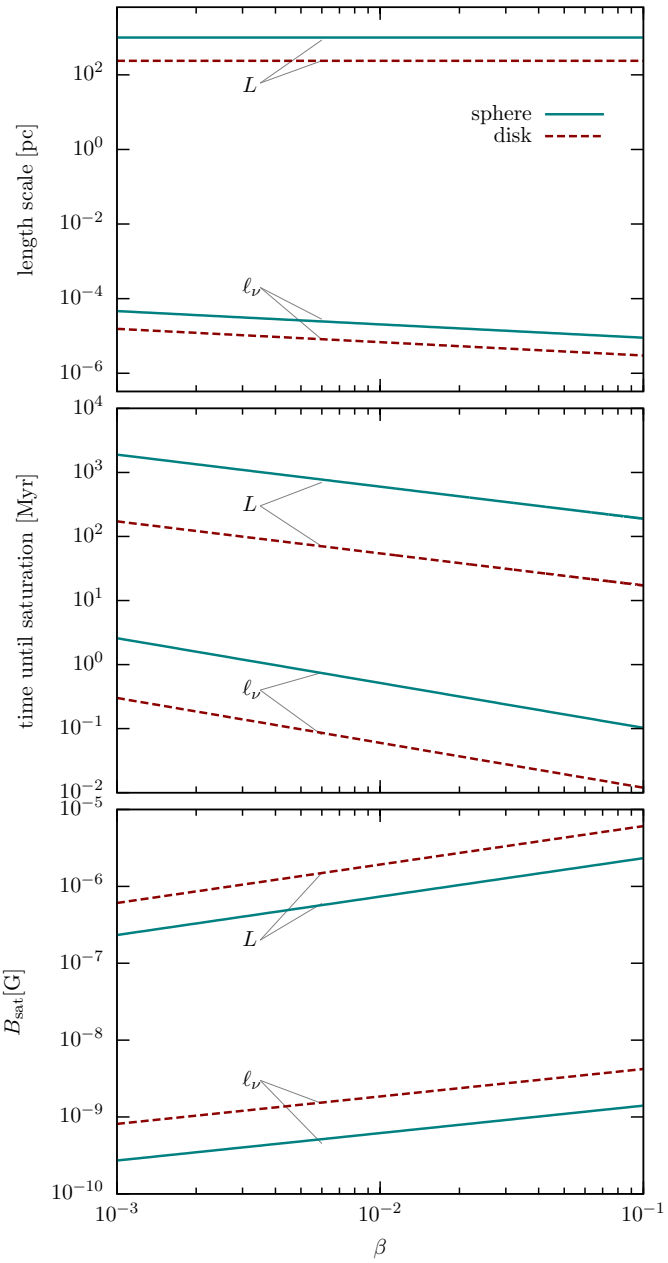

Figure 7.5:
The dependency of the accretion-driven small-scale dynamo mechanism on the percentage of kinetic energy that goes into turbulence β. The upper panel shows the different length scales, the middle panel the time until saturation, i.e. t_ν and t_L, and the lower panel the saturation magnetic field strength $B_{\rm sat}$. We plot all quantities on the viscous scale ℓ_ν and on the turbulent forcing scale L as indicated in the figure. The solid blue lines show the results for a spherical galaxy, the dashed red lines the ones for a disk.
image credit: Schober et al. (2013)

7.2.2 Magnetic Fields from Stellar Feedback

Distributing Stellar Magnetic Fields by Supernovae

A natural source for magnetic fields in the ISM of galaxies are stellar magnetic fields that get distributed over large volumes by SN explosions. Schober et al. (2012b) have shown that the small-scale dynamo can produce strong magnetic fields during primordial star formation. Hints to dynamical important magnetic fields during the formation of the first stars also come from high-resolution numerical simulations (Federrath et al., 2011; Turk et al., 2012; Sur et al., 2012) and further semi-analytical calculations (Schleicher et al., 2010). Thus, we expect the first and second generations of stars to be magnetized.

Properties of Supernova Candidates We assume that a typical star that ends in a supernova has a mass of

$$M_{\rm star} = 10\ M_\odot \tag{7.43}$$

and a radius of

$$R_{\rm star} = \left(\frac{M_{\rm star}}{M_\odot}\right)^{0.8} R_\odot \tag{7.44}$$

with the solar mass $M_\odot = 2 \times 10^{33}$ g and radius $R_\odot = 7 \times 10^5$ km.
It is very difficult to estimate the magnetic energy in a typical population III star, as there is not much theoretical work on that topic so far. In principle, one could assume that a certain percentage of the total energy of the SN energy is within the magnetic field. If the magnetic energy $B^2_{\rm star}/(8\pi)\ 4/3\pi R^3_{\rm star}$ equals e.g., 0.001 $E_{\rm SN}$, the stellar magnetic field would have a very high value of $B_{\rm star} = 8 \times 10^6$ G.
Here, however, we use as a crude estimate for the magnetic field of population III stars based on observations of present-day massive stars. In most high-mass stars no magnetic fields are detected, there are few percent of stars with an enhanced magnetic field (see Donati & Landstreet (2009)). These so-called "peculiar A or B" stars have a typical dipole field strength of

$$B_{\rm star} = 10^4 \text{ G}. \tag{7.45}$$

We take this value as an upper limit of magnetic fields in primordial stars, but also test lower stellar field strengths in the following.

Evolution of a Supernova Remnant Stars with masses above 8 solar are expected to explode as a core-collapse supernova, introducing additional turbulent energy into the ISM (Choudhuri, 1998; Padmanabhan, 2001). Initially the shock front of a SN expands freely, i.e. the pressure of the surrounding ISM is negligible. The shock velocity $v_{\rm e}$ can then be determined by

$$E_{\rm SN} = \frac{1}{2} M_{\rm e} v_{\rm e}^2, \tag{7.46}$$

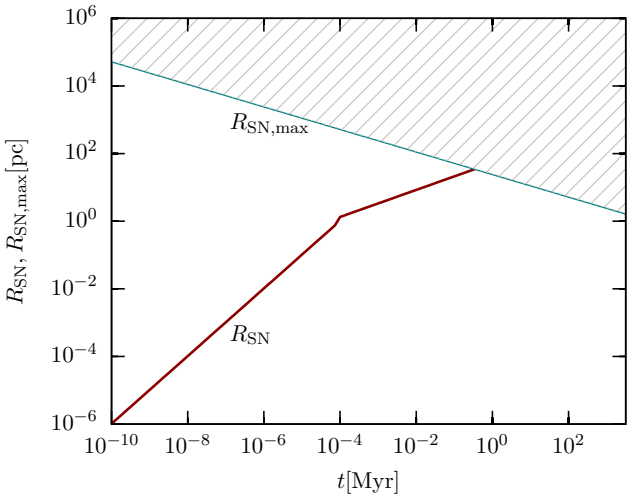

Figure 7.6:
The red line shows the radius of a SN shock $R_{\rm SN}(t)$ as a function of time. Up to roughly 100 yr the SN shock expands freely, then the Sedov-Taylor expansion sets in. The available maximum radius for SNe $R_{\rm SN,max}(t)$ as a function of time is shown for the case of a spherical halo by the blue line. This radius decreases in time, as the number of SN in the protogalactic core increases. The first SN shocks collide after a time of approximately 0.36 Myr.
image credit: Schober et al. (2013)

where $E_{\rm SN}$ is the energy of a SN (neglecting the energy loss by neutrinos) and $M_{\rm e}$ the ejected mass. The shock radius $R_{\rm SN}$ as a function of time t is thus

$$R_{\rm SN}(t) = \left(\frac{2E_{\rm SN}}{M_{\rm e}}\right)^{1/2} t. \tag{7.47}$$

The free expansion phase ends, when the accumulated mass of the ISM in front of the shock is of order of $M_{\rm e}$. This happens at the so-called sweep-up radius $R_{\rm sw}$ defined by

$$M_{\rm e} = \frac{4}{3}\pi R_{\rm sw}^3 \rho \tag{7.48}$$

with ρ being the mean density of the ISM. The shock front reaches $R_{\rm sw}$ at a time

$$t_{\rm sw} = \frac{R_{\rm sw}}{v_{\rm e}} = \left(\frac{3}{4\pi\rho}\right)^{1/3} \left(\frac{1}{2E_{\rm SN}}\right)^{1/2} M_{\rm e}^{5/6}, \tag{7.49}$$

which is in our model on the order of 100 yr. For $t > t_{\rm sw}$ the expansion of the supernova remnant is driven adiabatically by thermal pressure, which is known as the Sedov-Taylor phase (Sedov, 1946; Taylor, 1950; Sedov, 1959). We can estimate the radius of the shock in this case with

$$\frac{\rm d}{{\rm d}t}\left(4\pi R_{\rm SN}^3 \rho \dot{R}_{\rm SN}\right) = 4\pi R_{\rm SN}^2 P, \tag{7.50}$$

where the $\dot{}$ indicates a time derivative and the pressure P is given by

$$P = (\gamma - 1)\frac{E_{\rm SN}}{\frac{4}{3}\pi R_{\rm SNR}^3} \tag{7.51}$$

with $\gamma = 5/3$ for adiabatic expansion. We can solve equation (7.50) with a simple power-law ansatz and find

$$R_{\mathrm{SN}}(t) = \left(\frac{25 E_{\mathrm{SN}}}{4\pi\rho}\right)^{1/5} t^{2/5}. \tag{7.52}$$

Thus, the evolution of the SN remnant can be described by (Choudhuri, 1998)

$$R_{\mathrm{SN}}(t) = \begin{cases} \left(\dfrac{2E_{\mathrm{SN}}}{M_{\mathrm{e}}}\right)^{1/2} t & t < t_{\mathrm{sw}} \\ \left(\dfrac{25E_{\mathrm{SN}}}{4\pi\rho}\right)^{1/5} t^{2/5} & t > t_{\mathrm{sw}}. \end{cases} \tag{7.53}$$

We assume now that the energy released in a SN explosion is $E_{\mathrm{SN}} = 10^{51}$ erg and that about 10 percent of the mass of the progenitor star is ejected, i.e. $M_{\mathrm{e}} \approx 0.1\ M_{\mathrm{star}}$. In our model the SN remnants evolve as described in equation (7.53) and shown in figure 7.6 until they collide. At later stages of shock evolution other energy loss mechanisms become dominant. The electrons lose their energy by ionization, bremsstrahlung, synchrotron emission and inverse Compton scattering. The latter is the most important energy loss channel at high redshifts as here the density of the CMB photons is considerably larger (Schleicher & Beck, 2013).
If the SNe are distributed homogeneously in the protogalaxy, each SN shell has a mean maximum radius at the first collision of

$$R_{\mathrm{SN,max}}(t) = \frac{R}{N_{\mathrm{SN}}(t)^{\xi}}, \tag{7.54}$$

where the radius of the galaxy R is given in equations (7.3) and (7.6) and the exponent ξ depends on the geometry of the galaxy. In case of a spherical halo $\xi = 1/3$, in case of a thin disk $\xi = 1/2$. The maximum expansion radius of the SN shock is shown in figure 7.6 for the spherical case.
By comparing (7.53) to (7.54) we find the typical time scale for SN collisions t_{SN}. At that point the SN bubbles fill approximately the whole galaxy. In the spherical case we find

$$t_{\mathrm{SN}} \approx 0.36 \text{ Myr}, \tag{7.55}$$

which we take as the typical timescale for SN collisions. Further, we use $R_{\mathrm{SN}}(t_{\mathrm{SN}})$ as the typical length scale of SN shocks.

Magnetic Field Evolution If now all the stellar magnetic energy is distributed into the volume available by the SN explosion and no significant magnetic energy is left in the stellar remnant, the resulting magnetic field strength in the ISM after the first SN generation is

$$B_{\mathrm{ISM}} = \left(\frac{R_{\mathrm{star}}}{R_{\mathrm{SN}}(t_{\mathrm{SN}})}\right)^2 B_{\mathrm{star}}. \tag{7.56}$$

Here, we assumed a spherical shape of the galaxy and flux freezing. All the following stars will produce roughly the same amount of magnetic energy, that is then distributed in the ISM by SN. Thus, the time evolution of the stellar magnetic fields in galaxies can be approximated by

$$B_{\rm ISM}(t) = \left(\frac{R_{\rm star}}{R_{\rm SN}(t_{\rm SN})}\right)^2 B_{\rm star}\,\frac{t}{t_{\rm SN}}. \tag{7.57}$$

The values of $R_{\rm SN}(t_{\rm SN})$ and $t_{\rm SN}$ depend obviously on the SN rate, which is determined by the parameter α as defined in (7.23). We obtain for the spherical case:

$$t_{\rm SN} \propto \alpha^{-5/11} \tag{7.58}$$

$$R_{\rm SN}(t_{\rm SN}) \propto \alpha^{-2/11} \tag{7.59}$$

leading to a dependency of the magnetic field distributed by SN on the efficiency of the SN rate of

$$B_{\rm ISM}(t) \propto \alpha^{9/11}\, t. \tag{7.60}$$

In figure 7.7 we show the evolution of the distributed magnetic fields for different mean magnetic fields of the stars (10^4 to 10^2 G) and for our fiducial case of $\alpha \approx 0.01$. Note that the case of 10^4 G is an upper limit of magnetic fields in massive stars. We assume the magnetic fields of the first stars to be considerably lower.
The distribution of stellar magnetic fields by SNe explosions thus does not seem to be important compared to the dynamo amplification in the ISM. However, after a sufficient time the SN could contribute to the magnetic energy in the ISM. If the equipartition field strength is roughly 10^{-6} G, the time after which SN distribution becomes important is

$$t \approx t_{\rm SN}\,\left(\frac{R_{\rm SN}(t_{\rm SN})}{R_{\rm star}}\right)^2\,\left(\frac{10^{-6}\ {\rm G}}{B_{\rm star}}\right). \tag{7.61}$$

For our fiducial model we find that this time is about 2.2×10^6 Myr in case of typical stellar field strengths of 10^4 G. Observations of present-day massive stars indicate that only a few percent have these high field strengths. We thus also consider the more likely case of lower mean stellar fields. For a mean strength of 10^3 G we find that a micro-Gauss ISM field is only reached after 2.2×10^7 Myr and for a mean strength of 10^2 G after 2.2×10^8 Myr. Thus, the typical timescales of distribution of stellar magnetic fields by supernovae exceed the age of the Universe by many orders of magnitude and this process cannot be an important contribution for the fields in the ISM, unless the first stars were much stronger magnetized than the present-day stars.
In the case of a flat disk-shaped galaxy, where we assume the parameter ξ in equation (7.54) to be 1/2, the distribution of stellar magnetic fields proceeds marginally faster. Here the typical time until a field strength of 10^{-6} G in the ISM is reached is roughly a factor of 10 more quickly.

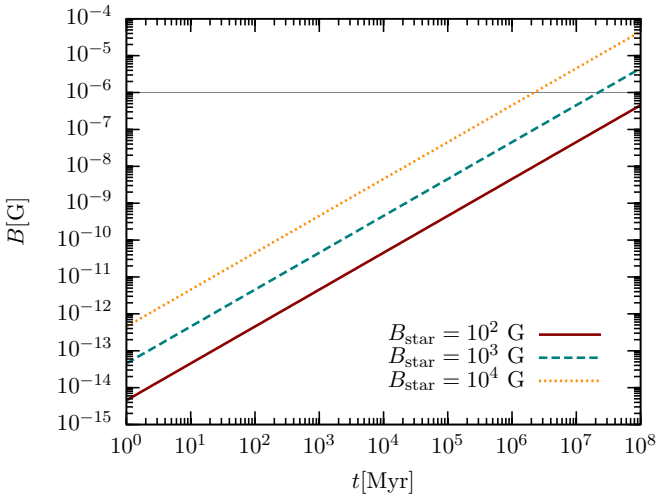

Figure 7.7:
The evolution of the magnetic field, when the only source of magnetic energy in the ISM are stellar magnetic fields distributed by SN explosions. The curves show the results for a spherical halo in our fiducial model with a SN efficiency of $\alpha = 0.01$. We show three different mean stellar field strengths: 10^4 G (yellow dotted line), 10^3 G (green dashed line) and 10^2 G (solid red line). With the thin gray line we further indicate the typical saturation strength of a magnetic field generated by a small-scale dynamo.
image credit: Schober et al. (2013)

In reality the evolution of magnetic fields in SN shock fronts is of course more complicated. In addition to simple flux freezing further amplification processes can take place. Miranda et al. (1998) argue that in a multiple explosion scenario of structure formation (Ostriker & Cowie, 1981; Miranda & Opher, 1997) magnetic seed fields on the order of 10^{-10} G can be produced on galactic scales. In their model a Biermann battery is operating in the shock of SN explosions of the first stars as here unparallel gradients of temperature and density can be established. Recently, Beck et al. (2013) have also analyzed the magnetic field evolution in protogalaxies based on SN explosions with the cosmological N-body code GADGET. They find that a combination of SNe and subsequent magnetic field amplification leads to magnetic field strengths of a few μG, which is comparable to our results, and that the strength of seed field is coupled to the star formation process.

Dynamo Amplification Driven by SN Turbulence

SN-driven Dynamo in a Spherical Galaxy In section 7.1.3 we discussed the generation of SN turbulence based on numerical simulations. Now we estimate the typical forcing scale $L_{\rm SN}$ and the fluctuation velocity on that scale $V_{\rm SN}$ in order to determine the Reynolds number (4.9) and the resulting growth rate of the kinematic small-scale dynamo (7.26). For that we assume that the turbulence driving in the galaxy is in equilibrium.
Then the turbulent pressure, which is roughly

$$P_{\rm turb} \approx V_{\rm SN}^2 \rho, \tag{7.62}$$

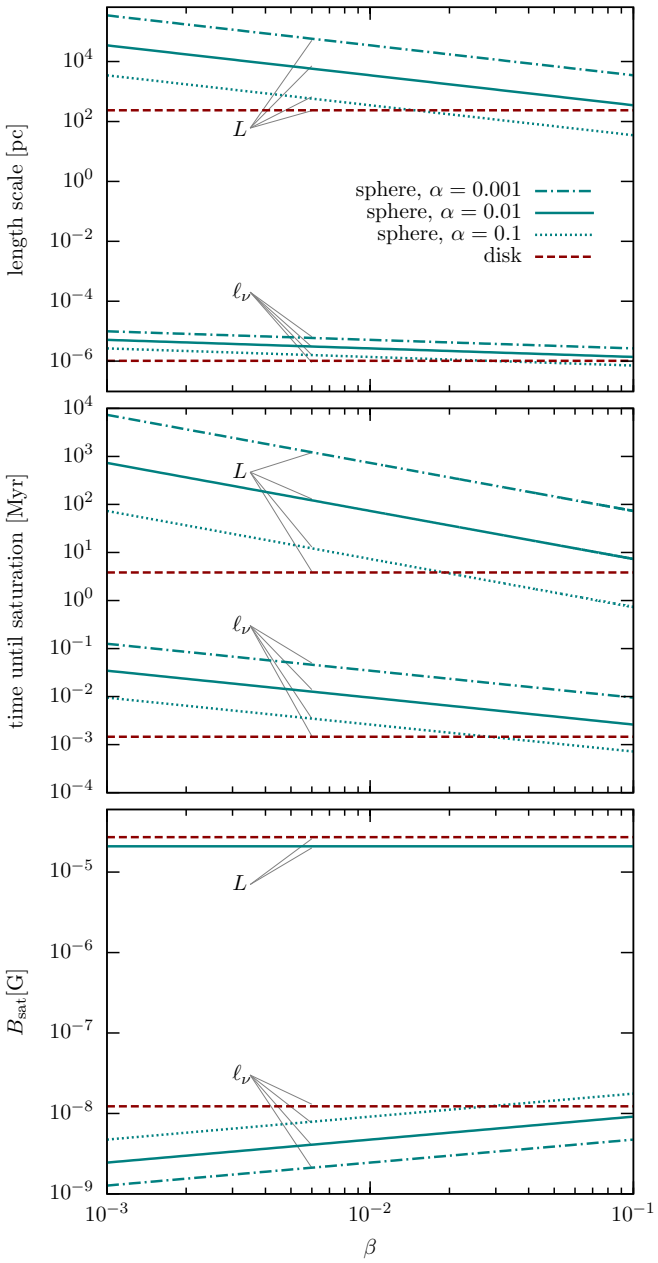

Figure 7.8:
The dependency of the SN-driven small-scale dynamo mechanism on the percentage of kinetic energy that goes into turbulence β and the SN efficiency α. The upper panel shows the different length scales, the middle panel the time until saturation, i.e. t_ν and t_L, and the lower panel the saturation magnetic field strength $B_{\rm sat}$. We plot all quantities on the viscous scale ℓ_ν and on the turbulent forcing scale L as indicated in the figure. The dashed-dotted blue line represents the case of a spherical galaxy with $\alpha = 0.001$, the solid blue line the fiducial case of $\alpha = 0.01$ and the dotted blue line the case of $\alpha = 0.1$. The dashed red line shows the results for a disk-like galaxy. There are only 6 lines in the lower plot instead of 8. This results from the fact, that in the spherical case the saturation field strength on the forcing scale does not depend on α nor on β, in contrast to L and t_L (see equations (7.69) to (7.73)).
image credit: Schober et al. (2013)

balances the hydrostatic pressure P determined by

$$\frac{\mathrm{d}P}{\mathrm{d}r} = \rho\ g(r). \tag{7.63}$$

The gravitational acceleration in the spherical case is roughly $g(r) = \frac{4}{3}\pi\rho G r$. Solving equation (7.63) and setting it equal to equation (7.62) yields the turbulent velocity V_{SN}. We find in the spherical case:

$$V_{\mathrm{SN}} \approx \left(\frac{2}{3}\pi\rho G\right)^{1/2} R_{\mathrm{sph}}. \tag{7.64}$$

The forcing length scale can be estimated by comparing the energy input rate with the dissipation rate:

$$SNR\ \beta\ E_{\mathrm{SN}} = \frac{\frac{1}{2}\rho V_{\mathrm{SN}}^2}{t_{\mathrm{dis}}}, \tag{7.65}$$

where the dissipation timescale is

$$t_{\mathrm{dis}} = \frac{L_{\mathrm{SN}}}{V_{\mathrm{SN}}} \tag{7.66}$$

and SNR is the supernova rate (7.23). Thus, we find the typical forcing scale of SN-driven turbulence

$$L_{\mathrm{SN}} = \frac{\rho\ V_{\mathrm{SN}}^3}{SNR\ \beta\ E_{\mathrm{SN}}}. \tag{7.67}$$

As in the case of the accretion-driven small-scale dynamo we start with an initial magnetic field strength on the viscous scale of

$$B_{\nu,0} = 10^{-20}\ \mathrm{G}. \tag{7.68}$$

The turbulence driven by SN shocks makes dynamo action possible, which leads to rapid amplification of the seed field according to equations (7.33) and (7.34). For the case of a spherical galaxy we find that the growth rate in the kinematic amplification phase is $7.1 \times 10^3\ \mathrm{Myr}^{-1}$. After a time of 15 Myr the saturation field strength of 2.1×10^{-5} G is reached on the forcing scale. The characteristic quantities of our fiducial models for the SN-driven dynamo are summarized in the right part of table 7.1.

As in case of accretion turbulence, the efficiency of the small-scale dynamo is sensible to the amount of kinetic energy that goes into turbulence β. Moreover, when modeling the scale of turbulence forcing we add another uncertainty namely the supernova rate, which includes the efficiency parameter α (see equation 7.23). In our fiducial model we choose $\alpha = 0.01$, but there could easily be a variation of a factor

10. The dependency of the quantities most important for the dynamo amplification on α and β in case of a spherical halo is the following:

$$\ell_{\nu,\mathrm{SN}} \propto (\alpha\beta)^{-0.28} \tag{7.69}$$
$$L_{\mathrm{SN}} \propto (\alpha\beta)^{-1} \tag{7.70}$$
$$V_{\mathrm{SN}} = \mathrm{const} \tag{7.71}$$
$$B_{\nu,\mathrm{sat,SN}} \propto (\alpha\beta)^{0.28} \tag{7.72}$$
$$B_{L,\mathrm{sat,SN}} = \mathrm{const} \tag{7.73}$$

We show the dependency of the length scales, the time until saturation and the saturation magnetic field strength on β and for different values of α in figure 7.8.

SN-driven Dynamo in a Disk-like Galaxy We perform the same analysis for the disk case. Here the gravitational acceleration becomes independent of the radius for a thin disk, i.e. $H_{\mathrm{disk}} \ll r$. In that approximation we find $g(r) \approx 2\pi\rho G H_{\mathrm{disk}}$, which leads to a turbulent velocity of

$$V_{\mathrm{SN}} \approx (2\pi\rho G R_{\mathrm{disk}} H_{\mathrm{disk}})^{1/2}\,. \tag{7.74}$$

The forcing scale can be determined by equation (7.67). In case of a disk-shaped galaxy we find that the typical forcing scale L_{SN}

$$L_{\mathrm{SN}} \approx H_{\mathrm{disk}}. \tag{7.75}$$

We find that the kinematic growth rate in our fiducial model is 1.9×10^4 Myr^{-1}. The time until saturation on the forcing scale is then only 3.8 Myr and the saturation field strength is 2.7×10^{-5} G.
In case of a disk-shaped galaxy all the quantities (79) to (7.73) are independent of α and β. For comparison with the spherical galaxy we show them, however, also in figure 7.8.

7.3 Summary of Our Dynamo Model in Young Galaxies

In this chapter we model the evolution of the (turbulent) magnetic field in a young galaxy. We find that weak magnetic seed fields get amplified very efficiently by the small-scale dynamo (see table 7.1), which is driven by turbulence from accretion and from supernova (SN) explosions. Dynamo theory predicts that the magnetic field is amplified in two phases: in the kinematic phase the field grows exponentially until the dynamo is saturated on the viscous scale. Then the non-linear phase begins, where the magnetic energy is shifted towards larger scales until saturation on the turbulent forcing scale.
For our fiducial models of a young galaxy we use a fixed particle density of 10 cm^{-3} and a temperature of 5×10^3 K. We concentrate on two different geometries: a

spherical and a disk-shaped galaxy (see section 7.1.1). We determine the viscosity of the plasma, which gets anisotropic when the plasma becomes magnetized, and the magnetic diffusivity. Turbulence is generated by accretion flows on the galactic core and also by SN shocks. With the typical driving scales and velocities we can determine the hydrodynamic and the magnetic Reynolds number. The magnetic field evolution depends strongly on the type of turbulence, which we assume to be $\vartheta = 0.4$ implying that the turbulence in our protogalaxy is a mixture of solenoidal and compressive modes.

For our fiducial model we find that the dynamo saturates on the largest scale in accretion-driven turbulence after a time of roughly 270 Myr in case of a spherical galaxy and after 24 Myr in case of a disk. Turbulence generated by SN shocks can amplify the magnetic field on shorter timescales, with saturation occuring after 15 Myr in a spherical galaxy and 3.8 Myr in a disk. The dynamo timescale is thus comparable to the free-fall time $t_{\rm ff} = (3\pi/(32G\rho))^{1/2} \approx 16$ Myr. The age of the Universe at the onset of galaxy formation, i.e. at a redshift of 10, is roughly 470 Myr, which is larger than the dynamo timescales by factor of 2 to 120 for our four fiducial models. In the models with the longest amplification times our assumption of constant accretion and supernova rates may thus not be very precise. Nevertheless, these models provide an order of magnitude estimate of the resulting magnetic strength. In case of a disk-like galaxy we can compare the dynamo timescales further to the typical time of one rotation, which turns out to be 340 Myr when using the Kepler velocity (7.38). Thus, we can expect that the small-scale dynamo is saturated within less then one reversal time, the turbulent magnetic field gets ordered and an $\alpha - \Omega$ dynamo, i.e. a galactic large-scale dynamo, sets in.

The magnetic field strengths predicted by our fiducial models are very high with values between 1.6×10^{-6} G and 4.3×10^{-6} G in the accretion-driven case and between 2.1×10^{-5} G and 2.7×10^{-5} G in the SN-driven case for a spherical galaxy and a disk, respectively. These field strengths are comparable with the ones observed in the local Universe, where the typical turbulent field component in present-day disk galaxies is $(2-3) \times 10^{-5}$ G in spiral arms and bars and up to $(5-10) \times 10^{-5}$ G in the central starburst regions (Beck, 2011). New radio observations detect also magnetic fields in dwarf galaxies. Their field strengths, which seem to be correlated with the SFR, are typically a factor of roughly three lower compared to the one in spiral galaxies (Chyży et al., 2011).

Our calculations suggest that the turbulent magnetic field of a galaxy was very high already at high redshifts. An observational confirmation of this result is very complicated. A hint towards an early generation of the turbulent magnetic field in galaxies comes from Hammond et al. (2012). They analyze the rotation measure of a huge catalog of extragalactic radio sources as a function of redshift and find that it is constant up to redshifts of 5.3, which is the maximum redshift in their dataset. A very powerful tool provides moreover the far-infrared (FIR) - radio correlation, which relates the star formation rate to the synchrotron loss of cosmic ray electrons. It is observed to be constant up to redshifts of roughly 2 (Sargent et al., 2010; Bourne et al., 2011), but is expected to break down at a higher redshift, which depends on

the star formation rate and the evolution of typical ISM densities (Schleicher & Beck, 2013). With new instruments like SKA and LOFAR our knowledge about the evolution of the cosmic magnetic fields will increase.
Besides our fiducial models we analyze the effect of changing the amount of kinetic energy that goes into turbulence and find that the dynamo is more efficient the larger the turbulent energy, which is intuitively clear. Furthermore we determine the small-scale dynamo evolution for a varying SNR, which is important for estimating the driving scale of SN turbulence in the case of a spherical core. As expected the time until saturation increases with increasing SNR. However, the typical largest scale of the magnetic field decreases with the SNR.
We further estimate the effect of magnetic field enrichment in galaxies by distributing stellar fields by SN explosions. As an estimate of the magnetic energy in the first stars is very hard, we determine the expected magnetic field evolution in the ISM for three different cases. An upper limit of magnetic field strengths of the primordial stars is 10^4 G, which is a value observed in a the few percent of present-day massive stars that are magnetized. Distributing these mean stellar fields by SNe in the ISM, we find that a ISM field strength of 10^{-6} G is reached after 1.4×10^2 Myr. For stellar fields of 10^3 G we find that a micro-Gauss ISM field is only reached after 1.4×10^3 Myr and for stellar fields of 10^2 G after 1.4×10^4 Myr. Thus, the dynamo increases the magnetic field strength much faster.
With our semi-analytical model we have shown that the small-scale dynamo can amplify weak magnetic seed fields in the ISM of early galaxies on relatively short time scales compared to other evolutionary timescales. This leads to the build-up of strong magnetic fields already at very early phases of (proto)galactic evolution, with potentially strong impact on ISM dynamics and subsequent star formation.

CHAPTER 8

Observational Signatures of Magnetic Fields in Redshifted Galaxies[1]

Besides analytical theory and numerical simulations, observations are the third pillar of astrophysics. It is always desirable to find an observational confirmation to a theory. However, direct observations of the early Universe, for example for the formation era of the first stars and galaxies are not possible. Only indirect observations of these astronomical objects are available. It becomes even more complicated to gain hints about the magnetic field evolution during this epoch.
This chapter follows Schober et al. (2014), who propose a method for estimating the magnetic field strength in star forming galaxies, which could be applicable up to intermediate redshifts.

8.1 The Need for Observational Tests

Observations show that magnetic fields contribute significantly to a galaxys energy budget. The current values for the solar neighborhood, for example, is 0.89 eV cm^{-3} for the magnetic energy density, which is comparable to the thermal kinetic energy density with roughly 0.49 eV cm^{-3}, and the energy density of cosmic rays to be 1.39 eV cm^{-3} (Draine, 2011). We note, however, that the quoted values include large uncertainties. The magnetic energy is distributed over many orders of magnitude in physical length scales. It is thus expected that the magnetic field plays a major role in the dynamics of the whole galaxy and also on smaller scales down to individual star formation processes.
The structure of magnetic fields in local galaxies is known quiet well (see the discussion in section 2.3). A spiral galaxy typically shows a large-scale magnetic field, which follows the optical spiral arms and is strongest in the interarm regions. The

[1] This section follows closely Schober et al. (2014).

typical coherence length is 10 kpc and the strength roughly 10^{-5} G. Even more important in terms of the energy density is the small-scale unordered magnetic field, which exceeds the one of the ordered field by a factor of a few.
The origin and evolution of galactic magnetic fields is still an active field of research with many open questions to answer (Kulsrud & Zweibel, 2008). Theory predicts that unordered fields were generated already in young galaxies by a turbulent dynamo. This mechanism amplifies weak magnetic seed fields by randomly stretching, twisting, and folding the field lines in turbulent motions (Kazantsev, 1968; Brandenburg & Subramanian, 2005; Schober et al., 2012c,a; Bovino et al., 2013). Semi-analytical calculations (Schober et al., 2013) as well as numerical simulations (Beck et al., 2012; Latif et al., 2013) show that the turbulent dynamo can produce a field of the order of 10^{-6} G within a few Myrs. The large-scale magnetic field is likely produced by a large-scale galactic dynamo, which operates on much longer timescales then the turbulent dynamo.
In order to test the evolution scenario of galactic fields, in addition to the analytical and numerical calculations an observational test is essential. However, the problem is that standard methods for magnetic field observations are difficult to pursue at high redshifts. Only indirect observations like the CMB bispectrum (Shiraishi et al., 2012), the non-detection of TeV blazers (Neronov & Vovk, 2010) and Faraday rotation measurements (Hammond et al., 2012), which detect the magnetic field strength along the line of sight, can be applied at high redshifts.
A very frequently used method to estimate magnetic field strengths in galaxies is synchrotron emission, which is observed in the radio band. This type of radiation is emitted by high energy cosmic ray electrons traveling through the magnetized interstellar medium (ISM). With the intensity of synchrotron emission one can calculate the energy density of cosmic rays. By assuming that cosmic rays and interstellar magnetic fields are in energy equilibrium the magnetic field strength can be computed (Beck & Krause, 2005).
A further important observation was made by Yun et al. (2001), who found a correlation between the radio flux and the far-infrared (FIR) flux. This FIR-radio correlation shows a coupling between the star formation rate (SFR), which determines the FIR flux, and the magnetic field in the ISM. A new interpretation of this correlation was suggested by Schleicher & Beck (2013). They claim that the supernova rate, which is proportional to the SFR, sets the amount of turbulence in the ISM, which in turn determines the magnetic energy produced by turbulent dynamo. Due to energy conservation and additional efficiency effects a turbulent dynamo can only convert a certain fraction of turbulent kinetic energy into magnetic energy (Federrath et al., 2011). A coupling between the SFR (FIR flux) and the magnetic field (radio flux) can thus be assumed in local galaxies.
But what happens in higher redshifted galaxies? Here one needs to take into account the rapidly growing number of cosmic microwave background (CMB) photons. These can interact with the cosmic ray electrons in inverse Compton scattering, typically resulting in X-ray photons. Schleicher & Beck (2013) have shown that inverse Compton scattering is in fact the dominant energy loss mechanism of cosmic ray

electrons at high redshifts. Thus, we expect a suppression of the FIR-radio correlation and X-ray bright galaxies above a critical redshift.
We propose here a method based on the inverse Compton scattering process to gain information about cosmic rays and magnetic fields in young galaxies. With a given SFR and interstellar radiation field (ISRF) we determine the inverse Compton component of the X-ray luminosity of a redshifted starforming galaxy. From this we calculate the energy of the cosmic ray electrons and the resulting total cosmic ray energy density. By assuming equipartition between the cosmic ray energy density and the magnetic energy density, we are able to predict an upper limit of the field strength.
New instruments provide exceptionally good data of galaxies at very high redshifts. Especially the deep fields of the *Chandra* satellite[2], the extended *Chandra* Deep Field-South (E-CDF-S) and the *Chandra* Deep Field-North (CDF-N), include lots of information about the X-ray properties of extremely low luminosity objects. As a very important future tool we discuss also limits that will be obtained by X-ray observatory *Athena+*[3]. Combination with the new FIR data from the Atacama Large Millimeter/submillimeter Array (ALMA[4]) can lead to new conclusions. The ALMA LABOCA E-CDF-S Submillimeter Survey makes a multi-wavelength analyses possible.
The chapter is structured as follows: We present our model of young galaxies in section 8.2, including the SFR, the ISRF and the cosmic ray spectrum. In section 8.3 we summarize the results of Schleicher & Beck (2013), who proposed the suppression of the FIR-radio correlation. The combination of our ISRF and the cosmic ray spectrum results in a typical inverse Compton spectrum. The derivation of the inverse Compton X-ray luminosity is given in section 8.4. We discuss additional X-ray sources in section 8.5. In the last section 8.6 we apply our model to some exemplary galaxies, for which data from *Chandra* and ALMA is available. We draw our conclusions in section 8.7.

[2]http://chandra.harvard.edu/
[3]http://www.the-athena-x-ray-observatory.eu/
[4]http://www.almaobservatory.org/

8.2 Model of Typical Galaxies

For exploring the X-ray properties of galaxies we use two different models: a model for a "normal" galaxy and one for a starburst galaxy. The models differ obviously in their star formation rates, which has important consequences for the interstellar radiation field and the number density of cosmic rays. We report the details of our models in the following.

8.2.1 General Aspects

We use a geometrically very simple model of a galaxy, which has the shape of a disk. The radius $R(z)$ and the scale height $H(z)$ evolve with redshift z. Ferguson et al. (2004) find a change of radius proportional to $(1+z)^{\mathbf{-3/2}}$ for a fixed circular velocity and proportional to $(1+z)^{\mathbf{-1}}$ for a fixed mass. Observations of galaxy evolution show that the mean scaling of the galaxy size lies in between these two extrema. For our model we choose a scaling of

$$R(z) = R_0(1+z)^{-1} \tag{8.1}$$

and a scale height of

$$H(z) = H_0(1+z)^{-1}, \tag{8.2}$$

leading to a galaxy volume of

$$V(z) = \pi R_0^2 H_0 (1+z)^{-3}. \tag{8.3}$$

The normalization of the radius and the scale height, R_0 and H_0, are set by the galaxies at present day. We analyze two types of galaxies: a normal Milky Way like galaxy, for which we use $R_0 = 1.5 \times 10^4$ pc and $H_0 = 500$ pc (Ferrière, 2001), and a starburst galaxy, which is of a similar type as M82. The radius of the central starburst region is roughly $R_0 = 300$ pc with a scale height of $R_0 = 200$ pc (de Cea del Pozo et al., 2009). We note, that our model of perfect disks is very idealized as the scale height usually changes with the radius.
Further, we assume the particle density of the ISM to scale as

$$n(z) = n_0(1+z)^3. \tag{8.4}$$

Our fiducial values for the present-day density n_0 are listed in table 8.1. With our model of a uniform density we simplify real galaxies, where there are gradients in density.
The evolution of the normalized density $n(z)/n(0)$ and galaxy volume $V(z)/V(0)$, which are proportional to $(1+z)^3$ or $(1+z)^{-3}$, respectively, are shown in figure 8.1. Note, that our model depends initially only on the normalized volume. Only when applied to real data in section 8.6, we need the volume of the galaxy when calculating the magnetic field strength from the total magnetic energy.

	normal galaxy	starburst core
R_0 [pc]	1.5×10^4	300
H_0 [pc]	500	200
n_0 [cm^{-3}]	3	300
$\dot{M}_\star(0)$ [M$_\odot$ yr^{-1}]	2	10
$\dot{\rho}_\star(0)$ [M$_\odot$ yr^{-1} pc^{-3}]	1.9×10^{-12}	3.5×10^{-8}

Table 8.1:
Properties of our two fiducial models: a normal galaxy comparable to the Milky Way and a starburst galaxy comparable to M82.

8.2.2 Star Formation Rate

Model for the Star Formation History

In section 8.4 we study the X-ray evolution of an idealized galaxy, which evolves according to the cosmic mean star formation history (Madau et al., 1996, 1998; Steidel et al., 1999; Madau & Pozzetti, 2000). The mean star formation rate of the Universe has been analyzed in simulations by Hernquist & Springel (2003). We use their relation to follow the evolution of a characteristic galaxy. With this model we get an idea of the inverse Compton scattering process as a function of redshift.
The star formation rate (SFR) of a galaxy is defined as

$$\dot{M}_\star(z) = V(z)\ \dot{\rho}_\star(z), \tag{8.5}$$

where $V(z)$ is the volume of the galaxy (8.3) and $\dot{\rho}_\star(z)$ is the star formation rate density (Hernquist & Springel, 2003)

$$\dot{\rho}_\star(z) \propto \frac{\kappa_2\ \exp[\kappa_1(z - z_\mathrm{m})]}{\kappa_2 - \kappa_1 + \kappa_1\ \exp[\kappa_2\ (z - z_\mathrm{m})]}(1+z)^3, \tag{8.6}$$

with the parameters $\kappa_1 = 3/5$, $\kappa_2 = 14/15$ and $z_\mathrm{m} = 5.4$. The factor $(1+z)^3$ in equation (8.6) comes from the conversion from comoving into physical units.
In figure 8.1 we show the evolution of the normalized star formation rate density $\dot{\rho}_\star(z)/\dot{\rho}_\star(0)$ and the normalized star formation rate $\dot{M}_\star(z)/\dot{M}_\star(0)$ with redshift. For the normalization of the star formation rate we use a typical value observed in the Milky Way $\dot{M}_\star(0) = 2$ M$_\odot$ yr^{-1} for the model of a normal galaxy. Note, that the proposals of the galactic SFR differ widely. While for example Diehl et al. (2006) find a value of 4 M$_\odot$ yr^{-1} from gamma ray observations, *Spitzer* observations suggest that the SFR is as low as $0.68-1.45$ M$_\odot$ yr^{-1} (Robitaille & Whitney, 2010). For the starburst model we use $\dot{M}_\star(0) = 10$ M$_\odot$ yr^{-1}, which is close to the observed value of the starburst galaxy M82 (Förster Schreiber et al., 2003).

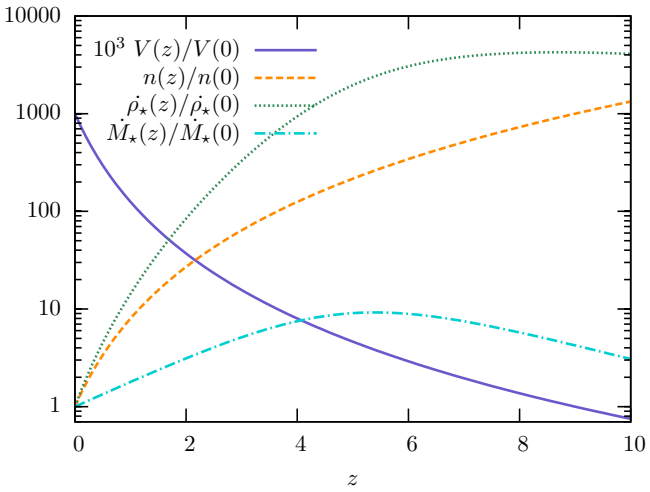

Figure 8.1:
The evolution of the normalized star formation rate density $\dot{\rho}_\star(z)/\dot{\rho}_\star(0)$ (Hernquist & Springel, 2003) and the star formation rate $\dot{M}_\star(z)/\dot{M}_\star(0)$ as a function of redshift z. We also show the evolution of the normalized volume of the galaxy $V(z)/V(0)$, which has been multiplied by a factor of 10^3 for better visualization, and the normalized particle density $n(z)/n(0)$. *image credit: Schober et al. (2014)*

Observed Star Formation Rate

The star formation history of an arbitrary galaxy will, however, differ significantly from this idealized picture. There will be phases of extremely high SFR induced, for example, by mergers with other galaxies followed by quiet phases. Thus, for getting information about the detailed emission processes of a single galaxy it is better to use direct observational input of the SFR. We use the model of the star formation history only in places, where we discuss the general trend of galaxy evolution, while we take a fixed SFR for single galaxies.
The SFR of a galaxy can be estimated from the observed infrared flux. Kennicutt (1998) finds the following correlation between the SFR $\dot{M}_\star$ and the infrared luminosity L_{IR}:

$$\dot{M}_\star(z) = 1.8 \times 10^{-10}\ \mathrm{M}_\odot\ \mathrm{yr}^{-1} \left(\frac{L_{\mathrm{IR}}}{\mathrm{L}_\odot}\right), \tag{8.7}$$

where $\mathrm{L}_\odot \approx 3.8 \times 10^{33}$ erg s^{-1} is the solar luminosity. In their data set Wang et al. (2013) employ NIR-through-radio SED fitting according to the work of Swinbank et al. (2013) to calculate L_{IR}. We will use examples of this multi-wavelength data set in section 8.6.

8.2.3 Supernova Rate

Cosmic rays are believed to originate in supernova shock fronts. Thus, for determination of the number and energy of the cosmic rays in a galaxy, the supernova rate is an important input.
We assume here a Kroupa initial mass function of stars, which decreases proportional to the stellar mass to the power of -1.3 in the range of 0.08 to 0.5 $\mathrm{M}_\odot$ and to the power of -2.3 for larger masses (Kroupa, 2002). The number of supernovae per

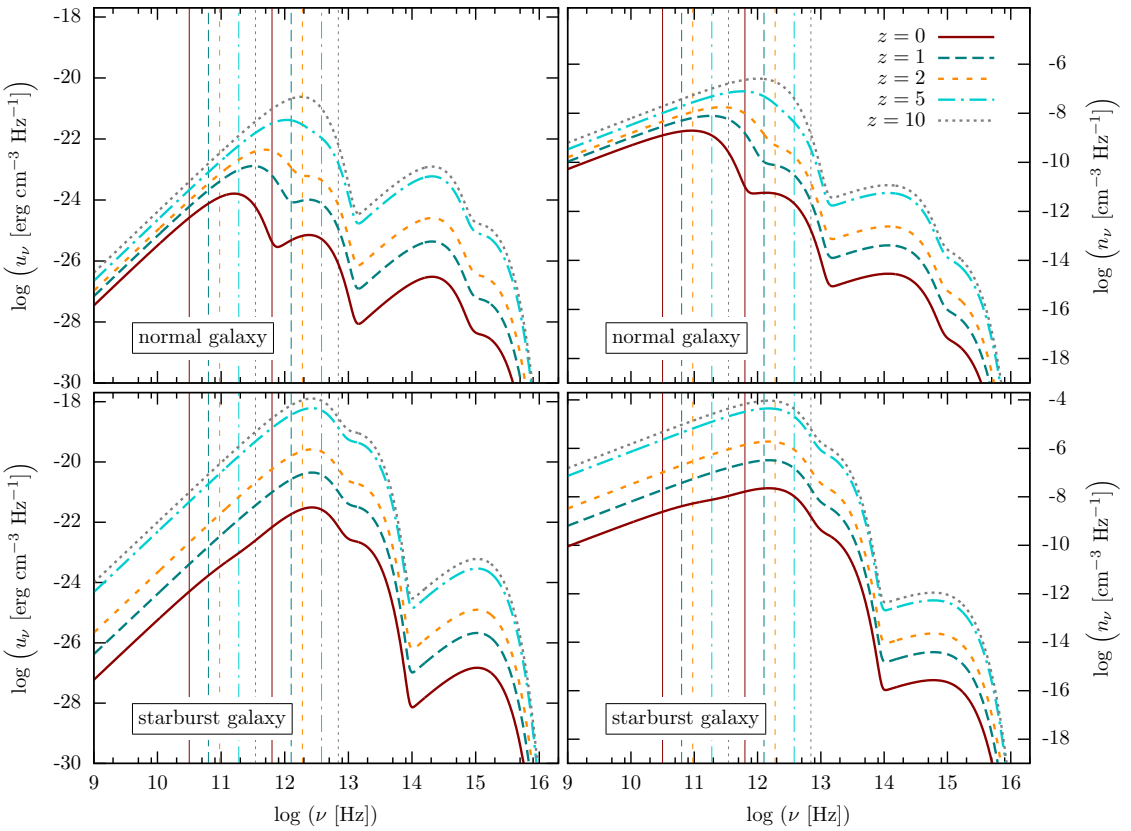

Figure 8.2:
The spectral energy density $u_{\mathrm{ISRF},\nu}$ (left hand side) and the spectral photon distribution $n_{\mathrm{ISRF},\nu}$ (right hand side) of the interstellar radiation field for different redshifts between $z = 0 - 10$. In the top panels we show our model for galaxies with a normal star formation rate and in the lower panels for a starburst galaxy. The parameters of the model are summarized in table 8.2. The vertical lines indicate the typical frequency range of photons that are inverse Compton scattered into the X-ray regime (see section 8.4.1 for more details).
image credit: Schober et al. (2014)

time is then roughly

$$\dot{N}_{\mathrm{SN}} = 0.156 \, \frac{\dot{M}_\star}{12.26 \ \mathrm{M}_\odot}, \tag{8.8}$$

with 12.26 $\mathrm{M}_\odot$ being the mean mass of a supernova candidate.

8.2.4 Interstellar Radiation Field

An essential role for the inverse Compton scattering plays the ISRF with which the cosmic rays interact. In our model we consider five different radiation components: the thermal (cold and warm) infrared (IR), optical (opt), ultraviolet (UV) radiation and the cosmic microwave background (CMB) (Cirelli & Panci, 2009; Chakraborty & Fields, 2013). The interstellar radiation field (ISRF) can then be approximated by the sum of the individual Planck spectra,

$$u_{\mathrm{ISRF},\nu} = \sum_i f_i \, \frac{8\pi h}{c^3} \, \frac{\nu^3}{\exp(h\nu/(kT_i) - 1}, \tag{8.9}$$

with $i = \mathrm{IR}, \mathrm{opt}, \mathrm{UV}, \mathrm{CMB}$. The dimensionless weights f_i as well as the different temperatures T_i at $z = 0$ are taken from Chakraborty & Fields (2013). Note, that we model a redshift dependence, which is given in table 8.2. For this we use $T_{\mathrm{CMB}}(z) = T_{\mathrm{CMB}}(0) \ (1 + z)$ and multiply the weights f_{IR}, f_{opt}, f_{UV} with the normalized star formation rate density $\dot{\rho}_\star(z)/\dot{\rho}_\star(0)$. The resulting spectral energy density $u_{\mathrm{ISRF},\nu}$ is shown in the left panel of figure 8.2.
The total energy density of the interstellar radiation field is

$$u_{\mathrm{ISRF}} = \int_0^\infty u_{\mathrm{ISRF},\nu} \ \mathrm{d}\nu = \frac{8 \ \pi^5 k^4}{15 \ c^3 h^3} \ \sum_i f_i T_i^4 \tag{8.10}$$

From the energy spectrum (8.9) we can calculate the photon distribution by

$$n_{\mathrm{ISRF},\nu} = \frac{u_{\mathrm{ISRF},\nu}}{h\nu}. \tag{8.11}$$

The result is shown in the right panel of figure 8.2. Note, that as well u_{ISRF} as n_{ISRF} increase with redshift, as the SFR density and the CMB density constantly increase with z. The peak of the CMB component further moves to higher frequencies with z due to the increasing CMB temperature.

8.2.5 Cosmic Rays

The origin of high energy cosmic rays is commonly believed to be first-order Fermi shock acceleration in supernova remnants and extragalactic sources (Bell, 1978a,b; Drury, 1983; Schlickeiser, 2002). However, there are additional models like acceleration by MHD waves (Schlickeiser & Miller, 1998; Brunetti et al., 2001; Fujita et al.,

	Normal Galaxy		Starburst Galaxy	
	f_i $[\dot{\rho}_\star(z)/\dot{\rho}_{\star,\mathrm{M82}}]$	T_i [K]	f_i $[\dot{\rho}_\star(z)/\dot{\rho}_{\star,\mathrm{MW}}]$	T_i [K]
UV	8.4×10^{-17}	1.8×10^4	3.2×10^{-15}	1.8×10^4
optical	8.9×10^{-13}	3.5×10^3	0.0	3.5×10^3
IR (warm)	-	-	3.61×10^{-5}	200
IR (cold)	1.3×10^{-5}	41	4.22×10^{-2}	45
CMB	1	$2.73(1+z)$	1	$2.73(1+z)$

Table 8.2:
A model of the interstellar radiation field, which includes five different radiation components: ultraviolet (UV) radiation, optical radiation, thermal (warm and cold) infrared (IR) radiation and the cosmic microwave background (CMB) (see Cirelli & Panci (2009) and Chakraborty & Fields (2013)). We give here the dimensionless weights compared to the CMB f_i, which include a scaling with the normalized star formation rate density $\dot{\rho}_\star(z)/\dot{\rho}_{\star,\mathrm{MW}}$ or $\dot{\rho}_\star(z)/\dot{\rho}_{\star,\mathrm{M82}}$, respectively, and the temperatures T_i.

2003) and magnetic reconnection (de Gouveia dal Pino & Lazarian, 2005). All these theoretical models result in a power-law distribution.
The injection spectrum of cosmic ray protons can be described by

$$Q_{\rm p}(\gamma_{\rm p}) = Q_{\rm p,0}\ \gamma_{\rm p}^{-\chi}, \tag{8.12}$$

with the Lorentz factor of protons $\gamma_{\rm p}$. The exponent χ depends strongly on the properties of the cosmic ray acceleration site, i.e. the supernova shock front. First-order Fermi acceleration theory predicts for strong shocks a value of $\chi = 2.0$ for non-relativistic gas and $\chi = 2.5$ for a relativistic gas (Bell, 1978b). More detailed models of supernova shock fronts (Bogdan & VÃűlk, 1983) result in $\chi = 2.1 - 2.3$. We will use here a fiducial value of $\chi = 2.2$.
We normalize the proton injection spectrum with the total energy injection rate $\xi E_{\rm SN}\dot{N}_{\rm SN}$, where $E_{\rm SN}$ is the energy of one supernova and $\dot{N}_{\rm SN}$ the supernova rate (8.8). This yields a proportionality factor in (8.12) of

$$Q_{\rm p,0} = \frac{\xi E_{\rm SN}\dot{N}_{\rm SN}(\chi-2)}{(m_{\rm p}c^2)^2\ \gamma_{\rm p,0}^{2-\chi}}. \tag{8.13}$$

A typical value of ξ, which is the fraction of the total energy released in supernovae that goes into cosmic rays, is given in the literature as 0.1. We use this as our fiducial value. Moreover, we will analyse values from $\xi = 0.05$ to $\xi = 0.2$, as simulations suggest that there is a density dependency of ξ (Dorfi, 2000). As the upper end of the cosmic ray energy spectrum, which extends up to 10^{21} eV per particle, does not contribute significantly to the total cosmic ray energy, only the lower end of the spectrum $\gamma_{\rm p,0}$ appears here. For the latter we use a value of $\gamma_{\rm p,0} = 10^9$ eV$/(m_{\rm p}c^2)$.
In this work we assume that cosmic rays consist only of protons p as well as electrons and positrons $e^{\pm}$. When the latter follow the same distribution as protons accelerated in supernova remnants one speaks of *primary cosmic ray* $e^{\pm}$, which have a similar injection rate as the protons (8.12). However, there is a second source of cosmic ray $e^{\pm}$: pionic secondaries from collisions of cosmic ray protons with the ambient gas. Electrons and positrons, which have been produced in this way, are called *secondary cosmic ray* $e^{\pm}$. The injection spectrum of secondaries can be estimated as (Lacki & Beck, 2013)

$$Q_{\rm e,sec} = \frac{f_\pi}{6}\frac{m_{\rm p}}{m_{\rm e}}\left(\frac{\gamma_{\rm p}}{\gamma_{\rm e}}\right)^2\ Q_{\rm p}(\gamma_{\rm p}). \tag{8.14}$$

When assuming that the fraction of proton energy that goes into pion production is $f_\pi = 0.2 - 0.5$ (Lacki et al., 2011), the ratio of secondary to total cosmic ray $e^{\pm}$ $Q_{\rm e}$,

$$f_{\rm sec} = \frac{Q_{\rm e,sec}}{Q_{\rm e}}, \tag{8.15}$$

is roughly 0.6 to 0.8. The energy of secondary electrons is $\gamma_{\rm e} = m_{\rm p}/(20m_{\rm e})\gamma_{\rm p}$ (Lacki & Beck, 2013).

In our analysis the cosmic ray $e^{\pm}$ play the most important role, as they are responsible for energy losses due to inverse Compton scattering. In order to find the steady-state spectrum of the $e^{\pm}$ $N_{\rm e}(\epsilon_{\rm e})$ one needs to solve the diffusion-loss equation (Longair, 2011):

$$\frac{\partial N(\gamma)}{\partial t} = Q(\gamma) + \frac{\rm d}{{\rm d}\gamma}\left[b(\gamma)N(\gamma)\right] - \frac{N(\gamma)}{\tau(\gamma)} + D\nabla^2 N(\gamma). \tag{8.16}$$

Here $Q(\gamma)$ is the injection spectrum, $b(\gamma) = -{\rm d}\gamma/{\rm d}t$ the energy loss rate, $\tau(\gamma)$ the timescale of escape or total losses, and D the spatial diffusion time scale. The diffusion loss equation is valid for $e^{\pm}$ (index e) and for protons (index p). For a homogeneous medium, Lacki & Beck (2013) find for the equilibrium proton spectrum, i.e. $\partial N_{\rm p}(\gamma_{\rm p})/\partial t = 0$,

$$N_{\rm p}(\gamma_{\rm p}) = Q_{\rm p}(\gamma_{\rm p})\ f_{\pi}\ \tau_{\pi}, \tag{8.17}$$

and for the equilibrium $e^{\pm}$ spectrum, i.e. $\partial N_{\rm e}(\gamma_{\rm e})/\partial t = 0$,

$$N_{\rm e}(\gamma_{\rm e}) = \frac{Q_{\rm e}(\gamma_{\rm e})\ \tau_{\rm e}(\gamma_{\rm e})}{\chi - 1}. \tag{8.18}$$

The characteristic timescales appearing here are the one for pion production,

$$\tau_{\pi} = 50\ {\rm Myr}\ (n/{\rm cm}^{-3})^{-1}, \tag{8.19}$$

and the electron cooling time, $\tau_{\rm e} = \epsilon_{\rm e}/b_{\rm e}(\epsilon_{\rm e})$, which is calculated as

$$\tau_{\rm e} = \left(\tau_{\rm synch}^{-1} + \tau_{\rm IC}^{-1} + \tau_{\rm ion}^{-1} + \tau_{\rm brems}^{-1}\right)^{-1}. \tag{8.20}$$

This equation takes into account different energy losses of cosmic ray electrons, including synchrotron emission ($\tau_{\rm synch}$), inverse Compton scattering ($\tau_{\rm IC}$), ionization ($\tau_{\rm ion}$) and bremsstrahlung ($\tau_{\rm brems}$). We will discuss the importance of the different loss timescales in the next section. Combination of the upper equations yields for the steady-state spectra of cosmic ray protons and electrons

$$N_{\rm p}(\gamma_{\rm p}) = f_{\pi}\tau_{\pi}Q_{\rm p,0}\gamma_{\rm p}^{-\chi} \tag{8.21}$$

$$N_{\rm e}(\gamma_{\rm e}) = \frac{20^{2-\chi} f_{\pi}}{6 f_{\rm sec}(\chi-1)}\tau_{\rm e}\left(\frac{m_{\rm e}}{m_{\rm p}}\right)^{1-\chi} Q_{\rm p,0}\gamma_{\rm e}^{-\chi}, \tag{8.22}$$

with the normalization of the proton injection spectrum $Q_{\rm p,0}$ given in equation (8.13).

With the spectral distribution the energy density of cosmic rays can be computed. The dominant part of the total cosmic ray energy $U_{\rm CR}$ is contributed from the protons. It can be calculated by

$$U_{\rm CR} = \int_{\gamma_{\rm p,0}}^{\infty} N_{\rm p}(\gamma_{\rm p})\ \gamma_{\rm p} m_{\rm p} c^2\ {\rm d}\gamma_{\rm p} + \int_{\gamma_{\rm e,0}}^{\infty} N_{\rm e}(\gamma_{\rm e})\ \gamma_{\rm e} m_{\rm e} c^2\ {\rm d}\gamma_{\rm e}, \tag{8.23}$$

where we assume a lower limit for the energy of cosmic ray $e^{\pm}$ of $\gamma_{\rm e,0} = 10^9\ {\rm eV}/(m_{\rm e}c^2)$. Note, that $U_{\rm CR}$ indicates the total energy, and not the energy density $u_{\rm CR}$. Assuming a Milky Way like galaxy with the properties given for a normal galaxy at $z = 0$ in table 8.1, we find a total cosmic ray density of $u_{\rm CR} = 1.33\ {\rm eVcm}^{-3}$.

8.3 Suppression of the FIR-Radio Correlation at High Redshifts

Observations of nearby galaxies show that there is a correlation between the far-infrared flux and the radio flux. Yun et al. (2001) combine data from the NRAO VLA Sky Survey, which includes the 1.4 GHz radio luminosity, with the FIR luminosity data from the IRAS Redshift Survey. In their sample of around 1800 galaxies they find a tight correlation over roughly five orders of magnitude in luminosity.
The origin of the FIR-radio correlation can be understood as a result of coupling between star formation, cosmic rays and the magnetic field. The FIR radiation arises from the thermal emission of dust, which is heated by the ultraviolet radiation of massive stars, and thus traces the SFR. The SFR is also directly connected to the supernova rate, and hence to the cosmic ray production, which has been discussed before. The highly energetic cosmic rays lose their energy when traveling through the ISM. At present day one of the most important energy loss mechanism for cosmic ray electrons is synchrotron emission, which results from the interaction with interstellar magnetic field and lies in the radio regime.
Besides the synchrotron (synch) emission, the cosmic ray $e^{\pm}$ can lose their energy also via inverse Compton scattering (IC), ionization (ion), and bremsstrahlung (brems), see also Oh (2001). The typical timescales of these processes are (Schleicher & Beck, 2013):

$$\tau_{\mathrm{synch}} = \frac{3\ m_{\mathrm{e}}\ c}{4\ \sigma_{\mathrm{T}}\ u_{\mathrm{B}}\ \gamma_{\mathrm{e}}} \tag{8.24}$$

$$\tau_{\mathrm{IC}} = \frac{3\ m_{\mathrm{e}}\ c}{4\ \sigma_{\mathrm{T}}\ u_{\mathrm{ISRF}}\ \gamma_{\mathrm{e}}} \tag{8.25}$$

$$\tau_{\mathrm{ion}} = \frac{\gamma_{\mathrm{e}}}{2.7\ c\ \sigma_{\mathrm{T}}\ (6.85 + 0.5\ \ln\gamma_{\mathrm{e}})\ n} \tag{8.26}$$

$$\tau_{\mathrm{brems}} = 3.12 \times 10^{7}\ \mathrm{yr}\ \left(\frac{n}{\mathrm{cm}^{-3}}\right)^{-1}. \tag{8.27}$$

Here $\gamma_{\mathrm{e}} = \epsilon_{\mathrm{e}}/(m_{\mathrm{e}}c^2)$ is the Lorentz factor of a an electron with energy ϵ_{e}, $u_{\mathrm{B}} = B^2/(8\pi)$ the magnetic energy density, u_{ISRF} the energy density of the ISRF (8.10), and n the particle density of the interstellar medium (8.4).
For calculating the timescale of synchrotron emission we use a scaling of the magnetic field strength of $B \propto \dot{M}_{\star}^{1/3}$, which has been observed in various galaxies (Niklas & Beck, 1997; Chyży et al., 2011). Schleicher & Beck (2013) derive this scaling behavior from a simple analytical galaxy model, while they assume that the magnetic energy is always a fixed fraction of the turbulent kinetic energy. This assumption is valid in the presence of a turbulent dynamo, which amplifies any weak seed field on short timescales. It leads to $B \propto \Sigma_{\mathrm{SFR}}^{1/3} n^{1/6}$, where Σ_{SFR} is the star formation surface density. In our model with $n \propto (1+z)^3$ we would thus expect an additional factor of $(1+z)^{1/2}$ in the evolution of the magnetic field strength. These considerations

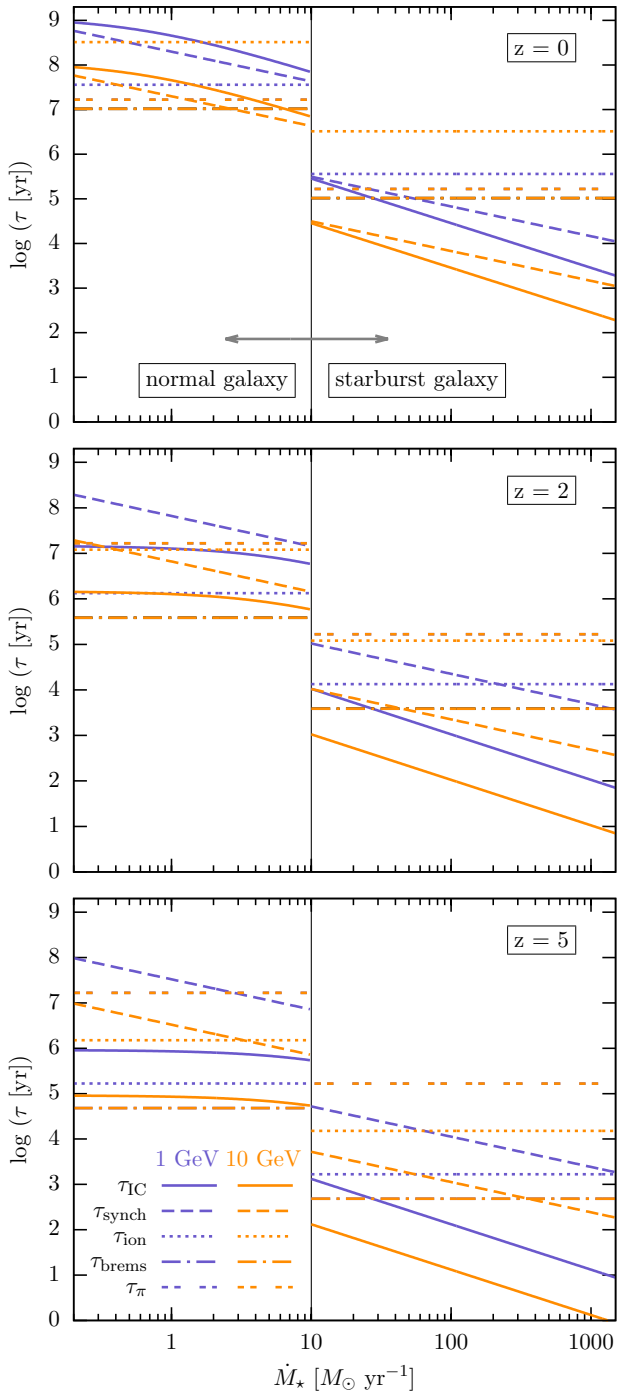

Figure 8.3:
Typical timescales of cosmic ray electrons with an energy of 1 GeV (blue lines) and 10 GeV (orange lines) as a function of the star formation rate $\dot{M}_\star$. The different panels present the timescales at different redshifts z. The solid line indicates the timescale of inverse Compton scattering $\tau_{\rm IC}$, the dashed line synchrotron emission $\tau_{\rm synch}$, the dotted line ionization $\tau_{\rm IC}$, the dashed-dotted bremsstrahlung $\tau_{\rm brems}$ and the dashed-dashed pion production τ_π. We show the case of a normal galaxy up to 10 $M_\odot yr^{-1}$, for larger $\dot{M}_\star$ we use the starburst properties. The jump in timescales results from the different particle densities of the two galaxy models. Note, that $\tau_{\rm brems}$ and τ_π are independent of the cosmic ray energy.
image credit: Schober et al. (2014)

suggest a total scaling relation of

$$B(z) \propto \dot{M}_\star^{1/3}(1+z)^{1/2}. \tag{8.28}$$

For the magnetic field strength at $z = 0$ we use $B_0 = 10^{-5}$ G for the normal galaxy and $B_0 = 2 \times 10^{-4}$ G for the starburst galaxy, which is motivated from observations of M82 (de Cea del Pozo et al., 2009).
In figure 8.3 we show the different timescales as a function of star formation rate at different redshifts. We present the timescales for two different $e^\pm$ energies, 1 GeV and 10 GeV, indicated by differently colored lines. Note, that the jump of the timescales in the transition from normal to starburst galaxies results from the increase of density in our model (see table 8.1). While losses by bremsstrahlung and synchrotron emission dominate in normal galaxies for low redshifts, in starburst galaxies inverse Compton scattering is the most important effect at high star formation rates already at $z = 0$. With increasing redshift figure 8.3 illustrates that the difference between synchrotron and inverse Compton increases continuously.
Form the analysis of the timescales we conclude that inverse Compton scattering is the dominant loss mechanism of cosmic ray electrons for normal galaxies only at high redshifts ($z \gtrsim 5$) and in starburst galaxies with high SFRs at basically all cosmological times. The typical frequency of photons that have been inverse Compton scattered with the CMB lies in the X-ray regime. Thus, we expect galaxies to become bright in X-ray above a critical redshift and star formation rate. In the next section we present a model for the typical X-ray emissivity due to inverse Compton scattering.

8.4 Expected X-Ray Luminosity from Inverse Compton Scattering

8.4.1 Characteristic Frequencies

In the process of inverse Compton scattering a low energy photon scatters on a high energy electron. Due to the radiation field the electron gets decelerated and transmits energy on the photon. The characteristic frequency of an inverse Compton scatted photon, which we observe today, is

$$\nu_{\mathrm{charac}}(z) = \gamma_{\mathrm{e},0}^2 \frac{\nu_{\mathrm{in}}}{1+z}, \tag{8.29}$$

where $\gamma_{\mathrm{e},0}$ is the typical energy of cosmic ray electrons and ν_{in} is the frequency of the incoming photon.
The energy range of the *Chandra* telescope, which we will use in our calculation if not indicated otherwise, is

$$\nu_{\mathrm{C1}} h = 0.5 \text{ keV} \tag{8.30}$$

$$\nu_{\mathrm{C2}} h = 10 \text{ keV}. \tag{8.31}$$

Thus, photons with frequencies between

$$\nu_{\mathrm{in},1} = \gamma_{\mathrm{e},0}^{-2}\ \nu_{\mathrm{C1}}\ (1+z) \approx 3.16 \times 10^{10}\ (1+z)\ \mathrm{Hz} \tag{8.32}$$

and

$$\nu_{\mathrm{in},2} = \gamma_{\mathrm{e},0}^{-2}\ \nu_{\mathrm{C2}}\ (1+z) \approx 6.31 \times 10^{11}\ (1+z)\ \mathrm{Hz} \tag{8.33}$$

can be inverse Compton scattered into the detection range. We indicate the range of suitable frequencies in figures 8.2 and 8.6 by vertical lines. The most important components are thus the CMB and the IR component. As there is a distribution in the incoming photon energy as well as in the the cosmic ray energy, also photons with an initially different frequency can be scattered into the *Chandra* range. However, we expect the majority of detected photons to origin from the calculated energy regime.

8.4.2 Inverse Compton Luminosity

In a galaxy, the initial photon spectrum can be approximated as the sum of several blackbody spectra, which we have modeled in (8.11), and the initial electron spectrum is a power-law (8.22). Blumenthal & Gould (1970) show that the spectral distribution of inverse Compton scattered photons, i.e. the total number of photons that are scattered into the energy $\epsilon = h\nu$ per time, is

$$Q_{\mathrm{IC},\nu}(\nu) = \int_0^\infty \int_{\gamma_{\mathrm{min}}}^\infty N_{\mathrm{e}}(\gamma_{\mathrm{e}}) Q_{\mathrm{IC,e}}(\gamma_{\mathrm{e}}, \nu_{\mathrm{in}})\ \mathrm{d}\gamma_{\mathrm{e}}\ \mathrm{d}\nu_{\mathrm{in}}, \tag{8.34}$$

with the contribution of a single electron of energy $\epsilon_{\mathrm{e}} = \gamma_{\mathrm{e}} m_{\mathrm{e}} c^2$ being

$$Q_{\mathrm{IC,e}}(\gamma_{\mathrm{e}}, \nu_{\mathrm{in}}) = \frac{\pi r_0^2 c h}{2\gamma_{\mathrm{e}}^4} \frac{n_{\mathrm{ISRF},\nu}(\nu_{\mathrm{in}})}{\nu_{\mathrm{in}}^2} \left(2\nu \ln\left(\frac{\nu}{4\gamma_{\mathrm{e}}^2 \nu_{\mathrm{in}}} \right) + \nu + 4\gamma_{\mathrm{e}}^2 \nu_{\mathrm{in}} - \frac{\nu^2}{2\gamma_{\mathrm{e}}^2 \nu_{\mathrm{in}}} \right). \tag{8.35}$$

This result is valid in the so-called Thomson limit, where the energy of the photon in the electron rest frame before scattering is much less then $m_e c^2$.
The aim of this work is to study objects, in which the cosmic ray $e^\pm$ losses are dominated by inverse Compton scattering. We thus assume, for the analytical calculation in this section, that the timescale τ_{IC} is shorter than τ_{synch}, τ_{ion} and τ_{brems} (see equations 8.24 to 8.27), which simplifies equation (8.20) to

$$\tau_{\mathrm{e}} \approx \tau_{\mathrm{IC}}. \tag{8.36}$$

The $e^\pm$ spectrum (8.22) reduces then to

$$N_{\mathrm{e}}(\gamma_{\mathrm{e}}) = \frac{20^{2-\chi} f_\pi}{6 f_{\mathrm{sec}} (\chi - 1)} \tau_{\mathrm{IC}} \left(\frac{m_{\mathrm{e}}}{m_{\mathrm{p}}} \right)^{1-\chi} Q_{\mathrm{p},0} \gamma_{\mathrm{e}}^{-\chi} \tag{8.37}$$

with the inverse Compton timescale τ_{IC} given in equation (8.25).
In the Thomson approximation the lower integration limit in (8.34) is $\gamma_{\mathrm{min}} = 1/2\ (\nu/\nu_{\mathrm{in}})^{1/2}$. Here ν_{in} is the frequency of the incoming photon, while ν is the frequency of the inverse Compton scattered photon. With the spectrum of cosmic ray $e^{\pm}$ (8.37) and the interstellar radiation field (8.11), integration over γ_{e} yields again to a power-law in the frequency

$$\begin{aligned} Q_{\mathrm{IC},\nu}(\nu) &= \frac{\pi h r_0^2 c^4 m_{\mathrm{e}}^{2-\chi} m_{\mathrm{p}}^{\chi} f_{\pi}}{f_{\mathrm{sec}} \sigma_{\mathrm{T}} u_{\mathrm{ISRF}}} Q_{\mathrm{p},0}\ \tilde{F}(\chi)\ (h\nu)^{-(\chi+2)/2} \\ &\quad \times \int_0^{\infty} (h\nu_{\mathrm{in}})^{\chi/2} n_{\mathrm{ISRF},\nu}(\nu_{\mathrm{in}})\ \mathrm{d}\nu_{\mathrm{in}}, \end{aligned} \tag{8.38}$$

with the abbreviation

$$\tilde{F}(\chi) = \frac{(\chi^2 + 6\chi + 16) 2^{5-\chi} 5^{2-\chi}}{(4+\chi)^2 (\chi+6)(\chi+2)(\chi-1)}. \tag{8.39}$$

Further evaluation of the integral over the ISRF (8.11) in equation (8.38) yields

$$Q_{\mathrm{IC},\nu}(\nu, z) = \frac{4\pi r_0^2 c m_{\mathrm{e}}^{2-\chi} m_{\mathrm{p}}^{\chi} f_{\pi}}{f_{\mathrm{sec}} h^2 \sigma_{\mathrm{T}} u_{\mathrm{ISRF}}}\ F(\chi)\ Q_{\mathrm{p},0}\ (h\nu)^{-(2+\chi)/2}\ \sum_i f_i\ (kT_i)^{(6+\chi)/2}. \tag{8.40}$$

Here we have defined

$$F(\chi) = \Gamma\left(\frac{6+\chi}{2}\right) \zeta\left(\frac{6+\chi}{2}\right)\ \tilde{F}(\chi), \tag{8.41}$$

where Γ is the Euler gamma function and ζ the Riemann zeta function. With the spectral distribution of inverse Compton scattered photons (8.40) we can calculate the spectral luminosity

$$L_{\mathrm{IC},\nu}(\nu, z) = Q_{\mathrm{IC},\nu}(\nu, z)\ h\nu \tag{8.42}$$

and the observed integrated X-ray luminosity

$$\begin{aligned} L_{\mathrm{IC}}(z) &= \int_{\nu_1}^{\nu_2} L_{\mathrm{IC},\nu}(\nu(1+z), z)\ (1+z)\ \mathrm{d}\nu \\ &= \frac{16\pi^2 r_0^2 c m_{\mathrm{e}}^{2-\chi} m_{\mathrm{p}}^{\chi} f_{\pi}}{f_{\mathrm{sec}} h^{(4+\chi)/2} \sigma_{\mathrm{T}} u_{\mathrm{ISRF}}}\ \frac{F(\chi)}{\chi - 2}\ Q_{\mathrm{p},0} (1+z)^{(2-\chi)/2} \\ &\quad \times \left(\nu_2^{1-\chi/2} - \nu_1^{1-\chi/2}\right) \sum_i f_i\ (kT_i)^{(6+\chi)/2}. \end{aligned} \tag{8.43}$$

The observed integrated X-ray luminosity that purely results from inverse Compton scattering is shown in figure 8.4. For this plot we use the model of the ISRF given in table 8.2 with the redshift-dependent SFR model from equation (8.5) in the upper panel, while we treat the SFR as a free parameter in the lower panels. A result from

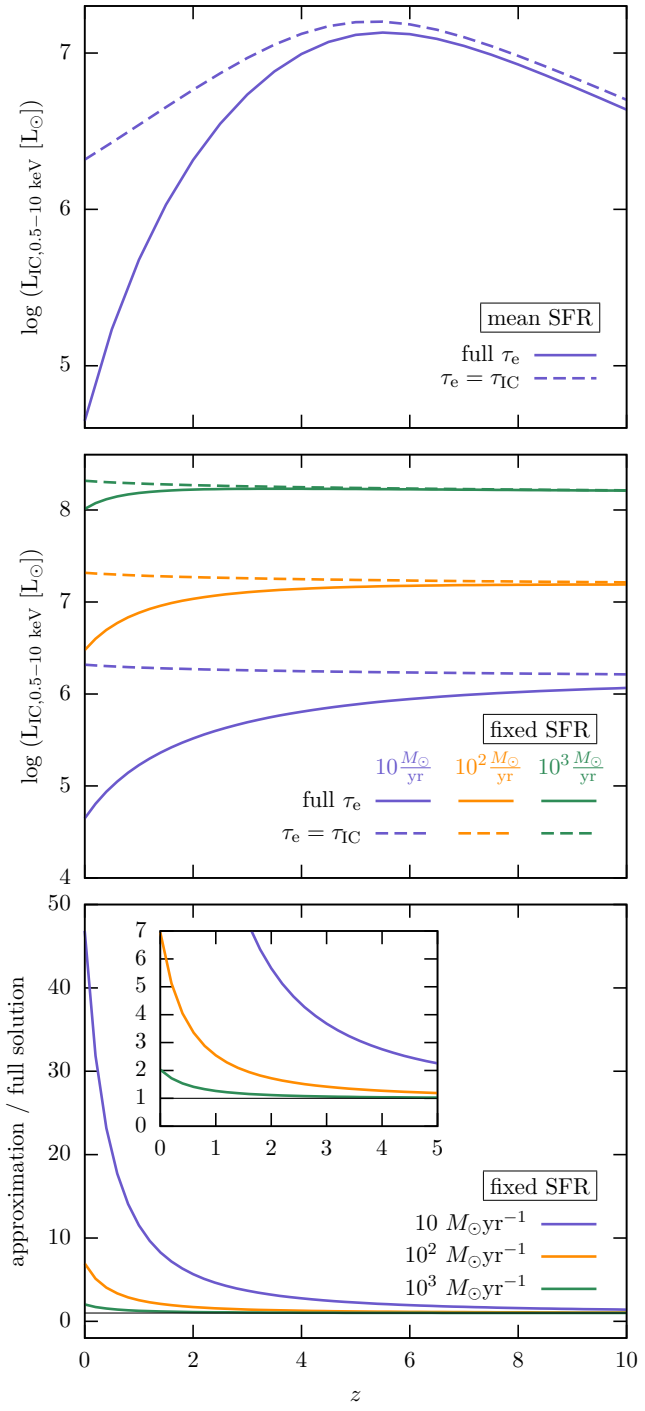

Figure 8.4:
Comparison of the solution for inverse Compton luminosity L_{IC} when employing the full cosmic ray timescale (8.20) with the analytical one in the approximation $\tau_e = \tau_{\mathrm{IC}}$. In the upper panel we apply an evolution of $\dot{M}_\star$ according to (8.5), while we use fixed $\dot{M}_\star$ in the lower panels. In the two upper panels we present the evolution of L_{IC} with redshift z in a starburst galaxy. The third panel shows the ratio of the approximation to the full solution for different $\dot{M}_\star$. Here we indicate 1 by a horizontal black line and provide a zoom-in to low redshifts in the inlay panel.
image credit: Schober et al. (2014)

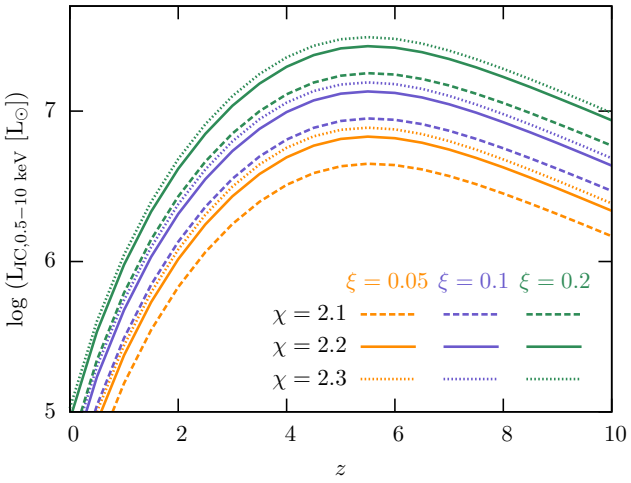

Figure 8.5:
A test of the influence of the cosmic ray spectrum (8.22) on the inverse Compton luminosity L_{IC}. We show here the numerical solution for the full cosmic ray timescale (8.20) and use the mean evolution of the star formation rate (8.5). The different line colors represent calculations with different normalizations of the cosmic ray spectrum ξ ranging from $\xi = 0.05$ (blue lines) over $\xi = 0.1$ (orange lines) up to $\xi = 0.2$ (green lines). In each case we also change the slope of the cosmic ray spectrum χ. The dashed lines are results for $\chi = 2.1$, the solid lines for $\chi = 2.2$ and the dotted lines $\chi = 2.3$.
image credit: Schober et al. (2014)

our timescale analysis is that the inverse Compton scattering is more efficient the higher the star formation rate is. Thus, in figure 8.4 and for most the further analysis we restrict ourselves to the starburst galaxy model. We present both solutions for the luminosity, the full numerical one with the cosmic ray timescale (8.20) and the analytical one (8.43), which is valid for $\tau_{\mathrm{e}} \approx \tau_{\mathrm{IC}}$. As expected from the timescale analysis from section 8.3, the approximation is only reasonable for high redshifts, as here the CMB temperature is higher and also the mean star formation rate is higher (for the SFR model from equation 8.5). The ratio of the approximative solution and the full numerical solution for the inverse Compton luminosity is shown in the third panel of figure 8.4. While for a low SFR of 10 $M_{\odot}\mathrm{yr}^{-1}$ the factor between the full solution and the approximative solution is 5.7 at $z = 2$, it is only 1.1 for 10^3 $M_{\odot}\mathrm{yr}^{-1}$ at the same redshift.
In figure 8.5 we test the influence of the cosmic ray spectrum, which is given in equation (8.18), for the full numerical solution of (8.34). The normalization of the cosmic ray spectrum ξ is varied from $\xi = 0.05$ to 0.2. From the figure one notes that with increasing ξ the luminosity increases, which can also be seen from equation (8.40) directly, where the total number of injected cosmic ray protons $Q_{\mathrm{p},0}$ appears, which is proportional to ξ (see equation 8.21). It is intuitively clear that with a larger number of cosmic ray protons the number of cosmic ray electrons and thus the number of scattering events increases, which leads to a larger inverse Compton luminosity. In figure 8.4 we also test the influence of changing the slope of the cosmic ray spectrum χ, which we vary from 2.1 to 2.3. We expect that this should

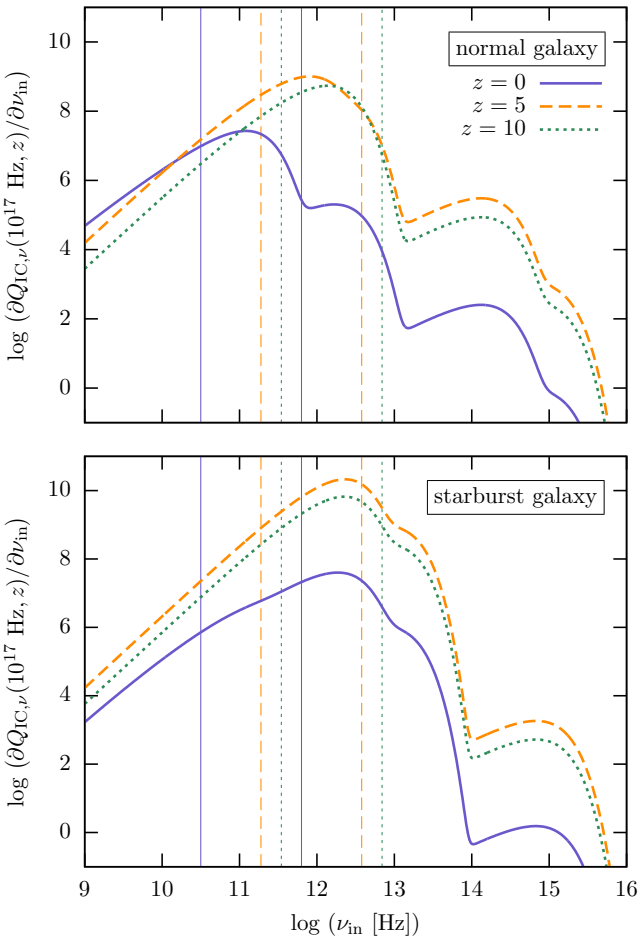

Figure 8.6:
The efficiency of inverse Compton scattering for our model of the interstellar radiation field as a function of the incoming photon frequency ν_{in}. The different line styles indicate the efficiency at different redshifts: The solid blue lines give $z = 0$, the dashed orange lines $z = 5$ and the dotted green lines $z = 10$. The upper panel shows the result for a galaxy with a normal SFR, the lower panel the one for a starburst galaxy. We use here the redshift-dependent SFR model (8.5), the cosmic ray spectrum (8.13) and the cosmic ray timescale (8.20). The different components of the ISRF are listed in table 8.2. The vertical lines indicate typical frequency range of photons that are inverse Compton scattered into the X-ray regime.
image credit: Schober et al. (2014)

not change significantly as the basic cosmic ray acceleration mechanism should be the same for all galaxies and redshifts. With an increasing χ the luminosity decreases.

From equation (8.38) we can calculate the spectral contribution to the inverse Compton scattering $\partial Q_{\mathrm{IC},\nu}(\nu, z)/\partial\nu_{\mathrm{in}}$, which is shown in figure 8.6 for the full energy loss timescale (8.20). For a typical resulting frequency we choose $\nu = 10^{17}$ Hz, which is motivated by equation (8.29) when using an incoming frequency of $\nu_{\mathrm{in}} = 10^{11}$ Hz and an electron energy of $\gamma_{\mathrm{e}} = 10^9$ eV$/(m_{\mathrm{e}}c^2)$ Hz. In the top panel of figure 8.6 we show the efficiency for the ISRF of a normal galaxy as a function of incoming frequency. In the case of $z = 0$ one can clearly distinguish the contributions of the different ISRF components. From the left to the right one can identify the CMB, the (cold) IR, the optical and the UV component, while the CMB dominates. When going to higher redshifts the temperature and with that the peak of the CMB shifts to higher frequencies. The contribution of the CMB becomes more and more important. Already at $z = 5$ the IR component is barley visible anymore. We note that the efficiency of inverse Compton scattering in our model decreases again above $z \approx 5$, as the mean SFR decreases above this redshift. To conclude, in a galaxy with normal star formation the CMB is the dominant incoming radiation field for inverse

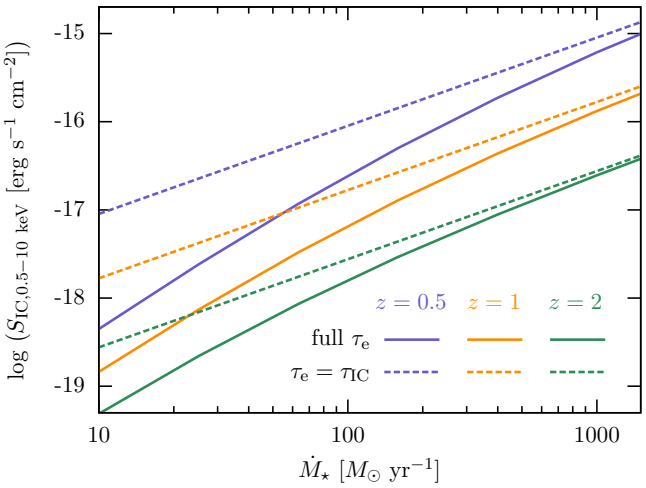

Figure 8.7:
The observed inverse Compton flux S_{IC} from a starburst galaxy as a function of star formation rate $\dot{M}_\star$. We compare the numerical solution for the full cosmic ray timescale with the analytical one for the assumption $\tau_e = \tau_{\mathrm{IC}}$ for different redshifts between $z = 0.5$ and $z = 0.5$.
image credit: Schober et al. (2014)

Compton scattering. For comparison we show the inverse Compton efficiency of a starburst galaxy in the lower panel of figure 8.6. Here the cold IR component is the dominant one for the inverse Compton mechanism. Even for the $z = 0$ case, the peak of the CMB is almost not visible. Due to the strong IR radiation field we expect starburst galaxies to be more efficient in inverse Compton scattering and will only consider these galaxies from now.

8.4.3 Inverse Compton Flux

With the luminosity distance,

$$d_{\mathrm{L}}(z) = (1+z)^2\ d_{\mathrm{A}}(z), \tag{8.44}$$

where the angular diameter distance d_{A} can be determined from the Mattig relation,

$$d_{\mathrm{A}}(z) = \frac{c}{H_0}\frac{2}{\Omega_{\mathrm{m}}^2(1+z)^2}\left(\Omega_{\mathrm{m}}z + (\Omega_{\mathrm{m}}-2)(\sqrt{1+\Omega_{\mathrm{m}}z}-1)\right), \tag{8.45}$$

we can moreover calculate the flux resulting from inverse Compton scattering. We use the latest cosmological parameters determined by the *Planck* satellite. The Hubble constant is $H_0 = 67.11\ \mathrm{km\ s^{-1}Mpc^{-1}}$ and the matter density parameter $\Omega_{\mathrm{m}} = 0.3175$ (Planck Collaboration et al., 2013b). We determine the spectral flux density by

$$S_{\mathrm{IC},\nu} = \frac{L_{\mathrm{IC},\nu}}{4\pi d_{\mathrm{L}}^2} \tag{8.46}$$

and the total flux density by

$$S_{\mathrm{IC}}(z) = \int_{\nu_1}^{\nu_2} S_{\mathrm{IC},\nu}(\nu, z)\ \mathrm{d}\nu. \tag{8.47}$$

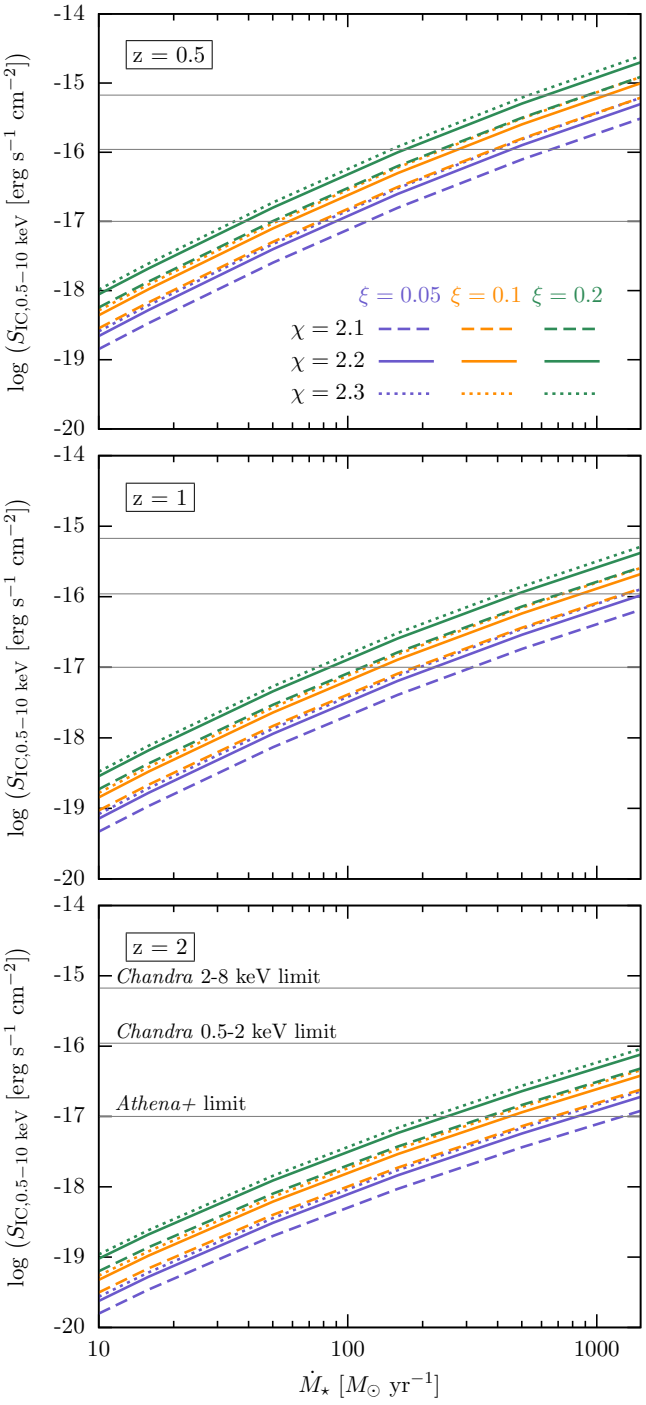

Figure 8.8:
The observed inverse Compton flux $S_{\rm IC}$ in the range 0.5-10 keV from a starburst galaxy as a function of star formation rate $\dot{M}_\star$. We present here the solution for the full cosmic ray timescale (8.20). The different panels represent different redshifts from $z = 0.5$ to $z = 2$. The line colors indicate the normalization of the cosmic ray spectrum ξ (see equation 8.21), while the linestyles show different slopes of the cosmic ray injection spectrum: $\chi = 2.1$ (dashed lines), $\chi = 2.2$ (solid lines) and $\chi = 2.3$ (dotted lines). We further indicate the sensitivity limits of *Chandra* and *Athena+* by the horizontal lines. *image credit: Schober et al. (2014)*

A comparison between the inverse Compton flux calculated for the full cosmic ray timescale (8.20) and the approximation $\tau_e = \tau_{IC}$ is shown in figure 8.7. We present the two different solutions as a function of star formation rate for a redshift range $z = 0.5 - 2$. The approximate analytical solution is comparable to the full numerical one for high star formation rates and high redshifts.
In figure 8.8 we test the influence of different cosmic ray spectra on the inverse Compton flux. The different line styles and colors cover our parameter space of the cosmic ray spectrum. We again vary ξ from 0.05 to 0.2 and χ from 2.1 to 2.3. The horizontal lines in the plot give the sensitivity limits of *Chandra* and the future X-ray observatory *Athena+*. For the Extended *Chandra* Deep Field the flux limit in the 0.5-2 keV range is 1.1×10^{-16} erg s^{-1}cm^{-3} and 6.7×10^{-16} erg s^{-1}cm^{-3} in the 2-8 keV range (Lehmer et al., 2005). The expected sensitivity limit for *Athena+* is 10^{-17} erg s^{-1}cm^{-3} in the 0.5-2 keV band (Nandra et al., 2013). With increasing redshift the inverse Compton flux moves more and more out of the detection limits. However, with *Athena+* the pure inverse Compton flux of objects with high SFRs should still be visible at redshifts larger than 2.

8.5 Distinguishing Other X-Ray Processes

A typical galaxy contains various sources of X-ray emission (Persic & Rephaeli, 2002). While normal stars only contribute a small fraction to the total X-ray emission, supernova remnants and the hot thermal ISM gas are more important. It has been shown, however, that the dominant sources are X-ray binaries. In the following we present two methods from literature, which estimate the X-ray emission from X-ray binaries. We further shortly discuss the X-ray emission from supernovae and active galactic nuclei.

8.5.1 X-Ray Binaries

Analytical Model for the Mean Evolution of X-Ray Binaries

Observations show that the emission of a normal galaxy is dominated by a few point sources, which have been identified as X-ray binaries (Fabbiano, 1995). Any model of the X-ray emission of a normal galaxy should thus show a characteristic scaling with the number of X-ray binaries and also with the SFR.
Ghosh & White (2001) provide an analytical model for the number of the different X-ray binary classes. The evolution of the number of high-mass X-ray binaries (HMXB) in a typical galaxy N_{HMXB} is governed by

$$\frac{\partial N_{\mathrm{HMXB}}(t)}{\partial t} = \alpha_{\mathrm{HMXB}} \frac{\dot{M}_\star}{10\mathrm{M}_\odot} - \frac{N_{\mathrm{HMXB}}(t)}{\tau_{\mathrm{HMXB}}}, \tag{8.48}$$

where the typical HMXB evolution timescale τ_{HMXB} is 5×10^6 yr. The parameter α_{HMXB} gives the rate of HMXB formation and can be estimated by $\alpha_{\mathrm{HMXB}} \approx$

$\frac{1}{2} f_{\rm binary} f_{\rm prim}^{\rm HMXB} f_{\rm SN}^{\rm HMXB}$. Here, $f_{\rm binary}$ is the fraction of stars that are in binaries, $f_{\rm prim}$ is the fraction of binaries, that are in the right mass range for evolving into a X-ray binary and $f_{\rm SN}$ is the fraction of the binary systems that survive the first supernova explosion.
The evolution of low-mass X-ray binaries (LMXB) is more complicated due to the similarity of the post supernova binary (PSNB) and the real LMXB timescales, $\tau_{\rm PSNB} \approx 1.9 \times 10^9$ yr and $\tau_{\rm LMXB} \approx 10^9$ yr. The total abundances $N_{\rm PSNB}$ and $N_{\rm LMXB}$ are described by the following coupled equations:

$$\frac{\partial N_{\rm PSNB}(t)}{\partial t} = \alpha_{\rm PSNB} \frac{\dot{M}_\star}{10 {\rm M}_\odot} - \frac{N_{\rm PSNB}(t)}{\tau_{\rm PSNB}} \tag{8.49}$$

$$\frac{\partial N_{\rm LMXB}(t)}{\partial t} = \frac{N_{\rm PSNB}(t)}{\tau_{\rm PSNB}} - \frac{N_{\rm LMXB}(t)}{\tau_{\rm LMXB}}. \tag{8.50}$$

Here the parameter $\alpha_{\rm PSNB}$ is defined as $\frac{1}{2} f_{\rm binary} f_{\rm prim}^{\rm LMXB} f_{\rm SN}^{\rm LMXB}$.
The values of the different fractions f (especially as a function of redshift) are very hard to estimate (Fabbiano, 1995). We thus use the observed number of X-ray binaries to calibrate $\alpha_{\rm HMXB}$ and $\alpha_{\rm LMXB}$ at $z = 0$. With a value of roughly 100 LMXBs and 50 HMXB in the Milky Way (Grimm et al., 2002) we find $\alpha_{\rm HMXB} \approx 5.00 \times 10^{-5}$ and $\alpha_{\rm LMXB} \approx 4.35 \times 10^{-7}$. The resulting numbers of HMXBs and LMXBs are shown in figure 8.9. We present here the evolution for the case of a starburst galaxy, which is expected to have more X-ray binaries due to a larger SFR. Note, that the evolution of the X-ray binary population follows closely the history of star formation. The number of HMXBs peaks at a redshift of roughly 5, which corresponds to the peak of the star formation rate (see figure 8.1), while the peak of the LMXB is at a smaller redshift of roughly 1.5. This evolutionary delay comes from the long LMXB timescales, $\tau_{\rm PSNB}$ and $\tau_{\rm LMXB}$, and results in the fact that the LMXBs are the dominant type of X-ray binaries at present day.
For computing the X-ray luminosity that results from the X-ray binaries in a galaxy, we need to know the typical luminosities of LMXBs and HMXBs. In a detailed study of the Milky Way Grimm et al. (2002) find that the total luminosity of all X-ray binaries in the 2-10 keV range is $\approx 2 - 3 \times 10^{39}$ erg s^{-1} (LMXB) and $\approx 2 - 3 \times 10^{38}$ erg s^{-1} (HMXB). With the total numbers of the X-ray binaries given above this corresponds to mean luminosities of $\approx 2.5 \times 10^{37}$ erg s^{-1} (LMXB) and $\approx 5.0 \times 10^{36}$ erg s^{-1} (HMXB) in the 2-10 keV band. In our study we use the 0.5-8 keV band and thus need to estimate the luminosity in this band. Wang et al. (2013) find a typical conversion factor of 1.21 between the two bands for X-ray binaries, which we apply here, too. We thus find for the total luminosity due to X-ray binaries in the 0.5-8 keV band

$$\begin{aligned} L_{XB}(z) &= 1.21 \times 2.5 \times 10^{37} \text{ erg s}^{-1} \, N_{\rm LMXB}(z) \\ &\quad + 1.21 \times 5.0 \times 10^{36} \text{ erg s}^{-1} \, N_{\rm HMXB}(z). \end{aligned} \tag{8.51}$$

The evolution of L_{XB} according to the analytical model is presented in figure 8.10, where we also plot the luminosities from inverse Compton scattering of a starburst for comparison.

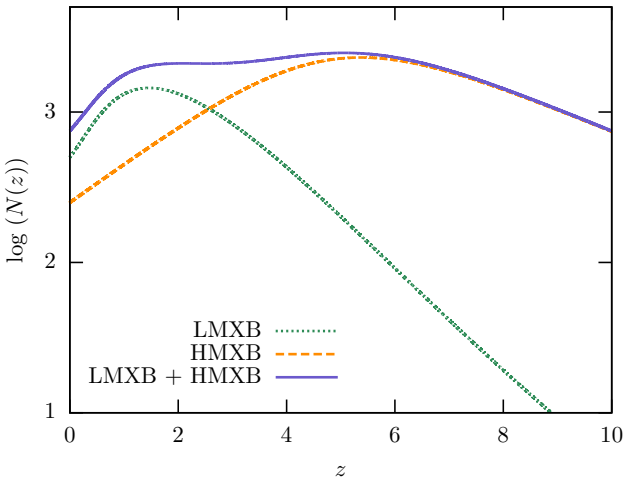

Figure 8.9:
The number of X-ray binaries in a starburst galaxy as a function of redshift z. We show the number of low-mass X-ray binaries (LMXB, orange lines), high-mass X-ray binaries (HMXB, green lines) and the sum of both (LMXB+HMXB, blue lines).
image credit: Schober et al. (2014)

Observational Relations of X-Ray Binaries

As HMXBs evolve on very short timescales (see above), they are a good tracer for the SFR. However, at SFRs comparable to the Milky Way or lower, the X-ray binary population is dominated by LMXBs, which in return provide a measure for the total stellar mass in a galaxy. Only in galaxies with high SFRs the X-ray luminosity from X-ray binaries is dominated by the emission of HMXBs (Persic & Rephaeli, 2007). For the X-ray binary emission, Lehmer et al. (2010) find the following correlation with the star formation rate

$$L_{\mathrm{XB}}^{2-10\ \mathrm{keV}} = 10^{39.43}\ \mathrm{erg\ s^{-1}} \left(\frac{\dot{M}_\star}{\mathrm{M_\odot yr^{-1}}} \right)^{0.74} . \tag{8.52}$$

This correlation is valid for the $2-10$ keV range and Kroupa IMF. Converting into the $0.5-8$ keV the X-ray luminosity changes to (Wang et al., 2013)

$$L_{\mathrm{XB}}^{0.5-8\ \mathrm{keV}} = 1.21 \times 10^{39.43}\ \mathrm{erg\ s^{-1}} \left(\frac{\dot{M}_\star}{\mathrm{M_\odot yr^{-1}}} \right)^{0.74} . \tag{8.53}$$

8.5.2 Supernova Remnants

Besides X-ray binaries, supernova remnants are point sources of X-ray emission in galaxies. The thermal X-ray radiation is emitted mostly during the free expansion and the Sedov-Taylor phase with a typical duration of less then $\tau_{\mathrm{SNR}} = 10^3$ yr (Woltjer, 1972; Chevalier, 1977). The typical number of X-ray emitting supernova remnants that are observed in a galaxy is

$$N_{\mathrm{SNR}} = \tau_{\mathrm{SNR}} \dot{N}_{\mathrm{SN}} = 12.72\ \frac{\dot{M}_\star}{\mathrm{M_\odot yr^{-1}}}, \tag{8.54}$$

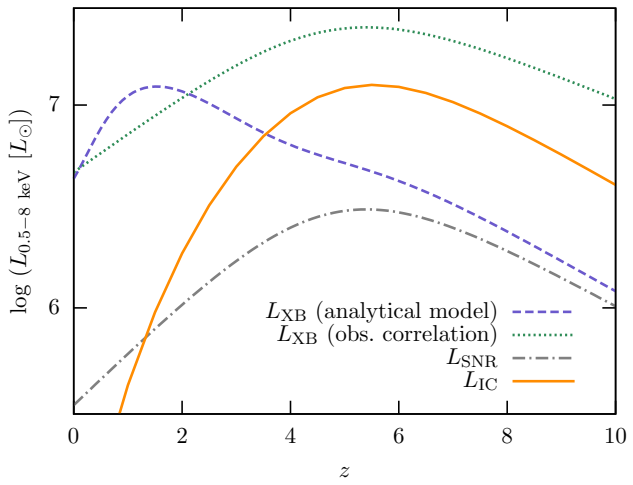

Figure 8.10:
The luminosities of various galactic X-ray sources as a function of redshift z. The luminosity from X-ray binaries is shown by the dashed blue line, when using the analytical evolutionary model, and by the dotted green line, when using the observational correlation. The X-ray luminosity contribution from supernova remnants are represented by the dashed-dotted gray line. For comparison we show the inverse Compton scattering luminosity (solid orange line) for our fiducial cosmic ray spectrum ($\xi = 0.1$ and $\chi = 2.2$) and the timescale given in (8.20). We use here the ISRF from table 8.2 and a starburst galaxy.
image credit: Schober et al. (2014)

where we use the supernova rate (8.8). With a typical X-ray luminosity of supernova remnants of 10^{37} erg s^{-1} the total X-ray emission of galaxies with star formation rates between 10 and 1500 $\mathrm{M}_\odot \mathrm{yr}^{-1}$ are roughly $10^4 - 10^6$ $\mathrm{L}_\odot$. Compared to the expected luminosity of X-ray binaries presented for example in figure 8.10, supernova remnants provide only a minor contribution to a galaxy's total X-ray emission.

8.5.3 Active Galactic Nuclei

If a galaxy hosts an active galactic nucleus (AGN) we expect additional X-ray emission. Typical X-ray luminosities of nearby AGNs are around 10^7 $\mathrm{L}_\odot$. We expect however, that a large fraction of the radiation from the central black hole is absorbed by dust. We thus use the observed values of the X-ray luminosity that are not corrected for dust absorption. Ideal for our analysis would be starburst galaxies at high redshifts without AGNs, which might be detected in future observations.

8.6 Application to Exemplary Galaxies

In this section we apply our model for the inverse Compton scattering to real galaxies in order to determine properties of cosmic rays and magnetic fields. Our strategy is illustrated in figure 8.11. As observational input we need the redshift z of an object, the FIR luminosity and the X-ray luminosity. The redshift can be determined spectroscopically or with photometry. For the FIR luminosity of objects at high redshift, from which we can determine the SFR $\dot{M}_\star$, there is a lot of data available from several surveys and also *ALMA* will be a powerful tool in the future, and we can use *Chandra* data for the X-ray luminosity L_X.
From z and $\dot{M}_\star$ we calculate the expected inverse Compton X-ray luminosity according to equation (8.43), which however includes the normalization of the cosmic ray spectrum $Q_{\mathrm{p},0}$. This quantity depends on the fraction of supernova energy that goes into cosmic rays ξ that is an open parameter of our model. We get an upper limit of $Q_{\mathrm{p},0}$ and accordingly ξ, from which we calculate the cosmic ray energy E_CR, by the equalizing $L_\mathrm{IC}(Q_{\mathrm{p},0})$ with the observed X-ray luminosity of a galaxy $L_\mathrm{X,obs}$. In this step we imply that all the X-ray luminosity results from inverse Compton scattering. With the additional assumption of energy equipartition between cosmic rays and the magnetic field, an assumption which is commonly made in present-day galaxies (Beck & Krause, 2005), we obtain an upper limit for the magnetic energy E_mag. If one further estimates the volume of the galaxy, also an upper limit to the magnetic field strength B is possible.
The single steps from above are described in more detail in the following.

8.6.1 Cosmic Ray Energy and the Equipartition Magnetic Field Strength

Cosmic Ray Energy as Function of the Free Parameter ξ

In section 8.4 we determine the expected inverse Compton flux of a galaxy with a given cosmic ray spectrum. We model the cosmic ray spectrum by assuming that a fraction ξ of the supernova energy is converted into kinetic energy of electrons and protons (see equation 8.13). The energy density of cosmic rays u_CR as a function of the ξ is

$$u_\mathrm{CR}(\xi) = \frac{f_\pi \ (m_\mathrm{p}c^2)^2 \ \gamma_{\mathrm{p},0}^{2-\chi} \ \tau_\pi(z)}{V(z) \ (\chi - 2)} \ Q_{\mathrm{p},0}(\xi), \tag{8.55}$$

with $Q_{\mathrm{p},0}(\xi)$ given in equation (8.21). We show $u_\mathrm{CR}(\xi)$ in figure 8.12 for different fixed SFRs and a galaxy volume scaling as in equation (8.3). Note, that the redshift dependence of $u_\mathrm{CR}(\xi)$ cancels as the timescale of pion production is also proportional to $(1+z)^{-3}$. With increasing SFR the cosmic ray energy increases for a fixed ξ. This is intuitively clear.

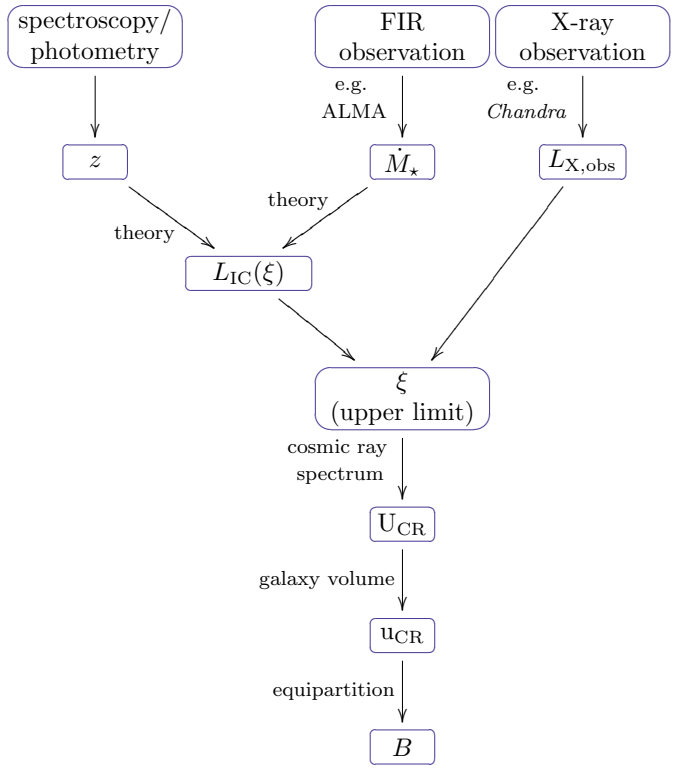

Figure 8.11:
Illustration of our strategy for determining the cosmic ray density the magnetic field strength in redshifted starforming galaxies from observations of the redshift, the far-infrared and the X-ray flux. For more details see section 8.6. *image credit: Schober et al. (2014)*

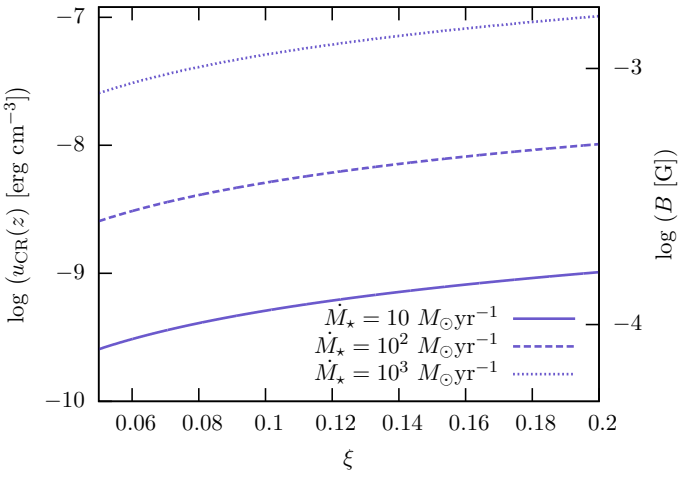

Figure 8.12:
The cosmic ray density u_{CR} and the equipartition magnetic field strength B as a function of the fraction of energy that goes into acceleration of cosmic rays in supernovae ξ. We use here a scaling of the galaxy volume proportional to $(1+z)^{-3}$ and the approximation $\tau_e \approx \tau_{\mathrm{IC}}$. The different curves represent different star formation rates: $\dot{M}_\star = 10\ \mathrm{M_\odot yr^{-1}}$ (solid line), $\dot{M}_\star = 100\ \mathrm{M_\odot yr^{-1}}$ (dashed line) and $\dot{M}_\star = 1000\ \mathrm{M_\odot yr^{-1}}$ (dotted line). *image credit: Schober et al. (2014)*

Determination of the Cosmic Ray Energy from the Observed X-Ray Luminosity

From the data we will now directly determine the normalization $Q_{\mathrm{p},0}$ and thus the free parameter ξ, to which the X-ray luminosity from inverse Compton scattering (8.43) is directly proportional. Solving equation (8.43) for $Q_{\mathrm{p},0}$ and using the observed luminosity $L_{\mathrm{X,obs}}$ as an input yields:

$$\begin{aligned} Q_{\mathrm{p},0}(L_{\mathrm{X,obs}}) &= \frac{f_{\mathrm{sec}} h^{(4+\chi)/2} m_{\mathrm{e}}^{\chi-2} \sigma_{\mathrm{T}}}{16\pi^2 c m_{\mathrm{p}}^{\chi} f_\pi r_0^2} \frac{\chi-2}{F(\chi)} \frac{u_{\mathrm{ISRF}}}{(1+z)^{(\chi-2)/2}} \left(\sum_i f_i \ (kT_i)^{(6+\chi)/2} \right)^{-1} \\ &\quad \times \frac{L_{\mathrm{X,obs}}}{\nu_2^{(2-\chi)/2} - \nu_1^{(2-\chi)/2}}. \end{aligned} \tag{8.56}$$

Note, that (8.56) depends on the star formation rate only via the total energy density of the radiation field $u_{\mathrm{ISRF}} \propto \sum_i f_i \, T_i^4$ and the sum over $f_i \, T_i^{3+\chi/2}$. With a value of χ very close to 2, these two terms cancel and u_{CR} becomes almost independent of the star formation rate. Also the dependence on redshift is small as again $(1+z)^{\chi/2-1}$ is almost constant.
With equation (8.56) our free parameter, the energy input of supernovae into cosmic ray acceleration ξ, can be expressed as

$$\xi(L_{\mathrm{X,obs}}) = \frac{(m_{\mathrm{p}} c^2)^2 \ \gamma_{\mathrm{p},0}^{2-\chi}}{E_{\mathrm{SN}} \dot{N}_{\mathrm{SN}} (\chi-2)} Q_{\mathrm{p},0}(L_{\mathrm{X,obs}}), \tag{8.57}$$

where we used equation (8.13). Further, the energy density of cosmic rays as a function of the observed X-ray luminosity can then be calculated with

$$u_{\mathrm{CR}}(L_{\mathrm{X,obs}}) = Q_{\mathrm{p},0}(L_{\mathrm{X,obs}}) \frac{\gamma_{\mathrm{p},0}^{2-\chi} m_{\mathrm{p}} c^2}{\chi-2} f_\pi \frac{\tau_\pi(z)}{V_{\mathrm{gal}}(z)}. \tag{8.58}$$

The luminosity is converted into the observed flux by equation (8.46). We plot the cosmic ray energy against the flux S_{IC} in figure 8.13. The different line colors represent different redshifts, while the line styles indicate different SFRs. The figure shows clearly that the SFR dependence vanishes in our model of the inverse Compton scattering, as the individual lines match almost perfectly. Note, however, that the flux itself depends on the SFR. As shown in figure 8.8, the flux increases with $\dot{M}_\star$. Actually, equations (8.46), (8.43), (8.21), and (8.8) indicate that $S_{\mathrm{IC}} \propto Q_{\mathrm{p},0} \propto \dot{N}_{\mathrm{SN}} \propto \dot{M}_\star$, connecting the inverse Compton flux with the number of cosmic rays, which is in our model directly proportional to the supernova rate and thus to the SFR.

Equipartition Assumption

In present-day galaxies the different energy components of the ISM, like the kinetic energy of the gas, the cosmic rays and the magnetic fields, are almost in equilibrium.

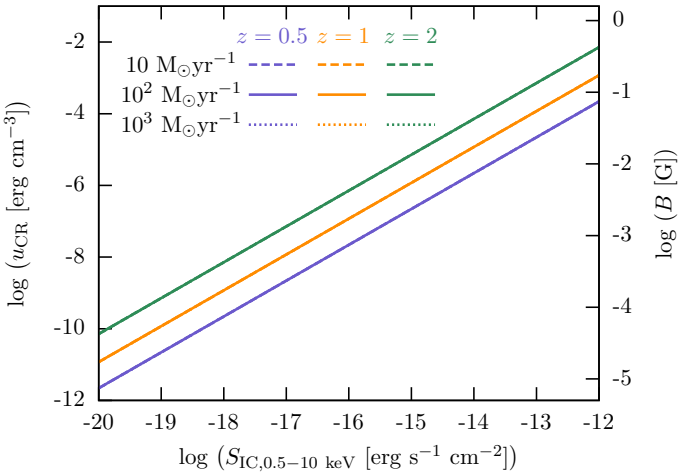

Figure 8.13:
The energy density of cosmic rays (electrons + protons) u_{CR} as a function of the observed flux from inverse Compton scattering S_{IC} for the approximation $\tau_e \approx \tau_{IC}$. The blue lines show the results at a redshift of $z = 0.5$, the orange lines at $z = 1$ and the green lines at $z = 2$. The different line styles refer to different star formation rates $\dot{M}_\star$. We use here the starburst model with different line styles corresponding to different star formation rates of 10 $M_\odot$ yr^{-1} (dashed lines), 10^2 $M_\odot$ yr^{-1} (solid lines) and 10^3 $M_\odot$ yr^{-1} (dotted lines). On the right hand side y axes we show the corresponding equipartition magnetic field strength B. *image credit: Schober et al. (2014)*

This is a result of the dynamical interplay between the individual components and known as energy equipartition. It provides a very important tool for studying the magnetic field strength from the observed synchrotron radiation, which is emitted by cosmic ray $e^{\pm}$ traveling through the magnetized interstellar medium (Beck & Krause, 2005).
In highly redshifted galaxies magnetic fields were assumed to be unimportant, because the timescales of a galactic large-scale dynamo are high and thus no strong magnetic field can result from this mechanism. However, recent semi-analytical (Schober et al., 2013) and numerical simulations (Beck et al., 2012; Latif et al., 2013) have shown that a turbulent dynamo can actually amplify weak magnetic seed fields in galaxies on Myr timescales by converting turbulent kinetic energy into magnetic energy. The turbulent dynamo can amplify fields up to a certain fraction of the turbulent kinetic energy even on galactic length scales Federrath et al. (see, e.g. 2011). With this strong unordered magnetic fields we can again use the assumption of energy equipartition:

$$u_{CR} = u_B. \tag{8.59}$$

With the magnetic energy density, $u_B = B^2/(8\pi)$, the magnetic field strength can be calculated as

$$B = (8\pi u_{CR})^{1/2}. \tag{8.60}$$

ALESS ID	z	$\dot{M}_\star$ [$M_\odot$ yr^{-1}]	$L_{\mathrm{obs,0.5-8\ keV}}$ [erg s^{-1}]
011.1	2.68	789	3.16×10^{43}
017.1	2.04	161	2.51×10^{42}
045.1	2.34	350	1.58×10^{42}
057.1	2.94	439	5.01×10^{43}
066.1	1.31	322	3.16×10^{44}
067.1	2.12	528	2.51×10^{42}
070.1	2.33	789	1.58×10^{43}
073.1	4.76	556	5.01×10^{43}
084.1	2.26	267	1.00×10^{43}
114.2	1.61	261	6.31×10^{42}

Table 8.3:
The properties of the ALESS sub-mm objects with X-ray counterparts in the E-CDF-S, which were discovered by Wang et al. (2013). We list here the ALESS ID, the redshift z, the star formation rate $\dot{M}_\star$ in $M_\odot$ yr^{-1} (converted into Kroupa IMF) and the uncorrected X-ray luminosity $L_{\mathrm{obs,0.5-8\ keV}}$ in erg s^{-1}. For more details see section 8.6.2.

Putting the equations together, one can show that the resulting magnetic field B scales with $Q_{\mathrm{p},0}^{1/2}$ and also depends on the slope of the cosmic ray spectrum χ. The equipartition field strengths are given on the right side of figures 8.12 and 8.13.

8.6.2 Available Observational Data at High Redshifts

The combination of X-ray data of the *Chandra* deep fields with the sub-millimeter data from ALMA, provides new insides in the properties of distant galaxies. Our analyses is based on the processed data given in Wang et al. (2013), who have identified 10 sub-mm counter sources with objects in the *Chandra* Deep Field - South (CDF-S).
Wang et al. (2013) use the X-ray data from the 4 Ms CDF-S (Lehmer et al., 2005) and the 250 ks E-CDF-S survey (Xue et al., 2011). The E-CDF-S has been observed by an ALMA Cycle 0 survey at 870 μm, which is called the ALMA LABOCA E-CDF-S Submm Survey (ALESS) (Hodge et al., 2013; Karim et al., 2013). The whole ALESS survey detected 99 sub-mm galaxies (SMGs), 10 of which Wang et al. (2013)

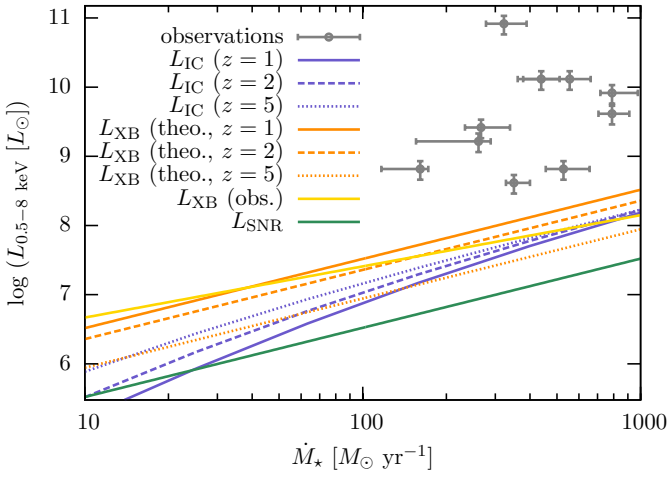

Figure 8.14:
The 0.5-8 keV X-ray luminosity as a function of star formation rate $\dot{M}_\star$. We compare the inverse Compton luminosity $L_{\rm IC}$ (for the full cosmic ray timescale 8.20) with the luminosity of X-ray binaries $L_{\rm XB}$ and the one of supernova remnants. Also plotted are the X-ray luminosities (with an 30% error as discussed in Xue et al. (2011)) of the *Chandra* deep field galaxies from Wang et al. (2013). Different line styles represent different redshifts in the model from $z = 1$ (solid lines) to $z = 2$ (dashed lines) to $z = 5$ (dotted lines).
image credit: Schober et al. (2014)

could identify with X-ray counterparts. These SMGs are listed in table 8.3, where besides their X-ray luminosities $L_{\rm X,obs}$, the corresponding redshifts z and SFRs $\dot{M}_\star$ are provided. Note, that Wang et al. (2013) used a Salpeter IMF to determine the SFRs. We converted their values to a Kroupa IMF by dividing by a factor of 1.8. Further, we use here the luminosity values, which are not corrected for dust attenuation, as we assume that the latter is most efficient for the X-ray emission from the central black hole. Most of the redshifts z are observed spectroscopically within the zLESS survey (Danielson et al. 2013, in preparation) or taken from literature, expect for ALESS 45.1, which is observed photometrically (Simpson et al., 2013). The SFRs listed in table 8.3 are derived by Wang et al. (2013) from the correlation with the infrared luminosity by Kennicutt (1998) (see equation 8.7).
The observed X-ray luminosities from Wang et al. (2013) are shown as a function of SFR in figure 8.14. All the sources from the catalog have extremely high SFRs from 161 $\rm M_\odot yr^{-1}$ up to 789 $\rm M_\odot yr^{-1}$. In the figure we show also the expected luminosity of X-ray binaries from the analytical model of Ghosh & White (2001) and the observational correlation from Lehmer et al. (2010) $L_{\rm XB}$, as well as the luminosity from supernova remnants $L_{\rm SNR}$ and the inverse Compton luminosity $L_{\rm IC}$. Most of the observed galaxies have very high luminosities, even above the X-ray binary predictions. Due to this fact and also as a result of additional tests most of the galaxies have clearly been classified as AGN hosts, except for ALESS 045.1 and ALESS 067.1. The X-ray luminosity of these two galaxies could be explained by X-ray binary emission. Alternatively a huge contribution of the luminosity could come from the inverse Compton scattering.

In the following we use ALESS 045.1 and ALESS 067.1 as examples, for which we will derive upper limits for the cosmic ray density from the inverse Compton effect. We make the assumption that the entire X-ray luminosity observed comes from inverse Compton scattering. With our model we then result in a value for the free parameter ξ, which is given in the first line of tables 8.4 and 8.5 for the two galaxies and different slopes of the cosmic ray spectrum χ. Note, that all the calculated values of ξ are larger than our fiducial value $\xi = 0.1$. This indicates that we are overestimating the contribution of the inverse Compton luminosity in all cases by factors up to 111. Consequently the magnetic field strength will be overestimated by a factor of roughly 3. The cosmic ray energies given in the second line of tables 8.4 and 8.5. can thus be only treated as upper limits. In the following lines of the table we present the cosmic ray densities and the equipartition magnetic field strengths for different fixed galaxy radii. As the galaxies are not spatially resolved in the observations, we do not have any information about their radius. With radii comparable to the one of M82 plus radii ten times smaller and larger then that (see numbers listed in table 8.1), we get hints to the energy density in the galaxies. For ALESS 045.1, which has a SFR of 350 $M_{\odot}yr^{-1}$, we find values between 9.05×10^{-5} G and 9.05×10^{-4} G for our fiducial cosmic ray spectrum with $\chi = 2.2$. For ALESS 067.1 the upper limits for the magnetic field strength is slightly higher with $B \approx 1.26 \times 10^{-4}$ G to $B \approx 1.26 \times 10^{-3}$ G.

8.6.3 Uncertainties in the Model and Possible Extensions

Our model for the determination of cosmic ray densities and magnetic fields in galaxies via the inverse Compton scattering process includes many assumptions. We will discuss the individual problems in the following.
As an input for our semi-analytical model we use integrated properties of the galaxies, like the volume, the total cosmic ray energy and the total luminosities. In reality the energy is not homogeneously distributed over the galaxy, but follows a certain radial and vertical profile. This profile might be superimposed with more complex structures like spiral arms. When applying our model to observational data, there is often no information about the spatial extension of the galaxies. In the context of observed point sources we thus can only estimate the total energies and no energy densities.
Further uncertainties enter the model of the cosmic ray spectrum. The injection of cosmic rays is entirely based on shock acceleration in supernova remnants, however cosmic rays might also origin from reconnection sites or extragalactic sources. For estimating the injection spectrum of cosmic rays we assume that a certain fraction of the supernova energy, which we treat as an open parameter, is converted into kinetic energy of charged particles. Also the slope of the spectrum is an open parameter in our model. For deriving the steady state spectrum we use the diffusion equation of cosmic rays. We assume spatial homogeneity, and by this ignore any spatial diffusion of the particles. This so-called leaky box approximation of the diffusion equation is very common, but implications of non-homogeneity would be interesting

	ALESS ID 045.1		
	$\chi = 2.1$	$\chi = 2.2$	$\chi = 2.3$
ξ	1.083	0.682	0.567
U_{CR} [erg]	8.63×10^{54}	5.44×10^{54}	4.51×10^{54}
$V_{\mathrm{gal}} = 0.1\ V_{\mathrm{M82}}$			
u_{CR} [erg cm^{-3}]	5.19×10^{-8}	3.27×10^{-8}	2.72×10^{-8}
B [G]	1.14×10^{-3}	9.07×10^{-4}	8.26×10^{-4}
$V_{\mathrm{gal}} = V_{\mathrm{M82}}$			
u_{CR} [erg cm^{-3}]	5.19×10^{-9}	3.27×10^{-9}	2.72×10^{-9}
B [G]	3.61×10^{-4}	2.87×10^{-4}	2.61×10^{-4}
$V_{\mathrm{gal}} = 10\ V_{\mathrm{M82}}$			
u_{CR} [erg cm^{-3}]	5.19×10^{-10}	3.27×10^{-10}	2.72×10^{-10}
B [G]	1.14×10^{-4}	9.07×10^{-5}	8.26×10^{-5}

Table 8.4:
Upper limits on the cosmic ray energy, the cosmic ray density and the magnetic field strength for two objects of the data catalog of Wang et al. (2013) ALESS ID 045.1, which have not been identified as hosting an AGN. We present results for the assumption that all X-ray luminosity is produced in inverse Compton scattering. As there are other processes emitting X-rays, this assumption results only in upper limits, which reflects in the high values of the fraction of supernova energy that is transformed into kinetic energy of cosmic rays ξ (theoretically expected: $\xi \approx 0.1$, see text). We show the resulting value of ξ obtained with this assumption in the first line. In the second line we present the total cosmic ray energy. For determining the cosmic ray densities u_{CR} and the equipartition field strengths B we use three different volumes of the starburst region: the volume of the starburst region in M82 V_{M82} and volumes ten times smaller and larger then V_{M82}.

	ALESS ID 067.1		
	$\chi = 2.1$	$\chi = 2.2$	$\chi = 2.3$
ξ	1.14	0.713	0.591
U_{CR} [erg]	1.68×10^{55}	1.05×10^{55}	8.71×10^{54}
$V_{\mathrm{gal}} = 0.1\ V_{\mathrm{M82}}$			
u_{CR} [erg cm^{-3}]	1.01×10^{-7}	6.33×10^{-8}	5.24×10^{-8}
B [G]	1.59×10^{-3}	1.26×10^{-3}	1.15×10^{-3}
$V_{\mathrm{gal}} = V_{\mathrm{M82}}$			
u_{CR} [erg cm^{-3}]	1.01×10^{-8}	6.33×10^{-9}	5.24×10^{-9}
B [G]	5.03×10^{-4}	3.99×10^{-4}	3.63×10^{-4}
$V_{\mathrm{gal}} = 10\ V_{\mathrm{M82}}$			
u_{CR} [erg cm^{-3}]	1.01×10^{-9}	6.33×10^{-10}	5.24×10^{-10}
B [G]	1.59×10^{-4}	1.26×10^{-4}	1.15×10^{-4}

Table 8.5:
Same contents as in table 8.4, but for ALESS ID 067.1.

to study in a more detailed model. We further assume that the cosmic ray protons only experience catastrophic losses, i.e. escape from the galaxy, while the cosmic ray $e^{\pm}$ are modeled to be confined within the galaxy. The latter loose their energy in our model only via different cooling mechanisms. Observations of cosmic rays are made via the cooling radiation of $e^{\pm}$. A potential problem is the interpolation of the energy in cosmic ray $e^{\pm}$ to the total cosmic ray energy, which is actually dominated by the protons. A more direct detection of the cosmic ray energy would be possible with simultaneous γ-ray observations.
For the energy loss of cosmic ray electrons to be dominated by inverse Compton scattering one needs to find galaxies at high redshift and with large star formation rates (see figure 8.3 and the discussion in section 8.3). If inverse Compton scattering is not the most important loss channel, but similar or below synchrotron emission or bremsstrahlung, the model of the steady state spectrum needs to be modified. A detailed analysis of the different energy loss mechanisms will be an interesting future test.
Another caveat in our calculation remains the influence of additional X-ray sources, such as X-ray binaries and AGNs. The contribution of these can potentially be investigated in more detail with observations in additional energy ranges. Furthermore, detailed models especially of the luminosity from the accretion on the central supermassive black hole are required. Galaxies without AGNs would be easier to handle in the framework of our model and result in better estimates of the cosmic ray properties. It is, however, very hard to find such objects at high redshifts, as their total luminosity is very low. Hopefully, future observatories like *Athena+* will detect more starburst galaxies without AGNs at large distances.

8.7 Conclusions from Our Inverse Compton Model

In this work we construct a model for the X-ray emission of starforming galaxies via inverse Compton scattering as a function of redshift. We model the star formation rate (SFR) history, the evolution of the interstellar radiation field (ISRF) and the cosmic ray spectrum. The inverse Compton scattering process between high energy cosmic ray electrons and the ISRF is quantified and analyzed in terms of different properties of the galaxy. We focus on two galaxy models: a galaxy with normal star formation rate, similar to the Milky Way, and a starburst galaxy similar to M82. With a detailed description of the ISRF and the steady state cosmic ray spectrum we are able to calculate the expected inverse Compton luminosity.
We with our galaxy models we find that the spectral energy distribution $u_{\mathrm{ISRF},\nu}$ of a normal galaxy is dominated by the cosmic microwave background (CMB), while the one of a starburst galaxy is dominated by the cold infrared (IR) component at least at moderate redshifts (see figure 8.2). The strong IR component makes inverse Compton scattering in starburst galaxies more efficient (see also figures 8.6 and 8.4). Our detailed analysis of the energy loss timescales of cosmic ray electrons (see figure 8.3) has shown, that the inverse Compton scattering is not dominant in galaxies with

normal star formation. At low redshifts z bremsstrahlung and synchrotron emission are most important. With increasing redshift the inverse Compton timescale decreases, but even at $z = 5$, bremsstrahlung is still dominating. On the other hand in starburst galaxies energy losses proceed mostly via inverse Compton scattering. These galaxies are thus in the focus of this work.
With the cosmic ray spectrum and the ISRF as an input we calculate the luminosity from inverse Compton scattering. We find that the X-ray flux from pure inverse Compton scattering can be detected with *Chandra* up to $z \approx 1$ for starburst galaxies with $\dot{M}_\star \gtrsim 200\ \mathrm{M_\odot yr^{-1}}$. With the future X-ray observatory *Athena+* detections up to $z \gtrsim 2$ will be possible (see figure 8.8). In order to estimate the significance of the inverse Compton scattering compared to other galactic X-ray sources, we investigate the role of X-ray binaries, which are one of the main X-ray sources in nearby galaxies. We summarize an analytical model for the number of high-mass X-ray binaries (HMXB) and low-mass X-ray binaries (LMXB) by Ghosh & White (2001). For comparison we also discuss an observational correlation for X-ray binary luminosity by Lehmer et al. (2010). Furthermore, we estimate the influence of supernova remnants on the total galactic X-ray luminosity. Comparison of the expected inverse Compton luminosity with other X-ray sources shows that supernova remnants are negligible. X-ray binaries play a more important role. In our model their luminosity is a factor of 2 brighter than the inverse Compton luminosity at present day. At redshifts above roughly 2 inverse Compton luminosity becomes comparable or even dominant over the X-ray binaries (see figure 8.10).
In the last part of the paper (section 8.6) we apply our model to real observations. As observational input we use M82 as a test case and two higher redshifted galaxies of the data set of Wang et al. (2013), which have not been identified as hosts of active galactic nuclei (AGNs). We compare the observed X-ray luminosity with the one resulting from our inverse Compton model. This way we can fix the free parameter in our model, namely the normalization of the cosmic ray spectrum. In the next step we calculate the total energy of cosmic rays and assume that it is in equipartition with the magnetic energy.
With our model the energy density of cosmic rays can be determined directly from the observed X-ray flux under the assumption that the flux only origins from inverse Compton scattering. The results for different redshifts are plotted in figure 8.13. We apply our model to the two galaxies from the data set of Wang et al. (2013) that have not been clearly identified as hosting an AGN. Our results for the fraction of energy going from supernovae into cosmic ray acceleration is higher then the theoretically expected value of 10 percent. This suggests that we are overestimating the inverse Compton luminosity and thus the energy of cosmic rays by a factor of up to 9. Our results for the cosmic ray density and the equipartition field strengths are thus only upper limits. Depending on the galactic volume we find values for the magnetic field strength of roughly $10^{-4} - 10^{-3}$ G for the exemplary galaxies (see tables 8.4 and 8.5).
There are several uncertainties in our model including the modeling of the cosmic ray spectrum, the additional X-ray sources and the evolution and total size of the

galaxy volume. Most of the galaxies observed at high redshift include AGNs. We try not to include the X-ray emission of these by using the uncorrected X-ray luminosities given in Wang et al. (2013). However, we still substantially overestimate the X-ray luminosity from inverse Compton scattering. It thus is essential to model the X-ray emission of galaxies in more detail in future. Given all the uncertainties discussed in section 8.6.3, we mention that our approach might not yet be suitable for practical usage. It rather provides first theoretical estimates for cosmic rays and magnetic fields in young galaxies based on a simplified galaxy model. Additional investigations and improvement of the theoretical models are necessary in order to draw more quantitative conclusions.

We expect that also the available data of high redshifted galaxies will increase in the next years. For our studies especially observations of distant starburst galaxies without active galactic nuclei would be important. With X-ray data from the *Chandra* deep fields the next step would be to identify infrared counterparts of X-ray galaxies, in order to determine their SFR. This is possible with the *ALMA* telescope. Further the next generation of X-ray telescopes is planned and we hopefully will receive a lot of data with *Athena+*.

With these new technologies our knowledge of the origin and evolution of galactic magnetic field hopefully will increase. This will help us to understand moreover the evolution of galaxies in total, as magnetic fields play a crucial role in many physical processes in the interstellar medium and the dynamics of the whole galaxy.

CHAPTER 9

Final Discussion

9.1 Summary of the Thesis

In this thesis we present the results of our studies on the evolution of cosmic magnetic fields. A particularly important epoch is the formation of the first stars and galaxies, which is associated with efficient driving of turbulence. By stretching, folding and twisting the field lines, a turbulent dynamo can amplify preexisting weak magnetic seed fields on short timescales. The energy of the unordered magnetic fields reaches a certain fraction of equipartition with the turbulent kinetic energy at saturation.
We investigate the amplification of magnetic fields by the turbulent dynamo within the Kazantsev theory. With a model for the correlation function of the turbulent velocity field we describe the effects of different types of turbulence, from incompressible Kolmogorov turbulence to highly compressible Burgers turbulence. We present calculations for the kinematic dynamo phase, in which the field strength grows exponentially, and the non-linear phase, where back reactions from the magnetic field lead to a time evolution that follows a power-law. With a simple model of an artificial magnetic energy dependent drift in the velocity field we make analytical predictions for the saturation efficiency of the dynamo. The analytical results are compared to simulations of the small-scale dynamo in turbulent box. The main results of the theoretical modeling of the evolution of a turbulent magnetic field are summarized in the following.

Results from the Turbulent Dynamo Theory

- Dynamo amplification only takes place when the magnetic Reynolds number Rm exceeds a critical Reynolds number $\mathrm{Rm}_{\mathrm{crit}}$. The numerical value of $\mathrm{Rm}_{\mathrm{crit}}$ depends on the type of turbulence and ranges from ≈ 100 for Kolomogorov turbulence to ≈ 2700 for Burgers turbulence. The results for various slopes of the turbulence spectrum are summarized in table 4.1.

- The Kazantsev equation describes the evolution of the magnetic field in the kinematic phase, where the magnetic field strength grows exponentially in time:

$$B(t) = B_0 \exp(\Gamma t). \tag{9.1}$$

The eigenvalues of the Kazantsev equation correspond to the growth rate Γ. Analytical solutions for the growth rate have been derived in the limit of large and small magnetic Prandtl numbers $\mathrm{Pm} = \mathrm{Rm}/\mathrm{Re}$:

$$\Gamma = \begin{cases} \dfrac{163 - 304\vartheta}{60} \dfrac{V}{L} \, \mathrm{Re}^{(1-\vartheta)/(1+\vartheta)} & \text{for } \mathrm{Pm} \gg 1 \\ \alpha \dfrac{V}{L} \, \mathrm{Rm}^{(1-\vartheta)/(1+\vartheta)} & \text{for } \mathrm{Pm} \ll 1 \end{cases} \tag{9.2}$$

with the turbulent velocity V on the forcing scale L and $\alpha \approx 0.027 - 0.0054$ depending on the slope of the turbulence spectrum. Moreover, Re and Rm are the hydrodynamical and magnetic Reynolds number, respectively, and ϑ is the slope of the turbulence spectrum, $v(\ell) \propto \ell^{\vartheta}$. We refer to table 4.1, in which the growth rates for different types of turbulence are listed.
These analytical results reproduce the limits of large and small Pm from a numerical solution of the Kazantsev equation by Bovino et al. (2013), which we present in figure 4.13.

- In the non-linear phase, back reactions from the magnetic field on the velocity field become significant. Under the assumption that the magnetic energy is shifted towards larger scales on the local eddy timescale, the magnetic field strength increases as

$$B(t) = (8\pi)^{1/2} (\tilde{C} t)^{\vartheta/(1-\vartheta)} \tag{9.3}$$

with $\tilde{C}$ given in equation (4.125). While there is no more dependence on Rm nor on Re or Pm, the evolution of the magnetic field in this stage still depends on the type of turbulence characterized by the spectral slope ϑ in the inertial range.

- Saturation of the turbulent dynamo can be modeled via an artificial drift in the velocity field, which leads to an increase of the resistivity η and likewise an decrease of the magnetic Reynolds numbers Rm. For large hydrodynamic Reynolds numbers we find that at saturation the magnetic energy equals roughly 35 % of the turbulent energy in case of Kolomgorov turbulence. For Burgers turbulence this fraction is, with approximately 2 %, considerably smaller.

- The results of various numerical simulations have been discussed. The onset of a small-scale dynamo is observed only above a resolution of 32 cells per Jeans length. This criterion can be associated with the critical magnetic Reynolds number. The exponential growth of the field strength is confirmed in simulations with the growth rates being lower for higher compressibility of the fluid. The saturation level of the turbulent dynamo is a function of the Mach number (see figure 4.23).

With the onset of turbulence during structure formation and preexisting weak seed fields, we expect the turbulent dynamo to play an outstanding role in the early Universe. We use semi-analytical models for the collapse of a primordial halos, including a detailed chemical network in order to follow the thermal evolution of the gas, to model the microphysics in primordial star formation. We assume that turbulence is driven by accretion and estimate the Reynolds number Re, from which we calculate the growth rate of the turbulent dynamo.

The Turbulent Dynamo in the Formation of the First Stars

- With a self-consistent chemical network we follow the thermal evolution and the change of MHD quantities in time or density, respectively. The mircoscopic quantities like viscosity and magnetic diffusivity are calculated within our framework. We find that the magnetic Reynolds and Prandtl number, Rm and Pm, decrease rapidly as the magnetic field strength increases in dynamo amplification.

- The evolution of magnetic energy is calculated including dynamo amplification, spherical compression of field lines and dissipation of magnetic energy by Ohmic and ambipolar diffusion. Especially ambipolar diffusion becomes very important as it increases rapidly with the magnetic field strength and the dissipation rate becomes comparable to the dynamo growth rate, when reaching saturation. Starting from a seed field of 10^{-20} G on the viscous scale, we find that the field strength grows extremely rapidly with the increase of density.

- The transport of the magnetic energy to larger scales is modeled by assuming that the peak of the magnetic spectrum moves on the turbulent eddy timescale. In our model the dynamo saturates on all scales, when the density has increased by a factor of 3 for Kolmogorov turbulence and a factor of 4 for Burgers turbulence. At saturation the magnetic field strength on the Jeans scale is of the order of 10^{-6} G.

- Magnetic field amplification continues via gravitational compression in the subsequent collapse. We compare the growth rate of the spherical compression of field lines with dissipation mechanisms on the Jeans scale and find that the magnetic energy is not dissipated up to high densities.

Our results suggest that the first stars form in a magnetized environment. If these magnetic fields do, however, remain until the formation of the population III protostars or if they dissipate at densities higher than in our calculation is not answered conclusively yet.
The next step presented in this thesis is the analysis of the turbulent dynamo in young galaxies, which form after the first stars in more massive cooling halos. We use semi-analytical one-dimensional models to study the magnetic field evolution in these objects. Turbulence is driven by two different mechanisms, accretion and supernova explosions. We estimate the properties of turbulence in young galaxies and use this as an input for our theoretical dynamo model. The central results of these studies are summarized in the following list.

The Turbulent Dynamo in the Young Galaxies

- In accretion driven turbulence we expect the forcing scales to be roughly the galactic radius ($L_{\rm acc} \approx 10^3$ pc in our model) for a spherical galaxy and the scale hight ($L_{\rm acc} \approx 240$ pc in our model) for a disk galaxy. With the typical Mach number found in numerical simulations we estimate the turbulent velocity in the spherical case, while we apply a certain percentage of the Kepler velocity in a disk. The length scales and velocities for supernova driven turbulence are estimated from the propagation of shocks in the ISM. We find $L_{\rm SN} \approx 700$ pc for a sphere and $L_{\rm SN} \approx 240$ pc for a disk. Both driving mechanisms are expected to lead to compressible turbulence.

- The scenario of magnetic field distribution by supernova explosions of magnetized stars is tested. For a stellar mean field strength of 10^3 G we find that a micro-Gauss ISM field is only reached after 2.2×10^7 Myrs and for a mean strength of 10^2 G after 2.2×10^8 Myrs. With these timescales being much higher than the Hubble timescale, the distribution of stellar magnetic fields cannot explain the fields in the present-day ISM.

- Dynamo amplification is a much more promising candidate for magnetic fields amplification in young galaxies. For our fiducial model we find that the dynamo saturates on the forcing scale in accretion-driven turbulence after a time of roughly 270 Myrs in case of a spherical galaxy and after 24 Myrs in case of a disk. Turbulence generated by supernova shocks can amplify the magnetic field on shorter timescales, with saturation after 15 Myrs in a spherical galaxy and 3.8 Myrs in a disk. The final field strengths generated by the dynamo are between a few times 10^{-6} G and 10^{-5} G in our galaxy models.

A potential probe for the evolution of magnetic fields in galaxies can be non-thermal X-ray emission from cosmic rays, which loose a certain fraction of their energy via inverse Compton scattering. We present a model for the inverse Compton emission

from a galaxy. With an expression for the star formation rate history we estimate the redshift dependence of the inverse Compton luminosity and compare it to other X-ray sources. We also present calculations for individual galaxies with a given star formation rate and derive upper limits for the cosmic ray energy density and the magnetic field strength. The main findings from this work are listed here.

Observational Signatures from Non-Thermal X-Ray Emission

- The spectral energy distribution of a normal galaxy is dominated by the cosmic microwave background (CMB), while the one of a starburst galaxy is dominated by the cold infrared (IR) component, at least at moderate redshifts (see figure 8.2). The strong IR component makes inverse Compton scattering in starburst galaxies very efficient (see also figures 8.6 and 8.4).

- Inverse Compton scattering is not dominant in galaxies with normal star formation, but becomes more and more important with increasing redshift. In starburst galaxies energy losses of cosmic ray electrons proceed mostly via inverse Compton scattering with the latter mechanism dominating for large star formation rates even at $z = 0$ (see figure 8.3).

- Our models predict that the X-ray flux from pure inverse Compton scattering can be detected with *Chandra* up to $z \approx 1$ for starburst galaxies with $\dot{M}_\star \gtrsim 200\ \mathrm{M_\odot yr^{-1}}$. With the future X-ray observatory *Athena+* detections up to $z \lesssim 2$ will be possible (see figure 8.8).

- Comparison of the expected inverse Compton luminosity with other X-ray sources shows that supernova remnants are negligible, while X-ray binaries play a more important role. Only at redshifts above roughly two inverse Compton luminosity becomes comparable or even dominant over the X-ray binaries (see figure 8.10). The modeling of the X-ray contribution of active galactic nuclei is very complicated.

- With our model the energy density of cosmic rays can be determined directly from the observed X-ray flux under the assumption that the flux origins exclusively from inverse Compton scattering. When applying the model to real observational data upper limits of the cosmic ray energy density and the magnetic field strength can be gained (see tables 8.4 and 8.5 for exemplary galaxies).

9.2 Open Questions and Outlook

During the last years a lot of progress has been made in understanding the evolution of magnetic fields with analytical methods and numerical simulations. Also observations were pushed further, which led to the detection of magnetic fields at higher and higher redshifts. However, still many open questions remain. In the following, we suggest possible extensions of the theoretical model and further projects that need to be investigated, some of which are straight-forward, while others are of a more complex nature.

Improvement of the Model for the Turbulence Spectrum

In order to solve the dynamo equation, the Kazantsev equation (4.41), we have to apply a model for the turbulence spectrum as an input. For Gaussian turbulence the fluctuating velocity field is determined by the two-point correlation function $\langle \delta v_i(\mathbf{r}_1, t) \delta v_j(\mathbf{r}_2, s) \rangle$ (see section 4.1.3).
When assuming a delta correlation in time we can separate the time from the spatial component of this correlation function. In this step we clearly lose some information about the velocity field, as in real turbulence we would expect a correlation time that is comparable to the eddy turnover time. However, the turbulent dynamo operates most efficiently on the viscose scale, where the eddy timescales are very short and the delta-correlation is a reasonable approximation. Analytical calculations suggest that a small but finite correlation time tends to increase the growth rate of the turbulent dynamo (Kleeorin et al., 2002). Testing a finite correlation time within our framework would still be very interesting, especially for the case of compressible turbulence.
Homogeneity tells us that the correlation function does not depend on the exact positions $\mathbf{r}_1$ and $\mathbf{r}_2$, but only on their difference $\mathbf{r}_2 - \mathbf{r}_1$. If we also assume the velocity field to be isotropic, one can show that the correlation function can only include terms proportional to δ_{ij}, $\mathrm{r}_i \mathrm{r}_j$, ϵ_{ijk} and functions of $r \equiv |\mathbf{r}_2 - \mathbf{r}_1|$ (Batchelor, 1953). The implications of dropping homogeneity and isotropy need to be investigated and probably require a numerical solution of the dynamo equations.
An effect that has been neglected in this thesis is helicity, a quantity that is given by $\mathbf{v} \cdot \nabla \times \mathbf{v}$. Helicity is identified with an additional term in the correlation function (4.27), which is of the form $\epsilon_{ijk} r_k H(r)$. The inclusion of this term leads to a more generalized form of the Kazantsev equation (e.g. Boldyrev et al., 2005). Malyshkin & Boldyrev (2007) find for incompressible turbulence at large Reynolds numbers that the bound eigenmodes, i.e. the growth rates, are significantly affected by kinetic helicity. The effects of helical motions on compressive turbulence are subjects for potential future studies.
The points discussed above show that there are several ways to extend and generalize the theoretical model for describing a turbulent dynamo.

Better Comparison with Numerical Simulations

In this thesis we started to compare the analytical results for the turbulent dynamo from the Kazantsev theory with the ones obtained from numerical simulations. While it is straightforward to compare the growth rates in the exponential dynamo phase, other dynamo properties are more difficult to compare. For example the critical magnetic Reynolds number is reflected in the critical resolution of simulations. It is, however, challenging to determine the value of the Reynolds numbers in simulations, as the latter are often controlled by numerical dissipation effects. Moreover, we use in the theoretical dynamo models the slope of the total turbulence spectrum as an input. In simulations one can also follow the evolution of energy in solenoidal and compressive modes. Different types of turbulent forcing result in a different distribution of the energy on these modes. For a detailed comparison we would benefit from an analytical prediction for the energy evolution in the different modes.

Transition to Ordered Large-Scale Fields

The magnetic fields observed in local galaxies have, besides the turbulent component, an ordered field component that reaches coherence length scales up to a few kpc (Beck & Wielebinski, 2013). With our model for the magnetic field amplification we predict only unordered magnetic fields on galactic scales. The step from the fluctuating field to large-scale ordered fields is related to large-scale motions like the rotation of the galaxy. At some point, probably an α-Ω dynamo sets in (see section 3.4.1) and an ordering of the field lines takes place. The details of this transition are, however, not clear.

Impact of Magnetic Reconnection

A mechanism that plays an important role in various astrophysical environments is magnetic reconnection (see e.g. Zweibel & Yamada, 2009, for a detailed review). In this process not only the topology of the magnetic field changes, but also magnetic energy is converted into kinetic energy or heat, which could be of crucial importance in the context of our studies. In the classical theory of reconnection (Parker, 1957; Sweet, 1958), magnetic field lines of opposite direction are brought together and reconnect at a typical reconnection velocity of $v_{\mathrm{A}}\mathrm{Rm}^{-1/2}$, where v_{A} is the Alfven velocity. We have seen that the magnetic Reynolds number Rm in astrophysical environments is typically very high, which results in a very slow classical reconnection. However, it has been suggested that reconnection becomes much faster in the presence of turbulence (Lazarian & Vishniac, 1999).
In any system in which a MHD dynamo operates, also reconnection needs to occur, as a dynamo is always associated with a change of magnetic topology. With fast reconnection efficiently converting magnetic energy into other forms of energy, the question arises which one of the two mechanisms is dominating: magnetic field dissipation by reconnection or amplification by a turbulent dynamo. It will be an

important future research project to compare these to processes in different astrophysical environments.

Effects of Magnetic Fields on Structure Formation in the Early Universe

The results presented in this thesis suggest that magnetic fields were already dynamically important in the primordial Universe. The consequences of these fields on the first stars and galaxies could be severe. Especially the possible transport of angular momentum will change the final mass and multiplicity of the first stars. This has been shown in first numerical simulations by Machida & Doi (2013). The effects of magnetic fields on the formation of the first stars need, however, to be studied in more detail to confirm these results. It will be very interesting to find, for example, results for the initial mass function in magnetized primordial star formation. With magnetic fields involved, the first stars could be more massive than currently expected, which has important consequences for their lifetimes, the final stellar objects and the subsequent stellar populations. For studying magnetized primordial star formation in detail, high-resolution numerical simulations are the best option.

Observations of Magnetic Fields at Higher Redshifts

Observations of magnetic fields up to higher redshifts are essential to test our theoretical models. Fortunately, we are entering an era which provides extremely good new telescopes for that purpose.
For observations of magnetic fields, radio telescopes are particularly interesting, since they can detect synchrotron radiation emitted by cosmic ray electrons spiraling in magnetic fields. With an assumption about the ratio of the energy density in cosmic rays to the one in magnetic fields, it is possible to get an estimate for the magnetic field strength (Beck & Krause, 2005). An important impact is expected to come from the *Square Kilometer Array* (SKA) and its pathfinders. SKA will be able to measure polarized synchrotron emission in galaxies up to redshifts of $z \lesssim 0.5$. Observations of the total synchrotron flux are possible up to $z \lesssim 1.5$ for Milky Way type galaxies and up to $z \lesssim 3$ for starbursts (Murphy, 2009). With the galaxy evolution model suggested in chapter 8 of this thesis we can easily predict the expected radio flux from distant galaxies as a function redshift and star formation rate. Once observational data is available, we can use the theoretical model to estimate the properties of young galaxies.
As discussed in chapter 8 of this thesis, inverse Compton scattering is expected to be the most important energy loss channel of cosmic ray electrons in galaxies at high redshift and/or with high star formation rates. The resulting non-thermal emission is typically in the X-ray regime. We have estimated in a simple one-dimensional model that this effect can be detected with the *Chandra* telescope up to redshifts of roughly one. The upcoming X-ray telescope *Athena+* should be able to detect this effect also at considerably higher redshifts. Observations in the X-ray regime

provide an additional measure for the magnetic field strength and will complement results gained by the radio observations.
For interpretation of the data we hope to receive from the new telescopes, detailed models of magnetic fields in galaxies are required. It is thus crucial to continue the improvement of the models, with a focus on the energy losses of cosmic rays and other observables.

9.3 Closing Remarks

The results presented in this thesis, which are based predominantly on semi-analytical argumentation, show that magnetic fields are already important in the early Universe. This conclusion is supported by numerical simulations of the formation of first stars and galaxies, in which an amplification of magnetic fields is observed (see, e.g. Sur et al., 2010; Latif et al., 2013).
Strong magnetic fields can potentially influence the dynamics of the primordial gas and might change our understanding of the very first stars and galaxies. In models of the early Universe, i.e. of the first stars and galaxies, we might have to deal with a situation of similar complexity as in the local Universe. Phenomena like efficient angular momentum transport, jets and outflows, and various magnetohydrodynamical instabilities need to be taken into account. This could change the properties of the first and second generation significantly. To conclude, magnetic fields make the modeling of the primordial Universe even more challenging.
With various upcoming observational machines and the increasing power of numerical simulations, we will be able to test some of the predictions suggested in this thesis and probably a number of fascinating discoveries lie ahead of us.

Astronomy compels the soul to look upwards
and leads us from this world to another.
(Plato, "The Republic", 360 B.C.)

Appendix

APPENDIX A

Derivation of the Kazantsev Equation

In this appendix we sketch the derivation of the Kazantsev equation, which describes the evolution of the fluctuating magnetic field component. We follow here closely the derivation in Subramanian (1997), who considers a very general case of helical turbulent and includes moreover a non-linear drift in the velocity field.
The velocity field $\boldsymbol{v}$ can be split in to a mean ($\langle \boldsymbol{v} \rangle$) and a fluctuating ($\delta \boldsymbol{v}$):

$$\boldsymbol{v} = \langle \boldsymbol{v} \rangle + \delta \boldsymbol{v}. \tag{A.1}$$

If we assume $\delta \boldsymbol{v}$ to be an isotropic, homogeneous Gaussian random field, which is delta-correlated in time, the correlation function can be written as

$$\langle \delta v_i(\boldsymbol{r}_1, t) \delta v_j(\boldsymbol{r}_2, t) \rangle = T_{ij}(r) \delta(t - s), \tag{A.2}$$

with

$$T_{ij}(r) = \left(\delta_{ij} - \frac{r_i r_j}{r^2} \right) T_{\mathrm{N}}(r) + \frac{r_i r_j}{r^2} T_{\mathrm{L}}(r). \tag{A.3}$$

Here, T_{N} is the transversal, T_{L} the longitudinal and H the helical correlation function. We further use $r = |\boldsymbol{r}_1 - \boldsymbol{r}_2|$
The magnetic field can be treated in a similar way. We start with decomposing it into a mean field $\langle \boldsymbol{B} \rangle$ and a fluctuation part $\delta \boldsymbol{B}$:

$$\boldsymbol{B} = \langle \boldsymbol{B} \rangle + \delta \boldsymbol{B}. \tag{A.4}$$

Now let us assume that the fluctuating component $\delta \boldsymbol{B}$, like the velocity field, is a homogeneous, isotropic Gaussian random field with zero mean. Then we can write the correlation function as

$$\langle \delta B_i(\boldsymbol{r}_1, t) \delta B_j(\boldsymbol{r}_2, t) \rangle = M_{ij}(r, t) \tag{A.5}$$

with the two-point correlation function

$$M_{ij}(r,t) = \left(\delta_{ij} - \frac{r_i r_j}{r^2}\right) M_{\rm N}(r,t) + \frac{r_i r_j}{r^2} M_{\rm L}(r,t). \tag{A.6}$$

Again, $M_{\rm N}$ and $M_{\rm L}$ are the transversal and the longitudinal part of the magnetic correlation function, respectively. As the magnetic field is always divergence-free, i.e. $\partial/\partial r_{1i}\ M_{ij}(r,t) = \partial/\partial r_{1j}\ M_{ij}(r,t) = 0$, we can derive a relation between the transverse and the longitudinal correlation function similar to (4.28):

$$M_{\rm N} = \frac{1}{2r}\frac{\mathrm{d}}{\mathrm{d}r}\left(r^2 M_{\rm L}\right), \tag{A.7}$$

where we have used that $(r_i r_j/r^2)M_{ij} = M_{\rm L}$ and $(r_i/r_j)M_{ij} = M_{\rm N}$.
The time derivative of $\langle \delta B_i \delta B_j \rangle$ is

$$\begin{aligned}
\frac{\partial M_{ij}}{\partial t} &= \frac{\partial}{\partial t}\left(\langle \delta B_i \delta B_j \rangle\right) \\
&= \frac{\partial}{\partial t}\left(\langle B_i B_j \rangle - \langle B_i \rangle \langle B_j \rangle\right) \\
&= \left\langle \frac{\partial B_i}{\partial t} B_j \right\rangle + \left\langle B_i \frac{\partial B_j}{\partial t} \right\rangle - \frac{\partial}{\partial t}\left(\langle B_i \rangle \langle B_j \rangle\right).
\end{aligned} \tag{A.8}$$

In the upper equation we can substitute the induction equation

$$\frac{\partial \boldsymbol{B}}{\partial t} = \boldsymbol{\nabla} \times \boldsymbol{v} \times \boldsymbol{B} - \eta \boldsymbol{\nabla} \times \boldsymbol{\nabla} \times \boldsymbol{B}, \tag{A.9}$$

where $\eta \equiv c^2/(4\pi\sigma)$ is the magnetic diffusivity with the speed of light c and the electrical conductivity σ, and the evolution equation of the magnetic mean field

$$\frac{\partial \langle \boldsymbol{B} \rangle}{\partial t} = \boldsymbol{\nabla} \times \left[\langle \boldsymbol{v} \rangle \times \langle \boldsymbol{B} \rangle - \eta_{\rm eff} \boldsymbol{\nabla} \times \langle \boldsymbol{B} \rangle\right] \tag{A.10}$$

with the effective parameter $\eta_{\rm eff} = \eta + T_{\rm L}(0)$. A lengthy calculation (see Appendix A of Brandenburg & Subramanian, 2005) leads to

$$\begin{aligned}
\frac{\partial M_{ij}}{\partial t} &= \left\langle \int {}^{y}R_{jpq}\left[\delta v_p(\boldsymbol{y},t)\ {}^{x}R_{ilm}\left(\delta v_l(\boldsymbol{x},s)\left[M_{mq} + \langle B(\boldsymbol{x})\rangle_m \langle B(\boldsymbol{y})\rangle_q\right]\right)\right]\ \mathrm{d}s \right\rangle \\
&+ \left\langle \int {}^{x}R_{ipq}\left[\delta v_p(\boldsymbol{x},t)\ {}^{y}R_{jlm}\left(\delta v_l(\boldsymbol{y},s)\left[M_{qm} + \langle B(\boldsymbol{x})\rangle_q \langle B(\boldsymbol{y})\rangle_m\right]\right)\right]\ \mathrm{d}s \right\rangle \\
&+ \left\langle \int {}^{y}R_{jpq}\left[\delta v_p(\boldsymbol{y},t)\ {}^{y}R_{qlm}\left(\delta v_l(\boldsymbol{y},s) M_{im}\right)\right]\ \mathrm{d}s \right\rangle \\
&+ \left\langle \int {}^{x}R_{ipq}\left[\delta v_p(\boldsymbol{x},t)\ {}^{x}R_{qlm}\left(\delta v_l(\boldsymbol{x},s) M_{mj}\right)\right]\ \mathrm{d}s \right\rangle \\
&+ \eta\left[\nabla_y^2 M_{ij} + \nabla_x^2 M_{ij}\right] \\
&+ {}^{y}R_{jpq}\left(\langle v(\boldsymbol{y})\rangle_p M_{iq}\right) + {}^{x}R_{ipq}\left(\langle v(\boldsymbol{x})\rangle_p M_{qj}\right).
\end{aligned} \tag{A.11}$$

Here the two operators

$$ {}^{x}R_{ipq} \equiv \epsilon_{ilm}\epsilon_{mpq}\frac{\partial}{\partial x_l} \tag{A.12} $$

$$ {}^{y}R_{ipq} \equiv \epsilon_{ilm}\epsilon_{mpq}\frac{\partial}{\partial y_l} \tag{A.13} $$

have been defined. The first two terms in (A.11) express the effect of velocity correlations on the magnetic fluctuations and the mean magnetic field. Term 3 and 4 represent the turbulent transport of magnetic fluctuations, while term 5 describes the microscopic diffusion. Finally, term 6 and 7 in (A.11) give the transport of magnetic fluctuations by the mean field.
Equation (A.11) can be simplified significantly when assuming that the mean field quantities are negligible compared to the fluctuating ones. If one further notes, that the relation

$$ M_{\mathrm{L}} = M_{ij}\frac{r_i r_j}{r^2} \tag{A.14} $$

holds, one can find an equation for M_L by multiplying (A.11) with $r_i r_j/r^2$. Subramanian (1997) finds for the evolution equation of M_L

$$ \frac{\partial M_{\mathrm{L}}}{\partial t} = 2\kappa_{\mathrm{diff}}M_{\mathrm{L}}'' + 2\left(\frac{4\kappa_{\mathrm{diff}}}{r} + \kappa_{\mathrm{diff}}'\right)M_{\mathrm{L}}' + \frac{4}{r}\left(\frac{T_{\mathrm{N}}}{r} - \frac{T_{\mathrm{L}}}{r} - T_{\mathrm{N}}' - T_{\mathrm{L}}'\right)M_{\mathrm{L}} \tag{A.15} $$

with

$$ \kappa_{\mathrm{diff}}(r) = \eta + T_{\mathrm{L}}(0) - T_{\mathrm{L}}(r). \tag{A.16} $$

The prime denotes differentiation with respect to r. The diffusion of the magnetic correlations, κ_{diff}, contains in addition to the magnetic diffusivity η the scale-dependent turbulent diffusion $T_{\mathrm{L}}(0) - T_{\mathrm{L}}(r)$.
With the solution of equation (4.38) we can calculate M_{N} also by using the relation (A.7) and so find the total correlation function of the magnetic field fluctuations M_{ij}. We note that this quantity is proportional to the energy density of the magnetic field, $B^2/(8\pi)$.
In order to separate the time from the spatial coordinates we use the ansatz

$$ M_{\mathrm{L}}(r,t) \equiv \frac{1}{r^2\sqrt{\kappa_{\mathrm{diff}}}}\psi(r)\mathrm{e}^{2\Gamma t}. \tag{A.17} $$

Substitution of this ansatz in equation (4.38) gives us

$$ -\kappa_{\mathrm{diff}}(r)\frac{\mathrm{d}^2\psi(r)}{\mathrm{d}^2 r} + U(r)\psi(r) = -\Gamma\psi(r). \tag{A.18} $$

This is the *Kazantsev equation*. It formally looks like the quantum-mechanical Schrödinger equation with a *mass* $\hbar^2/(2\kappa_{\mathrm{diff}})$ and the *potential*

$$ U(r) \equiv \frac{\kappa_{\mathrm{diff}}''}{2} - \frac{(\kappa_{\mathrm{diff}}')^2}{4\kappa_{\mathrm{diff}}} + \frac{2\kappa_{\mathrm{diff}}}{r^2} + \frac{2T_{\mathrm{N}}'}{r} + \frac{2(T_{\mathrm{L}} - T_{\mathrm{N}})}{r^2}. \tag{A.19} $$

It describes the *kinematic limit*, because U is independent of the time.

APPENDIX B

Validity of the WKB Approximation

B.1 Validity for Large Magnetic Prandtl Numbers

The WKB method is only an approximate solution of the Kazantsev equation. We have derived condition (4.52), $|f| \ll 1$, for which the WKB-method is valid in order to find solutions. In z space, f reads

$$f(z) \equiv \frac{z^2 p''(z) + 2zp'(z)}{4p(z)^2} - \frac{3}{16}\frac{[zp'(z)]^2}{p(z)^3}. \tag{B.1}$$

However, we have seen that the magnetic field is amplified most strongly on the scale $\ell_c(z) = \sqrt{\mathrm{Pm}/3}$, as here the potential U has its minimum. So we analyze $f(z, \Gamma)$ on this scale and get a dependency on the Prandtl number Pm. Hence we label $f(\ell_c, \Gamma) \equiv f(\mathrm{Pm}, \Gamma)$.
One can show that $f(\mathrm{Pm}, \Gamma)$ vanishes in the limit of large Prandtl number for all Γ and all turbulence types,

$$\lim_{\mathrm{Pm}\to\infty} f(\mathrm{Pm}, \Gamma) = 0. \tag{B.2}$$

This means that the WKB method is very good in the limit of large magnetic Prandtl number.

B.1.1 Validity for Kolmogorov Turbulence

In order to check also lower Prandtl numbers we plot $f(\mathrm{Pm}, \Gamma)$ for different normalized growth rates $\bar{\Gamma}$ (4.72) and Kolmogorov turbulence in figure B.1. However, one can show that $f(\mathrm{Pm}, \Gamma)$ does not depend on the Reynolds number for Kolmogorov turbulence. So we choose values for $\bar{\Gamma}$ between 0 and the maximal value $\bar{\Gamma}_{\max}$ for the plot in figure B.1, where $\bar{\Gamma}_{\max}$ is the value for an infinite Prandtl number and depends on the Reynolds number. One can see that the critical Prandtl number for

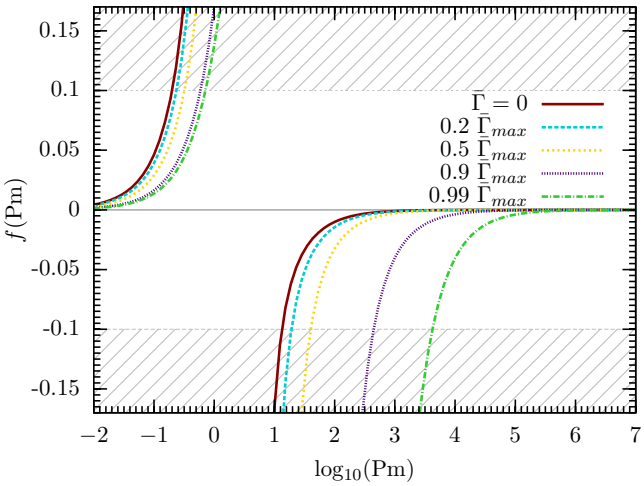

Figure B.1:
The function $f(\mathrm{Pm}, \bar{\Gamma})$ for different values of the normalized growth rate for Kolmogorov turbulence. $\bar{\Gamma}_{\max}$ is the normalized growth rate in the limit of infinite magnetic Prandtl numbers, $\bar{\Gamma}_{\max} = (37/36)\mathrm{Re}^{1/2}$ (see Sec. 4.2 for the derivation). The WKB approximation is valid within the non-hatched area, i.e., for $|f(\mathrm{Pm}, \Gamma)| < 0.1$. *image credit: Schober et al. (2012c)*

the WKB approximation gets larger with increasing normalized growth rate.
To make a more quantitative estimate of the critical Prandtl number, we have hatched the area above $f(\mathrm{Pm}, \bar{\Gamma}) = 0.1$ and below $f(\mathrm{Pm}, \bar{\Gamma}) = -0.1$. When f is not in this area its absolute value is smaller than 10% of 1. We take this as a threshold for our approximation.
We find that our method is applicable in the case of $\bar{\Gamma} = 0$ for

$$\mathrm{Pm} \gtrsim 13. \tag{B.3}$$

For higher normalized growth rates the critical Prandtl number increases.

B.1.2 Validity for Burgers Turbulence

We can analyze the validity of the WKB solutions for Burgers turbulence in the same way as for Kolmogorov turbulence using criterion (4.52).
However, we find that the function f given in (B.1) now depends not only on the normalized growth rate $\bar{\Gamma}$ and the Prandtl number Pm, but also on the Reynolds number Re. The result is shown in figure B.2, where we plot f against the Prandtl number for different Reynolds numbers and different normalized growth rates.
We again determine the critical Prandtl number for the WKB method for a vanishing normalized growth rate. For our different values of the Reynolds number we get the following critical Prandtl numbers at vanishing growth rate:

$$\mathrm{Pm}(\mathrm{Re} = 10^2) \gtrsim 500, \tag{B.4}$$
$$\mathrm{Pm}(\mathrm{Re} = 10^4) \gtrsim 1100, \tag{B.5}$$
$$\mathrm{Pm}(\mathrm{Re} = 10^8) \gtrsim 5100. \tag{B.6}$$

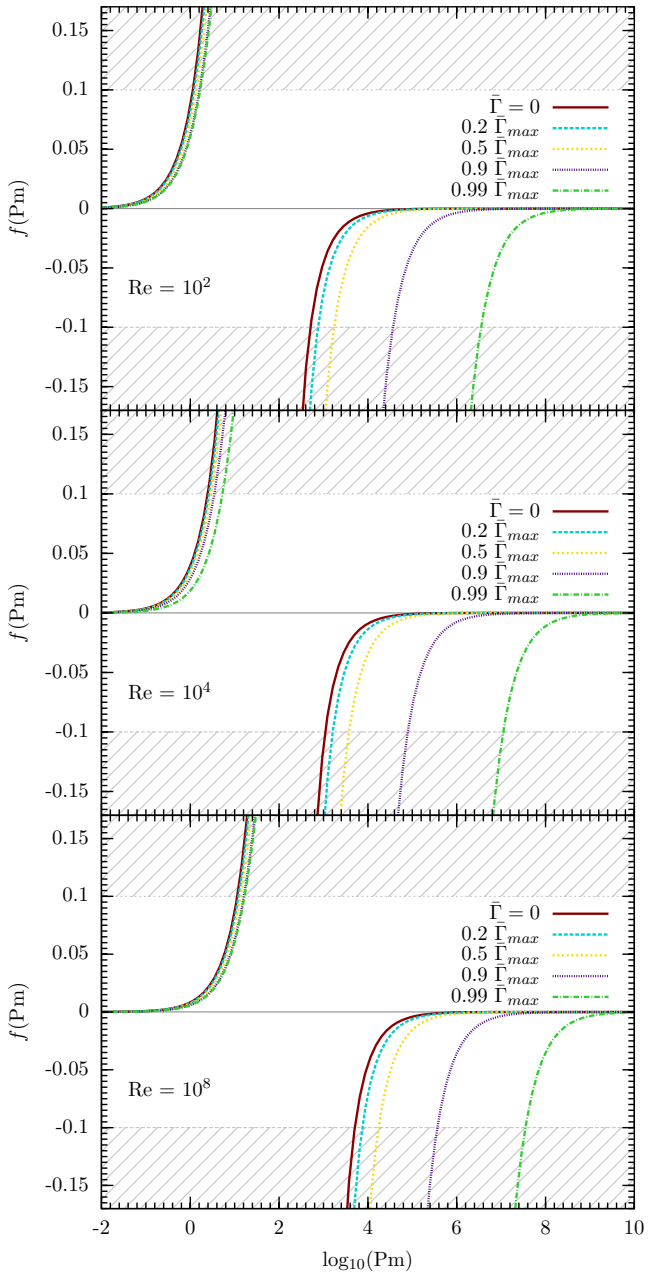

Figure B.2:
The function $f(\mathrm{Pm}, \bar{\Gamma})$ for fixed Reynolds numbers and different values of the normalized growth rate for Burgers turbulence. Notice that in the limit $\mathrm{Pm} \to \infty$ the normalized growth rates are $\bar{\Gamma} = 0.85$ for $\mathrm{Re} = 10^2$, $\bar{\Gamma} = 3.95$ for $\mathrm{Re} = 10^4$, and $\bar{\Gamma} = 85.1$ for $\mathrm{Re} = 10^8$. The WKB approximation is valid within the non-hatched area, i.e. for $f(\mathrm{Pm}, \Gamma) < 0.1$.
image credit: Schober et al. (2012c)

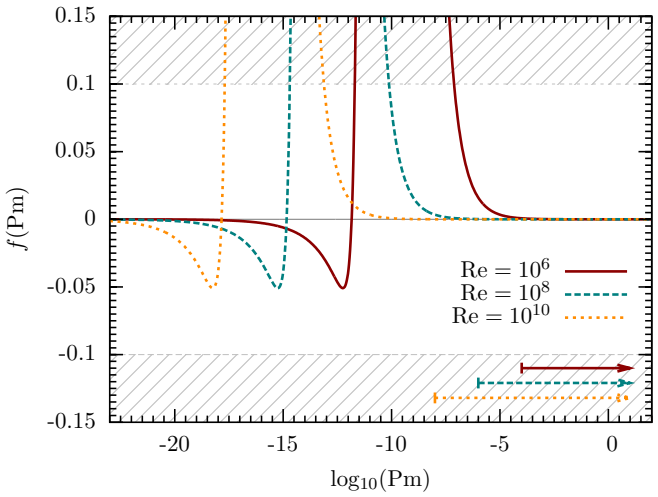

Figure B.3:
The function $f(\mathrm{Pm})$ for different hydrodynamic Reynolds numbers $\mathrm{Re} = 10^6$, $\mathrm{Re} = 10^8$ and $\mathrm{Re} = 10^{10}$ and Kolmogorov turbulence. We evaluated $f(\mathrm{Pm})$ at the minimum of the potential (4.42). The WKB approximation is valid for $f(\mathrm{Pm}) \to 0$. The critical magnetic Reynolds number gives a further restriction (see text) leading to possible values for Pm of $\mathrm{Pm} \gtrsim 10^{-4}$ ($\mathrm{Re} = 10^6$), $\mathrm{Pm} \gtrsim 10^{-6}$ ($\mathrm{Re} = 10^8$) and $\mathrm{Pm} \gtrsim 10^{-8}$ ($\mathrm{Re} = 10^{10}$), which we indicated by the corresponding arrows.
image credit: Schober et al. (2012a)

B.2 Validity for Small Magnetic Prandtl Numbers

In this section we show that the WKB approximation, which we use for solving the Kazantsev equation, is valid in the limit of small magnetic Prandtl numbers. Therefore, we have to analyze (4.53) for the inertial range of the turbulence spectrum. As f is a function of the distance x, i. e. r, we have to evaluate it on the characteristic scale in which we are interested. With the main amplification occurring at the minimum of the potential, it is rational to use this scale.
In figure B.3 we show $f(\mathrm{Pm})$ on the scale of the potential minimum for different Reynolds numbers, $\mathrm{Re} = 10^6$, $\mathrm{Re} = 10^8$ and $\mathrm{Re} = 10^{10}$. We choose the example of Kolmogorov turbulence for the discussion. The test of validity is of course similar for other types of turbulence.
The magnetic Reynolds number needs to exceed $\mathrm{Rm}_{\mathrm{crit}}$:

$$\mathrm{Rm} = \mathrm{Pm}\ \mathrm{Re} > \mathrm{Rm}_{\mathrm{crit}}. \tag{B.7}$$

For Kolmogorov turbulence $\mathrm{Rm}_{\mathrm{crit}} \approx 10^2$. Thus, for example in the curve with $\mathrm{Re} = 10^8$ in figure B.3 the threshold is only exceeded for $\mathrm{Pm} > 10^{-6}$. In this regime the WKB approximation is perfectly valid. In figure B.3 we use arrows to indicate the regimes, where the small-scale dynamo can operate.
In principle, figure B.3 states that our approximation is valid also for larger Pm up to $\mathrm{Pm} \to \infty$. However, at some point we face the problem in which the potential gets negative also below the viscous range. For $\mathrm{Pm} \to \infty$, the negative part of the potential in the viscous range clearly dominates. As we do not account for this range in the calculations above, our results are only valid for sufficiently small Pm.

APPENDIX C

Tables of Definitions and Constants

Symbol	Value (in cgs-units)	Name
c	2.998×10^{10} cm s^{-1}	speed of light
G	6.673×10^{-8} cm^3 s^{-2} g^{-1}	Gravitational constant
h	6.63×10^{-27} erg s	Planck constant
k	1.38×10^{-16} erg K^{-1}	Boltzmann constant
σ	5.67×10^{-5} erg cm^{-2} s^{-1} deg^{-4}	Stefan-Boltzmann constant
e	4.803×10^{-10} $\sqrt{\text{erg cm}}$	elementary charge
m_u	1.661×10^{-24} g	atomic mass unit
m_p	1.67×10^{-24} g	proton mass
m_e	9.109×10^{-28} g	electron mass
σ_T	6.65×10^{-25} cm^2	Thomson cross section

Table C.1: Table of physical constants.

Symbol	Value (in cgs-units)	Name
AU	1.50×10^{13} cm	astronomical unit
pc	3.086×10^{18} cm	parsec
$M_\odot$	1.99×10^{33} g	mass of the Sun
$R_\odot$	6.96×10^{10} cm	radius of the Sun
$L_\odot$	3.90×10^{33} erg s^{-1}	luminosity of the Sun
H_0	67.11 km Mpc^{-1} s^{-1}	Hubble constant
Ω_m	0.3175	matter density parameter

Table C.2: Table of astronomical constants.

cgs-Unit	SI-Unit	Physical Meaning
1 cm	1 m $= 10^2$ cm	distance
1 s	1 s	time
1 g	1 kg $= 10^3$ g	mass
1 dyn $=$ 1 cm g s^{-2}	1 N $= 10^5$ dyn	force
1 erg $=$ 1 cm^2 g s^{-2}	1 J $= 10^7$ erg	energy
1 esu $= 1\ \sqrt{\text{erg cm}}$	1 C $= 3.336 \cdot 10^{10} \sqrt{\text{erg cm}}$	electric charge
1 G	1 T $= 10^4$ G	magnetic field strength

Table C.3: Different unit systems: cgs verses SI.

Symbol	Definition	Meaning
x		scalar
$\boldsymbol{x}$		vector
$\boldsymbol{e}$		unit vector
δ_{ij}	$\delta_{ij} = \begin{cases} 0 & , i \neq j \\ 1 & , i = j \end{cases}$	Kronekar delta
ϵ_{ijk}	$\epsilon_{ijk} = \begin{cases} +1 & , \text{even permutation} \\ -1 & , \text{odd permutation} \\ 0 & , \text{repeated index} \end{cases}$	Levi-Civita tensor
$\boldsymbol{a} \cdot \boldsymbol{b}$	$\sum_i a_i b_i$	scalar product
$\boldsymbol{a} \times \boldsymbol{b}$	$\sum_{i,j} \epsilon_{ijk} a_i b_j \boldsymbol{e}_k$	cross product
∇	$\sum_i \dfrac{\partial}{\partial x_i}$	nabla operator
∇_u	$\sum_i \dfrac{\partial}{\partial u_i}$	nabla operator for velocity
$\dfrac{\partial}{\partial t}$		partial time derivative
$\dfrac{\mathrm{D}}{\mathrm{D}t}$	$\dfrac{\mathrm{D}}{\mathrm{D}t} = \dfrac{\partial}{\partial t} + \dot{\boldsymbol{x}}\nabla + \dot{\boldsymbol{u}}\nabla_u$	total time derviative
$...'$		one-dimensional spatial derivative
$\dot{...}$		time derivative
$\langle ... \rangle$		ensemble average

Table C.4: Table of the mathematical nomenclature and conventions.

Name	Definition	Physical Meaning
t		time
r		distance coordinate
$\boldsymbol{x}$		position
$\boldsymbol{v}$		velocity
m		mass
n		particle density
ρ	$\rho = mn$	mass density
μ		dynamic viscosity
ν	$\nu \equiv \dfrac{\mu}{\rho}$	kinematic viscosity
η	$\eta \equiv \dfrac{c^2}{4\pi\sigma}$	magnetic diffusivity
σ		electric conductivity
ω	$\omega = \nabla \times \mathbf{v}$	vorticity
$\boldsymbol{B}$		magnetic field
$\boldsymbol{E}$		electric field
$\boldsymbol{j}$		electric current density
ϑ		slope of the turbulence spectrum
Re	$\mathrm{Re} = \dfrac{VL}{\nu}$	hydrodynamical Reynolds number
Rm	$\mathrm{Re} = \dfrac{VL}{\eta}$	magnetic Reynolds number
Pm	$\mathrm{Pm} = \dfrac{\mathrm{Rm}}{\mathrm{Re}} = \dfrac{\nu}{\eta}$	magnetic Prandtl number
L		forcing scale of turbulence
ℓ_ν	$\ell_\nu = L\ \mathrm{Re}^{-1/(\vartheta+1)}$	viscous scale of turbulence
ℓ_η	$\ell_\eta = L\ \mathrm{Rm}^{-1/(\vartheta+1)}$	resistive scale

T^{ij}	$T_{ij}\delta(t-s) \equiv \langle \delta v_i(\mathbf{x},t)\delta v_j(\mathbf{y},s)\rangle$	correlation function of the turbulent velocity field
T_{L}		longitudinal correlation function of the turbulent velocity field
T_{N}		transversal correlation function of the turbulent velocity field
M_{ij}	$M_{ij} \equiv \langle \delta B_i(\mathbf{x},t)\delta B_j(\mathbf{y},t)\rangle$	correlation function of the turbulent magnetic field
M_{L}		longitudinal correlation function of the turbulent magnetic field
M_{N}		transversal correlation function of the turbulent magnetic field
$\psi(r)$	$M_{\mathrm{L}} \equiv \frac{1}{r^2\sqrt{\kappa_{\mathrm{diff}}}}\psi(r)\mathrm{e}^{2\Gamma t}$	eigenfunction of the Kazantsev equation
$\theta(x)$	$\psi(x) \equiv \mathrm{e}^{x/2}\theta(x)$	eigenfunction of the Kazantsev equation
$p(x)$	$p(x) \equiv -\frac{(\Gamma + U(x))\mathrm{e}^{2x}}{\kappa_{\mathrm{diff}}(x)} - \frac{1}{4}$	"p-function" (in Kazantsev equation)
Γ		growth rate
$\bar{\Gamma}$	$\bar{\Gamma} \equiv \frac{L}{V}\cdot\Gamma$	normalised growth rate
κ_{diff}		diffusion coeffient
U		"potential" in Kazantsev equation
c_{s}		sound speed
T_{ff}	$T_{\mathrm{ff}} \equiv (G\rho)^{-1/2}$	free-fall time
L_{J}	$L_{\mathrm{J}} \equiv \frac{c_{\mathrm{s}}}{\sqrt{G\rho}}$	Jeans length
M_{J}	$M_{\mathrm{J}} \equiv \frac{4}{3}\pi\left(\frac{L_{\mathrm{J}}}{2}\right)^3$	Jeans mass
$\dot{M}_\star$		star formation rate
z		redshift

Table C.5: Table of frequently used definitions for physical quantities.

APPENDIX D

Lists

D.1 List of Figures

D.2 List of Tables

APPENDIX E

Acknowledgements

This work would not have been possible without numerous people to whom I like to express my gratitude at this point.

First of all, I thank my supervisor Prof. Dr. Ralf Klessen for giving me the opportunity to explore some fascinating secrets of astrophysics during this PHD project. He contributed countless ideas to this thesis and supported and guided me during the last years. Further, I am deeply thankful to Prof. Dr. Dominik Schleicher who, as my second supervisor, was always available regardless of spatial distance. I learned a lot about magnetic fields and the early Universe from him during our discussions. Also I would like to thank Dr. Simon Glover for being a part of my thesis committee and for his valuable comments on my work.

I acknowledge the collaboration with Dr. Stefano Bovino, Dr. Christoph Federrath and Prof. Dr. Robi Banerjee, who are co-authors of different publications presented in this thesis. It was a pleasure working with them and to benefit from their expertise. Moreover, I owe my gratitude to Prof. Dr. Matthias Bartelmann for reviewing this thesis. Also I thank him and Prof. Dr. Norbert Christlieb for participating in my defence committee. I always enjoyed being a part of the star formation group of ITA and I like to acknowledge all the group members. I appreciated the exciting discussions and the lively environment in the institute very much. Helpful were also the seminars and schools organized by the graduate schools IMPRS and HGSFP.

Finally, I like to thank my boyfried Nicolai Christiansen for his endless patience and encouragement. I acknowledge not only his moral support but also our frequent discussions about physics. Further, I am eternally grateful to my parents, Monika Hess-Schober and Andreas Schober, and my sister Carolin Schober, on whom I can rely on anytime. I am also grateful to my grandparents, my whole family and friends for their support and interest in my studies.

Jennifer Schober
Heidelberg, July 2014

APPENDIX F

Bibliography

Abel T., Bryan G. L., and Norman M. L. The Formation of the First Star in the Universe. *Science*, 295:93, 2002.

Agra-Amboage V., Dougados C., Cabrit S., Garcia P. J. V., and Ferruit P. [O I] sub-arcsecond study of a microjet from an intermediate mass young star: RY Tauri. *Astron. & Astrophys.*, 493:1029, 2009.

Alvarez M. A., Bromm V., and Shapiro P. R. The H II Region of the First Star. *Astrophys. J.*, 639:621, 2006.

Alvén H. *Ark. f. Mat. Astro. o. Fysik*, 1942.

Arce H. G. Multi-molecular Line Observations of Protostellar Outflows. In *IAU Symposium*, volume 235 of *IAU Symposium*, page 237P, 2005.

Balbus S. A. and Hawley J. F. A powerful local shear instability in weakly magnetized disks. I - Linear analysis. II - Nonlinear evolution. *Astrophys. J.*, 376:214, 1991.

Balsara D. S., Kim J., Mac Low M.-M., and Mathews G. J. Amplification of Interstellar Magnetic Fields by Supernova-driven Turbulence. *Astrophys. J.*, 617:339, 2004.

Banerjee R. and Jedamzik K. Evolution of cosmic magnetic fields: From the very early Universe, to recombination, to the present. *Phys. Rev. D*, 70(12):123003, 2004.

Banerjee R. and Pudritz R. E. Outflows and Jets from Collapsing Magnetized Cloud Cores. *Astrophys. J.*, 641:949, 2006.

Banerjee R. and Pudritz R. E. Massive Star Formation via High Accretion Rates and Early Disk-driven Outflows. *Astrophys. J.*, 660:479, 2007.

Banerjee R., Klessen R. S., and Fendt C. Can Protostellar Jets Drive Supersonic Turbulence in Molecular Clouds? *Astrophys. J.*, 668:1028, 2007.

Barkana R. and Loeb A. Identifying the Reionization Redshift from the Cosmic Star Formation Rate. *Astrophys. J.*, 539:20, 2000.

Batchelor George K. *The theory of homogeneous turbulence*. Cambridge monographs on mechanics and applied mathematics. Cambridge University Press, Cambridge, 1953.

Baym G., Bödeker D., and McLerran L. Magnetic fields produced by phase transition bubbles in the electroweak phase transition. *Phys. Rev. D*, 53:662, 1996.

Beck A. M., Lesch H., Dolag K., Kotarba H., Geng A., and Stasyszyn F. A. Origin of strong magnetic fields in Milky Way-like galactic haloes. *Mon. Not. R. Astron. Soc.*, 422:2152, 2012.

Beck A. M., Dolag K., Lesch H., and Kronberg P. P. Strong magnetic fields and large rotation measures in protogalaxies from supernova seeding. *Mon. Not. R. Astron. Soc.*, 2013.

Beck R. Magnetism in the spiral galaxy NGC 6946: magnetic arms, depolarization rings, dynamo modes, and helical fields. *Astron. & Astrophys.*, 470:539, 2007.

Beck R. Magnetic Fields in Galaxies. *Space Sci. Rev.*, page 135, 2011.

Beck R. and Krause M. Revised equipartition and minimum energy formula for magnetic field strength estimates from radio synchrotron observations. *Astronomische Nachrichten*, 326:414, 2005.

Beck R. and Wielebinski R. *Magnetic Fields in Galaxies*, page 641. 2013.

Bell A. R. The acceleration of cosmic rays in shock fronts. I. *Mon. Not. R. Astron. Soc.*, 182:147, 1978a.

Bell A. R. The acceleration of cosmic rays in shock fronts. II. *Mon. Not. R. Astron. Soc.*, 182:443, 1978b.

Benzi Roberto, Biferale Luca, Fisher Robert T., Kadanoff Leo P., Lamb Donald Q., and Toschi Federico. Intermittency and Universality in Fully Developed Inviscid and Weakly Compressible Turbulent Flows. *Phys. Rev. Let.*, 100:234503, 2008.

Beresnyak A. Universal Nonlinear Small-Scale Dynamo. *Phys. Rev. Let.*, 108(3): 035002, 2012.

Bernet M. L., Miniati F., Lilly S. J., Kronberg P. P., and Dessauges-Zavadsky M. Strong magnetic fields in normal galaxies at high redshift. *Nature*, 454:302, 2008.

Biermann L. Über den Ursprung der Magnetfelder auf Sternen und im interstellaren Raum (mit einem Anhang von A. Schlüter). *Zeitschrift Naturforschung Teil A*, 5:65, 1950.

Birnboim Y. and Dekel A. Virial shocks in galactic haloes? *Mon. Not. R. Astron. Soc.*, 345:349, 2003.

Blandford R. D. and Payne D. G. Hydromagnetic flows from accretion discs and the production of radio jets. *Mon. Not. R. Astron. Soc.*, 199:883, 1982.

Blumenthal G. R. and Gould R. J. Bremsstrahlung, Synchrotron Radiation, and Compton Scattering of High-Energy Electrons Traversing Dilute Gases. *Reviews of Modern Physics*, 42:237, 1970.

Bogdan T. J. and VÃűlk H. J. Onion-shell model of cosmic ray acceleration in supernova remnants. *Astron. & Astrophys.*, 122:129, 1983.

Boldyrev Stanislav and Cattaneo Fausto. Magnetic-field generation in kolmogorov turbulence. *Phys. Rev. Let.*, 92:144501, 2004.

Boldyrev S., Nordlund Å., and Padoan P. Scaling Relations of Supersonic Turbulence in Star-forming Molecular Clouds. *Astrophys. J.*, 573:678, 2002.

Boldyrev S., Cattaneo F., and Rosner R. Magnetic-Field Generation in Helical Turbulence. *Phys. Rev. Let.*, 95(25):255001, 2005.

Bourke T. L., Myers P. C., Robinson G., and Hyland A. R. New OH Zeeman Measurements of Magnetic Field Strengths in Molecular Clouds. *Astrophys. J.*, 554:916, 2001.

Bourke T. L., Crapsi A., Myers P. C., Evans N. J., II, Wilner D. J., Huard T. L., Jørgensen J. K., and Young C. H. Discovery of a Low-Mass Bipolar Molecular Outflow from L1014-IRS with the Submillimeter Array. *Astrophys. J. Let.*, 633: L129, 2005.

Bourne N., Dunne L., Ivison R. J., Maddox S. J., Dickinson M., and Frayer D. T. Evolution of the far-infrared-radio correlation and infrared spectral energy distributions of massive galaxies over z= 0-2. *Mon. Not. R. Astron. Soc.*, 410:1155, 2011.

Bovino S., Tacconi M., Gianturco F. A., and Galli D. Ion chemistry in the early universe. Revisiting the role of HeH^+ with new quantum calculations. *Astron. & Astrophys.*, 529:A140, 2011a.

Bovino S., Tacconi M., Gianturco F. A., Galli D., and Palla F. On the Relative Abundance of LiH and LiH^+ Molecules in the Early Universe: New Results from Quantum Reactions. *Astrophys. J.*, 731:107, 2011b.

Bovino S., Schleicher D. R. G., and Schober J. Turbulent magnetic field amplification from the smallest to the largest magnetic Prandtl numbers. *New J. of Phys.*, 15 (1):013055, 2013.

Braginskii S. I. Transport Processes in a Plasma. *Reviews of Plasma Physics*, 1:205, 1965.

Brandenburg A. and Subramanian K. Astrophysical magnetic fields and nonlinear dynamo theory. *Phys. Rep.*, 417:1, 2005.

Bromm V. Formation of the first stars. *Reports on Progress in Physics*, 76:112901, 2013.

Bromm V. and Larson R. B. The First Stars. *Ann. Rev. Astron. Astrophys.*, 42:79, 2004.

Bromm V. and Yoshida N. The First Galaxies. *Ann. Rev. Astron. Astrophys.*, 49: 373, 2011.

Bromm V., Coppi P. S., and Larson R. B. The Formation of the First Stars. I. The Primordial Star-forming Cloud. *Astrophys. J.*, 564:23, 2002.

Bromm V., Yoshida N., Hernquist L., and McKee C. F. The formation of the first stars and galaxies. *Nature*, 459:49, 2009.

Brunetti G., Setti G., Feretti L., and Giovannini G. Particle reacceleration in the Coma cluster: radio properties and hard X-ray emission. *Mon. Not. R. Astron. Soc.*, 320:365, 2001.

Burgers J.M. *A Mathematical Model Illustrating the Theory of Turbulence*, volume 1 of *Advances in Applied Mechanics*. Elsevier, 1948.

Cabrit S. The accretion-ejection connexion in T Tauri stars: jet models vs. observations. In Bouvier J. and Appenzeller I., editors, *IAU Symposium*, volume 243 of *IAU Symposium*, page 203, 2007.

Cabrit S. and Bertout C. CO line formation in bipolar flows. III - The energetics of molecular flows and ionized winds. *Astron. & Astrophys.*, 261:274, 1992.

Caselli P. and Myers P. C. The Line Width–Size Relation in Massive Cloud Cores. *Astrophys. J.*, 446:665, 1995.

Chakraborty N. and Fields B. D. Inverse-Compton Contribution to the Star-forming Extragalactic Gamma-Ray Background. *Astrophys. J.*, 773:104, 2013.

Chandrasekhar S. The Stability of Non-Dissipative Couette Flow in Hydromagnetics. *Proceedings of the National Academy of Science*, 46:253, 1960.

Chang P., Broderick A. E., and Pfrommer C. The Cosmological Impact of Luminous TeV Blazars. II. Rewriting the Thermal History of the Intergalactic Medium. *Astrophys. J.*, 752:23, 2012.

Chapman S., Cowling T.G., and Társulat Magyar Történelmi. *The Mathematical Theory of Non-uniform Gases: An Account of the Kinetic Theory of Viscosity, Thermal Conduction and Diffusion in Gases. Prepared in Co-operation with D. Burnet.* University Press, 1953.

Charbonneau P. Dynamo Models of the Solar Cycle. *Living Reviews in Solar Physics*, 7:3, 2010.

Cheng B. and Olinto A. V. Primordial magnetic fields generated in the quark-hadron transition. *Phys. Rev. D*, 50:2421, 1994.

Chevalier R. A. The interaction of supernovae with the interstellar medium. *Ann. Rev. Astron. Astrophys.*, 15:175, 1977.

Childress Stephen and Gilbert Andrew D. *Stretch, twist, fold: the fast dynamo.* Number 37 in Lecture notes in physics : New series m, monographs ; 37 ; Lecture notes in physics / New series M. Springer, Berlin ; Heidelberg [u.a.], 1995. Literaturverz. S. 381 - 396.

Cho J., Vishniac E. T., Beresnyak A., Lazarian A., and Ryu D. Growth of Magnetic Fields Induced by Turbulent Motions. *Astrophys. J.*, 693:1449, 2009.

Choudhuri A. R. *The Physics of Fluids and Plasmas: An Introduction for Astrophysicists.* Cambrigde University Press, 1998.

Chyży K. T., Weżgowiec M., Beck R., and Bomans D. J. Magnetic fields in Local Group dwarf irregulars. *Astron. & Astrophys.*, 529:A94, 2011.

Cirelli M. and Panci P. Inverse Compton constraints on the Dark Matter e excesses. *Nuclear Physics B*, 821:399, 2009.

Clark P. C., Glover S. C. O., Smith R. J., Greif T. H., Klessen R. S., and Bromm V. The Formation and Fragmentation of Disks Around Primordial Protostars. *Science*, 331:1040, 2011.

Colless M., Dalton G., Maddox S., Sutherland W., Norberg P., Cole S., Bland-Hawthorn J., Bridges T., Cannon R., Collins C., Couch W., Cross N., Deeley K., De Propris R., Driver S. P., Efstathiou G., Ellis R. S., Frenk C. S., Glazebrook K., Jackson C., Lahav O., Lewis I., Lumsden S., Madgwick D., Peacock J. A., Peterson B. A., Price I., Seaborne M., and Taylor K. The 2dF Galaxy Redshift Survey: spectra and redshifts. *Mon. Not. R. Astron. Soc.*, 328:1039, 2001.

Condon J. J., Cotton W. D., Greisen E. W., Yin Q. F., Perley R. A., Taylor G. B., and Broderick J. J. The NRAO VLA Sky Survey. *The Astron. J.*, 115:1693, 1998.

Crutcher R. M. Magnetic Fields in Molecular Clouds: Observations Confront Theory. *Astrophys. J.*, 520:706, 1999.

Crutcher R. M. Magnetic Fields in Molecular Clouds. *Ann. Rev. Astron. Astrophys.*, 50:29, 2012.

Crutcher R. M., Nutter D. J., Ward-Thompson D., and Kirk J. M. SCUBA Polarization Measurements of the Magnetic Field Strengths in the L183, L1544, and L43 Prestellar Cores. *Astrophys. J.*, 600:279, 2004.

Cyburt R. H. Primordial nucleosynthesis for the new cosmology: Determining uncertainties and examining concordance. *Phys. Rev. D*, 70(2):023505, 2004.

Davidson P. A. *Turbulence: an introduction for scientists and engineers.* 2004.

de Cea del Pozo E., Torres D. F., and Rodriguez Marrero A. Y. Multimessenger Model for the Starburst Galaxy M82. *Astrophys. J.*, 698:1054, 2009.

de Gouveia dal Pino E. M. and Lazarian A. Production of the large scale superluminal ejections of the microquasar GRS 1915+105 by violent magnetic reconnection. *Astron. & Astrophys.*, 441:845, 2005.

Dekel A., Birnboim Y., Engel G., Freundlich J., Goerdt T., Mumcuoglu M., Neistein E., Pichon C., Teyssier R., and Zinger E. Cold streams in early massive hot haloes as the main mode of galaxy formation. *Nature*, 457:451, 2009.

Diehl R., Halloin H., Kretschmer K., Lichti G. G., Schönfelder V., Strong A. W., von Kienlin A., Wang W., Jean P., Knödlseder J., Roques J.-P., Weidenspointner G., Schanne S., Hartmann D. H., Winkler C., and Wunderer C. Radioactive ^{26}Al from massive stars in the Galaxy. *Nature*, 439:45, 2006.

Dijkstra M., Haiman Z., Rees M. J., and Weinberg D. H. Photoionization Feedback in Low-Mass Galaxies at High Redshift. *Astrophys. J.*, 601:666, 2004.

Dobbs C. L. and Price D. J. Magnetic fields and the dynamics of spiral galaxies. *Mon. Not. R. Astron. Soc.*, 383:497, 2008.

Donati J.-F. and Landstreet J. D. Magnetic Fields of Nondegenerate Stars. *Ann. Rev. Astron. Astrophys.*, 47:333, 2009.

Dorfi E. A. Cosmic Ray Production Rates in Supernova Remnants. *Astrophys. & Sp. Sci.*, 272:227, 2000.

Draine B. T. *Physics of the Interstellar and Intergalactic Medium.* 2011.

Drury L. On particle acceleration in supernova remnants. *Space Sci. Rev.*, 36:57, 1983.

Dumke M., Krause M., Wielebinski R., and Klein U. Polarized radio emission at 2.8cm from a selected sample of edge-on galaxies. *Astron. & Astrophys.*, 302:691, 1995.

Dunham M. M., Arce H. G., Mardones D., Lee J.-E., Matthews B. C., Stutz A. M., and Williams J. P. Molecular Outflows Driven by Low-mass Protostars. I. Correcting for Underestimates When Measuring Outflow Masses and Dynamical Properties. *Astrophys. J.*, 783:29, 2014.

Ellerbroek L. E., Podio L., Kaper L., Sana H., Huppenkothen D., de Koter A., and Monaco L. The outflow history of two Herbig-Haro jets in RCW 36: HH 1042 and HH 1043. *Astron. & Astrophys.*, 551:A5, 2013.

Elmegreen B. G. Supercloud formation by nonaxisymmetric gravitational instabilities in sheared magnetic galaxy disks. *Astrophys. J.*, 312:626, 1987.

Elmegreen B. G. and Burkert A. Accretion-Driven Turbulence and the Transition to Global Instability in Young Galaxy Disks. *Astrophys. J.*, 712:294, 2010.

Elmegreen B. G. and Scalo J. Interstellar Turbulence I: Observations and Processes. *Ann. Rev. Astron. Astrophys.*, 42:211, 2004.

Eyink G. L., Lazarian A., and Vishniac E. T. Fast Magnetic Reconnection and Spontaneous Stochasticity. *Astrophys. J.*, 743:51, 2011.

Fabbiano G. Normal galaxies and their X-ray binary populations. *X-ray Binaries*, page 390, 1995.

Fan Y. Magnetic Fields in the Solar Convection Zone. *Living Reviews in Solar Physics*, 6:4, 2009.

Federrath C., Klessen R. S., and Schmidt W. The Density Probability Distribution in Compressible Isothermal Turbulence: Solenoidal versus Compressive Forcing. *Astrophys. J. Let.*, 688:L79, 2008.

Federrath C., Roman-Duval J., Klessen R. S., Schmidt W., and Mac Low M.-M. Comparing the statistics of interstellar turbulence in simulations and observations. Solenoidal versus compressive turbulence forcing. *Astron. & Astrophys.*, 512:A81, 2010.

Federrath C., Chabrier G., Schober J., Banerjee R., Klessen R. S., and Schleicher D. R. G. Mach Number Dependence of Turbulent Magnetic Field Amplification: Solenoidal versus Compressive Flows. *Phys. Rev. Let.*, 107:114504, 2011.

Federrath C., Sur S., Schleicher D. R. G., Banerjee R., and Klessen R. S. A New Jeans Resolution Criterion for (M)HD Simulations of Self-gravitating Gas: Application to Magnetic Field Amplification by Gravity-driven Turbulence. *Astrophys. J.*, 731:62, 2011.

Federrath C., Schrön M., Banerjee R., and Klessen R. S. Modeling jet and outflow feedback during star cluster formation. *ArXiv e-prints: 1406.3625*, 2014.

Ferguson H. C., Dickinson M., Giavalisco M., Kretchmer C., Ravindranath S., Idzi R., Taylor E., Conselice C. J., Fall S. M., Gardner J. P., Livio M., Madau P., Moustakas L. A., Papovich C. M., Somerville R. S., Spinrad H., and Stern D. The Size Evolution of High-Redshift Galaxies. *Astrophys. J. Let.*, 600:L107, 2004.

Ferrario L. and Wickramasinghe D. T. High Field Magnetic White Dwarfs, Pulsars, Magnetars, and their Main Sequence Progenitors. In Napiwotzki R. and Burleigh M. R., editors, *15th European Workshop on White Dwarfs*, volume 372 of *Astronomical Society of the Pacific Conference Series*, page 163, 2007.

Ferraro V. C. A. The non-uniform rotation of the Sun and its magnetic field. *Mon. Not. R. Astron. Soc.*, 97:458, 1937.

Ferrière K. M. The interstellar environment of our galaxy. *Reviews of Modern Physics*, 73, 2001.

Field G. B., Goldsmith D. W., and Habing H. J. Cosmic-Ray Heating of the Interstellar Gas. *Astrophys. J. Let.*, 155:L149, 1969.

Förster Schreiber N. M., Genzel R., Lutz D., and Sternberg A. The Nature of Starburst Activity in M82. *Astrophys. J.*, 599:193, 2003.

Frank A., Ray T. P., Cabrit S., Hartigan P., Arce H. G., Bacciotti F., Bally J., Benisty M., Eislöffel J., Güdel M., Lebedev S., Nisini B., and Raga A. Jets and Outflows From Star to Cloud: Observations Confront Theory. 2014.

Frank-Kamenezki D. A. *Vorlesungen über Plasmaphysik*. Verlag deutscher Wissenschaften, 1967.

Frisch U. *Turbulence. The legacy of A. N. Kolmogorov*. 1995.

Fujita Y., Takizawa M., and Sarazin C. L. Nonthermal Emissions from Particles Accelerated by Turbulence in Clusters of Galaxies. *Astrophys. J.*, 584:190, 2003.

Gaensler B. M., Haverkorn M., Burkhart B., Newton-McGee K. J., Ekers R. D., Lazarian A., McClure-Griffiths N. M., Robishaw T., Dickey J. M., and Green A. J. Low-Mach-number turbulence in interstellar gas revealed by radio polarization gradients. *Nature*, 478:214, 2011.

Ghosh P. and White N. E. X-Ray Probes of Cosmic Star Formation History. *Astrophys. J. Let.*, 559:L97, 2001.

Girart J. M., Rao R., and Marrone D. P. Magnetic Fields in the Formation of Sun-Like Stars. *Science*, 313:812, 2006.

Glassgold A. E., Galli D., and Padovani M. Cosmic-Ray and X-Ray Heating of Interstellar Clouds and Protoplanetary Disks. *Astrophys. J.*, 756:157, 2012.

Glover S. C. O. and Abel T. Uncertainties in H_2 and HD chemistry and cooling and their role in early structure formation. *Mon. Not. R. Astron. Soc.*, 388:1627, 2008.

Glover S. C. O. and Savin D. W. Is H^+_3 cooling ever important in primordial gas? *Mon. Not. R. Astron. Soc.*, 393:911, 2009.

Gnedin N. Y., Ferrara A., and Zweibel E. G. Generation of the Primordial Magnetic Fields during Cosmological Reionization. *Astrophys. J.*, 539:505, 2000.

Goodman A. A. and Arce H. G. PV Cephei: Young Star Caught Speeding? *Astrophys. J.*, 608:831, 2004.

Grasso D. and Rubinstein H. R. Magnetic fields in the early Universe. *Phys. Rep.*, 348:163, 2001.

Greif T. H., Johnson J. L., Bromm V., and Klessen R. S. The First Supernova Explosions: Energetics, Feedback, and Chemical Enrichment. *Astrophys. J.*, 670: 1, 2007.

Greif T. H., Johnson J. L., Klessen R. S., and Bromm V. The first galaxies: assembly, cooling and the onset of turbulence. *Mon. Not. R. Astron. Soc.*, 387:1021, 2008.

Greif T. H., Springel V., White S. D. M., Glover S. C. O., Clark P. C., Smith R. J., Klessen R. S., and Bromm V. Simulations on a Moving Mesh: The Clustered Formation of Population III Protostars. *Astrophys. J.*, 737:75, 2011.

Greif T. H., Bromm V., Clark P. C., Glover S. C. O., Smith R. J., Klessen R. S., Yoshida N., and Springel V. Formation and evolution of primordial protostellar systems. *Mon. Not. R. Astron. Soc.*, 424:399, 2012.

Grimm H.-J., Gilfanov M., and Sunyaev R. Study of the galactic X-ray binary population. *Memorie Della Societá Astronomica Italiana*, 73:1053, 2002.

Gurnett D. A. and Bhattacharjee A. *Introduction to Plasma Physics*. 2005.

Guth A. H. Inflationary universe: A possible solution to the horizon and flatness problems. *Phys. Rev. D*, 23:347, 1981.

Hale G. E. On the Probable Existence of a Magnetic Field in Sun-Spots. *Astrophys. J.*, 28:315, 1908.

Hammond A. M., Robishaw T., and Gaensler B. M. A New Catalog of Faraday Rotation Measures and Redshifts for Extragalactic Radio Sources. *ArXiv e-prints: 1209.1438*, 2012.

Harwit M. and Pacini F. Infrared galaxies - Evolutionary stages of massive star formation. *Astrophys. J. Let.*, 200:L127, 1975.

Haugen N. E., Brandenburg A., and Dobler W. Simulations of nonhelical hydromagnetic turbulence. *Phys. Rev. E*, 70:016308, 2004a.

Haugen N. E. L., Brandenburg A., and Mee A. J. Mach number dependence of the onset of dynamo action. *Mon. Not. R. Astron. Soc.*, 353:947, 2004b.

Hawking S. W. The development of irregularities in a single bubble inflationary universe. *Phys. Let. B*, 115:295, 1982.

Heiles C. and Crutcher R. Magnetic Fields in Diffuse HI and Molecular Clouds. In Wielebinski R. and Beck R., editors, *Cosmic Magnetic Fields*, volume 664 of *Lecture Notes in Physics, Berlin Springer Verlag*, page 137, 2005.

Hennebelle P. and Ciardi A. Disk formation during collapse of magnetized protostellar cores. *Astron. & Astrophys.*, 506:L29, 2009.

Hennebelle P. and Teyssier R. Magnetic processes in a collapsing dense core. II. Fragmentation. Is there a fragmentation crisis? *Astron. & Astrophys.*, 477:25, 2008.

Hennebelle P., Commerçon B., Joos M., Klessen R. S., Krumholz M., Tan J. C., and Teyssier R. Collapse, outflows and fragmentation of massive, turbulent and magnetized prestellar barotropic cores. *Astron. & Astrophys.*, 528:A72, 2011.

Hernquist L. and Springel V. An analytical model for the history of cosmic star formation. *Mon. Not. R. Astron. Soc.*, 341:1253, 2003.

Hoang T. and Lazarian A. Radiative torque alignment: essential physical processes. *Mon. Not. R. Astron. Soc.*, 388:117, 2008.

Hodge J. A., Karim A., Smail I., Swinbank A. M., Walter F., Biggs A. D., Ivison R. J., Weiss A., Alexander D. M., Bertoldi F., Brandt W. N., Chapman S. C., Coppin K. E. K., Cox P., Danielson A. L. R., Dannerbauer H., De Breuck C., Decarli R., Edge A. C., Greve T. R., Knudsen K. K., Menten K. M., Rix H.-W., Schinnerer E., Simpson J. M., Wardlow J. L., and van der Werf P. An ALMA Survey of Submillimeter Galaxies in the Extended Chandra Deep Field South: Source Catalog and Multiplicity. *Astrophys. J.*, 768:91, 2013.

Indriolo N. and McCall B. J. Investigating the Cosmic-Ray Ionization Rate in the Galactic Diffuse Interstellar Medium through Observations of H_3^+. *Astrophys. J.*, 745:91, 2012.

Ipavich F. M. Galactic winds driven by cosmic rays. *Astrophys. J.*, 196:107, 1975.

Iskakov A. B., Schekochihin A. A., Cowley S. C., McWilliams J. C., and Proctor M. R. E. Numerical Demonstration of Fluctuation Dynamo at Low Magnetic Prandtl Numbers. *Phys. Rev. Let.*, 98(20):208501, 2007.

Karim A., Swinbank A. M., Hodge J. A., Smail I. R., Walter F., Biggs A. D., Simpson J. M., Danielson A. L. R., Alexander D. M., Bertoldi F., de Breuck C., Chapman S. C., Coppin K. E. K., Dannerbauer H., Edge A. C., Greve T. R., Ivison R. J., Knudsen K. K., Menten K. M., Schinnerer E., Wardlow J. L., Weiß A., and van der Werf P. An ALMA survey of submillimetre galaxies in the Extended Chandra Deep Field South: high-resolution 870 μm source counts. *Mon. Not. R. Astron. Soc.*, 432:2, 2013.

Kazantsev A. P. Enhancement of a Magnetic Field by a Conducting Fluid. *Soviet Journal of Experimental and Theoretical Physics*, 26:1031, 1968.

Kennicutt R. C., Jr. The Global Schmidt Law in Star-forming Galaxies. *Astrophys. J.*, 498:541, 1998.

Kim W.-T., Ostriker E. C., and Stone J. M. Magnetorotationally Driven Galactic Turbulence and the Formation of Giant Molecular Clouds. *Astrophys. J.*, 599: 1157.

Kim W.-T., Ostriker E. C., and Stone J. M. Three-dimensional Simulations of Parker, Magneto-Jeans, and Swing Instabilities in Shearing Galactic Gas Disks. *Astrophys. J.*, 581:1080, 2002.

Kitayama T. and Yoshida N. Supernova Explosions in the Early Universe: Evolution of Radiative Remnants and the Halo Destruction Efficiency. *Astrophys. J.*, 630: 675, 2005.

Kleeorin N. and Rogachevskii I. Growth rate of small-scale dynamo at low magnetic Prandtl numbers. *Physica Scripta*, 86(1):018404, 2012.

Kleeorin N., Rogachevskii I., and Sokoloff D. Magnetic fluctuations with a zero mean field in a random fluid flow with a finite correlation time and a small magnetic diffusion. *Phys. Rev. E*, 65(3), 2002.

Klessen R. S. and Hennebelle P. Accretion-driven turbulence as universal process: galaxies, molecular clouds, and protostellar disks. *Astron. & Astrophys.*, 520:A17, 2010.

Kolmogorov A. The Local Structure of Turbulence in Incompressible Viscous Fluid for Very Large Reynolds' Numbers. *Akademiia Nauk SSSR Doklady*, 30:301, 1941.

Komatsu E., Dunkley J., Nolta M. R., Bennett C. L., Gold B., Hinshaw G., Jarosik N., Larson D., Limon M., Page L., Spergel D. N., Halpern M., Hill R. S., Kogut A., Meyer S. S., Tucker G. S., Weiland J. L., Wollack E., and Wright E. L.

Five-Year Wilkinson Microwave Anisotropy Probe Observations: Cosmological Interpretation. *Astrophys. J. Suppl. Ser.*, 180:330, 2009.

Korpi M., Brandenburg A., and Touminen I. Driving Galactic Turbulence by Supernova Explosions. *Studia geoph. et deod.*, 42:410, 1998.

Kramers H. A. Wellenmechanik und halbzahlige Quantisierung. *Zeitschrift für Physik*, 39:828, 1926.

Krause F. and Raedler K.-H. *Mean-field magnetohydrodynamics and dynamo theory.* 1980.

Krause M., Wielebinski R., and Dumke M. Radio polarization and sub-millimeter observations of the Sombrero galaxy (NGC 4594). Large-scale magnetic field configuration and dust emission. *Astron. & Astrophys.*, 448:133, 2006.

Kritsuk A. G., Norman M. L., Padoan P., and Wagner R. The Statistics of Supersonic Isothermal Turbulence. *Astrophys. J.*, 665:416, 2007.

Kronberg P. P. Extragalactic magnetic fields. *Reports on Progress in Physics*, 57: 325, 1994.

Kronberg P. P., Lesch H., and Hopp U. Magnetization of the Intergalactic Medium by Primeval Galaxies. *Astrophys. J.*, 511:56, 1999.

Kroupa P. The Initial Mass Function of Stars: Evidence for Uniformity in Variable Systems. *Science*, 295:82, 2002.

Krumholz M. R. and McKee C. F. A General Theory of Turbulence-regulated Star Formation, from Spirals to Ultraluminous Infrared Galaxies. *Astrophys. J.*, 630: 250, 2005.

Kulsrud R., Cowley S. C., Gruzinov A. V., and Sudan R. N. Dynamos and cosmic magnetic fields. *Phys. Rep.*, 283:213, 1997.

Kulsrud R. M. and Zweibel E. G. On the origin of cosmic magnetic fields. *Reports on Progress in Physics*, 71(4):046901, 2008.

Lacki B. C. and Beck R. The equipartition magnetic field formula in starburst galaxies: accounting for pionic secondaries and strong energy losses. *Mon. Not. R. Astron. Soc.*, 430:3171, 2013.

Lacki B. C., Thompson T. A., Quataert E., Loeb A., and Waxman E. On the GeV and TeV Detections of the Starburst Galaxies M82 and NGC 253. *Astrophys. J.*, 734:107, 2011.

Landstreet J. D. Magnetic fields at the surfaces of stars. *Astron. & Astrophys. Rev.*, 4:35, 1992.

Larson R. B. Turbulence and star formation in molecular clouds. *Mon. Not. R. Astron. Soc.*, 194:809, 1981.

Latif M. A., Schleicher D. R. G., and Spaans M. The implications of dust for high-redshift protogalaxies and the formation of binary disks. *Astron. & Astrophys.*, 540:A101, 2012.

Latif M. A., Schleicher D. R. G., Schmidt W., and Niemeyer J. The small-scale dynamo and the amplification of magnetic fields in massive primordial haloes. *Mon. Not. R. Astron. Soc.*, 2013.

Lazarian A. and Vishniac E. T. Reconnection in a Weakly Stochastic Field. *Astrophys. J.*, 517:700, 1999.

Lehmer B. D., Brandt W. N., Alexander D. M., Bauer F. E., Schneider D. P., Tozzi P., Bergeron J., Garmire G. P., Giacconi R., Gilli R., Hasinger G., Hornschemeier A. E., Koekemoer A. M., Mainieri V., Miyaji T., Nonino M., Rosati P., Silverman J. D., Szokoly G., and Vignali C. The Extended Chandra Deep Field-South Survey: Chandra Point-Source Catalogs. *Astrophys. J. Suppl. Ser.*, 161:21, 2005.

Lehmer B. D., Alexander D. M., Bauer F. E., Brandt W. N., Goulding A. D., Jenkins L. P., Ptak A., and Roberts T. P. A Chandra Perspective on Galaxy-wide X-ray Binary Emission and its Correlation with Star Formation Rate and Stellar Mass: New Results from Luminous Infrared Galaxies. *Astrophys. J.*, 724: 559, 2010.

Leorat J., Pouquet A., and Frisch U. *J. of Fluids Mechanics*, 104:419, 1981.

Li Z.-Y. and Nakamura F. Cluster Formation in Protostellar Outflow-driven Turbulence. *Astrophys. J. Let.*, 640:L187, 2006.

Liddle A. *An Introduction to Modern Cosmology, Second Edition*. 2003.

Llama J., Vidotto A. A., Jardine M., Wood K., Fares R., and Gombosi T. I. Exoplanet transit variability: bow shocks and winds around HD 189733b. *Mon. Not. R. Astron. Soc.*, 436:2179, 2013.

Loeb A. *How Did the First Stars and Galaxies Form?* 2010.

Longair M. S. *High Energy Astrophysics*. 2011.

Lorimer D. R. Binary and Millisecond Pulsars. *Living Reviews in Relativity*, 11:8, 2008.

Love J. Reversals and excursions of the geodynamo. *Astronomy and Geophysics*, 40:14, 1999.

Mac Low M.-M. Turbulence Driven by Stellar Outflows. In Favata F., Kaas A., and Wilson A., editors, *Star Formation from the Small to the Large Scale*, volume 445 of *ESA Special Publication*, page 457, 2000.

Mac Low M.-M. and Klessen R. S. Control of star formation by supersonic turbulence. *Rev. Mod. Phys.*, 76(1):125, 2004.

Mac Low M.-M., Klessen R. S., Burkert A., and Smith M. D. Kinetic Energy Decay Rates of Supersonic and Super-Alfvénic Turbulence in Star-Forming Clouds. *Phys. Rev. Let.*, 80:2754, 1998.

Machida M. N. Population III Star Formation in Magnetized Primordial Clouds. *ArXiv e-prints: 1005.1707*, 2010.

Machida M. N. and Doi K. The formation of Population III stars in gas accretion stage: effects of magnetic fields. *Mon. Not. R. Astron. Soc.*, 435:3283, 2013.

Machida M. N., Tomisaka K., and Matsumoto T. First MHD simulation of collapse and fragmentation of magnetized molecular cloud cores. *Mon. Not. R. Astron. Soc.*, 348:L1, 2004.

Machida M. N., Omukai K., Matsumoto T., and Inutsuka S.-i. The First Jets in the Universe: Protostellar Jets from the First Stars. *Astrophys. J. Let.*, 647:L1, 2006.

Machida M. N., Inutsuka S.-i., and Matsumoto T. High- and Low-Velocity Magnetized Outflows in the Star Formation Process in a Gravitationally Collapsing Cloud. *Astrophys. J.*, 676:1088, 2008a.

Machida M. N., Matsumoto T., and Inutsuka S.-i. Magnetohydrodynamics of Population III Star Formation. *Astrophys. J.*, 685:690, 2008b.

Madau P. and Pozzetti L. Deep galaxy counts, extragalactic background light and the stellar baryon budget. *Mon. Not. R. Astron. Soc.*, 312:L9, 2000.

Madau P., Ferguson H. C., Dickinson M. E., Giavalisco M., Steidel C. C., and Fruchter A. High-redshift galaxies in the Hubble Deep Field: colour selection and star formation history to z˜4. *Mon. Not. R. Astron. Soc.*, 283:1388, 1996.

Madau P., Pozzetti L., and Dickinson M. The Star Formation History of Field Galaxies. *Astrophys. J.*, 498:106, 1998.

Maki H. and Susa H. Dissipation of Magnetic Flux in Primordial Gas Clouds. *Astrophys. J.*, 609:467, 2004.

Maki H. and Susa H. Dissipation of Magnetic Flux in Primordial Star Formation: From Run-away Phase to Mass-Accretion Phase. *Pub. of the Astron. Soc. of Japan*, 59:787, 2007.

Malyshkin L. and Boldyrev S. Magnetic Dynamo Action in Helical Turbulence. *Astrophys. J. Let.*, 671:L185, 2007.

Malyshkin Leonid M. and Boldyrev Stanislav. Magnetic dynamo action at low magnetic prandtl numbers. *Phys. Rev. Let.*, 105:215002, 2010.

Maunder E. W. Note on the distribution of sun-spots in heliographic latitude, 1874-1902. *Mon. Not. R. Astron. Soc.*, 64:747, 1904.

McKee C. F. and Ostriker E. C. Theory of Star Formation. *Ann. Rev. Astron. Astrophys.*, 45:565, 2007.

Mee A. J. and Brandenburg A. Turbulence from localized random expansion waves. *Mon. Not. R. Astron. Soc.*, 370:415, 2006.

Meiksin A. A. The physics of the intergalactic medium. *Reviews of Modern Physics*, 81:1405, 2009.

Meneguzzi M., Frisch U., and Pouquet A. Helical and nonhelical turbulent dynamos. *Phys. Rev. Let.*, 47:1060, 1981.

Mestel L. and Subramanian K. Galactic dynamos and density wave theory. *Mon. Not. R. Astron. Soc.*, 248:677, 1991.

Miranda O. D. and Opher R. Comparing Single-Cycle and Multicycle Explosive Scenarios for the Formation of Voids. *Astrophys. J.*, 482:573, 1997.

Miranda O. D., Opher M., and Opher R. Seed magnetic Fields Generated by Primordial Supernova Explosions. *Mon. Not. R. Astron. Soc.*, 301:547, 1998.

Moss D. and Shukurov A. Turbulence and magnetic fields in elliptical galaxies. *Mon. Not. R. Astron. Soc.*, 279:229, 1996.

Mouschovias T. C. and Paleologou E. V. The angular momentum problem and magnetic braking - an exact time-dependent solution. *Astrophys. J.*, 230:204, 1979.

Murphy E. J. The Far-Infrared-Radio Correlation at High Redshifts: Physical Considerations and Prospects for the Square Kilometer Array. *Astrophys. J.*, 706:482, 2009.

Myers P. C. and Goodman A. A. Evidence for magnetic and virial equilibrium in molecular clouds. *Astrophys. J. Let.*, 326:L27, 1988.

Nandra K., Barret D., Barcons X., Fabian A., den Herder J.-W., Piro L., Watson M., Adami C., Aird J., Afonso J. M., and al. The Hot and Energetic Universe: A White Paper presenting the science theme motivating the Athena+ mission. *ArXiv e-prints: 1306.2307*, 2013.

Nelson D., Vogelsberger M., Genel S., Sijacki D., Kereš D., Springel V., and Hernquist L. Moving mesh cosmology: tracing cosmological gas accretion. *Mon. Not. R. Astron. Soc.*, 429:3353, 2013.

Neronov A. and Vovk I. Evidence for Strong Extragalactic Magnetic Fields from Fermi Observations of TeV Blazars. *Science*, 328:73, 2010.

Neugebauer G., Habing H. J., van Duinen R., Aumann H. H., Baud B., Beichman C. A., Beintema D. A., Boggess N., Clegg P. E., de Jong T., Emerson J. P., Gautier T. N., Gillett F. C., Harris S., Hauser M. G., Houck J. R., Jennings R. E., Low F. J., Marsden P. L., Miley G., Olnon F. M., Pottasch S. R., Raimond E., Rowan-Robinson M., Soifer B. T., Walker R. G., Wesselius P. R., and Young E. The Infrared Astronomical Satellite (IRAS) mission. *Astrophys. J. Let.*, 278:L1, 1984.

Niklas S. and Beck R. A new approach to the radio-far infrared correlation for non-calorimeter galaxies. *Astron. & Astrophys.*, 320:54, 1997.

Oh S. P. Reionization by Hard Photons. I. X-Rays from the First Star Clusters. *Astrophys. J.*, 553:499, 2001.

Ossenkopf V. and Mac Low M.-M. Turbulent velocity structure in molecular clouds. *Astron. & Astrophys.*, 390:307, 2002.

Ostriker J. P. and Cowie L. L. Galaxy formation in an intergalactic medium dominated by explosions. *Astrophys. J. Let.*, 243:L127, 1981.

Padmanabhan T. *Theoretical Astrophysics - Volume 2, Stars and Stellar Systems.* 2001.

Pakmor R. and Springel V. Simulations of magnetic fields in isolated disc galaxies. *Mon. Not. R. Astron. Soc.*, 432:176, 2013.

Pakmor R., Marinacci F., and Springel V. Magnetic Fields in Cosmological Simulations of Disk Galaxies. *Astrophys. J. Let.*, 783:L20, 2014.

Parker E. N. The Formation of Sunspots from the Solar Toroidal Field. *Astrophys. J.*, 121:491, 1955a.

Parker E. N. Hydromagnetic Dynamo Models. *Astrophys. J.*, 122:293, 1955b.

Parker E. N. Sweet's Mechanism for Merging Magnetic Fields in Conducting Fluids. *J. of Geophys. Research*, 62:509, 1957.

Parker E. N. The Dynamical State of the Interstellar Gas and Field. *Astrophys. J.*, 145:811, 1966.

Passot T. and Vázquez-Semadeni E. Density probability distribution in one-dimensional polytropic gas dynamics. *Phys. Rev. E*, 58:4501, 1998.

Pérez-Sánchez A. F. and Vlemmings W. H. T. Linear polarization of submillimetre masers. Tracing magnetic fields with ALMA. *Astron. & Astrophys.*, 551:A15, 2013.

Persic M. and Rephaeli Y. X-ray spectral components of starburst galaxies. *Astron. & Astrophys.*, 382:843–859, 2002.

Persic M. and Rephaeli Y. Galactic star formation rates gauged by stellar end-products. *Astron. & Astrophys.*, 463:481, 2007.

Peters T., Banerjee R., Klessen R. S., and Mac Low M.-M. The Interplay of Magnetic Fields, Fragmentation, and Ionization Feedback in High-mass Star Formation. *Astrophys. J.*, 729:72, 2011.

Pinto C. and Galli D. Three-fluid plasmas in star formation. II. Momentum transfer rate coefficients. *Astron. & Astrophys.*, 492:1, 2008.

Pinto C., Galli D., and Bacciotti F. Three-fluid plasmas in star formation. I. Magneto-hydrodynamic equations. *Astron. & Astrophys.*, 484:1, 2008.

Piontek R. A. and Ostriker E. C. Saturated-State Turbulence and Structure from Thermal and Magnetorotational Instability in the ISM: Three-dimensional Numerical Simulations. *Astrophys. J.*, 629:849, 2005.

Planck Collaboration, Ade P. A. R., Aghanim N., Alves M. I. R., Armitage-Caplan C., Arnaud M., Ashdown M., Atrio-Barandela F., Aumont J., Aussel H., and al. Planck 2013 results. I. Overview of products and scientific results. *ArXiv e-prints: 1303.5062*, 2013a.

Planck Collaboration, Ade P. A. R., Aghanim N., Armitage-Caplan C., Arnaud M., Ashdown M., Atrio-Barandela F., Aumont J., Baccigalupi C., Banday A. J., and al. Planck 2013 results. XVI. Cosmological parameters. *ArXiv e-prints: 1303.5076*, 2013b.

Pope S. B. *Turbulent Flows*. 2000.

Press W. H. and Schechter P. Formation of Galaxies and Clusters of Galaxies by Self-Similar Gravitational Condensation. *Astrophys. J.*, 187:425, 1974.

Price D. J. and Bate M. R. The effect of magnetic fields on the formation of circumstellar discs around young stars. *Astrophys. & Sp. Sci.*, 311:75, 2007.

Price D. J. and Bate M. R. The effect of magnetic fields on star cluster formation. *Mon. Not. R. Astron. Soc.*, 385:1820, 2008.

Price R. and Duric N. New results on the radio-far-infrared relation for galaxies. *Astrophys. J.*, 401:81, 1992.

Pudritz R. E. and Norman C. A. Centrifugally driven winds from contracting molecular disks. *Astrophys. J.*, 274:677, 1983.

Pudritz R. E., Hardcastle M. J., and Gabuzda D. C. Magnetic Fields in Astrophysical Jets: From Launch to Termination. *Space Sci. Rev.*, 169:27, 2012.

Quashnock J. M., Loeb A., and Spergel D. N. Magnetic field generation during the cosmological QCD phase transition. *Astrophys. J. Let.*, 344:L49, 1989.

Rees M. J. The origin and cosmogonic implications of seed magnetic fields. *Q. J. R. Astron. Soc.*, 28:197, 1987.

Rees M. J. and Ostriker J. P. Cooling, dynamics and fragmentation of massive gas clouds - Clues to the masses and radii of galaxies and clusters. *Mon. Not. R. Astron. Soc.*, 179:541, 1977.

Reiners A. Observations of Cool-Star Magnetic Fields. *Living Reviews in Solar Physics*, 9:1, 2012.

Roberts Paul H. and Glatzmaier Gary A. Geodynamo theory and simulations. *Rev. Mod. Phys.*, 72:1081, 2000.

Roberts P. H. and King E. M. On the genesis of the Earth's magnetism. *Reports on Progress in Physics*, 76(9):096801, 2013.

Roberts P. H. and Soward A. M. Dynamo theory. *Annual Review of Fluid Mechanics*, 24:459, 1992.

Robitaille T. P. and Whitney B. A. The Present-Day Star Formation Rate of the Milky Way Determined from Spitzer-Detected Young Stellar Objects. *Astrophys. J. Let.*, 710:L11, 2010.

Rogachevskii I. and Kleeorin N. Intermittency and anomalous scaling for magnetic fluctuations. *Phys. Rev. E*, 56:417, 1997.

Russell C. T. Planetary Magnetospheres. *Science Progress*, 75:93, 1991.

Santos-Lima R., de Gouveia Dal Pino E. M., and Lazarian A. The Role of Turbulent Magnetic Reconnection in the Formation of Rotationally Supported Protostellar Disks. *Astrophys. J.*, 747:21, 2012.

Sargent M. T., Schinnerer E., Murphy E., Carilli C. L., Helou G., Aussel H., Le Floc'h E., Frayer D. T., Ilbert O., Oesch P., Salvato M., Smolčić V., Kartaltepe J., and Sanders D. B. No Evolution in the IR-Radio Relation for IR-luminous Galaxies at $z < 2$ in the COSMOS Field. *Astrophys. J. Let.*, 714:L190, 2010.

Schekochihin A. A., Cowley S. C., Hammett G. W., Maron J. L., and McWilliams J. C. A model of nonlinear evolution and saturation of the turbulent MHD dynamo. *New J. of Phys.*, 4:84, 2002.

Schekochihin A. A., Cowley S. C., Taylor S. F., Maron J. L., and McWilliams J. C. Simulations of the Small-Scale Turbulent Dynamo. *Astrophys. J.*, 612:276, 2004.

Schekochihin A. A., Haugen N. E. L., Brandenburg A., Cowley S. C., Maron J. L., and McWilliams J. C. The Onset of a Small-Scale Turbulent Dynamo at Low Magnetic Prandtl Numbers. *Astrophys. J. Let.*, 625:L115, 2005.

Schekochihin A. A., Iskakov A. B., Cowley S. C., McWilliams J. C., Proctor M. R. E., and Yousef T. A. Fluctuation dynamo and turbulent induction at low magnetic Prandtl numbers. *New J. of Phys.*, 9:300, 2007.

Schleicher D. R. G. and Beck R. A new interpretation of the far-infrared - radio correlation and the expected breakdown at high redshift. *Astron. & Astrophys.*, 556:A142, 2013.

Schleicher D. R. G., Galli D., Glover S. C. O., Banerjee R., Palla F., Schneider R., and Klessen R. S. The Influence of Magnetic Fields on the Thermodynamics of Primordial Star Formation. *Astrophys. J.*, 703:1096, 2009.

Schleicher D. R. G., Banerjee R., Sur S., Arshakian T. G., Klessen R. S., Beck R., and Spaans M. Small-scale dynamo action during the formation of the first stars and galaxies. I. The ideal MHD limit. *Astron. & Astrophys.*, 522:A115, 2010.

Schleicher D. R. G., Schober J., Federrath C., Bovino S., and Schmidt W. The small-scale dynamo: breaking universality at high Mach numbers. *New J. of Phys.*, 15 (2):023017, 2013.

Schlickeiser R. *Cosmic Ray Astrophysics*. 2002.

Schlickeiser R. Cosmic Magnetization: From Spontaneously Emitted Aperiodic Turbulent to Ordered Equipartition Fields. *Phys. Rev. Let.*, 109(26):261101, 2012.

Schlickeiser R. and Miller J. A. Quasi-linear Theory of Cosmic-Ray Transport and Acceleration: The Role of Oblique Magnetohydrodynamic Waves and Transit-Time Damping. *Astrophys. J.*, 492:352, 1998.

Schmidt W. and Federrath C. A fluid-dynamical subgrid scale model for highly compressible astrophysical turbulence. *Astron. & Astrophys.*, 528:A106, 2011.

Schmidt W., Federrath C., and Klessen R. Is the Scaling of Supersonic Turbulence Universal? *Phys. Rev. Let.*, 101(19):194505, 2008.

Schmidt W., Federrath C., Hupp M., Kern S., and Niemeyer J. C. Numerical simulations of compressively driven interstellar turbulence. I. Isothermal gas. *Astron. & Astrophys.*, 494:127, 2009.

Schober J., Schleicher D., Bovino S., and Klessen R. S. Small-scale dynamo at low magnetic Prandtl numbers. *Phys. Rev. E*, 86(6):066412, 2012a.

Schober J., Schleicher D., Federrath C., Glover S., Klessen R. S., and Banerjee R. The Small-scale Dynamo and Non-ideal Magnetohydrodynamics in Primordial Star Formation. *Astrophys. J.*, 754:99, 2012b.

Schober J., Schleicher D., Federrath C., Klessen R., and Banerjee R. Magnetic field amplification by small-scale dynamo action: Dependence on turbulence models and Reynolds and Prandtl numbers. *Phys. Rev. E*, 85(2):026303, 2012c.

Schober J., Schleicher D. R. G., and Klessen R. S. Magnetic field amplification in young galaxies. *Astron. & Astrophys.*, 560:A87, 2013.

Schober J., Schleicher D. R. G., and Klessen R. S. X-Ray Emission from Star-Forming Galaxies - Signatures of Cosmic Rays and Magnetic Fields. *ArXiv e-prints: 1404.2578*, 2014.

Sedov L. I. The movement of air in a strong explosion. *Dokl. Akad. Nauk. SSSR*, 52:17, 1946.

Sedov L. I. *Similarity and Dimensional Methods in Mechanics.* 1959.

Seifried D., Banerjee R., Klessen R. S., Duffin D., and Pudritz R. E. Magnetic fields during the early stages of massive star formation - I. Accretion and disc evolution. *Mon. Not. R. Astron. Soc.*, 417:1054, 2011.

Seifried D., Banerjee R., Pudritz R. E., and Klessen R. S. Disc formation in turbulent massive cores: circumventing the magnetic braking catastrophe. *Mon. Not. R. Astron. Soc.*, 423:L40, 2012.

Semelin B. and Combes F. New multi-zoom method for N-body simulations: application to galaxy growth by accretion. *Astron. & Astrophys.*, 441:55, 2005.

Seshadri T. R. and Subramanian K. Cosmic Microwave Background Bispectrum from Primordial Magnetic Fields on Large Angular Scales. *Phys. Rev. Let.*, 103 (8):081303, 2009.

She Zhen-Su and Leveque Emmanuel. Universal scaling laws in fully developed turbulence. *Phys. Rev. Let.*, 72(3):336, 1994.

Shetty R. and Ostriker E. C. Global Modeling of Spur Formation in Spiral Galaxies. *Astrophys. J.*, 647:997, 2006.

Shibata K. and Magara T. Solar Flares: Magnetohydrodynamic Processes. *Living Reviews in Solar Physics*, 8:6, 2011.

Shiraishi M., Nitta D., Yokoyama S., and Ichiki K. Optimal limits on primordial magnetic fields from CMB temperature bispectrum of passive modes. *J. of Cosmo. and Astropart. Phys.*, 3:041, 2012.

Shu F., Najita J., Ostriker E., Wilkin F., Ruden S., and Lizano S. Magnetocentrifugally driven flows from young stars and disks. 1: A generalized model. *Astrophys. J.*, 429:781, 1994.

Shu F. H., Najita J. R., Shang H., and Li Z.-Y. X-Winds Theory and Observations. *Protostars and Planets IV*, page 789, 2000.

Sigl G., Olinto A. V., and Jedamzik K. Primordial magnetic fields from cosmological first order phase transitions. *Phys. Rev. D*, 55:4582, 1997.

Silk J. On the fragmentation of cosmic gas clouds. I - The formation of galaxies and the first generation of stars. *Astrophys. J.*, 211:638, 1977.

Silk J. and Langer M. On the first generation of stars. *Mon. Not. R. Astron. Soc.*, 371:444, 2006.

Simon A. Diffusion of Like Particles Across a Magnetic Field. *Physical Review*, 100: 1557–1559, 1955.

Simpson J., Swinbank M., Smail I., Alexander D., Brandt N., Bertoldi F., de Breuck C., Chapman S., Coppin K., da Cunha E., Danielson A., Dannerbauer H., Greve T., Hodge J., Ivison R., Karim A., Knudsen K., Poggianti B., Schinnerer E., Thomson A., Walter F., Wardlow J., Weiss A., and van der Werf P. An ALMA Survey of Submillimeter Galaxies in the Extended Chandra Deep Field South: The Redshift Distribution and Evolution of Submillimeter Galaxies. *ArXiv e-prints: 1310.6363*, 2013.

Smith R. J., Glover S. C. O., Clark P. C., Greif T., and Klessen R. S. The effects of accretion luminosity upon fragmentation in the early universe. *Mon. Not. R. Astron. Soc.*, 414:3633, 2011.

Soida M., Beck R., Urbanik M., and Braine J. Magnetic fields in the absence of spiral density waves - NGC 4414. *Astron. & Astrophys.*, 394:47, 2002.

Solanki S. K. Sunspots: An overview. *Astron. & Astrophys. Rev.*, 11:153–286, 2003.

Spitzer L. *Physics of Fully Ionized Gases*. New York: Interscience Publishers, 1956.

Springel V., White S. D. M., Jenkins A., Frenk C. S., Yoshida N., Gao L., Navarro J., Thacker R., Croton D., Helly J., Peacock J. A., Cole S., Thomas P., Couchman H., Evrard A., Colberg J., and Pearce F. Simulations of the formation, evolution and clustering of galaxies and quasars. *Nature*, 435:629, 2005.

Stacy A., Greif T. H., and Bromm V. The first stars: formation of binaries and small multiple systems. *Mon. Not. R. Astron. Soc.*, 403:45, 2010.

Steenbeck M., Krause F., and Rädler K.-H. Berechnung der mittleren Lorentz-Feldstärke für ein elektrisch leitendes Medium in turbulenter, durch Coriolis-Kräfte beeinflußter Bewegung. *Zeitschrift Naturforschung Teil A*, 21:369, 1966.

Steidel C. C., Adelberger K. L., Giavalisco M., Dickinson M., and Pettini M. Lyman-Break Galaxies at $z \gtrsim 4$ and the Evolution of the Ultraviolet Luminosity Density at High Redshift. *Astrophys. J.*, 519:1, 1999.

Stevenson D. J. Planetary magnetic fields. *Earth and Planet. Sci. Let.* , 208:1, 2003.

Subramanian K. Dynamics of fluctuating magnetic fields in turbulent dynamos incorporating ambipolar drifts. *ArXiv e-prints: 9708216*, 1997.

Subramanian K. Unified Treatment of Small- and Large-Scale Dynamos in Helical Turbulence. *Phys. Rev. Let.*, 83:2957, 1999.

Sur S., Schleicher D. R. G., Banerjee R., Federrath C., and Klessen R. S. The Generation of Strong Magnetic Fields During the Formation of the First Stars. *Astrophys. J. Let.*, 721:L134, 2010.

Sur S., Federrath C., Schleicher D. R. G., Banerjee R., and Klessen R. S. Magnetic field amplification during gravitational collapse - influence of turbulence, rotation and gravitational compression. *Mon. Not. R. Astron. Soc.*, 423:3148, 2012.

Sweet P. A. The Neutral Point Theory of Solar Flares. In Lehnert B., editor, *Electromagnetic Phenomena in Cosmical Physics*, volume 6 of *IAU Symposium*, page 123, 1958.

Swift J. J. and Welch W. J. A Case Study of Low-Mass Star Formation. *Astrophys. J. Suppl. Ser.*, 174:202, 2008.

Swinbank A. M., Simpson J. M., Smail I., Harrison C. M., Hodge J. A., Karim A., Walter F., Alexander D. M., Brandt W. N., de Breuck C., da Cunha E., Chapman S. C., K. Coppin K. E., Danielson A. L. R., Dannerbauer H., Decarli R., Greve T. R., Ivison R. J., Knudsen K. K., Lagos C. D. P., Schinnerer E., Thomson A. P., Wardlow J. L., Weiß A., and Werf P. v. d. An ALMA survey of sub-millimetre Galaxies in the Extended Chandra Deep Field South: the far-infrared properties of SMGs. *Mon. Not. R. Astron. Soc.*, 2013.

Tabatabaei F. S., Schinnerer E., Murphy E. J., Beck R., Groves B., Meidt S., Krause M., Rix H.-W., Sandstrom K., Crocker A. F., Galametz M., Helou G., Wilson C. D., Kennicutt R., Calzetti D., Draine B., Aniano G., Dale D., Dumas G., Engelbracht C. W., Gordon K. D., Hinz J., Kreckel K., Montiel E., and Roussel H. A detailed study of the radio-FIR correlation in NGC 6946 with Herschel-PACS/SPIRE from KINGFISH. *Astron. & Astrophys.*, 552:A19, 2013.

Tan J. C. and Blackman E. G. Protostellar Disk Dynamos and Hydromagnetic Outflows in Primordial Star Formation. *Astrophys. J.*, 603:401, 2004.

Taylor G. The Formation of a Blast Wave by a Very Intense Explosion. I. Theoretical Discussion. *Royal Society of London Proceedings Series A*, 201:159, 1950.

Taylor G. I. Statistical Theory of Turbulence. *Royal Society of London Proceedings Series A*, 151:421, 1935.

Tegmark M., Blanton M. R., Strauss M. A., Hoyle F., Schlegel D., Scoccimarro R., Vogeley M. S., Weinberg D. H., Zehavi I., Berlind A., Budavari T., Connolly A., Eisenstein D. J., Finkbeiner D., Frieman J. A., Gunn J. E., Hamilton A. J. S., Hui L., Jain B., Johnston D., Kent S., Lin H., Nakajima R., Nichol R. C., Ostriker J. P., Pope A., Scranton R., Seljak U., Sheth R. K., Stebbins A., Szalay A. S., Szapudi I., Verde L., Xu Y., Annis J., Bahcall N. A., Brinkmann J., Burles S., Castander F. J., Csabai I., Loveday J., Doi M., Fukugita M., Gott J. R., III, Hennessy G., Hogg D. W., Ivezić Ž., Knapp G. R., Lamb D. Q., Lee B. C., Lupton R. H., McKay T. A., Kunszt P., Munn J. A., O'Connell L., Peoples J., Pier J. R., Richmond M., Rockosi C., Schneider D. P., Stoughton C., Tucker D. L., Vanden Berk D. E., Yanny B., York D. G., and SDSS Collaboration. The Three-Dimensional Power Spectrum of Galaxies from the Sloan Digital Sky Survey. *Astrophys. J.*, 606:702, 2004.

Tomisaka K. Collapse-Driven Outflow in Star-Forming Molecular Cores. *Astrophys. J. Let.*, 502:L163, 1998.

Trivedi P., Seshadri T. R., and Subramanian K. Cosmic Microwave Background Trispectrum and Primordial Magnetic Field Limits. *Phys. Rev. Let.*, 108(23): 231301, 2012.

Troland T. H. and Crutcher R. M. Magnetic Fields in Dark Cloud Cores: Arecibo OH Zeeman Observations. *Astrophys. J.*, 680:457–465, 2008.

Turk M. J., Abel T., and O'Shea B. The Formation of Population III Binaries from Cosmological Initial Conditions. *Science*, 325:601, 2009.

Turk M. J., Oishi J. S., Abel T., and Bryan G. L. Magnetic Fields in Population III Star Formation. *Astrophys. J.*, 745:154, 2012.

Turner M. S. and Widrow L. M. Inflation-produced, large-scale magnetic fields. *Phys. Rev. D*, 37(10):2743, 1988.

Vainshtein S. I. A theory for small-scale magnetic fields. *Zhurnal Eksperimental noi i Teoreticheskoi Fiziki*, 83:161, 1982.

Vainshtein S. I. and Zeldovich Ya. B. . *Sov. Phys. Usp.*, 15, 1972.

van der Kruit P. C. Observations of core sources in Seyfert and normal galaxies with the Westerbork synthesis radio telescope at 1415 MHz. *Astron. & Astrophys.*, 15: 110, 1971.

van der Kruit P. C. High-resolution Radio Continuum Observations of Bright Spiral Galaxies at 1415 MHz: A General Discussion. *Astron. & Astrophys.*, 29:263, 1973.

Vázquez-Semadeni E. Hierarchical Structure in Nearly Pressureless Flows as a Consequence of Self-similar Statistics. *Astrophys. J.*, 423:681, 1994.

Vazquez-Semadeni E., Canto J., and Lizano S. Does Turbulent Pressure Behave as a Logatrope? *Astrophys. J.*, 492:596, 1998.

Velikhov E. P. Stability of an Ideally Conducting Liquid Flowing Between Cylinders Rotating in a Magnetic Field. *Soviet Physics JETP*, 1959.

Vogelsberger M., Genel S., Sijacki D., Torrey P., Springel V., and Hernquist L. A physical model for cosmological simulations of galaxy formation. *ArXiv e-prints: 1305.2913*, 2013.

von Hoerner S. Eine Methode zur Untersuchung der Turbulenz der interstellaren Materie. Mit 10 Textabbildungen. *Z. für Astrophys.*, 30:17, 1951.

Waagan K., Federrath C., and Klingenberg C. A robust numerical scheme for highly compressible magnetohydrodynamics: Nonlinear stability, implementation and tests. *Journal of Computational Physics*, 230:3331, 2011.

Wang S. X., Brandt W. N., Luo B., Smail I., Alexander D. M., Danielson A. L. R., Hodge J. A., Karim A., Lehmer B. D., Simpson J. M., Swinbank A. M., Walter F., Wardlow J. L., Xue Y. Q., Chapman S. C., Coppin K. E. K., Dannerbauer H., De Breuck C., Menten K. M., and van der Werf P. An ALMA Survey of Submillimeter Galaxies in the Extended Chandra Deep Field-South: The AGN Fraction and X-Ray Properties of Submillimeter Galaxies. *Astrophys. J.*, 778:179, 2013.

Wardle M. and Ng C. The conductivity of dense molecular gas. *Mon. Not. R. Astron. Soc.*, 303:239, 1999.

Widrow L. M. Origin of galactic and extragalactic magnetic fields. *Reviews of Modern Physics*, 74:775, 2002.

Widrow L. M., Ryu D., Schleicher D. R. G., Subramanian K., Tsagas C. G., and Treumann R. A. The First Magnetic Fields. *Space Sci. Rev.*, 166:37, 2012.

Williams J. P. and Cieza L. A. Protoplanetary Disks and Their Evolution. *Ann. Rev. Astron. Astrophys.*, 49:67, 2011.

Wilson O. C., Minich G., Flather E., and Coffeen M. F. Internal Kinematics of the Orion Nebula. *Astrophys. J. Suppl. Ser.*, 4:199, 1959.

Wise J. H. and Abel T. Resolving the Formation of Protogalaxies. I. Virialization. *Astrophys. J.*, 665:899, 2007.

Wise J. H., Turk M. J., and Abel T. Resolving the Formation of Protogalaxies. II. Central Gravitational Collapse. *Astrophys. J.*, 682:745, 2008.

Woltjer L. Supernova Remnants. *Ann. Rev. Astron. Astrophys.*, 10:129, 1972.

Wood R., Bassett K., Foerster V., Spry C., and Tong L. 1.5 Tesla Magnetic Resonance Imaging Scanners Compared with 3.0 Tesla Magnetic Resonance Imaging Scanners: Systematic Review of Clinical Effectiveness [Internet]. *CADTH Rapid Response Report*, 2011.

Xu H., O'Shea B. W., Collins D. C., Norman M. L., Li H., and Li S. The Biermann Battery in Cosmological MHD Simulations of Population III Star Formation. *Astrophys. J. Let.*, 688:L57, 2008.

Xu H., Li H., Collins D. C., Li S., and Norman M. L. Evolution and Distribution of Magnetic Fields from Active Galactic Nuclei in Galaxy Clusters. II. The Effects of Cluster Size and Dynamical State. *Astrophys. J.*, 739:77, 2011.

Xue Y. Q., Luo B., Brandt W. N., Bauer F. E., Lehmer B. D., Broos P. S., Schneider D. P., Alexander D. M., Brusa M., Comastri A., Fabian A. C., Gilli R., Hasinger G., Hornschemeier A. E., Koekemoer A., Liu T., Mainieri V., Paolillo M., Rafferty D. A., Rosati P., Shemmer O., Silverman J. D., Smail I., Tozzi P., and Vignali C. The Chandra Deep Field-South Survey: 4 Ms Source Catalogs. *Astrophys. J. Suppl. Ser.*, 195:10, 2011.

Yun M. S., Reddy N. A., and Condon J. J. Radio Properties of Infrared-selected Galaxies in the IRAS 2 Jy Sample. *Astrophys. J.*, 554:803, 2001.

Zeldovich Y. B., Ruzmaikin A. A., and Sokoloff D. D. The Almighty Chance. *Science*, 249:573, 1990.

Zweibel E. G. and Yamada M. Magnetic Reconnection in Astrophysical and Laboratory Plasmas. *Ann. Rev. Astron. Astrophys.*, 47:291, 2009.

Eidesstattliche Erklärung:

Ich versichere, dass ich diese Arbeit selbstständig verfasst habe und keine anderen als die angegebenen Quellen und Hilfsmittel benutzt habe.

Heidelberg, den 3.8.2014

Jennifer Schober